Drift-kinetic simulations of Neoclassical Tearing Mode instabilities in finite collisionality tokamak plasmas

Sidney Leigh

Doctor of Philosophy

University of York
School of Physics, Engineering and Technology

December 2023

Abstract

Neoclassical tearing modes are resistive magnetohydrodynamic instabilities caused by filamentation of magnetic field-parallel current density, reconfiguring the field to form 'magnetic island' structures. Islands enhance radial transport, remove parallel bootstrap current and self-amplify, degrading confinement. Experiments indicate island growth occurs only when both a threshold island half-width w_c and poloidal beta are exceeded, the former comparable to the trapped ion banana orbit width $\rho_{b,i}$. Identifying the physical influences on w_c would inform NTM control methods in future tokamaks like ITER, where NTMs are anticipated. In this work, a new numerical simulation code "kokuchou" is developed to model the plasma response to a threshold-size magnetic island in a circular cross section, low inverse aspect ratio $\epsilon \ll 1$ tokamak under an ITER-like collisional banana regime, at the length scale $\rho_{b,i} \sim w \ll r_s$ where r_s is the minor radius of the rational surface where the island forms. Ions are iteratively tracked via a 4D drift-kinetic equation, then combined with an analytic electron response to self-consistently derive the electrostatic potential and ion flow-like momentum conservation term, both part of the 4D equation. Objectives included: (1) validation and verification of the new code, (2) studying the ion response from four full-scale runs at varying island half-width $\hat{w}[r_s]$ and plasma collisionality $\nu_\star$, and (3) calculating the island growth rate across varying $\hat{w}$, $\nu_\star$ and ion poloidal gyroradius $\hat{\rho}_{\theta,i}[r_s]$. A novel result for the threshold width dependence on both ion poloidal gyroradius and collisionality is obtained: $w_c[r_s] \approx 0.440\hat{\rho}_{\theta,i}[r_s] + 0.0178\nu_\star - 7.54 \times 10^{-5}$, over the range $\nu_\star = 0.005 - 0.020$. The interacting effects of collisions and "drift island" dynamics on island growth and their relevance to the computational problem are explored.

Contents

Acknowledgements

I would like to thank Howard Wilson for his supervision of the project, assistance with both physical and mathematical derivations, and for his guidance, patience and insight that have been crucial to keeping the project going, and I wish him the best of luck in his future endeavours. I thank Koki Imada for his co-supervision of the project, for introducing me to the `DK-NTM` code and the early versions of the new code `kokuchou`, and for providing mathematical derivations, computational assistance, and his valuable expertise working with the NTM codes. I also would like to thank Alexandra Dudkovskaia and Jack Connor for meaningful discussions on NTM physics, and for sharing their respective areas of specialism which have helped with understanding this field, and for discussing the `RDK-NTM` code. I thank David Dickinson for co-supervising the project, technical support, assistance with the procurement of computational resources, and for reviewing this thesis. I also thank Peter Hill for co-supervision of the project, thesis review, his advice on the software development, and his useful Fortran modules that were later used by the code. I thank Jacek Dobaczewski for advising the direction of the thesis and helping us plan ahead during difficult parts of the project. Finally, I thank my family for their enduring and unparalleled support, especially through the most challenging periods of the past 4 years.

Author's Declaration

I declare that this thesis is a presentation of original work that has not previously been presented for a degree or other qualification at the University of York or elsewhere.

- I declare the work presented is my own and I am the sole author.
- For work which is not my own, or which I have partly contributed to, the authors have been acknowledged via the appropriate citation.
- All sources are acknowledged as references.
- Numerical calculations were performed using the ARCHER2 UK National Supercomputing Service (https://www.archer2.ac.uk). Access to ARCHER2 was provided by the Plasma High End Computing consortium.

Chapter 1

Background

1.1 Fusion

Nuclear fusion is the process by which two nuclei approach close enough to overcome electrostatic repulsion, until the strong nuclear force combines them into a larger nucleus. If the total mass of the reactants exceeds that of the products, the mass excess Δm is directly converted to its energy equivalent under Einstein's formula $E = \Delta mc^2$, where $c \sim 3 \times 10^8$ ms^{-1} is the vacuum light speed. Fusion is among the most energy-dense reactions per unit mass known to physics, naturally occurring in stars [1]. Since its discovery, there have been attempts to harness controlled nuclear fusion on Earth for energy production. Over the past two centuries, Earth's growing human population has increasingly relied on non-renewable fossil fuels for energy, but it is well-understood that the environmental damage directly resulting from past and present fossil fuel consumption is worsening [2, Sec.A1-A2]. More recent discussion highlights the prolonged socioeconomic instability inflicted on fossil fuel-reliant economies during supply shocks, which are only expected to worsen under rising demand and tightening supply [3] [4, Sec.2.2]. The only scenario in which these two issues are overcome is one where fossil fuel use is phased out entirely.

Facilitating the necessary transition to alternative energy sources presents its own challenges. Renewables including solar, wind, hydroelectric and biofuels are expected to contribute substantially to the future global energy mix, but each has its own limitations pertaining to location, variability and energy density, requiring extensive storage and transmission infrastructure to respond to demand flexibly [4, Sec.6.6-6.7]. Nuclear fission overcomes these limitations, but introduces further issues around security, cost, waste management and the scarcity of its own fuel. Increasingly, fusion power is considered as an option, being a potentially low-carbon, low-waste,

energy-dense and abundant electricity source without the same spatial, temporal and safety considerations as conventional renewables or fission [5, Sec.1.1-1.2]. While it remains an emerging technology, interest in fusion power has been driven by recent milestone results from established experiments [6], and a growing private sector [7, Fig.6-7].

Fusion, unlike fission, is not a runaway chain reaction and instead requires very high densities and/or temperatures to initiate and sustain. Stars provide these confinement conditions under immense gravitational forces; on Earth, an artificial means of confinement must instead be developed and optimised for power production. The most energetically economical fusion reaction in lab conditions is of the hydrogen isotopes of deuterium and tritium, or D-T fusion [8]. It produces a helium-4 nucleus and a neutron, and a total of 17.6 MeV energy:

$$\mathrm{D}^2 + \mathrm{T}^3 \rightarrow \mathrm{He}^4(3.5\ \mathrm{MeV}) + \mathrm{n}^1(14.1\ \mathrm{MeV}) \tag{1.1.1}$$

Other reactions can also occur in this same environment, including D-D and D-He^3,

$$\mathrm{D}^2 + \mathrm{D}^2 \rightarrow \mathrm{He}^3 + \mathrm{n}^1 + 3.27\ \mathrm{MeV}$$
$$\mathrm{D}^2 + \mathrm{D}^2 \rightarrow \mathrm{T}^3 + \mathrm{H}^1 + 4.03\ \mathrm{MeV}$$
$$\mathrm{D}^2 + \mathrm{He}^3 \rightarrow \mathrm{He}^4 + \mathrm{H}^1 + 18.3\ \mathrm{MeV}$$

but the collisional probability or reaction cross section $\langle \sigma v \rangle$ of D-T fusion is over an order of magnitude higher than the others at lower temperatures of T = O(10 keV), (10^8 K), peaking at T = 30 keV [9]. Under these conditions, D-T fuel exists as a fully-ionised plasma that can be manipulated with electromagnetic fields. These temperatures must firstly be reached via external heating. Once reactions occur, the 3.5 MeV helium-4 nuclei can deliver heat back to the D-T reactants. The 14.1 MeV neutrons rarely interact with the reactants and are instead absorbed by the reactor walls, from which energy may be extracted for power generation via "blanket" structures. To operate continuously, the power released from fusion P_{fus} must exceed the external heating power required to maintain reaction conditions, P_{ext}. These are used to define a common measure of reactor performance and efficiency known as the gain $Q = P_{fus}/P_{ext}$, where the critical requirement for net output, known as *breakeven*, is $Q \geq 1$. The physical criteria for satisfying breakeven were studied by J. D. Lawson, which also requires that the D-T reaction occurs at minimum temperature of T > 3 keV to overcome radiative power losses [10]. When $Q \rightarrow \infty$, the reactor enters an *ignition* state and fusion self-sustains without external heating.

Reactor performance is often summarised by a single value known as the fusion triple product, which for ignition in D-T to occur, is approximated by:

$$nT\tau_E \geq \frac{12}{E_\alpha}\frac{T^2}{\langle\sigma v\rangle} \tag{1.1.2}$$

where τ_E is the energy confinement time over which power losses occur. Taking T to be as close as possible for peak D-T reactivity $\langle\sigma v\rangle$ to occur, ignition is then reached by maximising the fuel density n and/or confinement time τ_E.

The two main approaches to fusion power are magnetic confinement fusion (MCF) and inertial confinement fusion (ICF). ICF uses high-energy lasers or particles to compress a fuel target to high densities over an inherently short confinement time to achieve ignition. Conversely, In MCF, fuel is heated in a vacuum chamber into a charged plasma and kept in place over long confinement times with electromagnetic fields. A comprehensive review of progress toward breakeven and ignition in a range of ICF and MCF devices is given in Ref [6]. Prominent examples of MCF devices include JET (Joint European Torus) and its successor ITER, currently under construction. As of 2023, JET holds the record for gain ($Q = 0.7$) and confinement time ($\tau_E \approx 0.2$-0.3 s) [11]. ITER aims to achieve $Q \geq 10$ over a shot duration[1] of ≈ 500 s, [12, 13]. Successors to ITER, including DEMO [14] and STEP [15] plan to demonstrate electricity production in the mid-21st century. All are a type of device known as a tokamak, covered in Sec. 1.3. As the operating conditions of MCF devices approach the ignition criterion, preparations must be made to identify and prevent the possible phenomena that limit further increases in plasma density and confinement time, which necessitates a comprehensive understanding of plasma transport through theoretical modelling. This work will cover one particular performance-limiting plasma phenomenon that is especially relevant in the context of ITER and future devices.

[1] Shot duration is the *controlled* operating time, not determined by power losses as confinement time is.

1.2 Plasma

1.2.1 Introduction to plasmas

Plasma is a gas-like state of matter where a significant fraction of particles are ionised, typically at high temperatures in a vacuum [16, pp. 2–3]. The charged species in a plasma are ions and electrons. Their motion is determined by the Coulomb force, both at short-range by collisions and at long-range by electromagnetic fields, including those of other charged species, giving rise to the characteristic collective behaviour of plasmas. This allows plasma particles to screen out variations in the electrostatic potential over a characteristic scale, the Debye length λ_D. Beyond this scale, the plasma charge density is near-zero and said to be quasineutral.

Throughout this work, we consider a fusion plasma in ITER-like conditions at temperatures of $T_0 \sim O(10\text{ keV})$, densities of $n_0 \sim O(10^{20}\text{ m}^{-3})$ in a magnetic field of $B \sim O(5\text{ T})$ [13]. Under these conditions, plasma transport is governed primarily by long-range electromagnetic forces rather than by collisions and is considered *magnetised*. The phenomena of interest occur over length scales of $L \sim 0.01 - 1\text{ m}$ ($\gg \lambda_D$), over which quasineutrality holds, and so descriptions of such a system from Ref. [17] will be used. For simplicity and conformity with this theory, the plasma is fully ionised and consists solely of hydrogen ions[2] of charge number $Z_i = +1$, mass m_i, and electrons of charge number $Z_e = -1$ and mass m_e. Ion and electron quantities use subscripts i and e respectively, while equilibrated quantities for both species have subscript 0. Vector quantities, e.g. magnetic field $\mathbf{B}$, are in bold, whose magnitude is in italic. Magnetic field-parallel and perpendicular components of vector quantities use subscripts $\parallel$ and $\perp$ respectively. The following sections will cover fundamentals of plasma physics that comprise the theory within this work, much of which follows Refs. [18, 17].

[2] Any isotope of hydrogen will be applicable with the theory outlined here, and the quantities described later in Ch.2 are normalised to the ion mass, hence the final result applies equally to both proton-electron plasmas and deuteron-electron plasmas. Multi-ion systems like burning D-T plasmas would introduce complexity via collision dynamics and differences in orbit width between ion species, and so only one ion species is considered here.

1.2.2 Single charged particle motion

Eq.(1.2.1) describes the motion of a particle of species j, mass m_j, charge eZ_j and velocity $\mathbf{v}_j$, in an electric field $\mathbf{E}$ and magnetic field $\mathbf{B}$ (magnitude B):

$$m_j \frac{d\mathbf{v}_j}{dt} = eZ_j(\mathbf{E} + \mathbf{v}_j \times \mathbf{B}) \tag{1.2.1}$$

Here, $eZ_j\mathbf{E}$ is the electrostatic force, acting parallel to $\mathbf{E}$. The term $eZ_j\mathbf{v}_j \times \mathbf{B}$ is the Lorentz force, which depends only on the $\mathbf{B}$-perpendicular component of velocity, $v_\perp$. It is centripetal, causing circular motion perpendicular to $\mathbf{B}$ about a *guiding centre*, at a gyroradius $\rho_j = \frac{m_j v_\perp}{eZ_j B}$, or *Larmor radius*, and gyrofrequency $\omega_j = \frac{eZ_j B}{m_j}$. Assume the electromagnetic fields vary slowly in time relative to ω_j, and $\rho_j \ll L_B$, where $L_B^{-1} = |\nabla B|/|B|$ is the inverse of the magnetic field gradient length scale. It follows that Eq.(1.2.1) has two constants of motion correct to $O(\rho_j/L_B)$: the total energy $\mathcal{E}$ (constant as $\frac{d\mathbf{v}_j}{dt} \perp \mathbf{v}_j$) and magnetic moment $\mu = \frac{m_j v_\perp^2}{2B}$, the latter associated with the area enclosed by the gyro-orbit.

The particle's trajectory is dependent on the electromagnetic field geometry. For the special case where $\mathbf{E} = 0$ and $\mathbf{B}$ is homogeneous and straight, a particle moving perpendicular to the magnetic field ($v_\perp \neq 0$) experiences only the Lorentz force and has a circular trajectory. When field-parallel velocity $v_\parallel \neq 0$, the trajectory is helical, with the guiding centre following the magnetic field lines. If there is spatial or temporal variation in $\mathbf{E}$ or $\mathbf{B}$, the particle's guiding centre will drift relative to the magnetic field lines, with examples shown in Fig.1.1.

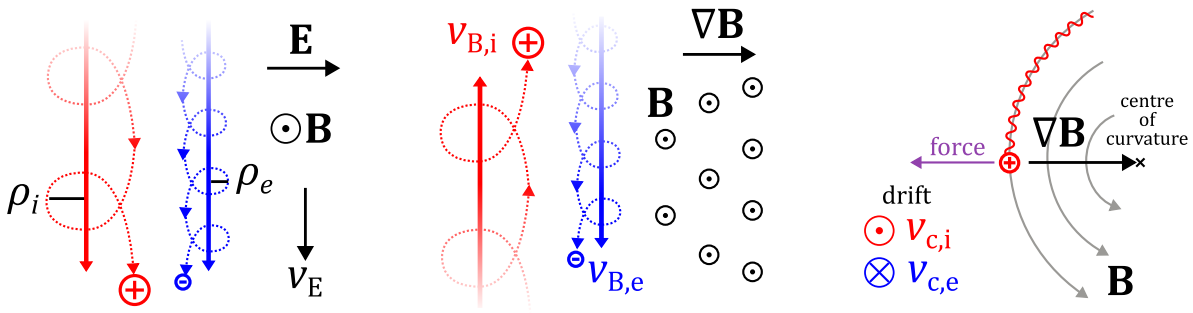

(a) $\mathbf{E} \times \mathbf{B}$ drift. (b) $\nabla\mathbf{B}$ drift. (c) Curvature drift.

Figure 1.1: Magnetic drift effects of an ion (red +) and electron (blue −) in an electromagnetic field. Particle trajectories shown by dashed red/blue curves with arrowheads indicating one gyro-orbit. Guiding centre trajectories shown by thick solid red/blue arrows.

The $\mathbf{E}\times\mathbf{B}$ drift, shown in Fig.1.1a, occurs under a finite $\mathbf{B}$-perpendicular electric field $E_\perp$. As the gyrating particle periodically moves with and against $\mathbf{E}$, its guiding centre drifts perpendicular

to both **E** and **B** with velocity $\boldsymbol{v}_E$, noting $\boldsymbol{v}_E$ is independent of charge and mass:

$$\boldsymbol{v}_E = \frac{\mathbf{E} \times \mathbf{B}}{B^2} \tag{1.2.2}$$

Magnetic drifts include the ∇B and curvature drifts, shown in Fig.1.1b and 1.1c respectively. Both are charge and mass dependent, generating current as ions and electrons drift in opposite directions. The ∇B drift occurs under inhomogeneous **B** fields. As **B** varies along each orbit, the perpendicular velocity $v_\perp$ must vary to conserve magnetic moment μ, while $v_\parallel$ also varies to conserve energy $\mathcal{E}$. Similarly, the curvature drift occurs under non-uniform, non-straight **B** fields, and the particle experiences a centrifugal force that produces a net drift. In an axisymmetric magnetic field, both magnetic drifts are perpendicular to both **B** and its gradient ∇B, and are expressed as a combination $\boldsymbol{v}_b$, where ∇B and curvature drifts are represented by the $\frac{1}{2}v_\perp^2$ and $v_\parallel^2$ terms respectively:

$$\boldsymbol{v}_b = \frac{v_\parallel^2 + \frac{1}{2}v_\perp^2}{\omega_j} \frac{\mathbf{B} \times \nabla B}{B^2} \tag{1.2.3}$$

Polarisation drift occurs under both a **B**-field and a time-varying **E**-field, and is parallel to **E** with velocity $\boldsymbol{v}_{pol} = \frac{1}{\omega_j B} \frac{\partial \mathbf{E}}{\partial t}$. Being charge-dependent, it induces a current known as the polarisation current.

Another important effect that occurs under a spatially-varying magnetic field is *trapping* or mirroring. Consider an axisymmetric **B**-field with increasing magnitude in a direction z as shown in Fig.1.2. A particle entering the stronger region of **B**-field will see its gyroradius reduce, and require $v_\perp$ to increase to conserve magnetic moment μ. To also conserve kinetic energy $\mathcal{E}$, $v_\parallel$ must decrease. If the particle velocity vector's angle of deviation from the field lines, or pitch angle, is sufficiently large, then $v_\parallel$ flips sign and the particle is reflected. Magnetic trapping leads to significant tokamak physics that is discussed later in Sec.1.3.3.

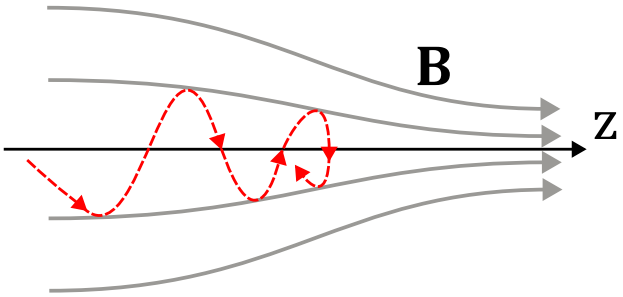

Figure 1.2: Guiding centre trajectory of a charged particle (red, dashed) reflected at a region of stronger **B**-field (grey, solid).

1.2.3 Kinetic description of a plasma

In Sec.1.2.2, single charged particle responses to external electromagnetic fields were considered. In modelling plasmas, every charged particle's motion is coupled to the fields of other particles, and vice versa. Computationally, this introduces the need for self-consistency, where particle motions and their fields must be iteratively recalculated against each other. This is complicated further by the very large number of particles in the system ($\sim 10^{23}$ in an ITER-like case, in a volume of $\sim O(10^3\ \mathrm{m}^3)$ [19]), so a statistical description is necessary. In kinetic theory, the distribution function $f_j(\mathbf{r}, \mathbf{v}, t)$ describes all particles of species j, with 3D position vector $\mathbf{r}$ and 3D velocity vector $\mathbf{v}$ at time t, as a number density per unit volume of 6D phase space near $(\mathbf{r}, \mathbf{v})$. Each volume element $d^3r d^3v$ therefore contains $f_j(\mathbf{r}, \mathbf{v}, t)\ d^3r\ d^3v$ particles at a time t. In general, $f_j(\mathbf{r}, \mathbf{v}, t)$ satisfies the 6D kinetic equation of motion:

$$\frac{\partial f_j}{\partial t} + \mathbf{v}_j \cdot \nabla_r(f_j) + \frac{\mathbf{F}}{m_j} \cdot \left(\frac{\partial f_j}{\partial \mathbf{v}}\right) = C_j(f_j) \tag{1.2.4}$$

where ∇_r and ∇_v are vector differential operators which, in 3D Cartesian coordinate space can be written as:

$$\nabla_r = \sum_{i=1}^{3} \frac{\partial}{\partial r_i} = \left(\frac{\partial}{\partial x}, \frac{\partial}{\partial y}, \frac{\partial}{\partial z}\right), \qquad \nabla_v = \sum_{i=1}^{3} \frac{\partial}{\partial v_i} = \left(\frac{\partial}{\partial v_x}, \frac{\partial}{\partial v_y}, \frac{\partial}{\partial v_z}\right) \tag{1.2.5}$$

and $C_j(f_j)$ is the collision operator, representing short-range effects. For a plasma, taking $\mathbf{F}$ to be the Lorentz force $eZ_j(\mathbf{E} + \mathbf{v} \times \mathbf{B})$ from Eq.(1.2.1), then Eq.(1.2.4) becomes the Fokker-Planck equation [20]:

$$\frac{\partial f_j}{\partial t} + \mathbf{v} \cdot \nabla f_j + \frac{eZ_j}{m_j}(\mathbf{E} + \mathbf{v} \times \mathbf{B}) \cdot \frac{\partial f_j}{\partial \mathbf{v}} = C_j(f_j) \tag{1.2.6}$$

Here, $\mathbf{E}$ and $\mathbf{B}$ now represent the macroscopic electric and magnetic fields respectively (i.e., over lengths $L \gg \lambda_D$), ignoring short-range fluctuations of individual particles which are instead encapsulated within the $C_j(f_j)$ collision operator. Here, $C_j(f_j)$ describes interactions of species j with all relevant species k in the system (including j itself):

$$C_j(f_j) = \sum_k C_{jk}(f_j, f_k) \tag{1.2.7}$$

Ignoring collisions ($C_j(f_j) = 0$), Eq.(1.2.6) becomes the Vlasov equation. Despite plasma transport in this work not being collision-dominated, their role is physically significant, and the exact

form of C_j will be discussed later after further information is given (see 2.2.1).

Because the 6D Fokker-Planck equation Eq.(1.2.6) is still computationally challenging, it is often simplified depending on the spatial and temporal scales of interest. For example, gyrokinetic theory accounts for variations at the scale of gyro-motion (ρ_j and ω_j). Drift-kinetic theory simplifies particle motion by averaging out variations in f_j over the gyro-scale, provided these are small relative to the system size L. Here, only particles' guiding centre motion is tracked via a gyro-averaged distribution function, $\bar{f}_j$. Working in the limit of small $\delta = \rho_j/L \ll 1$, gyro-averaging Eq.(1.2.6) gives an $O(\delta)$ approximation of the drift-kinetic equation [18, p. 128]:

$$\frac{\partial \bar{f}_j}{\partial t} + v_\parallel \nabla_\parallel \bar{f}_j + (\boldsymbol{v}_E + \boldsymbol{v}_b)\cdot\nabla \bar{f}_j + \frac{eZ_j}{m_j}\left(\frac{v_\parallel E_\parallel}{v}\frac{\partial \bar{f}_j}{\partial v} - \frac{(\boldsymbol{v}_E + \boldsymbol{v}_b)\cdot\nabla\Phi}{v}\frac{\partial \bar{f}_j}{\partial v}\right) = C(\bar{f}_j) \tag{1.2.8}$$

where Φ is the electrostatic potential, $E_\parallel$ is the $\mathbf{B}$-parallel component of the electric field, and gradient operator $\nabla_\parallel = \mathbf{b}\cdot\nabla$, where $\mathbf{b} = \mathbf{B}/B$ is the unit vector of $\mathbf{B}$. The terms $\boldsymbol{v}_E$ and $\boldsymbol{v}_b$ are the $\mathbf{E}\times\mathbf{B}$ and magnetic drifts respectively (see Sec.1.2.2). The drift-kinetic equation will be used throughout this work to track the ion distribution function for the phenomena of interest.

1.2.4 Fluid description of a plasma

Macroscopic plasma quantities in the kinetic equation are contained within velocity moments of the distribution function f_j. The 0^{th} moment, Eq.(1.2.9), gives the number density of species j:

$$n_j(\mathbf{r},t) = \int d^3v\ f_j(\mathbf{r},\mathbf{v},t) \tag{1.2.9}$$

and the 1^{st} moment gives the flow:

$$\mathbf{u}_j(\mathbf{r},t) = \frac{1}{n_j}\int d^3v\ \mathbf{v} f_j(\mathbf{r},\mathbf{v},t) \tag{1.2.10}$$

Similarly, taking velocity moments of the kinetic equation itself gives the *fluid* equations, which provide conservation laws for those macroscopic quantities by treating the system as a continuous fluid. This approximation is valid, provided the collisional mean free path is small, i.e., collisions are frequent over the *timescale of interest*. The 0^{th} moment of Eq.(1.2.6) gives the continuity equation (number density conservation in the absence of gains or losses),

$$\frac{\partial n_j}{\partial t} + \nabla(n_j \mathbf{u}_j) = 0 \tag{1.2.11}$$

and the 1st moment gives the force balance equation:

$$m_j n_j \left(\frac{\partial \mathbf{u}_j}{\partial t} + (\mathbf{u}_j \cdot \nabla)\mathbf{u}_j \right) = -\nabla \mathbf{p}_j + n_j e Z_j (\mathbf{E} + \mathbf{u} \times \mathbf{B}) + R_j \tag{1.2.12}$$

where $\mathbf{p}_j$ is the pressure, and R_j is a drag force originating from the collision operator of Eq.(1.2.6). Neglecting R_j for simplicity, from Eq.(1.2.12) a fluid current arises, found by rearranging for the perpendicular flow $u_{\perp,j}$:

$$u_{\perp,j} = \frac{\mathbf{E} \times \mathbf{B}}{B^2} + \frac{\mathbf{B} \times \nabla \mathbf{p}_j}{n_j e Z_j B^2} \tag{1.2.13}$$

The first right-hand term is the kinetic $\mathbf{E} \times \mathbf{B}$ drift $\boldsymbol{v}_E$, while the second term, the *diamagnetic drift*, originates from the fluid treatment. Under a finite $\mathbf{B}$-perpendicular pressure gradient, the difference in number of gyrating particles between adjacent field lines produces a net fluid flow, irrespective of individual particle motion. As diamagnetic drift is charge-dependent, the diamagnetic current $\mathbf{J}_D$ is induced perpendicular to $\mathbf{B}$. The total current induced is given by:

$$\mathbf{J}_D = \frac{\mathbf{B} \times \nabla \mathbf{p}}{B^2} \tag{1.2.14}$$

where $\mathbf{p}$ is the total plasma pressure.

The next unknown to determine is pressure $\mathbf{p}_j$. The 2nd moment of the kinetic equation determines $\mathbf{p}_j$ in terms of energy flux, itself determined by additional moments and unknowns. Introducing a *closure* relation limits further ordering. A common example is the adiabatic model, with $\mathcal{C}$ and γ as constants:

$$\frac{\partial}{\partial t}(\mathbf{p}_j n_j^{-\gamma}) = 0 \ , \qquad \rightarrow \mathbf{p}_j = \mathcal{C} n_j^{\gamma} \tag{1.2.15}$$

1.2.5 MHD description of a plasma

The ion-electron plasma in this work can be modelled as two distinct but coupled fluids. Where appropriate, ideal magnetohydrodynamic (MHD) theory can be employed, which uses one set of fluid equations for both species and neglects electron inertia due to the mass difference $m_e \ll m_i$. MHD is particularly useful for modelling small perturbations affecting an equilibrium state. Here, the continuity equation Eq.(1.2.11) becomes the mass conservation equation, where $nm_i \approx n(m_i + m_e)$ is the plasma mass density and $\mathbf{u}$ ($\approx \mathbf{u}_i$) is the flow of both species:

$$\frac{\partial}{\partial t}(nm_i) + \nabla \cdot (nm_i \mathbf{u}) = 0 \tag{1.2.16}$$

Similarly, the force balance equation Eq.(1.2.12) becomes:

$$nm_i \left(\frac{\partial \mathbf{u}}{\partial t} + (\mathbf{u} \cdot \nabla)\mathbf{u} \right) = -\nabla \mathbf{p} + \mathbf{J} \times \mathbf{B} \tag{1.2.17}$$

where $\mathbf{J} = ne(Z_i \mathbf{u}_i - \mathbf{u}_e)$ is the plasma current density and $\mathbf{p}$ is the total plasma pressure. To close the ideal MHD system, the adiabatic equation of state Eq.(1.2.15) becomes:

$$\frac{\partial \mathbf{p}}{\partial t} + (\mathbf{u} \cdot \nabla)\mathbf{p} = -\gamma \mathbf{p} \nabla \cdot \mathbf{u} \tag{1.2.18}$$

Plasma species, fields and currents are coupled through Maxwell's equations:

$$\nabla \times \mathbf{B} = \mu_0 \mathbf{J} - \frac{1}{c^2} \frac{\partial \mathbf{E}}{\partial t} \tag{1.2.19}$$

$$\nabla \times \mathbf{E} = -\frac{\partial \mathbf{B}}{\partial t} \tag{1.2.20}$$

$$\nabla \cdot \mathbf{B} = 0 \tag{1.2.21}$$

$$\nabla \cdot \mathbf{E} = \frac{1}{\epsilon_0} \sum_j n_j e Z_j \tag{1.2.22}$$

where c is the vacuum speed of light and μ_0 is the vacuum permeability. Eq.(1.2.19) is also known as Ampère's law. Fields and current density are linked via Ohm's law, for a given resistivity η:

$$\mathbf{E} + \mathbf{u} \times \mathbf{B} = \eta \mathbf{J} \tag{1.2.23}$$

When resistivity $\eta = 0$, $\nabla \cdot \mathbf{E} = 0$ and the displacement current $\frac{1}{c^2} \frac{\partial \mathbf{E}}{\partial t}$ of Eq.(1.2.19) is neglected, this case is known as ideal MHD. Here, the conservation of magnetic flux through any surface S applies, forcing the fluid elements of the plasma and the field to coevolve under the so-called *frozen-in condition*. In the case of resistive MHD where $\eta \neq 0$, collisional diffusion across field lines becomes significant, particularly in regions of high current density, and the frozen-in condition does not apply. Where energetically favourable, the magnetic geometry can then spontaneously reconfigure in a field line reconnection event [16, pp. 322–324]. The sudden transfer of magnetic energy to the plasma during reconnection can enhance the process, resulting in the growth of resistive MHD instabilities that can modify the global equilibrium even from a small initial state [21].

1.3 Tokamaks

1.3.1 Plasma in a toroidal magnetic field

Recalling Sec.1.1, in magnetic confinement fusion, ignition criteria are achieved by keeping a sufficiently hot, dense plasma in place with magnetic fields over long durations. It is possible to magnetically trap a plasma in a cylindrical magnetic field between two axisymmetric magnetic coils, but collisions will alter particles' pitch angle and de-trap them, leading to end losses. These losses can be avoided by joining the ends into a toroidal system, as in Fig.1.3:

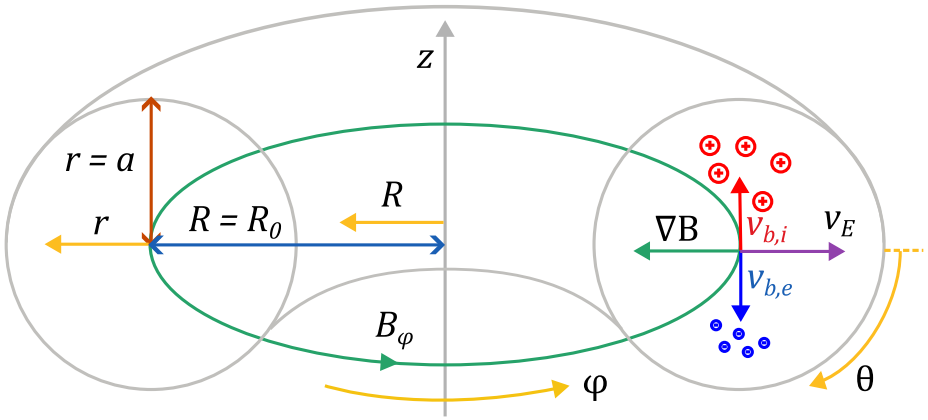

Figure 1.3: Plasma ions (red +) and electrons (blue −) in a purely toroidal magnetic field B_φ experiencing vertical magnetic drift v_B and radial $\mathbf{E} \times \mathbf{B}$ drift v_E.

Here, toroidal geometry is described by the major radius R, minor radius r, vertical direction z. A right-handed toroidal angle φ and poloidal angle θ are used with $\theta = 0$ at the outboard midplane, following the convention in Ref. [22]. Key locations are the central axis ($R = 0$), core ($R = R_0$, $r = 0$) and edge ($r = a$). The aspect ratio is defined as R_0/a; its inverse $\epsilon = a/R_0$ is used in transport physics. The externally-induced **B**-field of Fig.1.3 is toroidal, but its strength scales as $B_\varphi \propto R^{-1}$, with ∇B facing toward the central axis. This toroidal field alone does not provide sufficient confinement, as the ions and electrons will experience ∇B and curvature drifts in opposite vertical directions, inducing an **E**-field in z that causes both to $\mathbf{E} \times \mathbf{B}$-drift radially outward. To prevent this charge separation, the magnetic drifts can be averaged out by introducing a poloidal field component B_θ to make the total field helical. This is done either by: i) using shaped coils, as in *stellarator* devices, or ii) inducing a toroidal plasma current as in the aforementioned *tokamak* design from Sec.1.1. However, the inherent scaling of $B_\varphi \propto R^{-1}$ persists, which influences transport as Sec.1.3.3 will cover.

1.3.2 Tokamak equilibrium

In stability modelling, the *equilibrium* is the time-independent ($\partial/\partial t = 0$) steady state in which the plasma is unperturbed but not necessarily stable. In the case of stationary net fluid flow $\mathbf{u} \cdot \nabla \mathbf{u} = 0$, the ideal MHD force balance equation Eq.(1.2.17) reduces to:

$$\mathbf{J} \times \mathbf{B} = \nabla \mathbf{p} \tag{1.3.1}$$

To satisfy this, there must be field-perpendicular current[3], and no field-parallel pressure gradient:

$$\mathbf{B} \cdot \nabla \mathbf{p} = 0 \tag{1.3.2}$$

Both $\mathbf{B}$ and $\mathbf{J}$ must then lie on a set of nested, axisymmetric toroidal *flux surfaces* of constant pressure [17, pp. 117–124], as illustrated in Fig.1.4. Each surface is labelled by the poloidal flux ψ, with $\psi = 0$ at the core and $\psi = \psi_a$ at the edge.

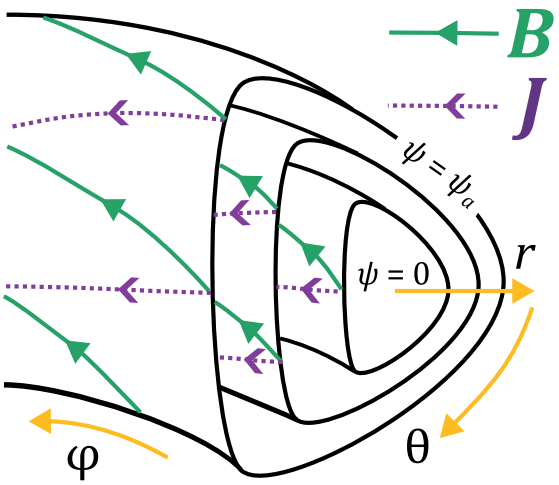

Figure 1.4: Poloidal cross section of a generic ideal MHD tokamak equilibrium with nested, shaped toroidal flux surfaces and Shafranov shift. Magnetic field (green) and current density (purple) are shown.

Conventionally, ψ is used instead of r as the radial coordinate, as pressure and other parallel transport-dominated quantities like temperature and density become functions of ψ. Using ψ also accounts for poloidal shaping and off-axis shifts of flux surfaces from $R = R_0$, known as Shafranov shift, as depicted in Fig.1.4. This Shafranov shift pushes inner flux surfaces outboard slightly, due to the imbalance of inboard and outboard pressure per unit area on a toroidal flux surface, as a direct result of pressure being constant on those surfaces.

[3] The diamagnetic current provides this, see Eq.(1.2.14)

In the limit of small $\delta = \rho_j/L \ll 1$, to the leading order the charged particles free-stream along the magnetic field, remaining within $O(\rho_j)$ of their flux surface. Good confinement is characterised by minimal transport between flux surfaces (e.g. via collisions), allowing high pressures and temperatures to be sustained in the core. For optimal confinement, the plasma pressure profile should be highest at the core to maximise reaction rate, and lowest at the edge to minimise radial transport to the wall. A high plasma beta β, the ratio of plasma pressure to magnetic pressure, is also desirable as it indicates the efficiency of the applied field at attaining the required core pressure for fusion [8, pp. 115–116]:

$$\beta = \frac{p}{B^2/2\mu_0} \tag{1.3.3}$$

A similar term, the poloidal beta β_θ, substitutes B for its poloidal component B_θ, and is also an important measure of performance.

Field line helicity is described by the safety factor q, the number of toroidal turns per poloidal turn that a magnetic field line executes around a flux surface. *Rational flux surfaces* are those where $q = m/n$ is a rational number, with m and n being the toroidal and poloidal mode numbers respectively. The rate of change in q across flux surfaces is described by the magnetic shear length scale L_q^{-1}, closely linked with plasma stability. The shear is defined via the dimensionless quantity:

$$\frac{1}{L_q} = \frac{1}{q}\frac{dq}{dr} \tag{1.3.4}$$

The periodicity of closed field lines on rational surfaces allows perturbations of corresponding mode to resonate, which can develop into plasma instabilities that negatively affect confinement.

1.3.3 Neoclassical transport in a large aspect ratio tokamak

Equilibrium geometry is often simplified by working in the limit of large aspect ratio where its inverse is small: $\epsilon = a/R_0 \ll 1$, then neglecting terms in $O(\epsilon^2)$ and smaller, including the Shafranov shift [17, p. 123]. Similarly, if the poloidal cross section of the outermost flux surface is assumed circular, then the inner surfaces are approximately so, as in Fig.1.5a. A further simplification treats field strength B as near-constant on each surface, as in the *classical* plasma transport model, where the primary radial transport mechanism across flux surfaces is collisional diffusion. However, due to $B \propto R^{-1}$, the variation in field strength on flux surfaces will introduce physics that dominates over classical transport[17, pp. 158–159].

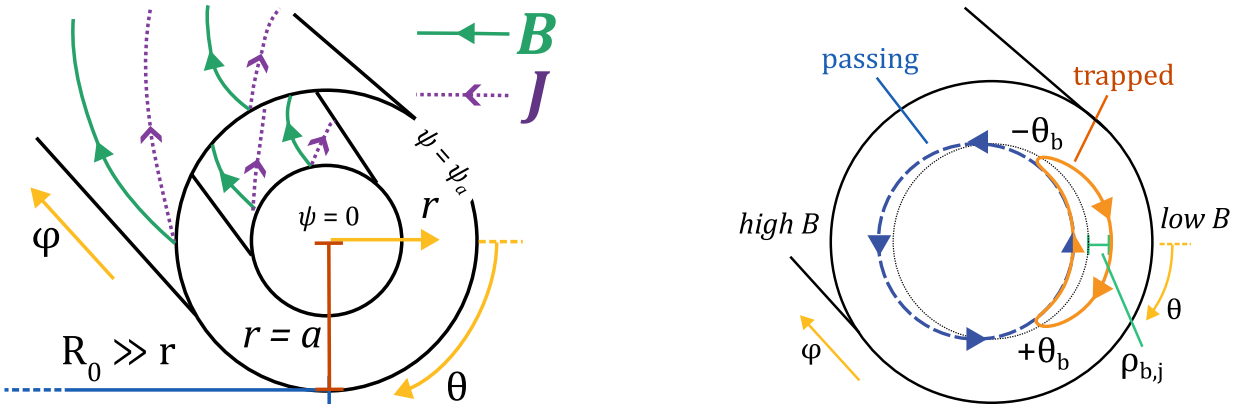

(a) Neoclassical equilibrium.

(b) Passing and trapped particle orbits.

Figure 1.5: Poloidal cutaway of a circular cross section tokamak plasma, $\epsilon \ll 1$, no Shafranov shift.

In *neoclassical* transport, the toroidal nature of the magnetic field geometry is retained, resulting in a fraction of particles with near-perpendicular velocity vectors ($|v_\parallel|/v_\perp \leq \sqrt{\epsilon}$) becoming magnetically trapped on the outboard weak-field side of flux surfaces, confined to a characteristic banana-shaped orbit, as shown in Fig.1.5b. The poloidal extent of the trapped orbit from the midplane is known as the *bounce point* θ_b. Non-trapped *passing* particles follow helical guiding centre trajectories that are either parallel or anti-parallel to the field, while trapped orbits reverse direction every half-orbit. Both types of orbit are shifted radially from their flux surface due to magnetic drifts[4]. Each half of a banana orbit is shifted in opposite directions, giving it a finite radial width $\rho_{b,j}$ which, in the $\epsilon \ll 1$ limit, is approximately:

$$\rho_{b,j} \approx \sqrt{\epsilon}\rho_{\theta,j} \ , \qquad \rho_{\theta,j} = \frac{m_j v_{\mathrm{th},j}}{eB_\theta} \tag{1.3.5}$$

Here, $\rho_{\theta,j}$ is the poloidal gyroradius, the projection of gyroradius ρ_j onto the poloidal field component B_θ only, and $v_{\mathrm{th},j}$ is the thermal velocity of species j. Note that the poloidal gyroradius exceeds the full gyroradius, i.e., $\rho_{\theta,j} > \rho_j$, and due to the mass difference the ion banana width greatly exceeds that of electrons, $\rho_{b,i} \gg \rho_{b,e}$.

The neoclassical transport regime depends on collision frequency, as collisions can result in the trapping or de-trapping of particles via a change in pitch angle. This is important for particles whose velocity pitch-angle lies near the *trapped-passing boundary* where $|v_\parallel|/v_\perp = \sqrt{\epsilon}$, where most interactions between passing and trapped particles occur. The plasma collisionality $\nu_\star$ is

[4]Passing particles will deviate by $O(\epsilon\rho_{\theta,j})$, whereas the deviation of trapped particles is a factor $O(\epsilon^{-1/2})$ larger as they slow down near the bounce points.

defined here as the dimensionless ratio of the frequency of de-trapping collisions to the banana orbit frequency [17, pp. 148–150]. In the Pfirsch-Schlüter regime ($\nu_\star > 1$), trapped particles are de-trapped before completing an orbit, so their impact is not significant. Modern, higher-temperature tokamaks operate in the low-collisionality banana-plateau regimes where $\nu_\star < 1$. In the limit $\epsilon \ll 1$, the banana and plateau regimes are distinct; the banana regime is where $\nu_\star \ll \epsilon^{3/2} \ll 1$ and the plateau regime is where $\epsilon^{3/2} < \nu_\star < 1$, though complete trapped orbits only exist in the banana regime.

1.3.4 Bootstrap current

In the banana regime, a field-parallel self-induced current known as the bootstrap current is induced [23]. Consider two banana orbits on two adjacent flux surfaces as in Fig.1.6, where the outboard side of one orbit counterflows against the inboard side of another.

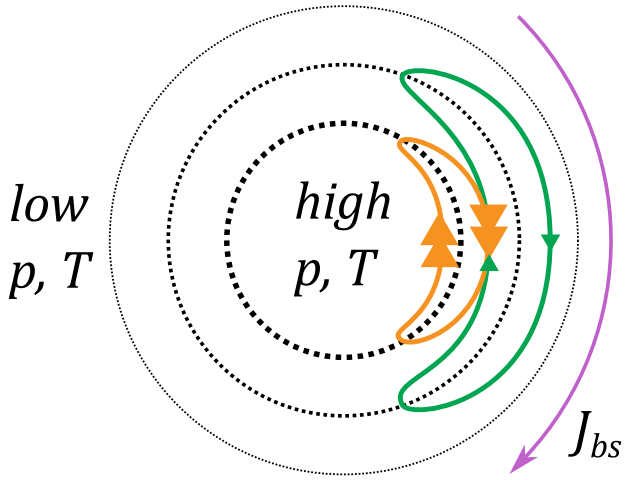

Figure 1.6: Two adjacent trapped particle orbits (orange, green) under a finite radial pressure and temperature gradient, inducing the bootstrap current J_{bs}. Arrow size indicates the number density of particles on each orbit.

In the presence of both a pressure and temperature gradient (i.e. inner orbit particles are more numerous and hotter), a net flow of trapped particles occurs in opposite directions for electrons and ions. Trapped particles then transfer momentum to passing particles through collisions, preferentially in one direction. The resulting net field-parallel current J_{bs}, carried by the passing particles, which for a $\epsilon \ll 1$ circular cross section tokamak has the approximate form [24, 25]:

$$J_{bs} \approx -2.44 \frac{\sqrt{\epsilon}}{B_\theta} \frac{dp}{dr} \tag{1.3.6}$$

The bootstrap current can be comparable to or larger than other field-parallel currents in the

plasma, such as the Ohmic current [17, pp. 208–209]. The poloidal field it induces can benefit confinement by supplementing the externally-induced fields or, in theory, replacing them entirely for steady-state operation [26]. In ITER, J_{bs} is expected to provide $> 50\%$ of the plasma current [27]. However, perturbations in the bootstrap current can drive the neoclassical tearing mode MHD instability that limits the performance of the tokamak, which will be covered in the following chapters.

1.4 Neoclassical Tearing Modes (NTMs)

1.4.1 Introduction to NTMs

Recall the equilibrium described in Sec 1.3.2 with flux surfaces as in Fig.1.7a. Good confinement is provided by the predominantly field-parallel transport along these flux surfaces, sustaining high core pressures and poloidal beta β_θ. While ideal MHD gives a reasonable approximation of this system, the small but finite resistivity that does exist in the plasma allows magnetic reconnection to occur where energetically favourable. This gives rise to resistive MHD instabilities which can modify the global field geometry, and are often deleterious to confinement. One such instability is the neoclassical tearing mode (NTM), characterised by the formation of magnetic island structures as shown in Fig.1.7b.

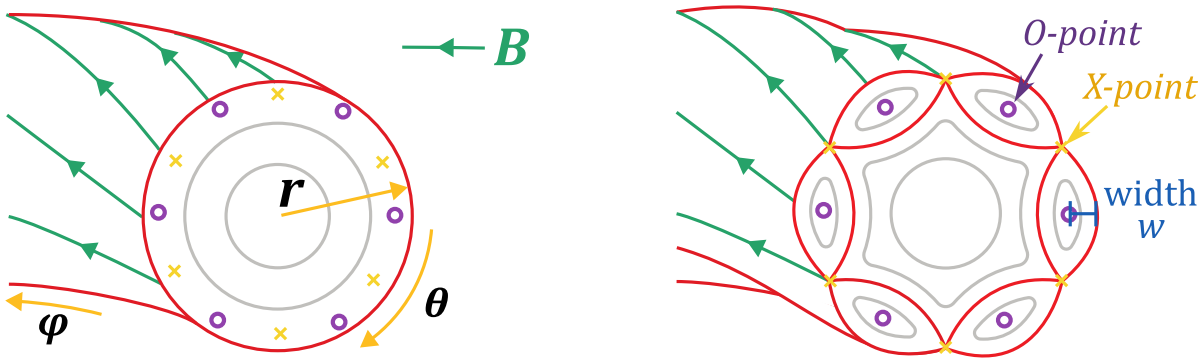

(a) Equilibrium (b) NTM onset

Figure 1.7: Poloidal cross section of a tokamak plasma showing magnetic island formation on a rational flux surface (red). Also shown are the magnetic field (green), island O-points where parallel current filaments are concentrated (purple) and X-points (yellow).

NTMs are driven by a filamentation of the field-parallel current density $J_\parallel$, or preferential counter-flow on certain field lines (producing 'holes' in the total $J_\parallel$, indicated by 'O's in Fig.1.7a) and not others [28, 21]. The seed perturbations that trigger NTMs often follow other MHD events including sawtooth crashes, fishbone activity and ELMs [29], though spontaneous 'triggerless' NTMs have also been observed at high β_θ [30]. NTMs occur exclusively on rational surfaces where such a perturbation may resonate with the magnetic field geometry, with $m/n = 2/1$ modes usually being the largest in amplitude and the most destructive [31]. Under Ampère's law, the perturbed current induces a radial field perturbation at those filaments. Provided there is finite resistivity[5] near this surface, magnetic reconnection ensues, 'tearing' the flux surface to

[5]We consider finite resistivity within a thin layer in r surrounding the rational surface where the island forms.

form magnetic islands of finite radial half-width w, as in Fig.1.7b. These islands short-cut radial transport, as particles can free-stream from one side of an island to the other. This results in the loss of radial pressure gradient dp/dr inside islands, reducing the overall core pressure and temperature as in Fig.1.8a. The field-parallel bootstrap current $J_{bs} \propto dp/dr$ is also lost inside the island, as in Fig.1.8b, exacerbating the filamentation and causing the island to grow. This continues until a saturation width is reached, at which the island is maintained at that size by the perturbed bootstrap current. This saturation occurs as a consequence of the greater bending of magnetic field lines as the island enlarges. The saturation island width can be a large fraction of the tokamak minor radius a, affecting plasma transport globally as the enlarged island persists.

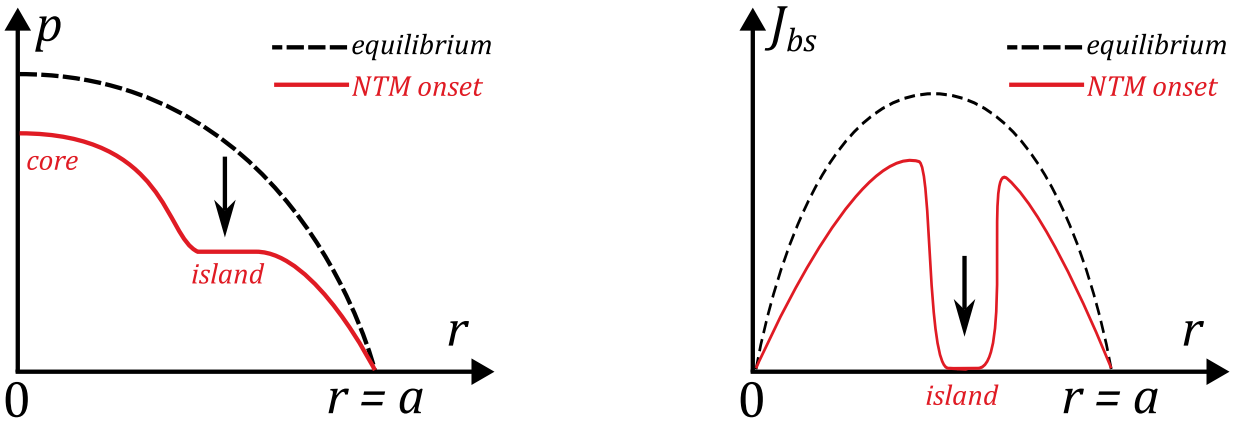

(a) Pressure

(b) Bootstrap current

Figure 1.8: Radial profiles of tokamak plasma parameters before and after NTM onset.

NTM onset is dependent on the initial half-width w of the seed island and the poloidal beta $\beta_\theta \propto p$. Experiments on a range of devices [32] identified minimum thresholds for w and β_θ, both of which must be exceeded for a small island to grow. Otherwise, the island shrinks and the NTM subsides. High-β_θ tokamaks are therefore more susceptible to NTMs, and their onset effectively limits the attainable β_θ and gain. In severe cases, large saturated islands may induce eddy currents extending into the reactor walls, decelerating the plasma rotation and leading to mode locking [33, 34], triggering further growth. This often leads to confinement terminating in a disruption, possibly damaging the reactor [35]. NTMs are thus a major concern in ITER and other future high-β_θ tokamaks [27, 19, 36], and must be mitigated if energy gain targets are to be achieved. Ongoing work focuses on the mechanisms influencing NTM threshold physics, and how they may be utilised to control NTMs while continuing to pursue high-β_θ operation. The threshold width w_c and the factors influencing it are the subject of this study.

Elsewhere, ideal MHD applies to a reasonably good approximation.

1.4.2 Modified Rutherford equation (MRE)

Early tearing mode theory [28, 37] considered classical transport in a 'slab' plasma, where only the induced parallel currents contributed to the growth of the island. The main result of [37] is the Rutherford equation, describing the time evolution of the island half-width[6] dw/dt:

$$\frac{2\tau_R}{r_s^2}\frac{dw}{dt} = \Delta'(w) \tag{1.4.1}$$

Here, $\tau_R \sim \frac{\mu_0 r_s^2}{\eta}$ is the timescale of resistive diffusion, μ_0 is the vacuum permeability, r_s is the minor radius of the rational surface where the island forms, and η is the resistivity there. $\Delta'(w)$ is the *classical* tearing mode stability parameter, which is *destabilising* or driving island growth when $\Delta'(w) > 0$. $\Delta'(w)$ represents the free energy available in the plasma current for island-forming magnetic reconnection to occur, which requires finite resistivity η. The method for determining Δ' involves solving for the perturbed poloidal flux ψ using the ideal MHD equations outside a narrow layer of thickness l surrounding the rational surface at $r = r_s$, where $w \ll l \ll r_s$. Boundary conditions at the plasma core and wall then result in a discontinuity at $r = r_s$, which arises from currents flowing in the layer, and indeed the term in $\frac{dw}{dt}$ of Eq.(1.4.1) arises from the currents induced in the layer as the island grows. Then Δ' is the size of this discontinuity, given by Eq.(1.4.2):

$$\Delta' = \lim_{l\to 0}\frac{1}{\psi}\left[\left.\frac{d\psi}{dr}\right|_{r=r_s+l} - \left.\frac{d\psi}{dr}\right|_{r=r_s-l}\right] \tag{1.4.2}$$

Large islands will modify the equilibrium to an extent that $\Delta' < 0$, resulting in a saturation width where $dw/dt = 0$ [38]. For small islands ($w \ll r_s$), Δ' is determined by the *global* equilibrium plasma profile and becomes independent of w.

The classical theory has since been extended into a toroidal geometry, giving rise to additional layer currents and leading to the development of the modified Rutherford equation (MRE) [35]. This introduces *local* effects from neoclassical physics that become important especially for small islands. It will be shown that, even when the classical theory predicts global stability ($\Delta' < 0$), that the local neoclassical physics can drive island growth, particularly at $w \ll r_s$, giving rise to the *neoclassical* tearing mode.

[6] A factor 2 has been added to Eq.(1.4.1), as this work defines w as the *half*-width of the island rather than the full width in the literature.

Tokamak curvature drive

The first of these neoclassical modifications is tokamak curvature, as identified by Glasser, Greene and Johnson in 1975. Denoted Δ_{cur}, it is found to be purely stabilising ($\Delta_{cur} < 0$) and scales as $\Delta_{cur} \propto \epsilon^2 w^{-1}$ [39]. It therefore could provide a threshold width when Δ_{cur} balances $\Delta'(w)$. However, Δ_{cur} is considered insignificant in high aspect ratio analysis in the $\epsilon \ll 1$ limit, and is disregarded in this study. The effect of curvature on NTMs is nonetheless an active research area, particularly for low aspect ratio "spherical" tokamaks [40, 41, 42, 43].

Bootstrap current drive

The second major MRE contribution comes from the bootstrap current, as presented in 1985-86 by Qu and Callen [24] and Carrera et al [25], respectively using fluid MHD and drift-kinetic theory in the high aspect ratio banana regime. Both predicted the bootstrap current contribution to the MRE to be:

$$\Delta_{bs} \propto -\epsilon^{1/2} \frac{L_q}{L_p} \frac{\beta_\theta}{w} \tag{1.4.3}$$

Here, $L_q = \left(\frac{1}{q}\frac{dq}{dr}\right)^{-1}$ is the shear length scale and $L_p = \left(\frac{1}{p}\frac{dp}{dr}\right)^{-1}$ is the pressure gradient length scale, where normally $L_q/L_p < 0$ in a tokamak[7], making this form of Δ_{bs} generally destablilising. In this form, any small island will be amplified by Δ_{bs}, even in a classically stable plasma ($\Delta' < 0$), which would fundamentally limit the achievable β_θ in any tokamak. This theory was tested when NTMs were experimentally observed for the first time, during high-β banana regime operation in the TFTR tokamak in 1995 [44]. Good agreement with the theory of [24, 25] was seen in the island growth rate during its initial growth and saturation, though less so during its decay. Notably, the experiment observed that only islands of initial width $w \gtrsim O(1-2$ cm) amplified, providing the first evidence of a threshold width. However, the theory could not predict the size let alone the existence of this threshold, nor could islands smaller than ~ 0.5 cm be detected by the experiment. Ref. [44] noted that, at this length scale, kinetic effects and diffusive transport will become significant in influencing the evolution of small islands.

One proposed origin of the observed NTM threshold is the effect of radial diffusion [45, 46, 47]. When the island is sufficiently small, field-perpendicular diffusive transport can compete with parallel transport, partially restoring the pressure and density gradients flattened across the

[7] Exclusively, $L_p < 0$ under the definition given here, as pressure must be highest in the core. Reverse sheared plasmas where $L_q < 0$ will indeed result in $\Delta_{bs}(w) < 0$, but presents its own physics challenges. For further information on reverse shear ITER scenarios, see Sec.2.5.2 in [19].

island, weakening the bootstrap current drive. The effect is localised to a thin *resistive boundary layer*[8] surrounding the island separatrix and X-points where heat flux is highest. An alternative form of Eq.(1.4.3) accounting for radial diffusion is given in [45]:

$$\Delta_{bs} \propto \sqrt{\epsilon}\frac{L_q}{L_p}\frac{\beta_\theta}{w}\frac{w^2}{w^2+w_\chi^2} \tag{1.4.4}$$

Here, w_χ is a threshold width that is determined by balancing the field-perpendicular and parallel diffusive transport coefficients, assuming $\Delta' < 0$. However, the physics governing perpendicular transport is not well-understood, requiring a rigorous treatment of turbulence at the gyrokinetic scale, making it unclear whether this is the dominant mechanism determining the threshold width. Under ITER-like parameters, a threshold width of $w_\chi \sim 1$ cm is predicted, comparable to the expected value of the trapped ion banana width $\rho_{b,i}$ [48]. This produces differing kinetic responses from ions and electrons, resulting in the so-called *finite orbit width* effect [49, 50, 51, 52, 53] which gives rise to another neoclassical current contribution to the modified Rutherford equation.

Polarisation current drive

The third neoclassical drive term in the MRE, denoted Δ_{pol}, originates from a polarisation current induced due to the poloidal rotation of a chain of small islands. Here, the propagation frequency of this island chain relative to the $\mathbf{E}\times\mathbf{B}$ flow of the equilibrium plasma is denoted ω_E, in the frame where the electric field far from the island is zero. Regarding the finite orbit width effect, when w approaches the trapped ion banana orbit width ($w \sim \rho_{b,i} = \epsilon^{-1/2}\rho_{\theta,i}$), the ions and electron responses differ due to the relative sizes of their orbit widths, as $\rho_{b,i} \gg \rho_{b,e}$ (by a factor $\sqrt{m_e/m_i} \simeq 40$). At this scale, the ion response is dominated by the $\mathbf{E}\times\mathbf{B}$ drift, while electron transport is predominantly field-parallel due to their higher thermal velocity. To maintain quasineutrality and an overall divergence-free current density ($\nabla\cdot\mathbf{J} = 0$), an electrostatic potential Φ is generated in the vicinity of the island. The $\mathbf{E}\times\mathbf{B}$ response of the trapped particles to the local potential then differ; trapped electrons will experience the local variations in Φ, while trapped ions will only respond to the average of Φ over their banana orbits. The differing $\mathbf{E}\times\mathbf{B}$ responses produce an electric field $d\mathbf{E}/dt$ that varies sinusoidally in time with the rotating island chain, though this rotation is generally slow relative to the particle gyro-frequencies ($\omega_{c,j} \gg \omega_E$). Recalling Sec.1.2.2, a finite $d\mathbf{E}/dt$ induces a polarisation current perpendicular to $\mathbf{B}$ as a return

[8] This separatrix boundary layer is distinct from the layer of finite resistivity defined in classical tearing mode analysis [28], which is described by linear physical processes rather than nonlinear processes.

current, though this is not necessarily divergence-free. In response, a further small electric field is generated that then accelerates the electrons along field lines, creating a parallel current density to restore $\nabla \cdot \mathbf{J} = 0$. This final induced *parallel* current does contribute to the MRE via Δ_{pol}.

The polarisation current drive can be stabilising or destabilising depending on complex, interconnected factors, including the ion-ion collision frequency ν_{ii} and its relative size to island propagation frequency, i.e. whether $\nu_{ii} \ll \epsilon\omega_E$ [50, 54, 55]. Early approximations for Δ_{pol} have been derived in both a collisional fluid model [49] and a collisionless drift-kinetic model [50]:

$$\Delta_{pol} \propto g(\epsilon, \nu_{ii}) \left(\frac{L_q}{L_p}\right)^2 \frac{\beta_\theta}{w} \left(\frac{\rho_{\theta,i}}{w}\right)^2 , \qquad g(\epsilon, \nu_{ii}, \omega_E) = \begin{cases} 1.64\epsilon^{1/2} & \nu_{ii}/\epsilon\omega_E \ll 1 \\ \epsilon^{-1} & \nu_{ii}/\epsilon\omega_E \gg 1 \end{cases} \tag{1.4.5}$$

The collision frequency and island rotation rate dependence of the two models is encapsulated within the model coefficient $g(\epsilon, \nu_{ii}, \omega_E)$, which notably differ by $O(\epsilon^{3/2})$. Eq.(1.4.5) shows $\Delta_{pol} \propto w^{-3}$ will be of comparable magnitude to Δ_{bs} within the MRE for small islands. When Δ_{pol} is stabilising, Ref. [50] predicted a threshold width of $w_c \sim O(\rho_{b,i})$ but assumed $w \gg \rho_{b,i}$, neglecting the finite orbit width effect and radial diffusion in the collisionless limit. Separate to the resistive separatrix boundary layer discussed in Ref. [45], Ref. [50] described a *dissipation layer* in velocity pitch-angle space surrounding the trapped-passing boundary, where there is a discontinuity in the ion distribution. The width of the separatrix boundary layer is negligibly small, and so its contribution to Δ_{pol} was neglected by Ref.[50] in the collisionless limit. However, subsequent works [47, 56] found that the polarisation current generated by particles in the dissipation layer was non-negligible, being of similar magnitude to that of the equilibrium plasma but of opposite sign, making Δ_{pol} stabilising in certain conditions. An accurate treatment of this dissipation layer is therefore necessary to determine the behaviour of Δ_{pol} and its effect on the threshold width. However, modelling these transport processes is challenging, complicated further by island rotation with respect to the equilibrium plasma [52, 51, 57]. Other works investigated Δ_{pol} experimentally; [58] studies ω_E dependence, finding island propagation to be in the same direction as the ion diamagnetic drift but challenging to measure its size. Refs. [59, 60] defined an empirical model based on measurements from the TCV tokamak describing Δ_{pol} when $w \sim \rho_{b,i}$:

$$\Delta_{pol} \propto g(\epsilon, \nu_{ii}, \omega_E) \left(\frac{L_q}{L_p}\right)^2 \beta_\theta \frac{w\rho_{b,i}^2}{\sqrt{w^4 + \rho_{b,i}^4}} , \qquad g(\epsilon, \nu_{ii}, \omega_E) = \begin{cases} \epsilon^{3/2} & \nu_{ii} \leq 0.3 \\ 1 & \text{otherwise} \end{cases} \tag{1.4.6}$$

The complexity of the theory behind the polarisation current drive has meant it remains an area of active work.

Application in NTM control

A complete predictive model of NTM growth at the threshold width scale would inform the control and prevention of the instability from threatening high-gain confinement in future tokamaks. The control method proposed for ITER involves driving an electron cyclotron current (ECCD) inside magnetic islands to substitute the lost bootstrap current, as demonstrated successfully in ASDEX-U [61, 62], DIII-D [63] and other tokamaks [19]. This would introduce a stabilising Δ_{ECCD} term to the MRE, which if large enough to counteract the destabilising terms, will drive the island to lower widths until $w < w_c$, at which point the island heals away unassisted. Such a system must respond pre-emptively to growing islands by combining real-time modelling with the detection of NTM triggers [64], and deliver the required current for suppression precisely into the rotating island [65]. The high power consumption of ECCD, which can be $10-20\%$ or more of the total heating power available [19], means that accurate predictions of the required current - and where it should be delivered - would help optimise the system for long-pulse confinement.

Full modified Rutherford equation

Combining Eq.(1.4.3) and (1.4.5), the full modified Rutherford equation in the high aspect ratio banana regime is given by:

$$\frac{2\tau_R}{r_s^2}\frac{dw}{dt} = \Delta'(w) + \Delta_{cur}(w) + \Delta_{bs}(w) + \Delta_{pol}(w) + \Delta_{ECCD} \tag{1.4.7}$$

$$= \Delta'(w) + a_{cur}\frac{\epsilon^2}{w} + a_{bs}\sqrt{\epsilon}\frac{L_q}{L_p}\frac{\beta_\theta}{w}\frac{w^2}{w^2+w_\chi^2} + a_{pol}g(\epsilon,\nu_{ii},\omega_E)\left(\frac{L_q}{L_p}\right)^2\frac{\beta_\theta}{w}\left(\frac{\rho_{\theta,i}}{w}\right)^2 + \Delta_{ECCD} \tag{1.4.8}$$

where again, τ_R is the resistive time scale, r_s is the minor radius of the rational surface where the island of half-width w forms, $\epsilon \ll 1$ is the inverse aspect ratio, $\rho_{\theta,i}$ is the ion poloidal gyroradius, w_χ is the threshold width predicted by radial diffusion [45], $\beta_\theta = 2\mu_0 p B_\theta^{-2}$ is the poloidal beta, p is the plasma pressure, B_θ is the poloidal magnetic field, $g(\epsilon,\nu_{ii},\omega_E)$ is a model term associated with the polarisation current drive, and a_{cur}, a_{bs} and a_{pol} are numerical constants corresponding to tokamak curvature, bootstrap current and polarisation current respectively. The threshold width w_c is determined by rearranging Eq.(1.4.7) for w at $dw/dt = 0$. At small w and ϵ, both Δ' and the

curvature drive $\Delta_{cur} \propto \epsilon^2$ are small relative to the bootstrap and polarisation current drives and are ignored. At large $w \gg \rho_{\theta,i}$, the polarisation term is small, but can compete with the bootstrap term when $w \sim \rho_{\theta,i}$. Assuming the polarisation drive is stabilising ($\Delta_{pol} < 0$) and can exceed the bootstrap drive in magnitude, a threshold width w_c occurs where $\Delta_{bs}(w_c) + \Delta_{pol}(w_c) = 0$, yielding $w_c \sim \rho_{b,i} = \epsilon^{1/2}\rho_{\theta,i}$ in the low collision frequency limit where $w \gg w_\chi$. This also requires that some threshold value of poloidal beta $\beta_{\theta,c}$ is also exceeded, if $\Delta' < 0$. For sub-threshold β_θ, there is no threshold width and magnetic islands of any size are predicted to shrink away under this equation. In the above-threshold or 'high' beta case, $\beta_\theta > \beta_{\theta,c}$, we note there will be two values in w where $dw/dt = 0$: the stable point at the saturation width $w = w_{sat}$, and the unstable point at the threshold width w_c. This study focuses on determining the latter. A sketch of dw/dt is illustrated in Fig.1.9. Two cases are shown, where β_θ is above or at its threshold, $\beta_{\theta,c}$:

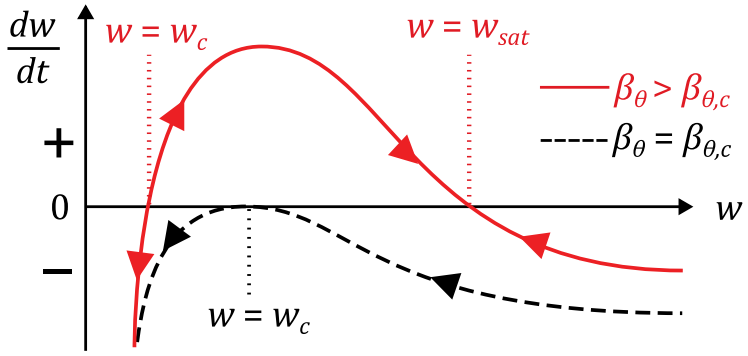

Figure 1.9: Island width growth rate dw/dt vs. w for above-threshold poloidal beta (red) and critical poloidal beta (black dashed), where $\Delta' < 0$ is assumed. Arrows indicate direction of change in w.

An accurate treatment of the bootstrap and polarisation currents is essential for determining the threshold width from the modified Rutherford equation. However, experimental observations from various tokamaks have found w_c to be approximately $1-1.5$ trapped ion banana orbit widths $\rho_{b,i}$ [32, 66][9]. This is the length scale where much of the existing analysis no longer applies, and requires a new theory. This thesis develops the software required to implement such a theory.

[9] Within Refs. [32, 66], w is defined as the full island width, not half-width.

1.5 Objectives

This work seeks to develop a new computational model for small islands near the threshold width w_c, where $\rho_{b,e} \ll w_c \sim \rho_{b,i}$, requires a kinetic treatment for the ions, with care taken at the separatrix boundary layer and the trapped-passing boundary dissipation layer. Given $\rho_e \ll \rho_i \ll w$, a simplification to the drift-kinetic model is reasonable, but including the required physical detail remains a substantial computational challenge, as this thesis will investigate. The $w \sim \rho_{b,i}$ limit was explored previously using a numerical particle-in-cell code to solve the ion response [67, 55], and by a fully analytic approach focusing on passing ions only [68] (following [46]). Both works confirmed that the ion density and pressure gradient across small islands were partially restored, weakening the Δ_{bs} drive term, but neglected the electron response, and also the trapped ion response in the case of [68]. Recall in Sec.1.4 that the differing ion and electron responses to the small island produces a perturbed electrostatic potential Φ, which needs to be calculated self-consistently with the responses. This was included in the more recent work of Imada et al [69, 70, 41] by combining a numerically-derived 4D drift-kinetic ion response (both passing and trapped) with the analytic electron response of Ref. [50], using the assumption that $\rho_{b,e} \ll w \sim \rho_{b,i} \ll r_s$, and expanding in the limit of small $\Delta = w/r_s \ll 1$ (not to be confused with island growth parameter Δ'). Its associated drift-kinetic NTM code, "`DK-NTM`" solves the ion response and the electrostatic potential Φ iteratively until a self-consistent solution is obtained. This work also extended [50] into a finite collision frequency regime, however the handling of collisions around the thin separatrix boundary layer becomes computationally challenging as Ch.3 discusses. Dudkovskaia et al [41, 42, 43] then developed a reduced dimension 3D version of this theory that is valid in the limit of low collision frequency. Its associated code, "`RDK-NTM`", introduces other physical details such as a numerically-calculated electron response, relaxing the assumption $w \gg \rho_{b,e}$. The two codes were compared in Refs. [41] and [43]. Both `DK-NTM` and `RDK-NTM` approaches captured the two layers and accounted for quasineutrality, and by doing so, two key results were found.

Firstly, for small islands, the distribution function of passing ions follows structures of identical topology to the magnetic island but shifted radially due to magnetic drifts, as shown in Fig.1.10. The shift is of $O(\rho_{\theta,i})$, where $\rho_{\theta,i}$ is the ion poloidal gyroradius. It occurs in opposite directions depending on the sign of the field-parallel velocity $v_{\parallel,i}$; i.e. it is opposite for co-passing and counter-passing ions. These structures are referred to throughout this work as *drift islands*[10].

[10] Similar "drift islands" were described in Ref. [71], though far smaller islands of $\rho_{\theta,e} < w \ll \rho_{\theta,i}$ were considered,

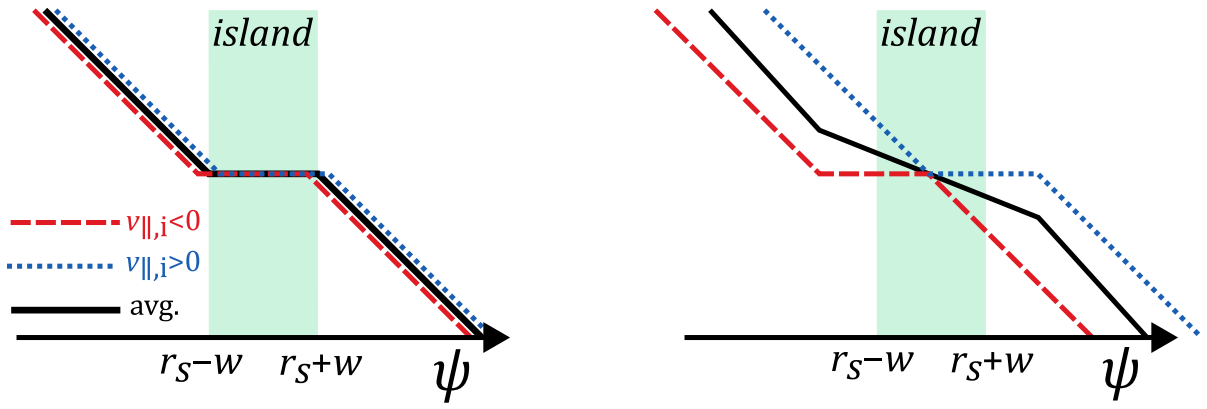

(a) $w \gg \rho_{\theta,i}$ (b) $w \sim \rho_{\theta,i}$

Figure 1.10: Sketch of the passing ion distribution function vs poloidal flux ψ for (a) $w \gg \rho_{\theta,i}$ and (b) $w \sim \rho_{\theta,i}$. Shown are the ion populations where $v_{\|} > 0$ (red), $v_{\|} < 0$ (blue), and the average of the two streams (black), which provides a measure of density.

When $w \gg \rho_{\theta,i}$ the radial shift of drift islands is negligible relative to the island size; the drift islands align with the magnetic island and the overall density gradient is flattened inside the magnetic island, as in Fig.1.10a. When $w \simeq \rho_{\theta,i}$, the drift islands no longer align, whose combination results in a substantial density gradient being restored across the magnetic island, as in Fig.1.10b. Secondly, by accounting for the electron response and the perturbed potential required for quasineutrality, the electrons were found to provide a stabilising bootstrap current drive term $\Delta_{bs,e}$ that exceeded the destabilising ion bootstrap drive $\Delta_{bs,i}$ at small island widths, the latter being weakened by the effect of drift islands [70]. Ongoing work requires comparing the approaches of the two codes; as the `RDK-NTM` code uses an analytic treatment for the separatrix boundary layer physics, it uses the `DK-NTM` code as a benchmark [41, 43]. However, while the `DK-NTM` model employs a complete numerical treatment for the ion response at the thin separatrix boundary layer and the trapped-passing boundary dissipation layer, the computation is rigorous and highly challenging, particularly at low collision frequency.

As part of this ongoing study, this thesis presents the development of a new 4D drift-kinetic NTM numerical code and explore the effect of collisionality on both the code and result, following three objectives that will form the chapters Ch.4, (5) and (6) respectively:

Objective (1) is to redevelop and validate the `DK-NTM` algorithm, resolve computational issues, develop tests and identify limitations. This resulted in `DK-NTM` being rewritten as a new code, named `kokuchou`, whose constituent procedures must be unit tested.

and from the perspective of electrons rather than ions.

Objective (2) is to obtain self-consistent, numerically stable results from a small number of simulations. This will involve conducting 4 "case study" runs of `kokuchou` for two values of island width w ($\ll \rho_{\theta,i}$ and $> \rho_{\theta,i}$), and a new study at two values of collisionality $\nu_\star$. Analytically-derived results will be used to benchmark the full-size numerical result.

Objective (3) is to obtain an updated result for the threshold width scaling factor with the ion poloidal gyroradius $\rho_{\theta,i}$, a relationship previously explored in literature. This is accomplished via a large-scale parameter scan in w and $\rho_{\theta,i}$. This work will extend previous attempts by also scanning the plasma collisionality $\nu_\star$, and observing its influence on the layer physics.

Summary

This chapter covered the prerequisite physics for this modelling study of neoclassical tearing mode instabilities, which degrade confinement in modern high-beta tokamaks. This section introduced the neoclassical layer currents that influence the rate of growth for magnetic islands of near-threshold width. We seek to identify this threshold island width that critically determines NTM onset. The state-of-the-art of NTM research is that the existing theory needs to be adapted into a framework targeting the length scale of $w \sim \rho_{b,i}$, where the threshold width has been observed [32, 34]. To account for the relevant phenomena, the plasma will be self-consistently modelled using the drift-kinetic equation. Ch.2 will cover the 4D drift-kinetic theory in more detail, including the derivation of the drift-kinetic transport equation for the ion response to the NTM instability, and how the equation is made computationally tractable at the relevant length scale. Ch.3 will present a new numerical code for solving this drift-kinetic NTM equation, based on the original `DK-NTM` code, and will discuss the modifications made to address challenges with the old code. The results of this thesis are split into three chapters following the project objectives. Ch.4 will discuss the validation of the new `kokuchou` NTM code and the results of unit tests, ahead of full-scale simulations to be shown in the subsequent chapters. Ch.5 will present full results from the new code from 4 runs at 2 values in collisionality $\nu_\star$ and 2 magnetic island widths, representing extremes of the code's operating parameter space. Numerical results will be benchmarked using analytic results representing the neoclassical equilibrium far from the island. Ch.6 will extend these results into a parameter scan of 125 runs, varying the magnetic island width, collisionality and ion poloidal gyroradius. The key result is the threshold magnetic island width and its relationship with the latter two parameters, which will be compared with results from similar studies.

Chapter 2

Theory

This chapter presents equations describing the response of a quasineutral hydrogenic tokamak plasma to a small magnetic island during the onset of the neoclassical tearing mode (NTM) instability. The island's growth is driven by a perturbation in the field-parallel current density, localised to a resistive layer in minor radius surrounding the flux surface where the island is situated. By evaluating the currents in this layer, the island's growth rate can be determined from the modified Rutherford equation 1.4.7 which, in the limits of small w and ϵ, is influenced primarily by the layer currents. This work will employ this expression to determine the threshold island width, below which the island shrinks and the NTM subsides, and also to discuss the mechanisms that influence this threshold. Here, we revisit the derivation of Imada et al [69, 70] in additional detail [72], itself based on Wilson et al's study in the collisionless limit [50] extended to a finite collisionality banana regime, using results from Helander and Sigmar [17] and others. We consider a small single helicity magnetic island of half-width w (in minor radius r) forming on a $m/n = 2/1$ rational surface of minor radius r_s in a high aspect ratio ($\epsilon \ll 1$) circular cross section tokamak, neglecting Shafranov shift. The length scale ordering $\rho_i \ll w \sim \rho_{b,i} \ll r_s$ is assumed, where $\rho_{b,i} = \epsilon^{1/2}\rho_{\theta,i}$ is the trapped ion banana width, ρ_i is the ion gyroradius, $\rho_{\theta,i}$ is the ion poloidal gyroradius based on the poloidal magnetic field only. In the limit of small $\Delta = w/r_s \ll 1$, we seek steady state equations of motion for the plasma response in the island's vicinity. At this length scale, the drift-kinetic equation is used to track the guiding centre motion of ions, while analytic results for electrons from Ref. [50] can be used, given their small banana width $\rho_{b,e} \ll \rho_{b,i}$. As with Ref. [50], the effects of sheared plasma flows and error fields are neglected. The derivation in Secs. 2.1-2.5 provides the basis for a numerical algorithm described in Ch.3. Sec.2.6 summarises my contributions to the derivation made during this work.

2.1 Magnetic topology

An orthogonal 3D $\{\psi, \theta, \varphi\}$ spatial coordinate system as in Fig.1.5a is used[1], where ψ is the poloidal magnetic flux, θ is the poloidal angle clockwise from the outboard midplane ($\theta = 0$), and φ is the toroidal angle, counterclockwise when viewing the torus from above. The equilibrium helical magnetic field is:

$$\mathbf{B}_0 = I(\psi)\nabla\varphi + \nabla\varphi \times \nabla\psi \ , \tag{2.1.1}$$

where $I(\psi) = RB_\varphi$, B_φ is the toroidal component of $\mathbf{B}$, while the poloidal field is represented via the 2nd term: $rB_\theta\nabla\theta = \nabla\varphi \times \nabla\psi$. The magnitude of $\mathbf{B}_0$ in a large aspect ratio tokamak, to the leading order in $\epsilon \ll 1$ is approximately:

$$B_0(\theta) = B_\varphi(1 - \epsilon\cos\theta) \ . \tag{2.1.2}$$

A magnetic perturbation is introduced, satisfying Maxwell's equation $\nabla \cdot \mathbf{B} = 0$:

$$\mathbf{B}_1 = \nabla \times \left(A_\parallel \boldsymbol{b}_0\right) \ , \tag{2.1.3}$$

where $\mathbf{b}_0 = \mathbf{B}_0/B_0$ is the equilibrium field unit vector and $A_\parallel$ is the magnetic field-parallel vector potential that describes the perturbation. Here, the field-perpendicular component of the vector potential is neglected. Applying the "constant-ψ" approximation used in NTM literature [37], we define:

$$A_\parallel = -\frac{\tilde{\psi}}{R}\cos n\xi \ , \quad \tilde{\psi} = \frac{w_\psi^2}{4}\frac{q_s'}{q_s} \ , \quad w_\psi = RB_\theta w \ , \tag{2.1.4}$$

where $\tilde{\psi}$ is the amplitude of $A_\parallel$ and w_ψ is the island half-width in ψ-space, $q_s = m/n$ ($= 2/1$ in this work) is the local safety factor at the rational surface whose ψ-derivative is q_s':

$$q_s' = \left.\frac{dq}{d\psi}\right|_{\psi=\psi_s} ,$$

and ξ is the helical angle in the island rotational rest frame:

$$\xi = m\left(\theta - \frac{\varphi}{q_s}\right) . \tag{2.1.5}$$

[1] used by Boozer [22] et al for ITER modelling, also known as the *COCOS 11* tokamak coordinate convention [73]

Expanding in terms of small $\Delta = w/r_s \ll 1$ and $\epsilon \ll 1$, the first-order perturbed magnetic field correct to $O(\epsilon^{3/2}\Delta^2)$ (see Appendix Sec.8.2) is found to be:

$$\mathbf{B}_1 = m\tilde{\psi}\sin\xi\,\nabla\theta\times\nabla\phi + \frac{\partial R}{\partial\psi}\frac{\tilde{\psi}}{R}\cos\xi\,\nabla\phi\times\nabla\psi + O(\epsilon^2\Delta^2). \tag{2.1.6}$$

The total magnetic field with the perturbation is then (with orderings below):

$$\mathbf{B} = I(\psi)\nabla\phi + \nabla\phi\times\nabla\psi + m\tilde{\psi}\sin\xi\,\nabla\theta\times\nabla\phi + \frac{\partial R}{\partial\psi}\frac{\tilde{\psi}}{R}\cos\xi\,\nabla\phi\times\nabla\psi. \tag{2.1.7}$$
$$1 \qquad \epsilon \qquad \epsilon\Delta^2 \qquad \epsilon\Delta^2$$

For simplicity, steady state is assumed, so that $\tilde{\psi}$ is time-independent. Throughout this work, the subscript s denotes quantities evaluated at the rational surface $r = r_s$, and superscript $'$ (prime) denotes its derivative with respect to ψ. Note also that because we assume the toroidal mode number $n = 1$[2], it will be omitted for simplicity.

When describing flux surface geometry, for convenience we switch the coordinate system from $\{\psi, \theta, \varphi\}$ to $\{\psi, \xi, \theta\}$. In the limit of small $x = (\psi - \psi_s)/\psi_s$, assuming a long, thin magnetic island, Taylor expanding $q(\psi)$ about the rational surface then integrating across a helical field line (see Eq.(4) of [48]), the following function Ω is obtained as a constant of integration, which satisfies $\mathbf{B}\cdot\mathbf{\Omega} = 0$:

$$\Omega(\psi,\xi) = \frac{2(\psi-\psi_s)^2}{w_\psi^2} - \cos\xi. \tag{2.1.8}$$

This perturbed flux function Ω labels the modified flux surfaces in the presence of an island. The island's innermost flux 'surface' or *O-point* is defined as $\Omega = -1$, while its outer boundary or *separatrix* lies at $\Omega = +1$. Perturbed surfaces outside of the separatrix have $\Omega > +1$. Far from the island at large ψ, the ξ-dependence of Ω becomes small and $\Omega(\psi,\xi) \propto \psi^2$. Later in Sec.2.3.4 a similar expansion will be performed for the full drift-kinetic equation for ions.

Velocity coordinates

Alongside the $\{\psi, \xi, \theta\}$ spatial coordinates, we define a 2D gyro-orbit averaged velocity space coordinate system, $\{\lambda, v; \sigma\}$ where v is the total speed of a particle, λ is its pitch angle:

$$\lambda = \frac{\mu}{\mathcal{E}} = \frac{v_\perp^2}{v^2 B}, \tag{2.1.9}$$

[2]Other modes, such as $m/n = 3/2$, are commonly observed, but we focus on the 2/1 mode for continuity with Refs. [69, 70, 41] which this work follows

Here, $\mu = m_j v_\perp^2/2B$ is the magnetic moment, $\mathcal{E} = m_j v^2/2$ is the kinetic energy, and $v_\perp$ is the field-perpendicular velocity. The field-parallel velocity is: $v_\parallel = \sigma v\sqrt{1-\lambda B}$, and σ is its sign with respect to the direction of B. Then, $\lambda_c = B_{\max}^{-1}$ corresponds to the trapped/passing boundary. For the trapped particles where $\lambda > \lambda_c$, bounce points θ_b are such that $\lambda B(\theta_b) = 1$.

2.2 Drift-kinetic equation

At the relevant length scale $\rho_e, \rho_i, \rho_{b,e} \ll w \sim \rho_{b,i}$, the drift-kinetic equation (1.2.8) can be used to track the guiding centre motion of ions at the island width scale, while an analytic response can be used for electrons (see Sec.2.4). In steady state in the island rest frame, neglecting gravitational, centrifugal and Coriolis forces, the drift-kinetic equation is given by Ref. [18] Eq(4.44):

$$v_\parallel \nabla_\parallel f_j + \boldsymbol{v}_E \cdot \nabla f_j + \boldsymbol{v}_b \cdot \nabla f_j - \frac{eZ_j}{m_j}\frac{v_\parallel \nabla_\parallel \Phi}{v}\frac{\partial f_j}{\partial v} - \frac{eZ_j}{m_j}\frac{\boldsymbol{v}_b \cdot \nabla\Phi}{v}\frac{\partial f_j}{\partial v} = C_j(f_j), \tag{2.2.1}$$

where $\boldsymbol{v}_E$ and $\boldsymbol{v}_b$ are the $\mathbf{E}\times\mathbf{B}$ drift and magnetic drift velocities respectively (see Sec.1.2):

$$\boldsymbol{v}_E = \frac{\mathbf{B}\times\nabla\Phi}{B^2}\ , \quad \boldsymbol{v}_b = -\frac{v_\parallel \mathbf{B}}{B}\times\nabla\left(\frac{v_\parallel}{\omega_{c,j}}\right)\ , \tag{2.2.2}$$

and $\omega_{c,j} = \frac{eZ_jB}{m_j}$ is the gyrofrequency of species j, and $\mathbf{b} = \mathbf{B}/B$ is the unit vector of the total magnetic field. The perturbed electrostatic potential Φ arises from the differing ion and electron responses (see Sec.2.5) and is obtained by applying quasineutrality. $C_j(f_j)$ is the model collision operator, whose form is introduced in Sec.2.3. The spatial derivatives of Eq.(2.2.1) are taken at constant kinetic energy, $\mathcal{E} = m_j v^2/2$, and magnetic moment, $\mu = m_j v_\perp^2/2B$. Assuming $eZ_j\Phi/T_j \ll 1$, the distribution function f_j of species j is expressed as:

$$f_j = \left(1 - \frac{eZ_j\Phi}{T_j}\right) f_{M,j} + g_j\ , \tag{2.2.3}$$

where g_j is the perturbation to f_j in the vicinity of the magnetic island. It is assumed the equilibrium plasma follows a Maxwell-Boltzmann distribution given by $f_{M,j}(\psi, v)$:

$$f_{M,j}(\psi, v) = \frac{n_0(\psi)}{\pi^{3/2} v_{\mathrm{th},j}^3(\psi)} \exp\left[-\frac{v^2}{v_{\mathrm{th},j}^2} - \frac{eZ_j\Phi}{T_j}\right], \tag{2.2.4}$$

which, given $eZ_j\Phi/T_j \ll 1$, reduces the Maxwellian to a function $F_{M,j}$:

$$F_{M,j}(\psi, v) = \frac{n_0(\psi)}{\pi^{3/2} v_{\mathrm{th},j}^3(\psi)} e^{-v^2/v_{\mathrm{th},j}^2}, \tag{2.2.5}$$

where $n_0(\psi)$ is the equilibrium plasma density (equal for ions and electrons under quasineutrality) and $v_{th,j}$ is the thermal velocity[3] of species j:

$$v_{th,j} = \sqrt{\frac{2T}{m_j}} \ . \tag{2.2.6}$$

Thermal equilibrium between both species is assumed ($T = T_i \equiv T_e$), hence $v_{th,e} = v_{th,i}\sqrt{\frac{m_i}{m_e}} \approx 40\ v_{th,i}$. The derivatives of the Maxwellian function Eq.(2.2.7) in ψ and speed v are, respectively:

$$F'_{M,j} = \frac{\partial F_{M,j}}{\partial \psi} = \frac{\omega_{\star,j}^T}{\omega_{\star,j}} \frac{n_0'}{n_0} F_{M,j} \ , \tag{2.2.7}$$

$$\frac{\partial F_{\mathrm{M}j}}{\partial v} = -2\frac{v}{v_{\mathrm{th}j}^2} F_{M,j} \ . \tag{2.2.8}$$

Here, the diamagnetic frequency $\omega_{\star,j}$ for species j is defined as:

$$\omega_{\star,j} = k_\theta \rho_j v_{th,j} \frac{dn}{dr} = k_\theta \frac{m_j v_{th,j}^2}{eZ_j B} \frac{dn}{dr} \tag{2.2.9}$$

where ρ_j is the species' gyrofrequency, m_j is its mass, Z_j is its charge, and $k_\theta = m/r$ is the poloidal wavenumber (m being the poloidal mode number). In Eq.(2.2.7), the term $\omega_{\star,j}^T$ is obtained from the ψ-derivative of $F_{M,j}$:

$$\frac{\omega_{\star,j}^T}{\omega_{\star,j}} = 1 + \left(\frac{v^2}{v_{th,j}^2} - \frac{3}{2} \right) \eta_j \ , \tag{2.2.10}$$

where $\eta = L_n/L_T$ is the ratio of the density gradient length scale L_n to temperature gradient length scale L_T for both species[4], defined here as:

$$L_n^{-1} = \frac{n_0'}{n_0} = \frac{1}{n_0}\frac{dn_0}{dr} \ , \qquad L_T^{-1} = \frac{T'}{T} = \frac{1}{T}\frac{dT}{dr} \tag{2.2.11}$$

[3] normalised such that the Boltzmann constant $k_b = 1$.

[4] Care must be taken as these length scales are defined with minus signs in Refs. [50, 74, 53, 75]

2.2.1 Collision operator

Following Ref. [50], the following simple momentum-conserving collision operators are defined to provide closure to the system. These are based on Eq.(3.40) in Ref. [17, p192] for a two-fluid system where one species is a slow-moving Maxwellian. For ions we consider only ion-ion collisions, due to the negligible effect of ion-electron collisions on ions [50]. For electrons, both electron-electron and electron-ion collisions are considered. The same-species and electron-ion collision operators are given by, respectively:

$$C_{jj}(f_j) = 2\nu_{jj}(v)\left[\frac{\sqrt{1-\lambda B}}{B}\frac{\partial}{\partial\lambda}\left(\lambda\sqrt{1-\lambda B}\frac{\partial f_j}{\partial\lambda}\right) + \frac{v_\parallel \bar{u}_{\parallel,j}(f_j)}{v_{\mathrm{th},j}^2}F_{M,j}(\psi)\right], \tag{2.2.12}$$

$$C_{ei}(f_e) = 2\nu_{ei}(v)\left[\frac{\sqrt{1-\lambda B}}{B}\frac{\partial}{\partial\lambda}\left(\lambda\sqrt{1-\lambda B}\frac{\partial f_e}{\partial\lambda}\right) + \frac{v_\parallel U_{\parallel,i}}{v_{\mathrm{th},e}^2}F_{M,e}(\psi)\right], \tag{2.2.13}$$

where the momentum-conserving parallel flow of species j is defined as:

$$\bar{u}_{\parallel,j}(f_j) = \frac{1}{n_0\langle\nu_{jj}\rangle_v}\int d^3\boldsymbol{v}\,\nu_{jj}(v)v_\parallel\, f_j(\boldsymbol{v}) \tag{2.2.14}$$

and the ion parallel flow is:

$$U_{\parallel,i}(f_i) = \frac{1}{n_0}\int d^3\boldsymbol{v}\, v_\parallel\, f_i(\boldsymbol{v}), \tag{2.2.15}$$

where in $\{\lambda, v\}$ velocity coordinates, the volume integral over velocity-space takes the form:

$$\int d^3\boldsymbol{v} = \pi B\sum_\sigma\int_0^\infty dv\, v^2\int_0^{B^{-1}}\frac{d\lambda}{\sqrt{1-\lambda B}}, \tag{2.2.16}$$

which is performed at fixed spatial variables ψ, θ and ξ. Within Eq.(2.2.14), the same-species 90° collision frequency ν_{jj} normalised to the same-species Coulomb collision frequency ν_{jj}^C is given by Eq.(3.38) in Ref. [17][5]:

$$\nu_{jj}(u) = \nu_{jj}^{(C)}\frac{\phi(u)-G(u)}{u^3} \to \begin{cases}\frac{4}{3u^2\sqrt{\pi}} & u\to 0\\ \frac{1}{u^3}-\frac{1}{2u^5} & u\to\infty\end{cases}, \qquad u = \frac{v}{v_{th,j}}, \tag{2.2.17}$$

[5] A simpler form $\nu_{jj} = v^{-3}$ is used in previous works [50, 74, 53, 75] and more recently in the `RDK-NTM` code [41]. The more complex form Eq.(2.2.17) was introduced in [69, 70] for better compatibility with neoclassical theory.

where $G(u)$ is the Chandrasekhar function, describing drag forces on a particle by collisions with a slow Maxwellian particle population:

$$G(u) = \frac{\phi(u) - u\phi'(u)}{2u^2} \rightarrow \begin{cases} \frac{2u}{3\sqrt{\pi}} & u \rightarrow 0 \\ \frac{1}{2u^2} & u \rightarrow \infty \end{cases} \tag{2.2.18}$$

and $\phi(u)$ is the error function, $\mathrm{erf}(u)$:

$$\phi(u) \equiv \mathrm{erf}(u) = \frac{2}{\sqrt{\pi}} \int_0^u e^{-t^2}\, dt, \quad \phi'(u) \equiv \frac{d\phi}{du} = \frac{2}{\sqrt{\pi}} e^{-u^2}. \tag{2.2.19}$$

Also within Eq.(2.2.14) is the velocity-space average of $\nu_{jj}(u)$, whose operator $\langle ... \rangle_v$ is defined by Eq.(4.26) of Ref. [17], based on a symmetric, spherical Maxwellian (see also Ref.[76] Eq.(4.30)) is given by:

$$\langle f(v) \rangle_v = \frac{8}{3\sqrt{\pi}} \int_0^\infty dv\, v^4 e^{-v^2} f(v). \tag{2.2.20}$$

2.3 Ion response

The guiding centre motion of the ions is tracked by the drift-kinetic equation Eq.(2.2.1). Given $w \sim \rho_{\theta,i}$, the ion response will be influenced by both parallel free-streaming and magnetic drifts. In a high-temperature banana regime plasma, the following orderings are assumed:

$$\frac{eZ_j\Phi}{T_i} \sim \Delta, \qquad k_\theta w \sim \Delta, \qquad \nu_* \ll 1 \sim O(\Delta). \tag{2.3.1}$$

Eq.(2.2.1) is solved for ions by Taylor expanding Eq.(2.2.3) in small $\Delta = w/r \ll 1$, retaining up to $O(\epsilon^{3/2}\Delta^2)$. In Eq.(2.2.3), the perturbation g_i is also expanded in powers of Δ:

$$g_i = \sum_k \Delta^k g_{i,k}\ . \tag{2.3.2}$$

In the $\{\psi, \theta, \xi\}$ toroidal coordinate system, the parallel derivative operator is given by:

$$\nabla_\parallel = \frac{\mathbf{B}\cdot\nabla}{B} = \frac{1}{Rq}\left.\frac{\partial}{\partial\theta}\right|_{\xi,\psi} + k_\parallel \left.\frac{\partial}{\partial\xi}\right|_{\Omega,\theta} \tag{2.3.3}$$

where $k_\parallel = \frac{-m(\psi-\psi_s)}{Rq}\frac{q_s'}{q_s}$ is the parallel wavenumber. When writing out $\nabla_\parallel$ in full in terms of $\{\psi, \xi, \theta\}$, we note that:

$$\frac{\partial}{\partial\psi} = \frac{1}{RB_\theta}\frac{\partial}{\partial r}\,, \qquad \frac{\partial}{\partial r} \sim \begin{cases} 1/r & \text{on equilibrium quantities} \\ 1/w & \text{on perturbed quantities} \end{cases} \tag{2.3.4}$$

which leads to some perturbed and equilibrium terms having different orderings. A full derivation of these terms is given in the Appendix, Sec.8.3.1.

Written in full, the differential operators within Eq.(2.2.1) (with orderings) are:

$$\begin{aligned} v_\parallel\nabla_\parallel &= \underset{1}{\frac{v_\parallel}{Rq}}\left[\underset{1}{\left.\frac{\partial}{\partial\theta}\right|_\psi} + \underset{\Delta}{m\left(1-\frac{q}{q_s}\right)\frac{\partial}{\partial\xi}} + \underset{\Delta(\Delta^2)_{\text{eqm}}}{m\tilde{\psi}\sin\xi\,\frac{\partial}{\partial\psi} + \frac{\partial R}{\partial\psi}\frac{\tilde{\psi}}{R}\cos\xi\left(\frac{\partial}{\partial\theta}+m\frac{\partial}{\partial\xi}\right)}_{\Delta^2}\right], \\ \boldsymbol{v}_b\cdot\nabla &= \underset{\epsilon(\Delta)_{\text{eqm}}}{\frac{Iv_\parallel}{Rq}\left[\frac{\partial}{\partial\theta}\left(\frac{v_\parallel}{\omega_c}\right)\frac{\partial}{\partial\psi} - \underset{\Delta}{\frac{\partial}{\partial\psi}\left(\frac{v_\parallel}{\omega_c}\right)\frac{\partial}{\partial\theta}}\right]} - \underset{\Delta}{\frac{mIv_\parallel}{Rq}\frac{\partial}{\partial\psi}\left(\frac{v_\parallel}{\omega_c}\right)\frac{\partial}{\partial\xi}}, \\ \boldsymbol{v}_E\cdot\nabla &= \underset{\Delta}{\frac{1}{q}\left(\frac{\partial\Phi}{\partial\psi}\frac{\partial}{\partial\theta} - \underset{\Delta(\Delta^2)_{\text{eqm}}}{\frac{\partial\Phi}{\partial\theta}\frac{\partial}{\partial\psi}}\right)} + \underset{\Delta}{\frac{m}{q}\left(\frac{\partial\Phi}{\partial\psi}\frac{\partial}{\partial\xi} - \underset{\Delta(\Delta^2)_{\text{eqm}}}{\frac{\partial\Phi}{\partial\xi}\frac{\partial}{\partial\psi}}\right)}, \end{aligned} \tag{2.3.5}$$

here, the following notation for spatial derivatives is implied (but omitted for simplicity):

$$\frac{\partial}{\partial\theta} = \left.\frac{\partial}{\partial\theta}\right|_{\xi,\psi}\,, \qquad \frac{\partial}{\partial\xi} = \left.\frac{\partial}{\partial\xi}\right|_{\theta,\psi}\,, \qquad \frac{\partial}{\partial\psi} = \left.\frac{\partial}{\partial\psi}\right|_{\xi,\theta} \tag{2.3.6}$$

then, inserting Eq.(2.3.5) into (2.2.1), the ion drift kinetic equation, correct to $O(\epsilon^{3/2}\Delta^2)$ is:

$$\begin{aligned} &\frac{v_\parallel}{Rq}\left.\frac{\partial f_i}{\partial\theta}\right|_\psi + \frac{mv_\parallel}{Rq}\left(1-\frac{q}{q_s}\right)\frac{\partial f_i}{\partial\xi} + \frac{v_\parallel}{Rq}m\tilde{\psi}\sin\xi\frac{\partial f_i}{\partial\psi} \\ &+ \frac{Iv_\parallel}{Rq}\frac{\partial}{\partial\theta}\left(\frac{v_\parallel}{\omega_{c,i}}\right)\frac{\partial f_i}{\partial\psi} - \frac{Iv_\parallel}{Rq}\frac{\partial}{\partial\theta}\left(\frac{v_\parallel}{\omega_{c,i}}\right)\left.\frac{\partial f_i}{\partial\theta}\right|_\psi - \frac{mIv_\parallel}{Rq}\frac{\partial}{\partial\psi}\left(\frac{v_\parallel}{\omega_{c,i}}\right)\frac{\partial f_i}{\partial\xi} \\ &+ \frac{1}{q}\left(\frac{\partial\Phi}{\partial\psi}\frac{\partial f_i}{\partial\theta} - \frac{\partial\Phi}{\partial\theta}\frac{\partial f_i}{\partial\psi}\right) + \frac{m}{q}\left(\frac{\partial\Phi}{\partial\psi}\frac{\partial f_i}{\partial\xi} - \frac{\partial\Phi}{\partial\xi}\frac{\partial f_i}{\partial\psi}\right) \\ &- \frac{eZ_i}{m_iv}\left(v_\parallel\nabla_\parallel\Phi + \boldsymbol{v}_b\cdot\nabla\Phi\right)\frac{\partial f_i}{\partial v} = C_{ii}(f_i), \end{aligned} \tag{2.3.7}$$

2.3.1 $O(\Delta^0)$ ion response

For the ion distribution f_i, the $O(\Delta^0)$ terms of Eq.(2.2.1) are:

$$\frac{v_\parallel}{Rq}\frac{\partial f_{i,0}}{\partial \theta} = C_i(f_{i,0}). \tag{2.3.8}$$

which, in neoclassical equilibrium analysis, is equivalent to $f_{i,0} = F_{M,i}$, the Maxwellian function. But assuming $eZ_j\Phi/T_j \sim \Delta$ (see Eq.(2.3.1)), the Boltzmann factor containing Φ can be expanded:

$$\begin{underset{1}{f_i} = \underset{1}{\left(1 - \frac{eZ_i\Phi}{T_i}\right)}\underset{\Delta}{F_{M,i}(\psi)} + \underset{\Delta}{g_1}\ .} \tag{2.3.9}$$

Here, the 'perturbed' contribution to f_i from g_1 is determined at the next 2 orders in Δ.

2.3.2 $O(\Delta^1)$ ion response

The $O(\Delta^1)$ contributions to Eq.(2.2.1) are:

$$\begin{aligned}
&-\frac{v_\parallel}{Rq}\frac{eZ_i}{T_i}\frac{\partial\Phi}{\partial\theta}\bigg|_\psi F_{M,i} + \frac{v_\parallel}{Rq}\frac{\partial g_1}{\partial\theta}\bigg|_\psi \\
&+\frac{Iv_\parallel}{Rq}\frac{\partial}{\partial\theta}\left(\frac{v_\parallel}{\omega_{c,i}}\right)\frac{\partial F_{M,i}}{\partial\psi} - \frac{Iv_\parallel}{Rq}\frac{\partial}{\partial\theta}\left(\frac{v_\parallel}{\omega_{c,i}}\right)\frac{eZ_i}{T_i}\frac{\partial\Phi}{\partial\psi}F_{M,i} + \frac{Iv_\parallel}{Rq}\frac{\partial}{\partial\theta}\left(\frac{v_\parallel}{\omega_{c,i}}\right)\frac{\partial g_1}{\partial\psi} \\
&-\frac{eZ_i}{m_i v}\frac{v_\parallel}{Rq}\left[\frac{\partial\Phi}{\partial\theta}\bigg|_\psi + I\frac{\partial}{\partial\theta}\left(\frac{v_\parallel}{\omega_{c,i}}\right)\frac{\partial\Phi}{\partial\psi}\right]\frac{\partial F_{M,i}}{\partial v} = 0,
\end{aligned} \tag{2.3.10}$$

Using the Maxwellian derivatives in Eq.(2.2.7), and also the following relation:

$$-\frac{eZ_j}{m_j v}\frac{\partial F_{M,j}}{\partial v} = \frac{2eZ_j}{m_j v_{\mathrm{th},j}^2}F_{M,j} = \frac{eZ_j}{T_j}F_{M,j},$$

then in Eq.(2.3.10), all of the Φ terms cancel out:

$$\begin{aligned}
&\frac{v_\parallel}{Rq}\left[\frac{\partial g_1}{\partial\theta}\bigg|_\psi + I\frac{\partial}{\partial\theta}\left(\frac{v_\parallel}{\omega_{c,i}}\right)\frac{\partial g_1}{\partial\psi}\right] + \frac{Iv_\parallel}{Rq}\frac{\partial}{\partial\theta}\left(\frac{v_\parallel}{\omega_{c,i}}\right)\frac{\omega_{*i}^T}{\omega_{*i}}\frac{n_0'}{n_0}F_{\mathrm{M},i} \\
&\cancel{-\frac{v_\parallel}{Rq}\frac{eZ_i}{T_i}F_{\mathrm{M},i}\left[\frac{\partial\Phi}{\partial\psi} + I\frac{\partial}{\partial\theta}\left(\frac{v_\parallel}{\omega_{c,i}}\right)\frac{\partial\Phi}{\partial\psi}\right]} + \cancel{\frac{v_\parallel}{Rq}\frac{eZ_i}{T_i}F_{\mathrm{M},i}\left[\frac{\partial\Phi}{\partial\psi} + I\frac{\partial}{\partial\theta}\left(\frac{v_\parallel}{\omega_{c,i}}\right)\frac{\partial\Phi}{\partial\psi}\right]} = 0.
\end{aligned} \tag{2.3.11}$$

The remaining terms of the $O(\Delta^1)$ equation are:

$$\boxed{\left.\frac{\partial g_1}{\partial \theta}\right|_\psi + I\left.\frac{\partial}{\partial \theta}\right|_\psi \left(\frac{v_\parallel}{\omega_{c,i}}\right)\frac{\partial g_1}{\partial \psi} = -I\left.\frac{\partial}{\partial \theta}\right|_\psi \left(\frac{v_\parallel}{\omega_{c,i}}\right)\frac{\omega^T_{*,i}}{\omega_{*,i}}\frac{n_0'}{n_0}F_{\mathrm{M},i}} \tag{2.3.12}$$

Before proceeding to the next order, a unit conversion will be performed to simplify Eq.(2.3.12).

Transformation into toroidal canonical angular momentum

In neoclassical equilibrium transport, in addition to $\mathcal{E}$ and μ, there is a third constant of guiding centre motion: the *toroidal canonical angular momentum* p_φ:

$$p_\varphi(\psi,\theta) = (\psi - \psi_s) - \rho, \qquad \rho = \frac{I(\psi)v_\parallel}{\omega_{c,j}}, \tag{2.3.13}$$

where ρ represents the radial deviation of a particle from the flux surface at ψ (not to be confused with gyro-radii ρ_j or $\rho_{\theta,j}$) and $\omega_{c,j}$ is the gyrofrequency. Note that when $v_\parallel \sim v_{th,j}$, the term $\rho \simeq RB_\theta\rho_{\theta,j}$, where $\rho_{\theta,j}$ is the poloidal gyroradius. Thus, particle guiding centre orbits in an axisymmetric toroidal plasma will deviate radially from their flux surface by a factor $O(\rho_{\theta,j})$ as a consequence of ∇B and curvature drifts, as illustrated in Fig.2.1 for ions. While magnetic islands disrupt the toroidal symmetry that leads to the conservation of p_φ, in the limit of $w \ll r_s$ and to the leading order, the toroidal symmetry is approximately upheld. Utilising p_φ in place of $\{\psi,\theta\}$, the dimensionality of the problem can be reduced, making it more computationally tractable.

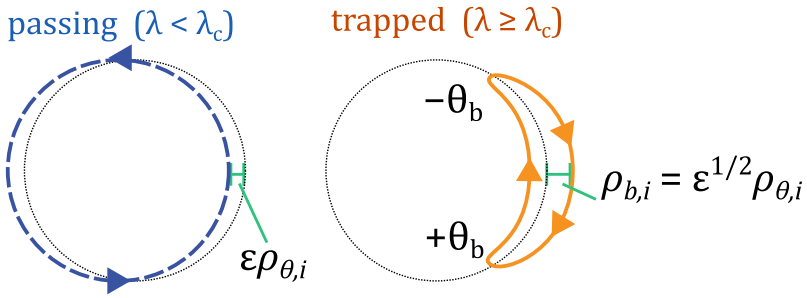

Figure 2.1: Poloidal cross section showing deviation of passing and trapped ion orbits (at constant p_φ) from a rational flux surface ψ_s (black dotted circle).

Transforming the spatial derivatives of the $\{\psi,\theta,\xi\}$ coordinates to $\{p_\varphi,\theta,\xi\}$ coordinates, with

orderings in Δ given below:

$$\frac{\partial}{\partial\psi} = \frac{\partial p_\varphi}{\partial\psi}\frac{\partial}{\partial p_\varphi}$$
$$\rightarrow \left.\frac{\partial}{\partial\psi}\right|_{\theta,\xi} = (1-\rho')\frac{\partial}{\partial p_\varphi}, \qquad \rho' = \frac{\partial\rho}{\partial\psi}. \tag{2.3.14}$$

$$1 : \Delta$$
$$\left.\frac{\partial}{\partial\theta}\right|_{\psi} = \left.\frac{\partial}{\partial\theta}\right|_{p_\varphi} + \left.\frac{\partial p_\varphi}{\partial\theta}\right|_{\psi}\frac{\partial}{\partial p_\varphi}$$
$$\rightarrow \left.\frac{\partial}{\partial\theta}\right|_{\psi} = \left.\frac{\partial}{\partial\theta}\right|_{p_\varphi} - I\frac{\partial}{\partial\theta}\left(\frac{v_\parallel}{\omega_{c,i}}\right)\frac{\partial}{\partial p_\varphi}. \tag{2.3.15}$$

Then, returning to the $O(\Delta)$ equation (2.3.12), we transform the θ-derivative at fixed ψ to fixed p. To do so, we use the following relation for the $\left(\frac{v_\parallel}{\omega_{c,i}}\right)$ term:

$$\left.\frac{\partial}{\partial\theta}\left(\frac{v_\parallel}{\omega_{c,i}}\right)\right|_{\psi} = \left.\frac{\partial}{\partial\theta}\left(\frac{v_\parallel}{\omega_{c,i}}\right)\right|_{p_\varphi} - I\left.\frac{\partial}{\partial\theta}\right|_{\psi}\left(\frac{v_\parallel}{\omega_{c,i}}\right)\frac{\partial}{\partial\psi}\left(\frac{v_\parallel}{\omega_{c,i}}\right), \tag{2.3.16}$$

and also the following relation, where the ρ' term is also $O(\Delta)$ smaller:

$$\frac{\partial g_1}{\partial\psi} = \frac{\partial g_1}{\partial p_\varphi}(1-\rho')\ . \tag{2.3.17}$$

Converting $\{\psi,\theta,\xi\}$ to $\{p_\varphi,\theta,\xi\}$ coordinates, the $O(\Delta^1)$ equation (2.3.12) becomes:

$$\frac{v_\parallel}{Rq}\left.\frac{\partial g_1}{\partial\theta}\right|_{p_\varphi} = -\frac{Iv_\parallel}{Rq}\left.\frac{\partial}{\partial\theta}\left(\frac{v_\parallel}{\omega_{c,i}}\right)\right|_{p_\varphi}\frac{\omega_{*i}^T}{\omega_{*i}}\frac{n_i'}{n_i}F_{\mathrm{M},i}. \tag{2.3.18}$$

which, after omitting $v_\parallel/Rq$ either side, can be integrated in θ to yield:

$$\boxed{g_1 = -\frac{Iv_\parallel}{\omega_{ci}}\frac{\omega_{*i}^T}{\omega_{*i}}\frac{n_i'}{n_i}F_{\mathrm{M},i} + \bar{g}_{(1)}} \tag{2.3.19}$$

Here, the bar on $\bar{g}$ indicates the quantity is θ-independent at fixed p_φ. The constant of integration is $\bar{g}_{(1)}(p_\varphi,\xi,\boldsymbol{v})$, to be determined from the $O(\Delta^2)$ contribution to the drift kinetic equation.

2.3.3 $O(\Delta^2)$ ion response

Proceeding to the next order, the $O(\Delta^2)$ ion response is:

$$
\begin{aligned}
&\overbrace{\frac{v_\parallel}{Rq}\left.\frac{\partial g_2}{\partial\theta}\right|_\psi}^{*1} - \overbrace{\frac{v_\parallel}{Rq} I\frac{\partial}{\partial\theta}\left(\frac{v_\parallel}{\omega_{c,i}}\right)\rho'\frac{\partial g_1}{\partial p_\varphi}}^{*2} + \frac{v_\parallel}{Rq}\left[m\left(1-\frac{q}{q_s}\right)\frac{\partial g_1}{\partial\xi} + m\tilde{\psi}\sin\xi\,\frac{\partial g_1}{\partial p_\varphi}\right] \\
&+ \frac{v_\parallel}{Rq} m\tilde{\psi}\sin\xi\,\frac{\partial F_{\mathrm{M},i}}{\partial\psi} - \cancel{\frac{v_\parallel}{Rq}\left[m\left(1-\frac{q}{q_s}\right)\frac{\partial\Phi}{\partial\xi} + m\tilde{\psi}\sin\xi\,\frac{\partial\Phi}{\partial\psi}\right]\frac{eZ_iF_{\mathrm{M},i}}{T_i}} \\
&- \frac{Iv_\parallel}{Rq}\left[\frac{\partial}{\partial\psi}\left(\frac{v_\parallel}{\omega_{c,i}}\right)\left(\cancel{\left.\frac{\partial g_1}{\partial\theta}\right|_{p_\varphi}}^{0} - \overbrace{I\frac{\partial}{\partial\theta}\left(\frac{v_\parallel}{\omega_{c,i}}\right)\frac{\partial g_1}{\partial p_\varphi}}^{*2}\right) + m\frac{\partial}{\partial\psi}\left(\frac{v_\parallel}{\omega_{c,i}}\right)\frac{\partial g_1}{\partial\xi}\right] + \overbrace{\frac{Iv_\parallel}{Rq}\frac{\partial}{\partial\theta}\left(\frac{v_\parallel}{\omega_{c,i}}\right)\frac{\partial g_2}{\partial\psi}}^{*1} \\
&\cancel{- \frac{Iv_\parallel}{Rq}\left[\frac{\partial}{\partial\psi}\left(\frac{v_\parallel}{\omega_{c,i}}\right)\left(\left.\frac{\partial\Phi}{\partial\theta}\right|_\psi + m\frac{\partial\Phi}{\partial\xi}\right)\right]\frac{eZ_iF_{\mathrm{M},i}}{T_i}} \\
&+ \frac{1}{q}\left[\frac{\partial\Phi}{\partial\psi}\left(\cancel{\left.\frac{\partial g_1}{\partial\theta}\right|_{p_\varphi}}^{0} - I\frac{\partial}{\partial\theta}\left(\frac{v_\parallel}{\omega_{c,i}}\right)\frac{\partial g_1}{\partial p_\varphi}\right) - \left.\frac{\partial\Phi}{\partial\theta}\right|_\psi\frac{\partial g_1}{\partial p_\varphi}\right] \\
&+ \frac{m}{q}\left(\frac{\partial\Phi}{\partial\psi}\frac{\partial g_1}{\partial\xi} - \frac{\partial\Phi}{\partial\xi}\frac{\partial g_1}{\partial p_\varphi}\right) - \frac{1}{q}\left(\left.\frac{\partial\Phi}{\partial\theta}\right|_\psi + m\frac{\partial\Phi}{\partial\xi}\right)\frac{\partial F_{\mathrm{M},i}}{\partial\psi} \\
&- \frac{eZ_i}{m_iv}\frac{\partial F_{\mathrm{M},i}}{\partial v}\frac{v_\parallel}{Rq}\cancel{\left[m\left(1-\frac{q}{q_s}\right)\frac{\partial\Phi}{\partial\xi} + m\tilde{\psi}\sin\xi\,\frac{\partial\Phi}{\partial\psi} - I\frac{\partial}{\partial\psi}\left(\frac{v_\parallel}{\omega_{c,i}}\right)\left.\frac{\partial\Phi}{\partial\theta}\right|_\psi - mI\frac{\partial}{\partial\psi}\left(\frac{v_\parallel}{\omega_{c,i}}\right)\frac{\partial\Phi}{\partial\xi}\right]} \\
&\qquad\qquad = C_{ii}(g_1).
\end{aligned}
\tag{2.3.20}
$$

Above, the terms marked $*1$ add together to become:

$$
*1 = \frac{v_\parallel}{Rq}\left.\frac{\partial g_2}{\partial\theta}\right|_\psi + \frac{Iv_\parallel}{Rq}\frac{\partial}{\partial\theta}\left(\frac{v_\parallel}{\omega_{c,i}}\right)\frac{\partial g_2}{\partial\psi} = \frac{v_\parallel}{Rq}\left.\frac{\partial g_2}{\partial\theta}\right|_{p_\varphi}
$$

the terms marked $*2$ add together into a small term that is neglected, noting $\rho' = \dfrac{\partial}{\partial\psi}\left(I\left(\frac{v_\parallel}{\omega_{c,i}}\right)\right)$:

$$
\begin{aligned}
*2 &= -I\frac{\partial}{\partial\theta}\left(\frac{v_\parallel}{\omega_{c,i}}\right)\frac{\partial}{\partial\psi}\left(I\left(\frac{v_\parallel}{\omega_{c,i}}\right)\right) + I\frac{\partial}{\partial\theta}\left(\frac{v_\parallel}{\omega_{c,i}}\right)\frac{\partial}{\partial\psi}\left(\frac{v_\parallel}{\omega_{c,i}}\right) \\
&= -I'I\frac{\partial}{\partial\theta}\left(\frac{v_\parallel}{\omega_{c,i}}\right)\left(\frac{v_\parallel}{\omega_{c,i}}\right) \quad\Rightarrow\quad O(\Delta)\text{ smaller.}
\end{aligned}
$$

Recalling Eq.(2.3.19), noting that the derivatives of g_1 in p_φ and ξ are, respectively:

$$\frac{\partial g_1}{\partial p_\varphi} = -\frac{\partial \rho}{\partial p_\varphi} F'_{\mathrm{M},i} + \bar{g}', \quad F'_{\mathrm{M},i} = \frac{\partial F_{\mathrm{M},i}}{\partial \psi}$$
$$\frac{\partial g_1}{\partial \xi} = \frac{\partial \bar{g}}{\partial \xi}.$$

Then, substituting for p_φ and using Eq.(2.3.16):

$$\frac{\partial g_1}{\partial p_\varphi} + F'_{\mathrm{M},i} = (1-\rho')F'_{\mathrm{M},i} + \bar{g}'$$
$$\simeq F'_{\mathrm{M},i} + \bar{g}'.$$

Then, Eq.(2.3.20) is simplified:

$$\begin{aligned} &\frac{v_\parallel}{Rq}\left.\frac{\partial g_2}{\partial \theta}\right|_{p_\varphi} + \frac{v_\parallel}{Rq}\left[m\left(1-\frac{q}{q_s}\right)\frac{\partial \bar{g}}{\partial \xi} + m\tilde{\psi}\sin\xi\left(\frac{\partial \bar{g}}{\partial p_\varphi} + F'_{\mathrm{M},i}\right)\right] \\ &-\frac{mIv_\parallel}{Rq}\frac{\partial}{\partial \psi}\left(\frac{v_\parallel}{\omega_{c,i}}\right)\frac{\partial \bar{g}}{\partial \xi} - \frac{1}{q}\left[\overbrace{\left.\frac{\partial \Phi}{\partial \theta}\right|_\psi + I\frac{\partial}{\partial \theta}\left(\frac{v_\parallel}{\omega_{c,i}}\right)\frac{\partial \Phi}{\partial \psi}}^{*}\right]\left(\frac{\partial \bar{g}}{\partial p_\varphi} + F'_{\mathrm{M},i}\right) \\ &\qquad + \frac{m}{q}\left[\frac{\partial \Phi}{\partial \psi}\frac{\partial \bar{g}}{\partial \xi} - \frac{\partial \Phi}{\partial \xi}\left(\frac{\partial \bar{g}}{\partial p_\varphi} + F'_{\mathrm{M},i}\right)\right] \quad = \quad C_{ii}(g_1). \end{aligned} \tag{2.3.21}$$

Here, $* \equiv \left.\frac{\partial \Phi}{\partial \theta}\right|_{p_\varphi}$, but since $\bar{g} = \bar{g}(p_\varphi, \xi)$, it is assumed that $\left.\frac{\partial \Phi}{\partial \theta}\right|_{p_\varphi} = O(0)$. Then, the $O(\Delta^2)$ equation for the ion response simplifies to:

$$\boxed{\begin{aligned} &\frac{v_\parallel}{Rq}\left.\frac{\partial g_2}{\partial \theta}\right|_{p_\varphi} + \frac{mv_\parallel}{Rq}\left[\left(1-\frac{q}{q_s}\right)\frac{\partial \bar{g}}{\partial \xi} + \tilde{\psi}\sin\xi\left(\frac{\partial \bar{g}}{\partial p_\varphi} + F'_{\mathrm{M},i}\right)\right] \\ &-\frac{mv_\parallel}{Rq}I\frac{\partial}{\partial \psi}\left(\frac{v_\parallel}{\omega_{c,i}}\right)\frac{\partial \bar{g}}{\partial \xi} + \frac{m}{q}\left[\frac{\partial \Phi}{\partial \psi}\frac{\partial \bar{g}}{\partial \xi} - \frac{\partial \Phi}{\partial \xi}\left(\frac{\partial \bar{g}}{\partial p_\varphi} + F'_{\mathrm{M},i}\right)\right] = C_{ii}(g_1) \end{aligned}} \tag{2.3.22}$$

To solve for $\bar{g}$ from Eq.(2.3.22), the higher order g_2 term must be eliminated. This is done by taking advantage of their periodicity in θ which, for passing particles, it is known that:

$$g_2(\theta = -\pi) = g_2(\theta = +\pi) \tag{2.3.23}$$

and for trapped particles, via the conservation of particle number at the bounce points:

$$g_2(\theta \pm \theta_b, \sigma = -1) = g_2(\theta \pm \theta_b, \sigma = +1), \tag{2.3.24}$$

recalling $\sigma = v_\parallel/|v_\parallel|$ is the sign of the particle's field-parallel velocity. Then, the g_2 terms can be eliminated by calculating the average of Eq.(2.3.22) over a period in θ at fixed p_φ, i.e., the average over the guiding centre orbit.

For passing particles, the orbit-averaging of Eq.(2.3.22) involves multiplying by $Rq/v_\parallel$, then integrating in $\theta = \{-\pi, +\pi\}$ at fixed p_φ, and dividing by 2π. For trapped particles, Eq.(2.3.22) is multiplied by $\sigma/2 \times Rq/v_\parallel$, integrated in $\theta = \{-\theta_b, +\theta_b\}$ and divided by 2π, then the two streams in σ are summed together (averaged, via the factor 1/2). Thus, any terms with odd powers in σ^n will sum to their value when $\sigma = +1$, while those even in σ^n (or σ-independent) will disappear from the trapped particle equation. Note that, in general, $g_1^t(\psi, \theta)$ is a function of σ, as it matters whether the particle is travelling parallel or anti-parallel to the field lines; the two such particles would be on different banana orbits, but $g_1^t(p_\varphi)$ itself is independent of σ (i.e. all the σ-dependence is encapsulated within p_φ).

To perform the orbit-averaging, the orbit paths at constant p_φ (hence varying ψ) need to be determined. Recall in Eq.(2.3.13) that the orbits of constant p_φ deviate from a flux surface at constant ψ by $O(\rho(\psi))$. Then, an implicit function for the variation in ψ along the integration paths, $\hat{\psi}(\theta)$, can be obtained by rearranging Eq.(2.3.13):

$$\hat{\psi}(p_\varphi, \theta) = p_\varphi + \rho(\hat{\psi}, \theta) \tag{2.3.25}$$

Alternatively, an explicit integral form of $\hat{\psi}$ can be obtained by considering:

$$dp_\varphi = (1 - \rho')d\psi - I\frac{\partial}{\partial\theta}\left(\frac{v_\parallel}{\omega_{c,i}}\right)d\theta.$$

Therefore, the θ-averaging operators at fixed p_φ are defined as:

$$\boxed{\begin{aligned} \langle F(\psi,\theta)\rangle_\theta^p &= \frac{1}{2\pi}\oint F(\hat{\psi},\theta)\,d\theta && \lambda < \lambda_c \text{ (passing ions)} \\ \langle F(\psi,\theta)\rangle_\theta^t &= \frac{1}{2\pi}\sum_\sigma \frac{\sigma}{2}\int_{-\theta_b}^{+\theta_b} F(\hat{\psi},\theta)\,d\theta && \lambda \geq \lambda_c \text{ (trapped ions)} \end{aligned}} \tag{2.3.26}$$

Again, note that the trapped orbit changes direction with respect to $v_\parallel$ every half-orbit, and hence the 'σ-average' of the integrated quantity is taken, which introduces a factor 1/2.

Returning to Eq.(2.3.22), we multiply Eq.(2.3.22) by $Rq/v_\parallel$ and perform θ-averaging at fixed p_φ, annihilating the term in g_2. Then, the remaining terms of the equation for $\bar{g}$ for the passing

particles:

$$\boxed{\begin{aligned} m\left\langle\left(1-\frac{q}{q_s}\right)\right\rangle_\theta^p \frac{\partial\bar{g}}{\partial\xi} + m\tilde{\psi}\sin\xi\left(\frac{\partial\bar{g}}{\partial p_\varphi}+F'_{\mathrm{M},i}\right) - m\left\langle I\frac{\partial}{\partial\psi}\left(\frac{v_\parallel}{\omega_{c,i}}\right)\right\rangle_\theta^p \frac{\partial\bar{g}}{\partial\xi} \\ + m\left\langle\frac{R}{v_\parallel}\frac{\partial\Phi}{\partial\psi}\right\rangle_\theta^p \frac{\partial\bar{g}}{\partial\xi} - m\left\langle\frac{R}{v_\parallel}\frac{\partial\Phi}{\partial\xi}\right\rangle_\theta^p \left(\frac{\partial\bar{g}}{\partial p_\varphi}+F'_{\mathrm{M},i}\right) = \left\langle\frac{Rq}{v_\parallel}C_{ii}(g_1)\right\rangle_\theta^p \end{aligned}} \tag{2.3.27}$$

For the trapped particles, the summation over σ (implied in the bracket: $\langle ... \rangle_\theta^t$) will eliminate any even-σ^n terms, leaving:

$$\boxed{\begin{aligned} m\left\langle\left(1-\frac{q}{q_s}\right)\right\rangle_\theta^t \frac{\partial\bar{g}}{\partial\xi} - m\left\langle I\frac{\partial}{\partial\psi}\left(\frac{v_\parallel}{\omega_{c,i}}\right)\right\rangle_\theta^t \frac{\partial\bar{g}}{\partial\xi} + m\left\langle\frac{R}{|v_\parallel|}\frac{\partial\Phi}{\partial\psi}\right\rangle_\theta^t \frac{\partial\bar{g}}{\partial\xi} \\ - m\left\langle\frac{R}{|v_\parallel|}\frac{\partial\Phi}{\partial\xi}\right\rangle_\theta^t \left(\frac{\partial\bar{g}}{\partial p_\varphi}+F'_{\mathrm{M},i}\right) = \left\langle\frac{Rq}{v_\parallel}C_{ii}(g_1)\right\rangle_\theta^t \end{aligned}} \tag{2.3.28}$$

Transforming the pitch-angle scattering terms

Returning to the collision operator term Eq.(2.2.12), the λ-derivatives are taken at fixed ψ, and must be transformed to those at fixed p_φ (as p_φ has λ-dependence through $v_\parallel$):

$$\begin{aligned} \left.\frac{\partial}{\partial\lambda}\right|_\psi &= \left.\frac{\partial}{\partial\lambda}\right|_{p_\varphi} + \left.\frac{\partial p_\varphi}{\partial\lambda}\right|_\psi \frac{\partial}{\partial p_\varphi} \\ &= \left.\frac{\partial}{\partial\lambda}\right|_{p_\varphi} - \frac{I}{\omega_{ci}}\frac{\partial v_\parallel}{\partial\lambda}\frac{\partial}{\partial p_\varphi}, \qquad \frac{\partial v_\parallel}{\partial\lambda} = \frac{\sigma v}{2}\frac{-B}{\sqrt{1-\lambda B}} \\ \rightarrow \left.\frac{\partial}{\partial\lambda}\right|_\psi &= \left.\frac{\partial}{\partial\lambda}\right|_{p_\varphi} + \frac{\sigma v}{2}\frac{I}{\omega_{ci}}\frac{B}{\sqrt{1-\lambda B}}\frac{\partial}{\partial p_\varphi} \end{aligned} \tag{2.3.29}$$

Then, the pitch-angle scattering term transforms to:

$$\begin{aligned} \lambda\sqrt{1-\lambda B}\left.\frac{\partial}{\partial\lambda}\right|_\psi &= \lambda\sqrt{1-\lambda B}\left.\frac{\partial}{\partial\lambda}\right|_{p_\varphi} + \frac{\sigma v}{2}\lambda B\frac{I}{\omega_{ci}}\frac{\partial}{\partial p_\varphi} \\ \rightarrow \left.\frac{\partial}{\partial\lambda}\left(\lambda\sqrt{1-\lambda B}\frac{\partial}{\partial\lambda}\right)\right|_\psi &= \left.\frac{\partial}{\partial\lambda}\left(\lambda\sqrt{1-\lambda B}\frac{\partial}{\partial\lambda}\right)\right|_{p_\varphi} + \frac{\sigma v}{2}B\frac{I}{\omega_{ci}}\frac{\partial}{\partial p_\varphi} + \frac{\sigma v}{2}\lambda B\frac{I}{\omega_{ci}}\frac{\partial^2}{\partial\lambda\partial p_\varphi} \\ &\quad + \frac{\sigma v}{2}\frac{I}{\omega_{ci}}\frac{B}{\sqrt{1-\lambda B}}\frac{\partial}{\partial p_\varphi}\left(\lambda\sqrt{1-\lambda B}\frac{\partial}{\partial\lambda}\right)\Big|_{p_\varphi} \\ &\quad + \frac{\sigma v}{2}\frac{I}{\omega_{ci}}\frac{B}{\sqrt{1-\lambda B}}\frac{\sigma v}{2}\frac{\partial}{\partial p_\varphi}\left(\lambda B\frac{I}{\omega_{ci}}\frac{\partial}{\partial p_\varphi}\right) \end{aligned}$$

Assuming $\dfrac{\partial B}{\partial p_\varphi} \approx \dfrac{\partial B}{\partial \psi} \sim \frac{B}{R}$ is small (by $O(\epsilon)$) compared to the leading order term, and noting also that $\sigma^2 \equiv +1$:

$$\frac{\partial}{\partial \lambda}\left(\lambda\sqrt{1-\lambda B}\frac{\partial}{\partial \lambda}\right)\bigg|_\psi = \frac{\partial}{\partial \lambda}\left(\lambda\sqrt{1-\lambda B}\frac{\partial}{\partial \lambda}\right)\bigg|_{p_\varphi} + \frac{\sigma v}{2}\lambda B\frac{I}{\omega_{ci}}\frac{\partial}{\partial p_\varphi} + 2\frac{\sigma v}{2}\lambda B\frac{I}{\omega_{ci}}\frac{\partial^2}{\partial\lambda\partial p_\varphi} + \frac{v^2}{4}\frac{B}{\sqrt{1-\lambda B}}\lambda B\left(\frac{I}{\omega_{ci}}\right)^2\frac{\partial^2}{\partial p_\varphi^2}$$

$$\therefore \ \frac{\sqrt{1-\lambda B}}{B}\frac{\partial}{\partial \lambda}\left(\lambda\sqrt{1-\lambda B}\frac{\partial}{\partial \lambda}\right)\bigg|_\psi = \frac{\sqrt{1-\lambda B}}{B}\frac{\partial}{\partial \lambda}\left(\lambda\sqrt{1-\lambda B}\frac{\partial}{\partial \lambda}\right)\bigg|_{p_\varphi} + \frac{1}{2}\frac{Iv_\parallel}{\omega_{ci}}\frac{\partial}{\partial p_\varphi} + \frac{Iv_\parallel}{\omega_{ci}}\lambda\frac{\partial^2}{\partial\lambda\partial p_\varphi} + \frac{\lambda B}{4}\left(\frac{Iv}{\omega_{ci}}\right)^2\frac{\partial^2}{\partial p_\varphi^2}. \tag{2.3.30}$$

Here,

$$\frac{\partial}{\partial \lambda}\left(\lambda\sqrt{1-\lambda B}\frac{\partial}{\partial \lambda}\right) = \left[\sqrt{1-\lambda B} - \frac{\lambda B}{2\sqrt{1-\lambda B}}\right]\frac{\partial}{\partial \lambda} + \lambda\sqrt{1-\lambda B}\frac{\partial^2}{\partial\lambda^2} \tag{2.3.31}$$

$$= \frac{(2-3\lambda B)}{2\sqrt{1-\lambda B}}\frac{\partial}{\partial \lambda} + \lambda\sqrt{1-\lambda B}\frac{\partial^2}{\partial\lambda^2}. \tag{2.3.32}$$

Hence:

$$\frac{\sqrt{1-\lambda B}}{B}\frac{\partial}{\partial \lambda}\left(\lambda\sqrt{1-\lambda B}\frac{\partial}{\partial \lambda}\right)\bigg|_\psi = \frac{\sqrt{1-\lambda B}}{B}\frac{(2-3\lambda B)}{2\sqrt{1-\lambda B}}\frac{\partial}{\partial \lambda}\bigg|_{p_\varphi} + \frac{\sqrt{1-\lambda B}}{B}\lambda\sqrt{1-\lambda B}\frac{\partial^2}{\partial\lambda^2}\bigg|_{p_\varphi} + \frac{1}{2}\frac{Iv_\parallel}{\omega_{ci}}\frac{\partial}{\partial p_\varphi} + \frac{Iv_\parallel}{\omega_{ci}}\lambda\frac{\partial^2}{\partial\lambda\partial p_\varphi} + \frac{\lambda B}{4}\left(\frac{Iv}{\omega_{ci}}\right)^2\frac{\partial^2}{\partial p_\varphi^2}. \tag{2.3.33}$$

Inserting the above expressions into the collision operator term in Eqs.(2.3.27) and (2.3.28) gives:

$$\frac{Rq}{v_\parallel}C_{ii}(g_1) = 2\nu_{ii}\left[\frac{Rq}{B}\frac{1}{\sigma v}\frac{(2-3\lambda B)}{2\sqrt{1-\lambda B}}\frac{\partial g_1}{\partial \lambda}\bigg|_{p_\varphi} + \frac{Rq}{B}\frac{1}{\sigma v}\lambda\sqrt{1-\lambda B}\frac{\partial^2 g_1}{\partial\lambda^2}\bigg|_{p_\varphi} + \frac{Rq}{2}\frac{I}{\omega_{ci}}\frac{\partial g_1}{\partial p_\varphi} + \frac{Rq}{v_\parallel}\frac{\lambda B}{4}v^2\left(\frac{I}{\omega_{ci}}\right)^2\frac{\partial g_1}{\partial p_\varphi^2} + Rq\frac{I}{\omega_{ci}}\lambda\frac{\partial^2 g_1}{\partial\lambda\partial p_\varphi} + Rq\frac{\bar{u}_{\parallel i}(g_1)}{v_{\mathrm{th}i}^2}F_{\mathrm{M},i}\right]. \tag{2.3.34}$$

But, $B(\theta) \propto R^{-1}(\theta)$ (i.e. they have the same θ-dependence), so Rq/B has no θ-dependence. Then, the θ-averaged collision term is:

$$\left\langle \frac{Rq}{v_\parallel} C_{ii}(g_1) \right\rangle_\theta = 2\nu_{ii}(v)\frac{R_0 q_0}{B_0}\left[\frac{1}{\sigma v}\left\langle \frac{(2-3\lambda B)}{2\sqrt{1-\lambda B}}\right\rangle_\theta \left.\frac{\partial g_1}{\partial \lambda}\right|_{p_\varphi} + \frac{\lambda}{\sigma v}\left\langle \sqrt{1-\lambda B}\right\rangle_\theta \left.\frac{\partial^2 g_1}{\partial \lambda^2}\right|_{p_\varphi}\right.$$
$$+ \frac{B_0}{2}\frac{I}{\omega_{ci0}}\frac{\partial g_1}{\partial p_\varphi} + \frac{\sigma v}{4}\lambda B_0^2 \left\langle \frac{1}{\sqrt{1-\lambda B}}\right\rangle_\theta \left(\frac{I}{\omega_{ci0}}\right)^2 \frac{\partial^2 g_1}{\partial p_\varphi^2} \qquad (2.3.35)$$
$$\left. + \frac{I}{\omega_{ci0}}\lambda B_0 \frac{\partial^2 g_1}{\partial \lambda \partial p_\varphi} + \frac{\left\langle B\bar{u}_{\parallel i}(g_1)\right\rangle_\theta}{B_0 v_{\mathrm{th}i}^2} F_{\mathrm{M},i}\right]$$

Note that here, the term in $\dfrac{\partial^2 g_1}{\partial p^2}$ corresponds with neoclassical diffusion, and is the only transport term in the model that provides cross-field transport *across* p_φ-orbits.

2.3.4 Expansion at the rational surface

Next, we Taylor expand g_1 at the rational surface where the island forms ($\psi = \psi_s$), which further simplifies Eq.(2.3.35). Recall the form of ion distribution function, (2.3.9) and (2.3.19):

$$f_i = \left(1 - \frac{eZ_i\Phi}{T_i}\right) F_{\mathrm{M},i}(\psi) + g_1 + ..., \quad g_1 = -\frac{Iv_\parallel}{\omega_{ci}} F'_{\mathrm{M},i} + \bar{g}, \quad F'_{\mathrm{M},i} = \frac{\omega_{*i}^T}{\omega_{*i}}\frac{n'}{n} F_{\mathrm{M},i}.$$

In the vicinity of the island, the Maxwellian $F_{M,i}$ can be expanded in $\Delta = \rho_{\theta,i}/w$ at $\psi = \psi_s$:

$$F_{\mathrm{M},i}(\psi) \simeq F_{\mathrm{M}is}(\psi_s) + (\psi - \psi_s)F'_{\mathrm{M}is} + O(F''_{\mathrm{M},i}). \qquad (2.3.36)$$

Here, subscript s denotes quantities local to the rational surface ψ_s. Expanding f_i, to the leading order in Δ:

$$f_i = \left(1 - \frac{eZ_i\Phi}{T_i}\right) F_{\mathrm{M}is} + \left[(\psi - \psi_s) - \frac{Iv_\parallel}{\omega_{ci}}\right] F'_{\mathrm{M}is} + \bar{g} + ...$$
$$\rightarrow \; f_i = \left(1 - \frac{eZ_i\Phi}{T_i}\right) F_{\mathrm{M}is} + p_\varphi F'_{\mathrm{M}is} + \bar{g} + O(\Delta^2). \qquad (2.3.37)$$

For the orbit-averaged terms in Eqs.(2.3.27) and (2.3.28), θ-averaging at fixed p_φ, $\langle ... \rangle_\theta^{p_\varphi}$, needs to be applied in full to perturbed quantities (those varying on the length-scale of w or $\rho_{\theta,i}$ like $\bar{u}_{\parallel,i}$ and Φ), but the θ-average at fixed ψ , $\langle ... \rangle_\theta^{\psi}$, is sufficient for equilibrium quantities varying on the length-scale of r, namely the pitch-angle scattering terms in Sec.2.3.3. Returning to Eq.(2.3.27) and Eq.(2.3.28), we expand the first two terms at the rational surface, changing the θ-averaging

operators appropriately:

$$1-\frac{q}{q_s}=1-\frac{1}{q_s}\left(q_s+(\psi-\psi_s)q_s'+...\right)=-\frac{q_s'}{q_s}\left(p_\varphi+\frac{Iv_\parallel}{\omega_{ci0}}\right).$$
$$\Rightarrow\ \left\langle 1-\frac{q}{q_s}\right\rangle_\theta^{p_\varphi}=-\frac{q_s'}{q_s}p_\varphi-\frac{q_s'}{q_s}I\left\langle\frac{v_\parallel}{\omega_{ci0}}\right\rangle_\theta^{\psi}$$
$$=-\frac{q_s'}{q_s}p_\varphi-\frac{q_s'}{q_s}\sigma v\frac{IB_0}{\omega_{ci0}}\left\langle\frac{\sqrt{1-\lambda B}}{B}\right\rangle_\theta^{\psi}.$$

where above we have used $\left\langle\frac{v_\parallel}{\omega_{ci0}}\right\rangle_\theta^{\psi}\simeq\left\langle\frac{v_\parallel}{\omega_{ci0}}\right\rangle_\theta^{p_\varphi}$ due to its small size, and:

$$\frac{\partial}{\partial\psi}\left(\frac{v_\parallel}{\omega_{ci0}}\right)=\frac{\sigma v}{\omega_{ci0}}\frac{\partial B}{\partial\psi}\left[\frac{-\lambda}{2\sqrt{1-\lambda B}}-\frac{\sqrt{1-\lambda B}}{B}\right]$$
$$\Rightarrow\ \left\langle\frac{\partial}{\partial\psi}\left(\frac{v_\parallel}{\omega_{ci0}}\right)\right\rangle_\theta^{\psi}=-\frac{\sigma vB_0}{\omega_{ci0}}\left[\frac{1}{2}\left\langle\frac{B'}{B^2}\frac{\lambda B}{\sqrt{1-\lambda B}}\right\rangle_\theta^{\psi}+\left\langle\frac{B'}{B}\sqrt{1-\lambda B}\right\rangle_\theta^{\psi}\right].$$

Likewise for the collision operator, the surviving terms in Eq.(2.3.35) are:

$$\left\langle\frac{Rq}{v_\parallel}C_{ii}(g_1)\right\rangle_\theta^{p_\varphi}=2\nu_{ii}(v)\frac{R_0q_0}{B_0}\left[\frac{1}{\sigma v}\left\langle\frac{(2-3\lambda B)}{2\sqrt{1-\lambda B}}\right\rangle_\theta^{\psi}\frac{\partial\bar{g}}{\partial\lambda}\bigg|_{p_\varphi}+\frac{\lambda}{\sigma v}\left\langle\sqrt{1-\lambda B}\right\rangle_\theta^{\psi}\frac{\partial^2\bar{g}}{\partial\lambda^2}\bigg|_{p_\varphi}\right.$$
$$+\frac{B_0}{2}\frac{I}{\omega_{ci0}}\left(F_{\mathrm{M},i}'+\frac{\partial\bar{g}}{\partial p_\varphi}\right)+\frac{\sigma v}{4}\lambda B_0^2\left\langle\frac{1}{\sqrt{1-\lambda B}}\right\rangle_\theta^{\psi}\left(\frac{I}{\omega_{ci0}}\right)^2\frac{\partial^2\bar{g}}{\partial p_\varphi^2}$$
$$\left.+\frac{I}{\omega_{ci0}}\lambda B_0\frac{\partial^2\bar{g}}{\partial\lambda\partial p_\varphi}+\frac{\left\langle B\bar{u}_{\parallel i}(g_1)\right\rangle_\theta^{p_\varphi}}{B_0v_{\mathrm{th}i}^2}F_{\mathrm{M},i}\right].$$

Writing out Eqs.(2.3.27) and (2.3.28) in full,

$$\begin{aligned}
&m\left[-\frac{q_s'}{q_s}p_\varphi\Theta_y-\frac{q_s'}{q_s}\sigma v\frac{IB_0}{\omega_{ci0}}\left\langle\frac{\sqrt{1-\lambda B}}{B}\right\rangle_\theta^{\psi}+\left\langle\frac{R}{v_\parallel}\frac{\partial\Phi}{\partial\psi}\right\rangle_\theta^{p_\varphi}\right.\\
&\quad\left.-I\frac{\sigma vB_0}{\omega_c}\left(\frac{1}{2}\left\langle\frac{B'}{B^2}\frac{\lambda B}{\sqrt{1-\lambda B}}\right\rangle_\theta^{\psi}+\left\langle\frac{B'}{B}\sqrt{1-\lambda B}\right\rangle_\theta^{\psi}\right)\right]\frac{\partial\bar{g}}{\partial\xi}\\
&+\left[m\tilde{\psi}\sin\xi\,\Theta_y-m\left\langle\frac{R}{v_\parallel}\frac{\partial\Phi}{\partial\xi}\right\rangle_\theta^{p_\varphi}-R_0q_0\nu_{ii}\frac{I}{\omega_{ci0}}\Theta_y\right]\left(\frac{\partial\bar{g}}{\partial p_\varphi}+F_{\mathrm{M}is}'\right)\\
&-\frac{\sigma v}{2}\nu_{ii}R_0q_0\lambda B_0\left(\frac{I}{\omega_{ci0}}\right)^2\left\langle\frac{1}{\sqrt{1-\lambda B}}\right\rangle_\theta^{\psi}\frac{\partial^2\bar{g}}{\partial p_\varphi^2}-2\nu_{ii}R_0q_0\frac{I}{\omega_{ci0}}\lambda\Theta_y\frac{\partial^2\bar{g}}{\partial\lambda\partial p_\varphi}\\
&-\frac{\nu_{ii}}{\sigma v}\frac{R_0q_0}{B_0}\left\langle\frac{2-3\lambda B}{\sqrt{1-\lambda B}}\right\rangle_\theta^{\psi}\frac{\partial\bar{g}}{\partial\lambda}\bigg|_{p_\varphi}-\frac{2\nu_{ii}}{\sigma v}\frac{R_0q_0}{B_0}\lambda\left\langle\sqrt{1-\lambda B}\right\rangle_\theta^{\psi}\frac{\partial^2\bar{g}}{\partial\lambda^2}\bigg|_{p_\varphi}\\
&\quad=2\nu_{ii}R_0q_0\frac{\left\langle B\bar{u}_{\parallel,i}(g_1)\right\rangle_\theta^{p_\varphi}}{B_0v_{\mathrm{th},i}^2}F_{\mathrm{M}is}
\end{aligned}\tag{2.3.38}$$

where we introduce the left-handed Heaviside step function Θ_y to eliminate passing-only (σ-even) terms in the trapped region ($\lambda \geq \lambda_c$), where:

$$\Theta_y = \Theta(\lambda_c - \lambda) \begin{cases} 1 & \lambda < \lambda_c \\ 0 & otherwise \end{cases} . \tag{2.3.39}$$

2.3.5 Normalised NTM equation

Many of the terms in Eq.(2.3.38) contain common factors including the major radius R, rational surface minor radius r_s (length), ion thermal velocity $v_{\mathrm{th},i}$, gyrofrequency $\omega_{c,j}$ (specifically ω_{cj0} at the rational surface), and the maximum equilibrium field strength magnitude $B_{0,\max}$. To simplify the equation, many of the terms are normalised to these units; the normalised terms are denoted by a hat, e.g. $\hat{w}$. Also, in the remainder of this subsection, the subscript i for ion quantities is omitted but implied.

The following normalisations are introduced to the coordinate system and field geometry:

$$\begin{aligned} &\psi_s = RB_\theta r_s; \qquad x = \frac{r - r_s}{r_s} \quad \Rightarrow \quad \frac{\partial}{\partial \psi} = \frac{1}{RB_\theta r_s}\frac{\partial}{\partial x} \\ &u = \frac{v}{v_{\mathrm{th},i}}; \qquad y = \lambda B_{0,\max} \quad \Rightarrow \quad \frac{\partial}{\partial \lambda} = B_{0,\max}\frac{\partial}{\partial y} \\ &b = \frac{B_0}{B_{0,\max}} = \frac{1 - \epsilon\cos\theta}{1+\epsilon} \quad \Rightarrow \quad \lambda B = yb \\ &\hat{\nu}_{jj} = \overbrace{\nu^C_{jj}\tilde{\nu}_{jj}(u)}^{\nu_{jj}(v)} \frac{Rq}{v_{\mathrm{th}}} = \epsilon^{3/2}\nu_\star \tilde{\nu}_{jj}(u), \end{aligned} \tag{2.3.40}$$

Here, $y = 1$ corresponds with the trapped passing boundary at $\lambda = \lambda_c$. The ξ and θ angle coordinates remain in units of radians. $\tilde{\nu}_{jj}(u)$ is the velocity-dependent part of the collision frequency (see Eq.(2.2.17)). Then, Length scales including the magnetic island width w, the ion poloidal gyroradius $\rho_{\theta,i}$, are normalised to r_s, and Ω is also rewritten:

$$\hat{w} = \frac{w}{r_s}, \qquad \hat{\rho}_{\theta,i} = \frac{\rho_{\theta,i}}{r_s} = \frac{1}{r_s}\frac{v_{\mathrm{th},i}}{\omega_{cj0}} ; \qquad \Omega(x,\xi) = \frac{2x^2}{\hat{w}} - \cos\xi, \tag{2.3.41}$$

likewise the gradient length scales for density L_n, temperature L_T, magnetic field strength L_B,

magnetic shear L_q have also been normalised to r_s:

$$\begin{aligned}\hat{L}_n^{-1} &= \frac{r_s}{n_s}\frac{dn_s}{dr}; \qquad \hat{L}_T^{-1} = \frac{r_s}{T}\frac{dT}{dr}; \qquad \hat{L}_B^{-1} = \frac{r_s}{B}\frac{\partial B}{\partial r} = \frac{-\epsilon(r)\cos\theta}{r_s} \\ \hat{L}_q^{-1} &= \frac{r_s}{q_s}\left.\frac{dq}{dr}\right|_s \equiv \frac{\psi_s}{q_s}q_s'; \qquad \eta = \frac{\hat{L}_n}{\hat{L}_T}\end{aligned} \tag{2.3.42}$$

Then, normalising the perturbation amplitude from Eq.(2.1.4),

$$\tilde{\psi} = \frac{w_\psi^2}{4}\frac{q_s'}{q_s} = \frac{R^2B_\theta^2 w^2}{4}\frac{1}{RB_\theta}\left.\frac{dq}{dr}\right|_s\frac{1}{q_s}\frac{r_s^2}{r_s^2} = \frac{1}{4}\frac{\hat{w}^2}{\hat{L}_q}RB_\theta r_s. \tag{2.3.43}$$

The coordinate p is the canonical toroidal angular momentum p_φ normalised to $RB_\theta r_s$:

$$p = x - \hat{\rho}_{\theta,i}u_\parallel, \tag{2.3.44}$$

$$\begin{aligned}\Rightarrow\ p_\varphi &\equiv \psi - \psi_s - \frac{Iv_\parallel}{\omega_{c,i}} = RB_\theta x - \frac{RB_\phi m_i v_{\mathrm{th},i}u_\parallel}{eZ_iB} = RB_\theta r_s(x - \hat{\rho}_{\theta,i}u_\parallel) \\ \therefore\ p_\varphi &= RB_\theta r_s p. \\ \Rightarrow\ \frac{\partial}{\partial p_\varphi} &= \frac{1}{RB_\theta r_s}\frac{\partial}{\partial p}.\end{aligned} \tag{2.3.45}$$

The ion distribution function is normalised to $\frac{\pi^{3/2}v_{th,i}^3}{n_s}$, where $n_s = n_0(\psi_s)$:

$$\begin{aligned}\hat{\Phi} &= \frac{e\Phi}{T(\psi_s)}; \qquad \hat{F}_\mathrm{M} = e^{-u^2}\ , \qquad \frac{\partial\hat{F}_\mathrm{M}}{\partial x} = \frac{\omega_{\star,i}^T}{\omega_{\star,i}}\frac{n_s'}{n_s}\hat{F}_\mathrm{M}\ , \\ \hat{g} &= \frac{\pi^{3/2}v_{th,i}^3}{n_s}\bar{g}\ , \qquad \hat{g}_1 = \hat{g} + p\hat{F}_\mathrm{M}'\end{aligned} \tag{2.3.46}$$

After extensive derivation of the normalised coefficients, given in full in the Appendix Sec.8.3.2, the final normalised drift-kinetic NTM equation for $\hat{g}$ (2.3.38) is:

$$\begin{aligned}&-m\left[\frac{p}{\hat{L}_q}\Theta_y + \frac{\hat{\rho}_{\theta,i}}{\hat{L}_q}\hat{\omega}_D - \frac{\hat{\rho}_{\theta,i}}{2}\left\langle\frac{1}{u_\parallel}\frac{\partial\hat{\Phi}}{\partial x}\right\rangle_\theta^p\right]\frac{\partial\hat{g}}{\partial\xi} \\ &+\left[\frac{m}{4}\frac{\hat{w}^2}{\hat{L}_q}\sin\xi\,\Theta_y - m\frac{\hat{\rho}_{\theta,i}}{2}\left\langle\frac{1}{u_\parallel}\frac{\partial\hat{\Phi}}{\partial\xi}\right\rangle_\theta^p - \hat{\nu}_{ii}\hat{\rho}_{\theta,i}\Theta_y\right]\left(\frac{\partial\hat{g}}{\partial p} + \hat{F}_{\mathrm{M}s}'\right) \\ &-\frac{\hat{\nu}_{ii}}{2}\frac{\sigma u}{(1+\epsilon)}\hat{\rho}_{\theta,i}^2 y\left\langle\frac{1}{\sqrt{1-yb}}\right\rangle_\theta^x\frac{\partial^2\hat{g}}{\partial p^2} - 2\hat{\nu}_{ii}\hat{\rho}_{\theta,i}y\Theta_y\frac{\partial^2\hat{g}}{\partial y\partial p} - \frac{\hat{\nu}_{ii}}{\sigma u}(1+\epsilon)\left\langle\frac{(2-3yb)}{\sqrt{1-yb}}\right\rangle_\theta^x\left.\frac{\partial\hat{g}}{\partial y}\right|_p \\ &\qquad -\frac{2\hat{\nu}_{ii}}{\sigma u}(1+\epsilon)y\left\langle\sqrt{1-yb}\right\rangle_\theta^x\left.\frac{\partial^2\hat{g}}{\partial y^2}\right|_p = 2\hat{\nu}_{ii}(1+\epsilon)\hat{\bar{U}}_{\parallel i}(\hat{g} + p\hat{F}_{\mathrm{M}s}')\hat{F}_{\mathrm{M}s}\end{aligned} \tag{2.3.47}$$

Here, the Heaviside step function $\Theta_y = 1$ for passing particles, and $\Theta_y = 0$ for trapped particles. Eq.(2.3.47) is analogous to Eq.(A.1) of Ref. [70], but with some amendments (see Sec.2.6). Where we have defined the normalised ion drift frequency $\hat{\omega}_D$ (a length-less drift velocity), to be the combination of the terms in $\dfrac{\partial \hat{g}}{\partial \xi}$:

$$\hat{\omega}_D = \frac{\sigma u}{(1+\epsilon)} \left[\left\langle \frac{\sqrt{1-yb}}{b} \right\rangle_\theta^x - \frac{\hat{L}_q}{2} \left\langle \frac{1}{b} \frac{1}{\hat{L}_B} \frac{(2-yb)}{\sqrt{1-yb}} \right\rangle_\theta^x \right]. \tag{2.3.48}$$

and the ion flow-like collision operator term $\bar{u}_{\|i}$ Eq.(2.2.14) in normalised form is given by:

$$\hat{\bar{U}}_{\|i}(\hat{f}) = \frac{1}{\sqrt{\pi}\,\langle \hat{\nu}_{ii} \rangle_v} \left\langle \sum_\sigma \sigma \int_0^\infty du\, u^3 \hat{\nu}_{ii} \int_0^{b^{-1}} dy\, \hat{f} \right\rangle_\theta^p. \tag{2.3.49}$$

where $\hat{f} = \frac{\pi^{3/2} v_{\mathrm{th},i}^3}{n} f$ is the normalised ion distribution.

2.3.6 Boundary conditions

In solving Eq.(2.3.47) for $\hat{g}$, boundary conditions are applied in ξ-, p- and y-space. In ξ, $\hat{g}$ and its derivatives must be periodic as we concern a single-helicity island:

$$\hat{g}(\xi = -\pi) = \hat{g}(\xi = +\pi) \ , \qquad \left.\frac{\partial \hat{g}}{\partial \xi}\right|_{\xi=-\pi} = \left.\frac{\partial \hat{g}}{\partial \xi}\right|_{\xi=+\pi} . \tag{2.3.50}$$

For p, we assume that the island perturbation's effect on the ion distribution must be localised to its vicinity. This requires that $\hat{g}$ must tend to a constant far from the island ($p \to \pm\infty$), so that $\dfrac{\partial \hat{f}_i}{\partial p} \to \hat{F}'_{\mathrm{M},i}$. This results in the following Dirichlet boundary condition:

$$\lim_{p\to\pm\infty} \frac{\partial \hat{g}}{\partial p} = 0, \tag{2.3.51}$$

which will give a special form for the calculation of the second derivative, $\dfrac{\partial^2 \hat{g}}{\partial p^2}$.

For y, we note that Eq.(2.3.47) has different forms for passing and trapped particles, and also that certain equation terms have divergent behaviour as $y \to y_c \equiv 1$, specifically those with factor $v_\parallel^{-1}$ or $(1 - yb(\theta))^{-1/2}$, as $b(\theta \to \pi) \to 1$. Therefore, $\hat{g}$ cannot be solved explicitly at the trapped-passing boundary and must be approximated using a set of matching conditions [50] that enforce continuity between passing ($\sigma = +1$), anti-passing ($\sigma = -1$) and trapped ions across it:

$$\sum_\sigma \sigma \hat{g}_p^\sigma = 0 \tag{2.3.52}$$

$$\sum_\sigma \hat{g}_p^\sigma = 2\hat{g}_t \tag{2.3.53}$$

$$\sum_\sigma \frac{\partial \hat{g}_p^\sigma}{\partial y} = 2\frac{\partial \hat{g}_t}{\partial y}. \tag{2.3.54}$$

Here, subscripts p and t denote the solutions in passing and trapped regions, respectively. Eq.(2.3.52) and Eq.(2.3.53) result from matching $\hat{g}$ across the trapped-passing boundary, as $\hat{g}$ must be independent of σ there. Eq.(2.3.54) originates from continuity as, in steady state, the rate at which trapped particles are scattered into the passing region must equal the passing particles scattered into the trapped region. These matching conditions are necessary as Eq.(2.3.47) has fundamentally different forms for the passing and trapped particles, and different definitions of the orbit-averaging operator(2.3.26). Separately in y, while there is not a strict external boundary condition, we note that the $\left\langle \sqrt{1 - yb} \right\rangle_\theta$ term of $\dfrac{\partial^2 \hat{g}}{\partial y^2}$ in Eq.(2.3.47) vanishes at both $y = 0$

and $y = \max(y) = 1/b$, effectively resulting in a Neumann boundary condition. This will give a special form for the first derivative, $\dfrac{\partial \hat{g}}{\partial y}$, that ensures it remains finite.

2.4 Electron response and quasineutrality

We now have an equation for the drift-kinetic ion response and have defined its boundary conditions. As discussed in Sec.1.2.3 with relation to other NTM literature, the plasma response must be self-consistent with terms dependent on the distribution function, including the normalised electrostatic potential $\hat{\Phi}$ satisfying quasineutrality, and the ion flow-like momentum-conserving collision operator term $\hat{\bar{U}}_{\|i}(\hat{g} + p\hat{F}'_{\mathrm{M}s})$, neither of which should be neglected. The ion response Eq.(2.3.47) must therefore be solved iteratively with $\hat{\Phi}$ and $\hat{\bar{U}}_{\|i}(\hat{g} + p\hat{F}'_{\mathrm{M}s})$. However, $\hat{\Phi}$ also requires the electron response to account for plasma quasineutrality.

Assuming the collision frequency and poloidal gyroradius of electrons are negligibly small, i.e., $\rho_{\theta,e} \ll \rho_{\theta,i} \sim w$, then the analytic description of the electron response in [50] can be used. Starting with a similar Maxwellian-based distribution function for the electrons as with the ions:

$$f_e = \left(1 + \frac{eZ_e\Phi}{T_e}\right) F_{M,e} + (\psi - \psi_s)F'_{M,e} + g_e \ , \qquad F_{M,e}(\psi) = \frac{n_0(\psi)}{\pi^{3/2}v_{\mathrm{th},e}^3} e^{-v^2/v_{\mathrm{th},e}^2}, \tag{2.4.1}$$

we expand in the perturbed electron distribution g_e in the limit of small $\delta_e = \rho_{\theta,e}/w$ and $\Delta = w/r$:

$$g_e = \sum_{l,k} = \delta_e^l \Delta^k g_e^{(l,k)} \tag{2.4.2}$$

and assuming the following orderings:

$$\frac{eZ_e\Phi}{T} \sim \Delta \ , \qquad k_\theta w \sim \Delta \ , \qquad \frac{k_\| v_\|}{\omega_{\star,e}} \gg 1 \ , \qquad \frac{g_e}{F_{M,e}} \sim \Delta \ , \qquad \nu_{ee} + \nu_{ei} \leq k_\| v_{\mathrm{th},e} \tag{2.4.3}$$

then, considering the relevant terms of the $O(\delta_e\Delta)$ drift-kinetic equation (2.2.1), the electron distribution takes the form of Ref. [70] Eq.(17):

$$f_e = \left(1 + \frac{e\Phi}{T}\right) F_{M,e}(\psi) - F_{M,e}\frac{n'_0}{n_0}\frac{\omega^T_{\star,e}}{\omega_{\star,e}}\frac{[\psi - h(\Omega)]}{\psi_s}, \tag{2.4.4}$$

$$\simeq \left(1 + \frac{e\Phi}{T}\right) F_{\mathrm{M,s}} + \cancel{F'_{\mathrm{M,s}}\psi} - F_{\mathrm{M,s}}\frac{n'_0}{n_0}\frac{\omega^T_{\star,e}}{\omega_{\star,e}}[\cancel{\psi} - h(\Omega)] \tag{2.4.5}$$

$$= \left(1 + \frac{e\Phi}{T}\right) F_{\mathrm{M,s}} + F_{\mathrm{M,s}}\frac{n'_0}{n_0}\frac{\omega^T_{\star,e}}{\omega_{\star,e}}h(\Omega), \tag{2.4.6}$$

where:

$$\frac{\omega^T_{*,e}}{\omega_{*,e}} = 1 + \left(\frac{v^2}{v_{\mathrm{th},e}} - \frac{3}{2}\right)\eta. \tag{2.4.7}$$

Here, $h(\Omega)$ is the constraint equation Eq.(55) from Ref. [50], representing the density gradient of the electron response near the island, determined using a model form of radial transport. $h(\Omega)$ is defined to be zero both at and inside the island separatrix ($\Omega \leq 1$):

$$h(\Omega) = \Theta(\Omega - 1)\frac{w}{2\sqrt{2}}\int_1^\Omega \frac{d\Omega'}{Q(\Omega)}\ , \qquad h(\Omega) = \begin{cases} 1 & \Omega > 1 \\ 0 & \Omega \leq 1 \end{cases} \tag{2.4.8}$$

where Θ is the left-handed Heaviside step function, w is the island half-width, and:

$$Q(\Omega) = \frac{1}{2\pi}\int_{-\xi_b}^{+\xi_b} d\xi\ \sqrt{\Omega(\xi) + \cos(\xi)}\ , \qquad \xi_b = \begin{cases} \pi & \Omega \geq 1 \\ \arccos(-\Omega) & \Omega < 1 \end{cases} \tag{2.4.9}$$

where ξ_b is the helical angle bounce point on a given flux surface. The electron density is obtained by integrating Eq.(2.4.4) across velocity-space, using Eq.(2.2.16):

$$n_e = \int d^3\boldsymbol{v}\ f_e, \qquad \int d^3\boldsymbol{v} = \pi B \sum_\sigma \int_0^\infty dv\ v^2 \int_0^{B^{-1}} \frac{d\lambda}{\sqrt{1-\lambda B}}.$$

Using the following identities (see Appendix Sec.8.1):

$$B\int_0^{B^{-1}} \frac{d\lambda}{\sqrt{1-\lambda B}} = 2, \qquad \int_0^\infty dv\ v^2 e^{-v^2} = \frac{\sqrt{\pi}}{4}, \qquad \int_0^\infty dv\ v^4 e^{-v^2} = \frac{3\sqrt{\pi}}{8}, \tag{2.4.10}$$

the normalised electron density ($\hat{n}_e = n_e/n_s$) is calculated to be:

$$\begin{aligned}
n_e &= \pi B \sum_\sigma \int_0^\infty dv\ v^2 \int_0^{B^{-1}} \frac{d\lambda}{\sqrt{1-\lambda B}} \left[\left(1 + \frac{e\Phi}{T}\right) F_{\mathrm{M,s}} + F_{\mathrm{M,s}} \frac{\omega^T_{\star,e}}{\omega_{*e}} \frac{n_0'}{n_0} h(\Omega)\right] \\
&= 2\pi \sum_\sigma \int_0^\infty dv\ \left(1 + \frac{e\Phi}{T} + \left[1 - \frac{3}{2}\eta_e\right]\frac{n_0'}{n_0}h(\Omega)\right) v^2 F_{\mathrm{M,s}} + \left(\frac{n_0'}{n_0}h(\Omega)\eta_e\right) v^4 F_{\mathrm{M,s}} \\
&= 2n_0 \frac{\cancel{\pi^{3/2}}}{\cancel{\pi^{3/2}}}(2)\left[\left(1 + \frac{e\Phi}{T} + \left[1 - \frac{3}{\cancel{2}}\cancel{\eta_e}\right]\frac{n_0'}{n_0}h(\Omega)\right)\frac{1}{4} + \cancel{\frac{n_0'}{n_0}h(\Omega)\eta_e}\frac{3}{8}\right] \\
&= n_0\left[1 + \frac{e\Phi}{T} + \frac{n_0'}{n_0}h(\Omega)\right]\ .
\end{aligned}$$

Introducing unit normalisations: $\hat{\Phi} = \frac{e\Phi}{T}$, $\hat{L}_n^{-1} = \frac{n_0'}{n_0}$, then the electron density normalised to n_s is:

$$\hat{n}_e = 1 + \hat{\Phi} + \frac{h(\Omega)}{\hat{L}_{n,0}^{-1}}, \tag{2.4.11}$$

By balancing the ion and electron densities, the normalised electrostatic potential perturbation $\hat{\Phi}$ can be determined. However, noting that a similar form of the total ion density can be obtained:

$$f_i = \left(1 - \frac{e\Phi}{T}\right) F_{\mathrm{M,s}} + \frac{\omega_*^T}{\omega_{*i}} \frac{F_{\mathrm{M,s}}}{\hat{L}_n} p_\varphi + g, \tag{2.4.12}$$

$$\hat{n}_i = 1 - \hat{\Phi} + \frac{x}{\hat{L}_n} + \delta n_i, \tag{2.4.13}$$

by equating with Eq.(2.4.11), the perturbed electrostatic potential $\hat{\Phi}$ is given by:

$$\hat{n}_i = \hat{n}_e \quad \Rightarrow \quad \hat{\Phi} = \frac{\delta n_i}{2} + \frac{x - h(\Omega)}{2\hat{L}_n}, \tag{2.4.14}$$

where $L_{n,0}$ is the density gradient length scale in the limit of zero equilibrium radial electric field ($\hat{\omega}_E = 0$). The normalised perturbed ion density δn_i is obtained from the $O(\Delta^1)$ perturbed ion distribution function $\hat{g}$, the solution of Eq.(2.3.47):

$$\delta n_i(\theta, x, \xi) = \{\hat{g}\}_v = \frac{b}{\sqrt{\pi}} \sum_\sigma \int_0^\infty u^2 du \int_0^{b^{-1}} dy \frac{\hat{g}}{\sqrt{1 - yb}} \ . \tag{2.4.15}$$

Within Eq.(2.4.14), note that the contribution to $\hat{\Phi}$ from pF_M' for ions is accounted for ($\{pF_M'\}_v = x/L_{n,i}$, see 4.1.8), and that the respective contributions from the equilibrium ions and electrons will cancel under quasineutrality. Far from the magnetic island, $h(\Omega) \to x$ and δn_i should tend toward a constant (under the boundary condition $\dfrac{\partial g}{\partial p} = 0$), and hence $\hat{\Phi}$ should also tend to a constant. This would lead to $\dfrac{\partial \hat{\Phi}}{\partial x} \to 0$ far from the island, i.e., the perturbed electric field is localised to the vicinity of the magnetic island.

2.5 Current density and island growth

Once a self-consistent ion response to the drift-kinetic equation is obtained, the field-parallel layer currents and their contributions to the modified Rutherford equation can be calculated.

Parallel currents

The total field-parallel current density of species j is simply provided by its parallel flow:

$$J_{\parallel,j} = eZ_j u_{\parallel,j} \tag{2.5.1}$$

where $Z_j = +1$ for ions, and -1 for electrons, and e is the elementary charge. In [70, 41] and subsequent works, the "bootstrap current density" J_{bs} is the part of $J_{\parallel,j}$ that is projected out after flux surface-averaging at fixed Ω:

$$J_{bs,j} = \langle J_{\parallel,j} \rangle_\Omega \tag{2.5.2}$$

Likewise, the "polarisation current density" is considered to be the part that disappears after flux-surface averaging, though technically this could comprise similar contributions from other sources:

$$J_{pol,j} \approx J_{\parallel,j} - \langle J_{\parallel,j} \rangle_\Omega \tag{2.5.3}$$

where $\langle ... \rangle_\Omega$ the flux surface average operator. Here, the flux surface average of a quantity is a volume average between two closely-neighbouring flux surfaces ψ and $\psi + \delta\psi$. Based on [17] Eq. (7.5), it is given by:

$$\begin{aligned} \langle ... \rangle_\Omega &= \frac{S(...)}{S(1)} = \frac{\oint d\xi \ ... \left(\Omega + \cos\xi\right)^{-1/2}}{\oint d\xi \ \left(\Omega + \cos\xi\right)^{-1/2}} \\ S(...) &= \frac{1}{2\pi} \int_{-\xi_b}^{+\xi_b} \frac{d\xi}{\sqrt{\Omega + \cos\xi}} \ , \qquad \xi_b = \begin{cases} \pi & \Omega \geq 1 \\ \arccos(-\Omega) & \Omega < 1 \end{cases} \end{aligned} \tag{2.5.4}$$

and $\xi_b(\Omega)$ is the extent of the helical angle on a given $n = 1$ flux surface. When computing the flux surface average, because Ω is symmetric in ψ, $S(...)$ must be computed for both sides in ψ, then the average of the two sides is taken.

Analytic electron flow

The analytic result for the parallel electron flow $u_{\parallel,e}$ in Ref.[70] Eq.(22) is used to determine the electron current[6]. Notably, it depends on the ion flow $u_{\parallel,i}$, calculated numerically from Eq.(2.2.15)

[6] This corresponds with [50] Eq.(74) converted from the lab frame to the island rest frame by setting $\omega = -\omega_E$.

from the self-consistent ion response:

$$\frac{u_{\parallel,e}}{v_{th,e}} = \frac{-f_t}{1+f_t}\frac{\hat{\rho}_{\theta,e}}{L_n}\left(\frac{1+\eta(1+\frac{1}{2}k_{neo}f_p)}{\omega_{\star,e}}\frac{\partial h}{\partial x} - \frac{\omega_E}{\omega_{\star,e}}\right) + \frac{f_p}{1+f_t}\frac{u_{\parallel,i}}{v_{th,i}}, \tag{2.5.5}$$

where $v_{th,e} = \sqrt{\frac{m_i}{m_e}}v_{th,i}$ is the electron thermal speed and $\hat{\rho}_{\theta,e} = -\sqrt{\frac{m_e}{m_i}}\hat{\rho}_{\theta,i}$ is the electron poloidal gyroradius, both using the same normalisations as ions. k_{neo} is the coefficient of the neoclassical poloidal flow from Helander and Sigmar's derivation of the drift-kinetic equation for a quasineutral ion-electron plasma in the high aspect ratio banana regime (Ref.[17], Eq.(11.26)), acting as a constant of proportionality between the poloidal ion flow and poloidal magnetic field B_θ:

$$k_{neo} = \frac{\left\langle (v^2 - \frac{5}{2})\tilde{\nu}_{jj}\right\rangle_v}{\langle \tilde{\nu}_{jj}\rangle_v} \simeq -1.173... \ , \tag{2.5.6}$$

where $\langle ... \rangle_v$ is the velocity volume integral given by Eq.(2.2.20). f_p is the fraction of passing particles in the population, approximated in a high aspect ratio, given by [17] Sec.(11) Eq.(11.24):

$$f_p = \frac{3B_0^2}{4}\int_0^{\lambda_c}\frac{\lambda\ d\lambda}{\langle 1-\lambda B\rangle_\theta^\psi} \simeq 1 - 1.46\sqrt{\epsilon}\ , \tag{2.5.7}$$

likewise $f_t = 1 - f_p$ is the trapped particle fraction. Normalised and converted to ion units, the analytic electron flow expression Eq.(2.5.5) becomes:

$$\frac{u_{\parallel,e}}{v_{th,i}} = \frac{-f_t}{1+f_t}\frac{\hat{\rho}_{\theta,i}}{L_n}\left(\frac{1+\eta(1+\frac{1}{2}k_{neo}f_p)}{\omega_{\star,e}}\frac{\partial h}{\partial x} - \frac{\omega_E}{\omega_{\star,e}}\right) + \frac{f_p}{1+f_t}\frac{u_{\parallel,i}}{v_{th,i}}\ . \tag{2.5.8}$$

Note that the parallel current $J_\parallel \propto u_{\parallel,e} - u_{\parallel,i} \propto f_t$, as expected for the bootstrap current density, and the factor $\sqrt{\frac{m_i}{m_e}}$ introduced by the LHS $v_{th,e}$ term is cancelled out by its inverse in $\hat{\rho}_{\theta,e}$. Therefore, the choice of isotope for the ion species (whether deuterium or protons) will not significantly affect the final result, given that the ion mass-dependent $\hat{\rho}_{\theta,i}$ and $v_{th,i}$ are parameters.

Dispersion relation

The dispersion relation that relates magnetic field with field-parallel current density $J_\parallel$ is derived from Ampère's law. For long thin islands whose width w is much smaller than their length, as is the case in a high aspect ratio tokamak, Ampère's law relates ψ to $J_\parallel$:

$$\frac{1}{R}\frac{d^2\psi}{dr^2} = \mu_0 J_\parallel \tag{2.5.9}$$

Integrating Ampère's law across real-space (while performing θ-averaging), and projecting out the $\cos\xi$ component gives the nonlinear dispersion relation relating the current density J with the island perturbation[7]. Integrating the discontinuity in $\psi(r)$ across the island gives the parameter Δ_{loc}, the island growth parameter due to perturbed local neoclassical layer currents in the vicinity of the island:

$$\Delta_{loc} = -\mu_0 R \int_{-1}^{\infty} d\Omega \oint d\xi \left\langle J_\parallel \right\rangle_\theta \cos n\xi \tag{2.5.10}$$

$$= -\frac{\mu_0 R}{2\tilde{\psi}} \int_{-\infty}^{+\infty} d\psi \oint d\xi \ \left\langle J_\parallel \right\rangle_\theta^\psi \cos\xi \tag{2.5.11}$$

$$= -\frac{1}{2}\left(\frac{w^2}{4}\frac{q_s'}{q_s}\right)^{-1} \int_{-\infty}^{+\infty} d\psi \ \oint d\xi \ \left\langle J_\parallel \right\rangle_\theta^\psi \cos\xi \tag{2.5.12}$$

Here, $J_\parallel$ may be substituted for J_{bs} or J_{pol} for either species to identify that corresponding contribution to the total Δ_{loc}. The $\cos\xi$ component[8] of $J_\parallel$ is resonant with the island perturbation and contributes to the island growth rate via the modified Rutherford equation Eq.(1.4.7), which we rewrite as:

$$\frac{1}{r_s^2}\frac{dw}{dt} = -\frac{1}{\tau_R}\frac{1}{2}\left(\frac{w^2}{4\hat{L}_q}\right) \int_{-\infty}^{+\infty} dx \oint d\xi \ \left\langle J_\parallel \right\rangle_\theta^\psi \cos\xi \tag{2.5.13}$$

As discussed in Sec.1.4, in our working parameters, we are interested only in the bootstrap and polarisation currents, and have neglected the small contributions from curvature effects ($\propto \epsilon^2$) and the classical tearing parameter ($\Delta'(w \to 0) \to 0$).

2.6 Amendments

This work makes the following corrections to the derivation last published in Ref. [70]:
Eq.(A.1) - Eq.(2.3.47):

- Added missing factor $\hat{\rho}_{\theta,i}$ to $\dfrac{\partial^2 \hat{g}}{\partial p^2}$, thereby making the term $\propto \hat{\rho}_{\theta,i}^2$. This derivative controls diffusion across particle orbits and this change consequently affects the physics of the separatrix boundary layer surrounding the island.
- Added missing coefficient $\hat{\nu}_{ii}\hat{\rho}_{\theta,i}$ to $\dfrac{\partial \hat{g}}{\partial p}$. This affects the behaviour of the solution near the magnetic island.

[7] This corresponds with Eq.(17) in [50] (noting that $L_q = q_s/q_s'$ is in the reverse direction in this work, hence the inclusion of a minus sign in this work)

[8] The inclusion of $\cos\xi$ will also eliminate the ξ-independent component of the current far from the island in ψ, so only the ξ-dependent perturbation contributes.

- Added missing factor m to existing coefficients of $\hat{F}'_{\mathrm{M}is}$, and missing $\hat{\nu}_{ii}\hat{\rho}_{\theta,i}\Theta_y$ term.
- Collision operator term $\hat{\bar{U}}_{\|i}(\hat{g})$ changed to $\hat{\bar{U}}_{\|i}(\hat{g} + p\hat{F}'_{\mathrm{M}s})$, thereby reflecting the full form of g_1. Note that the $p\hat{F}'_{\mathrm{M}}$ term is eliminated in the trapped region by averaging over σ, but the region will be affected by this change to the passing solution through the matching condition.
- Introduced minus sign to Δ_{loc} dispersion relation Eq.(2.5.10).

Eq.(A.11) - Eq.(2.4.14): $\hat{\Phi}$ has been modified to remove L_n^{-1} from δn_i.

Summary

This chapter presented a derivation for the steady state drift-kinetic plasma response to a small magnetic island ($w \sim \rho_{b,i} \ll r_s$) in a high aspect ratio ($\epsilon \ll 1$), circular cross section tokamak in the island rest frame. Here, a numerical approach is required for ions to account for kinetic effects at the relevant length scale, while analytic results for electrons from Ref. [50] will be used to ensure quasineutrality is maintained in the electrostatic potential Φ. The extended derivation included in this section is given in the Appendix 8.3. The next chapter introduces a new numerical code, `kokuchou` [77], to implement this derivation. Recalling the project aims, Objective (1) the code is designed after the `DK-NTM` algorithm within Refs. [69, 70, 41]. Amendments and corrections to the original derivation from these works have been summarised in this section, which is expected to produce a new result that needs to be tested and verified.

Chapter 3

Methodology

In Ch.2, the drift-kinetic ion response to a near threshold-size ($w_c \sim \rho_{b,i} = \epsilon^{1/2}\rho_{\theta,i}$ [34, 66]) magnetic island and its associated quantities were derived in the island rest frame, following previous work [50, 70]. These will be used to determine the parallel currents in the vicinity of the island, to predict its growth rate and the threshold width where that rate is zero. To account for quasineutrality and momentum conservation, an iterative numerical scheme is needed for the perturbed ion distribution $\hat{g}$ to be self-consistent with the electrostatic potential $\hat{\Phi}(\hat{g})$ and the ion flow-like momentum conservation term $\hat{\hat{U}}_{\|i}(\hat{g} + p\hat{F}'_{\mathrm{M}s})$.

This chapter introduces a new numerical code, `kokuchou`[77], to perform this calculation. Sec.3.1 outlines the stages of calculation, with specific stages covered in detail in each subsection. The challenges of this computationally intensive calculation and the methods by which these were addressed are discussed in Sec.3.1.6. Finally, Sec.3.2 describes the studies carried out for this work, and the resources used.

3.1 Algorithm

`DK-NTM`, developed by Imada et al [69, 70, 41] is a Fortran-based simulation code developed to iteratively solve the drift-kinetic equation and obtain a quasineutral, momentum-conserved plasma response to a magnetic island. It has previously been used to identify the physics of "drift island" structures exhibited by the ion response, and to determine the bootstrap current drive to island growth[69, 70]. Originally, `DK-NTM` was envisaged to be used for this thesis, building on the original published results; however, computational issues were identified. After these were resolved, further issues arose that prevented a stable result from being obtained when performing the usual iterative calculation [72]. As outlined in Sec.3.1.1, the stages of calculation

are complex, with multiple operations performed in each stage. The `DK-NTM` code reflected this process in its structure, consisting of large procedures and modules. However, `DK-NTM` lacked testing capabilities, and the complexity of these procedures made it challenging to isolate regions for debugging or testing. Verifying the code through its full-size result was also not viable due to the long duration of a simulation, thus a new approach was needed. This led to the redevelopment of `DK-NTM` as a new code named "`kokuchou`" [72], restructuring the old code into smaller, reusable modules and employing a test-driven development approach to validate them. This allowed any issues that emerged during development to be resolved quickly, and to ensure the stability and correctness of existing code as new modules were added. This thesis describes the development, testing and usage of `kokuchou`, which has been my responsibility since 2020.

This section outlines the design of the code itself, including specific stages and their challenges. Throughout this section, vector quantities are denoted in bold (e.g. $\mathbf{g}, \boldsymbol{\beta}$) while square matrices are denoted in bold font with an underline (e.g. $\underline{\mathbf{M}}, \underline{\boldsymbol{\alpha}}$), and subscript i for ion quantities is omitted for simplicity.

3.1.1 Stages of calculation

The numerical scheme followed in the `kokuchou` simulation code broadly follows that of `DK-NTM`, as outlined in the appendix of Ref. [70]. A flowchart illustrating the calculation steps is shown in Fig.3.1.

Eq.(2.3.47) is the equation `kokuchou` is designed to solve. It is a 3D integro-differential equation in $\{\xi, p, y\}$ where the normalised particle speed u and magnetic field-parallel velocity sign σ are parameters. The simulation domain used for this equation consists of two spatial $\{\xi, p\}$ and two velocity $\{y, u; \sigma\}$ coordinates. The radial variable p couples space and velocity, via Eq.(2.3.44). To keep space and velocity separate, the three spatial coordinates $\{\theta, x, \xi\}$ are also required. These describe terms of the equation that vary along ion orbits, including $\hat{\Phi}$, $\hat{\bar{U}}_{\parallel,i}$ and orbit-averages in θ at fixed x. For a given speed u, the equation is solved across $\{\xi, p, y\}$ applying boundary conditions in each dimension (see Sec.2.3.6) for the three ion populations, whose ranges in y and σ differ. These are the passing ($y < 1, \sigma = +1$), anti-passing ($y < 1, \sigma = -1$), and trapped ions ($y > 1, \sigma = \pm 1$)[1]. Given that Eq.(2.3.47) has different forms for passing and trapped particles, this requires an internal boundary condition to match the solution for $\hat{g}$ in y-space at $y = y_c \equiv 1$, the trapped-passing boundary. We seek to solve close to this boundary, due to its

[1]Trapped ions alternate between field-parallel ($\sigma = +1$) and anti-parallel ($\sigma = -1$) motion in their banana orbits. When the orbit-average is taken, i.e. the θ-average at fixed p, any even-σ^n quantities will average to zero and odd-σ^n quantities average to $\sigma^2 \equiv +1$

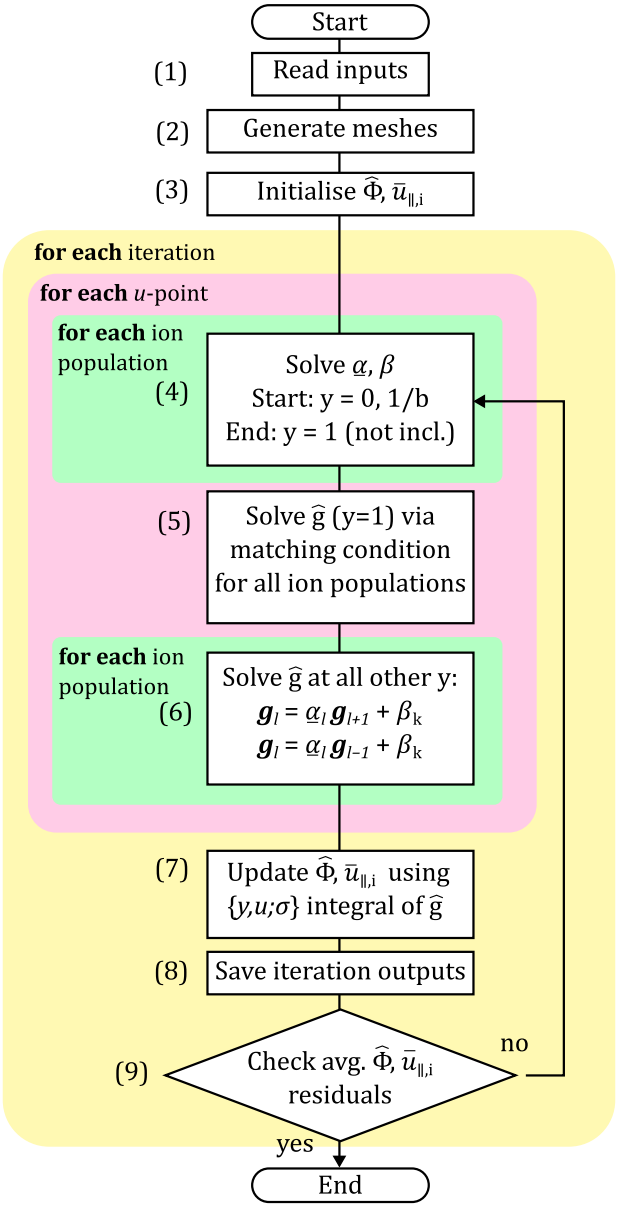

Figure 3.1: Stages of calculation of the perturbed ion distribution function $\hat{g}$ from the `kokuchou` NTM simulation code.

importance in determining the polarisation current. However, Eq.(2.3.47) cannot be explicitly evaluated there due to certain terms exhibiting divergent behaviour at $y = 1$, specifically those with factor $(1-yb(\theta))^{-1/2}$ including $1/v_{\|}$. Physically, this means that $\dfrac{\partial^2 \hat{g}}{\partial y^2}$ becomes very large and therefore collisions cannot be treated perturbatively there, as only small scatterings are needed for particles to cross the boundary. Hence, the matching conditions given in Sec.2.3.6 are used to couple the three ion populations across this discontinuity, and through fitting, approximate a value for $\hat{g}$ there that restores continuity.

To propagate the outer-y boundary conditions to the trapped-passing boundary for each population, a shooting method is used. Starting from the y-limits and discretising in $\{\xi, p, y\}$, a 2D matrix form of the drift-kinetic equation in $\{\xi, p\}$-space is constructed at each y point incrementally towards $y = y_c$, using a linear recurrence relation to couple the neighbouring y-points (see Sec.3.1.3). The result is a series of large, dense square matrices $\underline{\boldsymbol{\alpha}}_l$ and vectors $\boldsymbol{\beta}_l$, one for each point in y (index l), that are used to calculate a vector form of $\hat{g}$, denoted $\mathbf{g}_l$, at a given y-point from the neighbouring point using the aforementioned linear recurrence relation. There is a set of $\underline{\boldsymbol{\alpha}}_l$, $\boldsymbol{\beta}_l$ for the three ion populations at a given u that are obtained separately. These matrices and vectors are large, and of rank $n_\xi n_p \sim O(10^3)$, which imposes computational limitations on the implementation of the algorithm (see Sec.3.1.6). Here n_ξ and n_p are the number of the ξ- and p-mesh points in the spatial discretisation.

The first value of y where $\mathbf{g}_l$ is solved is at the trapped passing boundary $y = y_c$, using quadratic fits through three points either side of (and including) $y = y_c$ for each ion population. Applying the matching conditions, the equation for $\mathbf{g}(y = y_c)$ is introduced later in Sec.3.1.4. From the result for $\mathbf{g}(y = y_c)$, the linear recurrence relations $\mathbf{g}_l = \underline{\boldsymbol{\alpha}}_l \cdot \mathbf{g}_{l+1} + \boldsymbol{\beta}_l$ for passing ions and $\mathbf{g}_l = \underline{\boldsymbol{\alpha}}_l \cdot \mathbf{g}_{l-1} + \boldsymbol{\beta}_l$ for trapped ions are used to solve for $\mathbf{g}_l$ at each y-index l, back *towards* the y-limits - noting this is in the opposite direction in y to how $\underline{\boldsymbol{\alpha}}$ and $\boldsymbol{\beta}$ are obtained in the respective regions. The vectorised form $\mathbf{g}$ is then stored in the main array for $\hat{g}$ and the full numerical calculation is repeated for each point in speed u. Once the full range of $\hat{g}$ in u is found, $\hat{g}$ is remapped from $\{\xi, p\}$ to $\{\theta, x, \xi\}$ space, from which the electrostatic potential $\hat{\Phi}$ and $\hat{\bar{U}}_{\|,i}(\hat{g})$ are calculated from Eq.(2.4.14) and (2.3.49) respectively. For $\hat{\Phi}$, the density contribution is derived from the perturbed ion distribution $\hat{g}$ and combined with an analytically-derived electron density. The calculation of $\hat{g}(\hat{\Phi}, \hat{\bar{U}}_{\|,i})$, followed by the updating of $\hat{\Phi}$ and $\hat{\bar{U}}_{\|,i}(\hat{g})$ constitutes one *iteration* of the model, where on the I-th iteration, $\hat{g}(I)$ is calculated from $\hat{\Phi}(I-1), \hat{\bar{U}}_{\|(}I-1)$ and so on toward convergence.

At the start of the first iteration, the initial values of the electrostatic potential $\hat{\Phi}$ and

momentum-conserving ion flow term $\hat{\bar{U}}_{\parallel,i}$ are set. For $\hat{\Phi}$, an initial value of 0 is used[2], while the initial $\hat{\bar{U}}_{\parallel,i}$ is set to $\hat{\bar{U}}_{\parallel,i}(pF'_{\mathrm{M,s}})$ (derived later in Eq.(4.1.9)), both conditions representing an 'unperturbed' toroidally-symmetric Maxwellian ion distribution. Over successive iterations, these three quantities should each converge toward a state indicating self-consistency, satisfying quasineutrality and momentum conservation respectively from $\hat{\Phi}$ and $\hat{\bar{U}}_{\parallel(}\hat{g})$. The criterion for convergence and the challenges of achieving this are discussed in 3.1.5. Finally, from the converged result, the layer currents and the island growth parameters can be found using the equations described in 2.4.

The full process constitutes one *run* of the model, which gives a single value of $\Delta_{loc}(w)$ that, via the modified Rutherford equation Eq.(2.5.13), provides the contribution to the island growth rate dw/dt from the resistive layer for a given input island width w. To determine the threshold width w_c where $\Delta_{loc}(w = w_c) = 0$, runs are conducted for a range of island widths w to obtain a fit curve from which w_c is estimated. Varying a secondary parameter, such as ion poloidal gyroradius $\rho_{\theta,i}$, provides an estimate of the dependence of w_c on that parameter. This provides the basis for the threshold-width investigation that is discussed in Sec.3.2.

[2] A model form for the initial $\hat{\Phi}$ when ω_E is finite is programmed into the code, but is unused since $\omega_E = 0$ is used throughout this work.

The remainder of this section covers the specific stages of the algorithm in more detail.

3.1.2 Stage (2): Simulation domain and meshes

The spatial coordinates of the algorithm and their units (see Sec.2.3.5) include helical angle ξ $[radian]$, poloidal angle θ $[radian]$, radial coordinate x $[r_s]$ representing deviation from the island-forming rational flux surface $\psi = \psi_s$, and normalised canonical toroidal momentum p $[RB_\theta r_s]$, that is used in place of θ and x when calculating $\hat{g}$. A further dimensionless coordinate Ω (Eq.(2.1.8)) is also used when evaluating quantities that are flux surface functions. Velocity coordinates include normalised pitch angle y $[B_{0,\mathrm{max}}^{-1}]$ and velocity u $[v_{\mathrm{th},i}]$.

The angles θ and ξ are treated as uniformly-spaced meshes, as the phenomena of interest span the full range the values of these coordinates. For a single-helicity $n = 1$ island, both range from $\{-\pi, +\pi\}$ radians. The spatial meshes x and p are structured into three regions, as shown in Fig.3.2. These contain a central uniformly-spaced 'high-resolution' region containing the magnetic island, bounded either side by two nonuniformly-spaced regions where the mesh spacing increases exponentially further from the island. At the outer limits in p far from the island (generally 2-3 island widths from the inner region boundary), the $\partial\hat{g}/\partial p = 0$ boundary condition is applied. Both x and p are symmetric about 0. Recall in Sec.1.5 that within `DK-NTM` and in a separate code `RDK-NTM`, it was seen that the ion distribution follows *drift island* structures that are radially shifted from the magnetic island. The size of this radial shift is $\rho_{shift} = \hat{\rho}_{\theta,i}\hat{\omega}_D(y,u;\sigma)\hat{L}_q^{-1}\Theta(y_c - y)$, where $\hat{\omega}_D$ is the normalised drift frequency given by Eq.(2.3.48) and $\hat{L}_q^{-1}$ is the normalised inverse magnetic shear length scale, and corresponds to the $\hat{\omega}_D$ coefficient of $\dfrac{\partial\hat{g}}{\partial\xi}$ in Eq.(2.3.47). The maximum value of ρ_{shift} then determines the extent of the inner (fine mesh) regions of x and p.

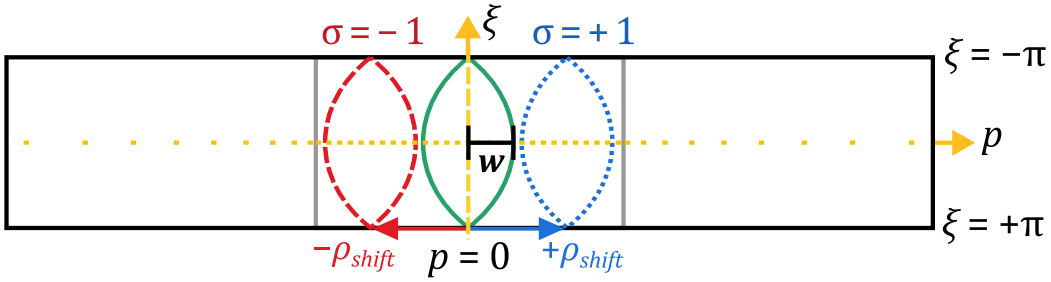

Figure 3.2: Sketch of the p-mesh, showing the magnetic island (green, solid) centred at $p = 0$ when $u = 0$, and the 'most radially-shifted' *drift islands* in $\hat{g}$ for passing (blue, dotted) and anti-passing (red, dashed) ions when $u = \max(u)$. Yellow arrows illustrate the relative spacings of mesh coordinates. The inner solid grey lines indicate the boundaries of the central uniformly-spaced region in p.

This scheme ensures the steep gradients of the drift islands in $\hat{g}$ are resolved sufficiently without over-resolving the slowly-varying region far from the island. The values of the region boundaries for x and p are designed to map onto one another through the relation: $p = x + \hat{\rho}_{\theta,i} v_{\parallel}(\max(u))\Theta_y$. This means the 'most shifted' drift island will always lie entirely within the inner regions of the x and p meshes.

The pitch-angle mesh y has a more complex structure, having a similar uniformly spaced 'high-resolution' region centred about $y = 1$ where the dissipation layer physics and trapped-passing matching need to be resolved accurately. Outside this region, non-uniform meshes with points concentrated at the mesh limits $y = 0$ and $\max(y) = 1/b$ are used, to apply the $\dfrac{\partial^2 \hat{g}}{\partial y^2}$ boundary conditions carefully.

The speed mesh u ranges from $\{0.1, 3.0\} v_{\mathrm{th},i}$. Here, we note that because ion-ion collision frequency $\hat{\nu}_{ii}(u)$ diverges at $u \to 0$, the equation cannot be evaluated accurately at very low velocities. At the same time, the maximum speed $\max(u) = 3 v_{\mathrm{th},i}$ is chosen as the dominant contribution of $\hat{g}$ to $\hat{\Phi}$ and $\hat{\bar{U}}_{\parallel,i}$ comes from within this range, due to the influence of the Maxwellian. Noting that the density and flow depend on the integrals of $u^2\hat{g}$ and $u^3\hat{g}$, the u-mesh has most of its points in the region $\{1.0, 3.0\} v_{\mathrm{th},i}$, and is uniformly spaced over this range. Between $\{0.1, 1.0\} v_{\mathrm{th},i}$, points are concentrated nearer to $u = 1 v_{\mathrm{th},i}$. Lastly, the $\Omega(x, \xi)$-mesh (Eq.(2.3.41)), which describes perturbed flux surface functions such as $h(\Omega)$ and the bootstrap current (from $\langle J_{\parallel} \rangle_{\Omega}$), contains many points concentrated near $\Omega = 1$, the magnetic island separatrix, where the fastest variations occur. It ranges from $\Omega = \{0, \Omega_{max}\}$, where 0 is the island O-point and $\Omega_{max} = 2\left(\frac{x_{max}}{\hat{w}}\right)^2 + 1$ corresponds with the furthest extent of the x-mesh at $\xi = \pm\pi$.

Integration and interpolation

For computational speed and ease of implementation, numerical integral quantities are estimated by a simple 1D composite trapezium rule for each dimension. Here, for a general mesh X, the definite integral between two points given by indices i_1 and i_2 is approximated by:

$$\int_{X_{i_1}}^{X_{i_2}} dX \; f(X) \approx \frac{1}{2}\left(\sum_{i=i_1}^{i_2-1} h(X_{i+1})\left[f(X_i) + f(X_{i+1})\right]\right), \qquad h(X_i) = X_i - X_{i-1}. \tag{3.1.1}$$

Integral quantities include the orbit-average at fixed x and p (2.3.26), the velocity average operator (2.2.20) applied to the collision frequency $\langle \hat{\nu}_{ii} \rangle_v$ in Eq.(2.3.47), and the velocity volume integral over $\{y, \sigma, v\}$ (2.2.16). Multidimensional integrals like Eq.(2.2.16) are nested trapezium rule procedures. Numerical integration was tested, and used within tests in `kokuchou`. For ex-

ample, a numerically-derived velocity average of $\langle \hat{\nu}_{ii} \rangle_v$ was tested against an analytic formula derived later in 4.1.6 using 100 u-points to within 1% relative error. The more accurate analytic form was used in `kokuchou` as the term is difficult to evaluate numerically at low u, where it is divergent.

In cases where a numerical integral cannot be evaluated in full, such as the $\theta-$average of $\left\langle \frac{1}{\sqrt{1-yb(\theta)}} \right\rangle_\theta^\psi$ which in the trapped region ($y > 1$) has a divergent integrand near $\theta \to \theta_b$, the numerical integral is calculated up to a point near the asymptote (generally one mesh spacing away), and an analytically-derived correction term is added to account for the missing part between this θ-mesh point and θ_b. Here, the correction for $\left\langle \frac{1}{\sqrt{1-yb(\theta)}} \right\rangle_\theta^\psi$ is obtained from a Taylor expansion in small y/b. Where an analytic expression cannot be derived (e.g. if the function to be evaluated is unknown), a quadratic extrapolation of the integrand is used instead. An example of this is the velocity volume integral of the ion flow $u_{\parallel,i}(\hat{g})$ that is divergent as $y \to b^{-1}$ (see Appendix Sec.8.4).

Interpolation of functions over a mesh X is performed by 1D linear interpolation using the two nearest known X-mesh points (index i) either side of a non-point X, given by X_i and X_{i+1}, and the value of $f(X)$ at those points:

$$f(X) \approx \frac{f(X_{i+1})(X - X_i) - f(X_i)(X - X_{i+1})}{X_{i+1} - X_i} , \qquad X_i < X < X_{i+1}. \tag{3.1.2}$$

Interpolation is used in various procedures, including the remapping between mesh coordinates, such as $\hat{g}(\xi, p) \to \hat{g}(x, \xi, \theta)$, and $h(\Omega) \to h(x, \xi)$.

Both integration and interpolation methods, while fast to compute, require a fine mesh resolution at areas of highly-varying, localised gradients. Another potential drawback of the linear interpolation method is that the first and second derivatives of the interpolated function are inherently discontinuous, which can generate numerical instability if the mesh resolution is insufficient at regions of rapidly-varying gradients, such as the drift island separatrix in the case of `kokuchou`. More accurate numerical methods, such as Gaussian quadrature integration and spline interpolation, have been considered as alternatives to the methods used. These would be of interest to explore in future work.

Finite difference approximation

Derivatives of a function f are approximated using the 2^{nd}-order accurate central finite difference method that couples a mesh point with its two neighbours. For a general monotonically-increasing

mesh X of size n, at an index i where the mesh spacing $h_i = X_i - X_{i-1}$, the individual terms of the m-th derivative finite difference approximation of $f(X_i)$ are represented by terms of $\Delta^{\pm}_{mx}$ (not to be confused with the expansion parameter $\Delta = w/r_s$ or island growth parameter Δ_{loc}). The 1st derivative is approximated by:

$$\frac{\partial f(X_i)}{\partial X} = \Delta^{-}_{1X(i)} f(X_{i-1}) + \Delta^{0}_{1X(i)} f(X_i) + \Delta^{+}_{1X(i)} f(X_{i+1}) \tag{3.1.3}$$

$$= \frac{-h_{i+1}}{h_i(h_{i+1}+h_i)} f(X_{i-1}) + \frac{h_{i+1}-h_i}{h_{i+1}h_i} f(X_i) + \frac{h_i}{h_{i+1}(h_{i+1}+h_i)} f(X_{i+1}) \tag{3.1.4}$$

The 2nd derivative is approximated by:

$$\frac{\partial^2 f(X_i)}{\partial X^2} = \Delta^{-}_{2X(i)} f(X_{i-1}) + \Delta^{0}_{2X(i)} f(X_i) + \Delta^{+}_{2X(i)} f(X_{i+1}) \tag{3.1.5}$$

$$= \frac{2}{h_i(h_{i+1}+h_i)} f(X_{i-1}) - \frac{2}{h_{i+1}h_i} f(X_i) + \frac{2}{h_{i+1}(h_{i+1}+h_i)} f(X_{i+1}) \tag{3.1.6}$$

This method is used to discretise the full NTM equation, Eq.(2.3.47), in the form of matrices. At the p-mesh limits ($p = p_{\min} \equiv p_{j=1}$), the Dirichlet boundary condition $\dfrac{\partial \hat{g}}{\partial p} = 0$ is applied:

$$\Delta^{+}_{1p1}\hat{g}_2 + \Delta^{0}_{1p1}\hat{g}_1 + \Delta^{-}_{1p1}\hat{g}_0 = 0,$$

where $\hat{g}_0$ corresponds to the value of the solution at a "ghost" mesh point just beyond the mesh boundary, if it were to exist. Solving for g_0:

$$\hat{g}_0 = \frac{(h_2^2 - h_1^2)}{h_2^2}\hat{g}_1 + \frac{h_1^2}{h_2^2}\hat{g}_2,$$

and substituting gives the following relation for $\hat{g}_0$ at $p_{j=1}$:

$$\boxed{\left.\frac{\partial^2 \hat{g}}{\partial p^2}\right|_{j=1} = \frac{2}{h_2^2}(\hat{g}_2 - \hat{g}_1), \qquad \Delta^{0}_{2p1} = -\frac{2}{h_2^2}, \quad \Delta^{+}_{2p1} = +\frac{2}{h_2^2}.} \tag{3.1.7}$$

Likewise, at $p = p_{\max} \equiv p_{j=n_p}$,

$$\begin{aligned} &\Delta^{+}_{1pn_p}\hat{g}_{n_p+1} + \Delta^{0}_{1pn_p}\hat{g}_{n_p} + \Delta^{-}_{1pn_p}\hat{g}_{n_p-1} = 0, \\ &\Rightarrow \quad \hat{g}_{n_p+1} = -\frac{(h_{n_p+1} - h_{n_p})}{h_{n_p}^2}\hat{g}_{n_p} + \frac{h_{n_p+1}^2}{h_{n_p}^2}\hat{g}_{n_p-1}. \end{aligned} \tag{3.1.8}$$

$$\boxed{\left.\frac{\partial^2 \hat{g}}{\partial p^2}\right|_{j=n_p} = -\frac{2}{h_{n_p}^2}(\hat{g}_{n_p} - \hat{g}_{n_p-1}), \qquad \Delta^0_{2pn_p} = -\frac{2}{h_{n_p^2}}, \quad \Delta^-_{2pn_p} = +\frac{2}{h_{n_p^2}}.} \tag{3.1.9}$$

For the ξ-mesh edges, the periodic condition (2.3.50) applies, hence $k = 1 \equiv n_\xi$:

$$\boxed{\left.\frac{\partial \hat{g}}{\partial \xi}\right|_{k=n_\xi} = \left.\frac{\partial \hat{g}}{\partial \xi}\right|_{k=1} = \frac{\hat{g}_{k=2} - \hat{g}_{n_\xi-1}}{2h_\xi}.} \tag{3.1.10}$$

Cross-derivatives, such as the $\left.\dfrac{\partial^2 \hat{g}}{\partial p \partial y}\right|_y$ term, are represented by a product:

$$\begin{aligned}
\frac{\partial^2 \hat{g}}{\partial p \partial y} &= \Delta^+_{1yl} \left.\frac{\partial \hat{g}_{l+1}}{\partial p}\right|_j + \Delta^0_{1yl} \left.\frac{\partial \hat{g}_l}{\partial p}\right|_j + \Delta^-_{1yl} \left.\frac{\partial \hat{g}_{l-1}}{\partial p}\right|_j \\
\rightarrow \frac{\partial^2 \hat{g}}{\partial p \partial y} &= \Delta^+_{1yl}\left(\Delta^+_{1pj}\hat{g}_{j+1,l+1} + \Delta^0_{1pj}\hat{g}_{j,l+1} + \Delta^-_{1pj}\hat{g}_{j-1,l+1}\right) \\
&\quad + \Delta^0_{1yl}\left(\Delta^+_{1pj}\hat{g}_{j+1,l} + \Delta^0_{1pj}\hat{g}_{j,l} + \Delta^-_{1pj}\hat{g}_{j-1,l}\right) \\
&\quad + \Delta^-_{1yl}\left(\Delta^+_{1pj}\hat{g}_{j+1,l-1} + \Delta^0_{1pj}\hat{g}_{j,l-1} + \Delta^-_{1pj}\hat{g}_{j-1,l-1}\right).
\end{aligned} \tag{3.1.11}$$

At p-mesh limits, the boundary condition (2.3.51) applies, so $\dfrac{\partial^2 \hat{g}}{\partial p \partial y} = 0$. At y-mesh limits, the coefficient of $\dfrac{\partial^2 \hat{g}}{\partial y^2}$ disappears, effectively resulting in $\dfrac{\partial \hat{g}}{\partial y}$ becoming constant there. Special forms for the matrix representation of $\dfrac{\partial \hat{g}}{\partial y}$ at the y-limits are derived using quadratic fitting, which are derived later in Sec.3.1.3 after discretising the ion drift-kinetic equation.

3.1.3 Stages (4) and (6): Matrix equation

We now describe stage (4) of the calculation in Fig.3.1 in further detail. At speed u, for a given ion population, $\hat{g}$ is represented by a solution vector[3], $\mathbf{g}_l(p, \xi)$, at each y-grid point. The indices of p, ξ, y are denoted by $j\{1, n_p\}, k\{1, n_\xi\}$ and $l\{1, n_y\}$ respectively, where n_p, n_ξ and n_y are the total number of points in each mesh. The matrix equation is constructed using 2D square matrices of rank $n_\xi n_p \times n_\xi n_p$, which couple (p, ξ, y)-points and represent the derivatives of $\mathbf{g}_l$.

[3]In practice, $\mathbf{g}_l(p, \xi)$ is a flattened 1D array of rank $n_\xi n_p$.

Converting to matrix form

The matrix form of Eq.(2.3.47) is as follows. For the convenience of avoiding $1/u$ in the limit $u \to 0$, we begin by multiplying Eq.(2.3.47) by $-u/\hat{\nu}_{ii}$:

$$\begin{aligned}
&\frac{mu}{\hat{\nu}_{ii}}\left[\frac{p}{\hat{L}_q}\Theta_y + \frac{\hat{\rho}_{\theta,i}}{\hat{L}_q}\hat{\omega}_D - \frac{\hat{\rho}_{\theta,i}}{2}\left\langle\frac{1}{u_\parallel}\frac{\partial\hat{\Phi}}{\partial x}\right\rangle_\theta^p\right]\frac{\partial\hat{g}}{\partial\xi}\\
&+\frac{u}{\hat{\nu}_{ii}}\left[-\frac{m}{4}\frac{\hat{w}^2}{\hat{L}_q}\sin\xi\,\Theta_y + m\frac{\hat{\rho}_{\theta,i}}{2}\left\langle\frac{1}{u_\parallel}\frac{\partial\hat{\Phi}}{\partial\xi}\right\rangle_\theta^p + \hat{\nu}_{ii}\hat{\rho}_{\theta,i}\Theta_y\right]\left(\frac{\partial\hat{g}}{\partial p} + \hat{F}'_{\mathrm{M}s}\right)\\
&+\frac{\sigma u^2}{2(1+\epsilon)}\hat{\rho}^2_{\theta,i}y\left\langle\frac{1}{\sqrt{1-yb}}\right\rangle_\theta^x\frac{\partial^2\hat{g}}{\partial p^2} + 2\hat{\rho}_{\theta,i}yu\Theta_y\frac{\partial^2\hat{g}}{\partial y\partial p} + \sigma(1+\epsilon)\left\langle\frac{(2-3yb)}{\sqrt{1-yb}}\right\rangle_\theta^x\frac{\partial\hat{g}}{\partial y}\Big|_p\\
&\qquad+2\sigma(1+\epsilon)y\left\langle\sqrt{1-yb}\right\rangle_\theta^x\frac{\partial^2\hat{g}}{\partial y^2}\Big|_p \;=\; -2u(1+\epsilon)\hat{\bar{U}}_{\parallel i}(\hat{g}+p\hat{F}'_{\mathrm{M}s})\hat{F}_{\mathrm{M}s}
\end{aligned} \tag{3.1.12}$$

Coefficients of $\hat{g}$, $\hat{F}_{\mathrm{M}s}$ and $\hat{F}'_{\mathrm{M}s}$ are represented by the following shorthands:

$$\begin{aligned}
C^1 &= \frac{mu}{\hat{\nu}_{ii}}\frac{p}{\hat{L}_q}\Theta_y, \quad C^2 = \frac{mu}{\hat{\nu}_{ii}}\frac{\hat{\rho}_{\theta,i}}{\hat{L}_q}\hat{\omega}_D,\\
C^3 &= -\frac{mu}{\hat{\nu}_{ii}}\frac{\hat{\rho}_{\theta,i}}{2}\left\langle\frac{1}{u_\parallel}\frac{\partial\hat{\Phi}}{\partial x}\right\rangle_\theta^p, \quad C^4 = -\frac{mu}{4\hat{\nu}_{ii}}\frac{\hat{w}^2}{\hat{L}_q}\sin\xi\,\Theta_y,\\
C^5 &= \frac{mu}{\hat{\nu}_{ii}}\frac{\hat{\rho}_{\theta,i}}{2}\left\langle\frac{1}{u_\parallel}\frac{\partial\hat{\Phi}}{\partial\xi}\right\rangle_\theta^p, \quad C^6 = \hat{\rho}_{\theta,i}u\Theta_y\\
C^7 &= \frac{\sigma u^2}{2(1+\epsilon)}\hat{\rho}^2_{\theta,i}y\left\langle\frac{1}{\sqrt{1-yb}}\right\rangle_\theta^x, \quad C^8 = 2\hat{\rho}_{\theta,i}yu\Theta_y,\\
C^9 &= (1+\epsilon)\sigma\left\langle\frac{(2-3yb)}{\sqrt{1-yb}}\right\rangle_\theta^x, \quad C^{10} = 2(1+\epsilon)\sigma y\left\langle\sqrt{1-yb}\right\rangle_\theta^x,\\
C^U &= -2u(1+\epsilon)\hat{\bar{U}}_{\parallel(}\hat{g}+p\hat{F}'_{\mathrm{M}s}).
\end{aligned} \tag{3.1.13}$$

Within this implementation of the algorithm, the finite difference discretisation of Eq.(3.1.12) in y-space is described by the following matrix-vector equation, which couples $\mathbf{g}_l(p,\xi)$ vectors at neighbouring y-points:

$$\underline{\mathbf{P}}_l\cdot\mathbf{g}_{l+1} + \underline{\mathbf{Q}}_l\cdot\mathbf{g}_l + \underline{\mathbf{R}}_l\cdot\mathbf{g}_{l-1} + \underline{\mathbf{L}}_l\cdot\mathbf{g}_l = \mathbf{D}_l. \tag{3.1.14}$$

Here, $\underline{\mathbf{P}}$, $\underline{\mathbf{Q}}$, and $\underline{\mathbf{R}}$ are sparse triband square matrices of rank $n_\xi n_p$, whose elements are denoted by column q and row r[4] contain the coefficients of $\frac{\partial\hat{g}}{\partial y}$, $\frac{\partial^2\hat{g}}{\partial y^2}$ and $\frac{\partial^2\hat{g}}{\partial p\partial y}$, multiplied by the

[4]Here, $q,r = \{1, n_\xi n_p\}$, and for a given ξ-index j and p-index k, the conversion between ξ, p and q/r indices is given by $(j-1)n_\xi + k$

corresponding $\Delta_l^{-/0/+}$ central difference term in y (see Eq.(3.1.3),(3.1.5)):

$$\begin{aligned}\underline{\mathbf{P}}_{q(j,k)r(j,k)} &= C^8_{q(j,k)}\Delta^+_{1yl}\Delta^0_{1pj} + C^9_{q(j,k)}\Delta^+_{1yl} + C^{10}_{q(j,k)}\Delta^+_{2yl} \\ \underline{\mathbf{P}}_{q(j,k)r(j\pm1,k)} &= C^8_{q(j,k)}\Delta^+_{1yl}\Delta^\pm_{1pj}\end{aligned} \tag{3.1.15}$$

$$\begin{aligned}\underline{\mathbf{Q}}_{q(j,k)r(j,k)} &= C^8_{q(j,k)}\Delta^0_{1yl}\Delta^0_{1pj} + C^9_{q(j,k)}\Delta^0_{1yl} + C^{10}_{q(j,k)}\Delta^0_{2yl} \\ \underline{\mathbf{Q}}_{q(j,k)r(j\pm1,k)} &= C^8_{q(j,k)}\Delta^0_{1yl}\Delta^\pm_{1pj}\end{aligned} \tag{3.1.16}$$

$$\begin{aligned}\underline{\mathbf{R}}_{q(j,k)r(j,k)} &= C^8_{q(j,k)}\Delta^-_{1yl}\Delta^0_{1pj} + C^9_{q(j,k)}\Delta^-_{1yl} + C^{10}_{q(j,k)}\Delta^-_{2yl} \\ \underline{\mathbf{R}}_{q(j,k)r(j\pm1,k)} &= C^8_{q(j,k)}\Delta^-_{1yl}\Delta^\pm_{1pj}\end{aligned} \tag{3.1.17}$$

The general banded matrix $\underline{\mathbf{L}}_l$ describes the ξ and p derivatives:

$$\underline{\mathbf{L}}^{(\xi)}_{q(j,k)r(j,k\pm1)} = \left(C^1_{q(j,k)} + C^2_{q(j,k)} + C^3_{q(j,k)}\right)\Delta^\pm_{1\xi k}, \tag{3.1.18}$$

where the periodic condition (2.3.50) replaces $k = n_\xi + 1$ with $k = 2$, and $k = 0$ with $k = n_\xi - 1$ (such that $k = 1$ is the same ξ-point as $k = n_\xi$). Next, the p-differential terms:

$$\begin{aligned}\underline{\mathbf{L}}^{(p)}_{q(j,k)r(j,k)} &= \left(C^4_{q(j,k)} + C^5_{q(j,k)} + C^6_{q(j,k)}\right)\Delta^0_{1pj} + C^7_{q(j,k)}\Delta^0_{2pj} \\ \underline{\mathbf{L}}^{(p)}_{q(j,k)r(j\pm1,k)} &= \left(C^4_{q(j,k)} + C^5_{q(j,k)} + C^6_{q(j,k)}\right)\Delta^\pm_{1pj} + C^7_{q(j,k)}\Delta^\pm_{2pj}\end{aligned} \tag{3.1.19}$$

where the differential coefficients $\Delta^{(\dots)}_{2pj}$ take into account the boundary conditions, using the forms given by Eq.(3.1.7) and Eq.(3.1.9). Lastly, $\mathbf{D}_l$ is a vector (rank $n_\xi n_p$) containing coefficients of $\hat{F}_\mathrm{M}$ and $\hat{F}'_\mathrm{M}$:

$$\mathbf{D}_{q(j,k)} = C^U_{q(j,k)}\hat{F}_{\mathrm{M}s} - (C^4_{q(j,k)} + C^5_{q(j,k)} + C^6_{q(j,k)})\hat{F}'_{\mathrm{M}s}. \tag{3.1.20}$$

Recurrence relation

In Fig.3.1, stage (4) of the calculation involves a shooting method that propagates the boundary condition at the y-limits toward the trapped-passing boundary. For passing particles, the linear recurrence relation that couples the y-point at index $l-1$, with the point l towards the trapped-passing boundary is given by:

$$\mathbf{g}^p_l = \underline{\boldsymbol{\alpha}}^p_l \cdot \mathbf{g}^p_{l+1} + \boldsymbol{\beta}^p_l, \tag{3.1.21}$$

$$\Rightarrow\ \mathbf{g}^p_{l-1} = \underline{\boldsymbol{\alpha}}^p_{l-1} \cdot \mathbf{g}^p_l + \boldsymbol{\beta}^p_{l-1}. \tag{3.1.22}$$

Here, $\underline{\boldsymbol{\alpha}}$ is a dense square matrix of rank $n_\xi n_p \times n_\xi n_p$, and $\boldsymbol{\beta}$ is a vector of equal rank, both of which operate on $\mathbf{g}_l$ at a y-point of index l to give $\mathbf{g}_{l-1}$ at the next point towards the deeply passing end. Following 8.5.2, this relation can be rewritten in terms of the matrices given in Sec.3.1.3.

$$\boxed{\underline{\boldsymbol{\alpha}}_l^p = -(\underline{\mathbf{M}}_l^p)^{-1} \cdot \underline{\mathbf{P}}_l^p, \quad \boldsymbol{\beta}_l^p = (\underline{\mathbf{M}}_l^p)^{-1} \cdot \left(\mathbf{D}_l^p - \underline{\mathbf{R}}_l^p \cdot \boldsymbol{\beta}_{l-1}^p\right), \quad \underline{\mathbf{M}}_l^p = \underline{\mathbf{Q}}_l^p + \underline{\mathbf{L}}_l^p + \underline{\mathbf{R}}_l^p \cdot \underline{\boldsymbol{\alpha}}_{l-1}^p} \tag{3.1.23}$$

Here, $\underline{\mathbf{M}}$ is a matrix of equal rank to $\underline{\boldsymbol{\alpha}}$ but is a common term of both $\underline{\boldsymbol{\alpha}}$ and $\boldsymbol{\beta}$, and is calculated first. Similarly, for trapped particles, this relation is in the opposite direction in y:

$$\Rightarrow \ \mathbf{g}_{l+1}^t = \underline{\boldsymbol{\alpha}}_{l+1}^t \cdot \mathbf{g}_l^t + \boldsymbol{\beta}_{l+1}^t. \tag{3.1.24}$$

which gives:

$$\boxed{\underline{\boldsymbol{\alpha}}_l^t = -(\underline{\mathbf{M}}_l^t)^{-1} \cdot \underline{\mathbf{R}}_l^p, \quad \boldsymbol{\beta}_l^t = (\underline{\mathbf{M}}_l^t)^{-1} \cdot \left(\mathbf{D}_l^t - \underline{\mathbf{P}}_l^t \cdot \boldsymbol{\beta}_{l+1}^t\right), \quad \underline{\mathbf{M}}_l^t = \underline{\mathbf{Q}}_l^t + \underline{\mathbf{L}}_l^t + \underline{\mathbf{P}}_l^t \cdot \underline{\boldsymbol{\alpha}}_{l+1}^t} \tag{3.1.25}$$

Solving at the deeply passing and trapped ends

Special forms of $\underline{\boldsymbol{\alpha}}$ and $\boldsymbol{\beta}$ are defined at the y-limits to apply the outer boundary conditions there. Here, quadratic fitting is performed:

$$\mathbf{g}_l^{t/p} = \mathbf{a} y_l^2 + \mathbf{b} y_l + \mathbf{c} \ , \qquad \left.\frac{\partial \mathbf{g}^{t/p}}{\partial y}\right|_{y_l} = 2\mathbf{a} y_l + \mathbf{b}, \tag{3.1.26}$$

where coefficients $\mathbf{a}$ and $\mathbf{b}$ are to be determined separately for the deeply passing and trapped ends, respectively (finding $\mathbf{c}$ is not required).

At the deeply passing end, by fitting Eq.(3.1.26) across $l = 1$, 2 and 3:

$$\begin{aligned} \mathbf{g}_1^p &= \mathbf{a} y_1^2 + \mathbf{b} y_1 + \mathbf{c} \ , \\ \mathbf{g}_2^p &= \mathbf{a} y_2^2 + \mathbf{b} y_2 + \mathbf{c} \ , \\ \mathbf{g}_3^p &= \mathbf{a} y_3^2 + \mathbf{b} y_3 + \mathbf{c} \ , \end{aligned} \tag{3.1.27}$$

then (following Sec.8.5.2), it can be shown that, equating for $\mathbf{c}$:

$$\therefore \ \mathbf{a} = \frac{(y_2 - y_3)\mathbf{g}_1^p - (y_1 - y_3)\mathbf{g}_2^p + (y_1 - y_2)\mathbf{g}_3^p}{(y_1 - y_2)(y_2 - y_3)(y_1 - y_3)} \ , \qquad \mathbf{b} = \frac{(\mathbf{g}_1^p - \mathbf{g}_2^p)}{(y_1 - y_2)} - (y_1 + y_2)\mathbf{a}. \tag{3.1.28}$$

Using the expression in Eq.(3.1.26) for $\dfrac{\partial \mathbf{g}}{\partial y}$, another relation for $\mathbf{a}$ and $\mathbf{b}$ is obtained:

$$\left.\frac{\partial \mathbf{g}^p}{\partial y}\right|_{y_1} = 2\mathbf{a}y_1 + \mathbf{b} = \frac{(y_1 - y_2) + (y_1 - y_3)}{(y_1 - y_2)(y_1 - y_3)}\mathbf{g}_1^p - \frac{(y_1 - y_3)}{(y_1 - y_2)(y_2 - y_3)}\mathbf{g}_2^p + \frac{(y_1 - y_2)}{(y_2 - y_3)(y_1 - y_3)}\mathbf{g}_3^p. \tag{3.1.29}$$

Rewriting the matrix equation (3.1.14) for $l = 1$ ($y = 0$):

$$\underline{\mathbf{P}}_1 \cdot \mathbf{g}_3 + \underline{\mathbf{Q}}_1 \cdot \mathbf{g}_2 + \underline{\mathbf{R}}_1 \cdot \mathbf{g}_1 + \underline{\mathbf{L}}_1 \cdot \mathbf{g}_1 = \mathbf{D}_1, \tag{3.1.30}$$

then solving for $\mathbf{g}_1$, the results for $\underline{\boldsymbol{\alpha}}_1$ and $\boldsymbol{\beta}_1$ (both containing matrix $\underline{\mathbf{M}}_1$) are:

$$\boxed{\begin{aligned} \underline{\boldsymbol{\alpha}}_1 &= \underline{\mathbf{M}}_1^{-1} \cdot \left(\underline{\mathbf{P}}_2 \cdot \underline{\mathbf{P}}_1^{-1} \cdot \underline{\mathbf{Q}}_1 - \underline{\mathbf{Q}}_2 - \underline{\mathbf{L}}_2\right), \\ \boldsymbol{\beta}_1 &= \underline{\mathbf{M}}_1^{-1} \cdot \left(\mathbf{D}_2 - \underline{\mathbf{P}}_2 \cdot \underline{\mathbf{P}}_1^{-1} \cdot \mathbf{D}_1\right), \\ \underline{\mathbf{M}}_1 &= \underline{\mathbf{R}}_2 - \underline{\mathbf{P}}_2 \cdot \underline{\mathbf{P}}_1^{-1} \cdot (\underline{\mathbf{R}}_1 + \underline{\mathbf{L}}_1) \end{aligned}} \tag{3.1.31}$$

Full derivations of the above are given in the Appendix, Sec.8.5.2. Similarly, at the deeply trapped end, quadratic fitting is performed at indices $l = n - 2$, $n - 1$ and n (where $n = n_y$). Following the same process as with the passing end, the results for $\underline{\boldsymbol{\alpha}}_n$ and $\boldsymbol{\beta}_n$ in the deeply trapped end are:

$$\boxed{\begin{aligned} \underline{\boldsymbol{\alpha}}_n &= \underline{\mathbf{M}}_n^{-1} \cdot \left(\underline{\mathbf{R}}_{n-1} \cdot \underline{\mathbf{R}}_n^{-1} \cdot \underline{\mathbf{Q}}_n - \underline{\mathbf{Q}}_{n-1} - \underline{\mathbf{L}}_{n-1}\right), \\ \boldsymbol{\beta}_n &= \underline{\mathbf{M}}_n^{-1} \cdot \left(\mathbf{D}_{n-1} - \underline{\mathbf{R}}_{n-1} \cdot \underline{\mathbf{R}}_n^{-1} \cdot \mathbf{D}_n\right), \\ \underline{\mathbf{M}}_n &= \underline{\mathbf{P}}_{n-1} - \underline{\mathbf{R}}_{n-1} \cdot \underline{\mathbf{R}}_n^{-1} \cdot (\underline{\mathbf{P}}_n + \underline{\mathbf{L}}_n) \end{aligned}} \tag{3.1.32}$$

Full derivations for the above are also given in the Appendix, Sec.8.5.2. After the deeply passing and trapped forms of $\underline{\boldsymbol{\alpha}}$ and $\boldsymbol{\beta}$ are calculated, the recurrence relations are used to find them for all other y-points up to but excluding the trapped-passing boundary.

3.1.4 Stage (5): Solving at the trapped-passing boundary

To apply the matching conditions given by Eqs.(2.3.52-2.3.54):

$$\sum_\sigma \sigma \hat{g}_p^\sigma = 0 \ , \qquad \sum_\sigma \hat{g}_p^\sigma = 2\hat{g}_t \ , \qquad \sum_\sigma \frac{\partial \hat{g}_p^\sigma}{\partial y} = 2\frac{\partial \hat{g}_t}{\partial y},$$

the matrix equation needs to be known at the nearby points to the trapped passing boundary $y = y_c \equiv 1$. As illustrated in Fig.3.3, we define these near-passing/trapped points in order of ascending y as: y_{pp}, y_p, y_t and y_{tt}:

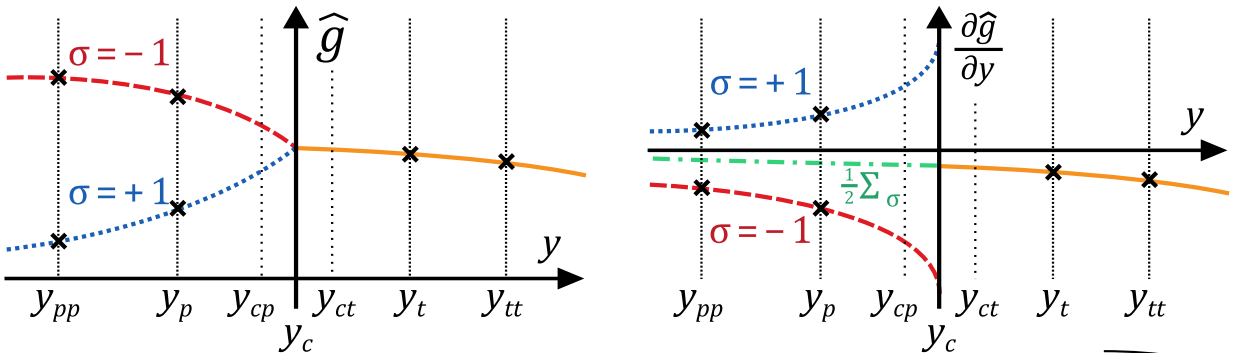

(a) Matching of $\hat{g}$ via Eq.(2.3.53).

(b) Matching of $\frac{\partial \hat{g}}{\partial y}$ via Eq.(2.3.54).

Figure 3.3: Sketch of the perturbed ion distribution profile $\hat{g}(y)$ and $\frac{\partial \hat{g}}{\partial y}$ at the trapped-passing boundary, showing anti-passing (red, dashed), passing (blue, dotted) and trapped (orange, solid) ions. The σ-average of passing ions is shown in (b) (green, dash-dot). Mesh points in y are shown by crosses. y_{cp} and y_{ct} are fictitious points infinitesimally close to $y = y_c$. Not to scale.

To fit across the discontinuity in 3.1.12 across $y = y_c$, we can consider a fictitious 'marginally passing' point $\hat{g}_{cp}^{\pm} = \hat{g}_c - \epsilon$ and 'marginally trapped' $\hat{g}_{ct} = \hat{g}_c + \epsilon$. The first two matching conditions imply that:

$$\lim_{\epsilon \to 0} \quad \hat{g}_{cp}^{+} = \hat{g}_{cp}^{-}, \quad \hat{g}_{cp}^{+} + \hat{g}_{cp}^{-} = 2\hat{g}_{ct} \equiv 2\hat{g}_c,$$

so that in the limit of $\epsilon \ll 1$, $\hat{g}_c$ has to be equal in value for all three ion populations, and hence it is valid to substitute y_c for y_{cp} and y_{ct} in our fitting. Quadratic fitting is performed either side of the discontinuity, using y-mesh points y_{pp}, y_p, y_c for the passing region and y_c, y_t and y_{tt} for

the trapped region. This provides a set of three equations for each region:

$$\begin{aligned} \mathbf{g}_{pp}^{\pm} &= \mathbf{a}^{\pm} y_{pp}^2 + \mathbf{b}^{\pm} y_{pp} + \mathbf{c} & \mathbf{g}_{tt} &= \mathbf{a}^{t} y_{tt}^2 + \mathbf{b}^{t} y_{tt} + \mathbf{c} \\ \mathbf{g}_{p}^{\pm} &= \mathbf{a}^{\pm} y_{p}^2 + \mathbf{b}^{\pm} y_{p} + \mathbf{c} & \mathbf{g}_{t} &= \mathbf{a}^{t} y_{t}^2 + \mathbf{b}^{t} y_{t} + \mathbf{c} \\ \mathbf{g}_{c}^{\pm} &= \mathbf{a}^{\pm} y_{c}^2 + \mathbf{b}^{\pm} y_{c} + \mathbf{c} & \mathbf{g}_{c} &= \mathbf{a}^{t} y_{c}^2 + \mathbf{b}^{t} y_{c} + \mathbf{c} \end{aligned}$$

Here, superscript $\pm$ indicates passing/anti-passing particles and t for trapped particles. Solving for $\mathbf{a}^{\pm/t}$ and $\mathbf{b}^{\pm/t}$ separately for the passing, anti-passing and trapped distributions, then inserting the matrix equation Eq.(3.1.14) for each y-point, after a lengthy derivation (given in full within Sec.8.5.2) we obtain a simple linear equation for $\mathbf{g}_c$:

$$\underline{\mathbf{A}} \cdot \mathbf{g}_c \;=\; \mathbf{B} \tag{3.1.33}$$

$$\begin{aligned} \underline{\mathbf{A}} &= 2\Delta_{cp}\underline{\mathbf{I}} + (\Delta_p \underline{\mathbf{I}} + \Delta_{pp}\underline{\boldsymbol{\alpha}}_{pp}^{+}) \cdot \underline{\boldsymbol{\alpha}}_{p}^{+} + (\Delta_p \underline{\mathbf{I}} + \Delta_{pp}\underline{\boldsymbol{\alpha}}_{pp}^{-}) \cdot \underline{\boldsymbol{\alpha}}_{p}^{-} \\ &\quad - 2\Delta_{ct}\underline{\mathbf{I}} - 2(\Delta_t \underline{\mathbf{I}} + \Delta_{tt}\underline{\boldsymbol{\alpha}}_{tt}) \cdot \underline{\boldsymbol{\alpha}}_{t} \\ \mathbf{B} &= -(\Delta_p \underline{\mathbf{I}} + \Delta_{pp}\underline{\boldsymbol{\alpha}}_{pp}^{+}) \cdot \boldsymbol{\beta}_{p}^{+} - (\Delta_p \underline{\mathbf{I}} + \Delta_{pp}\underline{\boldsymbol{\alpha}}_{pp}^{-}) \cdot \boldsymbol{\beta}_{p}^{-} - \Delta_{pp}(\boldsymbol{\beta}_{pp}^{+} + \boldsymbol{\beta}_{pp}^{-}) \\ &\quad + 2(\Delta_t \underline{\mathbf{I}} + \Delta_{tt}\underline{\boldsymbol{\alpha}}_{tt}) \cdot \boldsymbol{\beta}_{t} + 2\Delta_{tt}\boldsymbol{\beta}_{tt} \end{aligned}$$

Here, $\underline{\mathbf{I}}$ is the identity matrix, and:

$$\begin{aligned} \Delta_{cp} &= \frac{h_p + h_{cp}}{h_p h_{cp}}, & \Delta_{ct} &= -\frac{h_t + h_{ct}}{h_t h_{ct}}, \\ \Delta_{p} &= -\frac{h_{cp}}{h_p h_{pp}}, & \Delta_{t} &= \frac{h_{ct}}{h_t h_{tt}}, \\ \Delta_{pp} &= \frac{h_p}{h_{pp} h_{cp}}, & \Delta_{tt} &= -\frac{h_t}{h_{tt} h_{ct}} \end{aligned}$$

and the mesh spacings of those y-points are:

$$\begin{aligned} h_{cp} &= y_c - y_{pp} = h_p + h_{pp} & h_{ct} &= y_{tt} - y_c \equiv h_{tt} + h_t \\ h_p &= y_c - y_p & h_t &= y_t - y_c \\ h_{pp} &= y_p - y_{pp} & h_{tt} &= y_{tt} - y_t \end{aligned}$$

The solution of Eq.(3.1.4) is the first value of $\hat{g}$ calculated from the drift-kinetic ion equation, which is then solved elsewhere using the aforementioned linear recurrence relations.

3.1.5 Stage (9): Iterative convergence

The terms $\hat{g}$, $\hat{\Phi}$ and $\hat{\bar{U}}_{\parallel,i}$ are iteratively recalculated, starting from initial guesses $\hat{\Phi} = 0$ and $\hat{\bar{U}}_{\parallel,i} = \hat{\bar{U}}_{\parallel,i}(p\hat{F}'_{\mathrm{M}s})$. Provided these guesses are valid and the scheme is numerically stable, all three should converge towards values that are self-consistent. However this approach poses several questions: i) whether convergence will occur at all, ii) whether the converged state itself is valid, iii) how many iterations are required to reach convergence, iv) what degree of convergence is acceptable, and v) whether it is numerically stable (i.e. the 'converged' state does not then diverge on successive iterations). While there is no guarantee that i) and ii) will be fulfilled, we can use a higher mesh resolution to improve the accuracy of the numerical methods, though there are challenges of doing so as discussed later in Sec.3.1.6.

Regarding points iii)-v), the number of iterations that can be performed, as is the size of the simulation domain, is also subject to computational resource limitations. However, if the simulation is allowed to run unabated, there is also the possibility for even a slowly-changing result to suddenly diverge due to an initially small *numerical instability*, an issue previously observed in the `DK-NTM` code [72]. Therefore, the run needs to be stopped when some convergence criterion is satisfied, where the relative change in $\hat{g}$, $\hat{\Phi}$ and $\hat{\bar{U}}_{\parallel,i}$ between iterations, the "residual" is acceptably small. As `DK-NTM` did not have a strict definition of a converged solution (the final result over several iterations was assumed "converged"), a new method for tracking of the residuals was implemented into `kokuchou`. In `kokuchou`, the iterative residual $\mathcal{R}$ of a general quantity X at iteration I is based on a relative difference from the previous iteration $I-1$:

$$\mathcal{R}(X_I) = \frac{|X_I - X_{I-1}|}{|X_I| + |X_{I-1}|}$$

where x_I can represent a single iterated quantity, e.g. Δ_{loc}, or a point of an array. The form of Eq.(3.1.5) ensures there is no zero denominator unless both x_I and x_{I-1} are zero; this special case is handled by taking $\mathcal{R}(x_I) \approx 0/0$ to be 0. A similar convergence metric is used in the `RDK-NTM` code of Refs. [41, 43], whose formula varies slightly, $\mathcal{R}(x_I) = |x_I - x_{n-1}|/|x_I|$ [78]. For 3D arrays $\hat{\Phi}$ and $\hat{\bar{U}}_{\parallel,i}$, $\mathcal{R}(x_I)$ is calculated at all (θ, x, ξ) at each iteration. Note that on the first iteration 1, $x_0 = 0$ and hence $\mathcal{R}(x_1) \equiv 1$ if $\hat{\Phi}$ or $\hat{\bar{U}}_{\parallel,i}$ are initially zero.

A simple *convergence criterion* was implemented within `kokuchou` by which the code stops iterating when the array-averaged[5] residual $\bar{\mathcal{R}}(\hat{\Phi})$ and $\bar{\mathcal{R}}(\hat{\bar{U}}_{\parallel,i})$ are **both** below a user-defined tolerance value, which is checked at the end of each 'iteration' as shown in Fig.3.1. Noting

[5] Array average as in sum/number of points.

that the ion drift-kinetic equation(2.3.47) itself is accurate to $O(\epsilon^{3/2})$, where typically $\epsilon = 0.1$ is used [69, 70, 41], then a $\epsilon^1 \approx 10\%$ relative error can be used as the tolerance value for both residuals. However, the array average will hide individual points where $\mathcal{R}$ is large, so a more representative method for tracking the convergence state will be needed in future work.

3.1.6 Challenges and limitations

The iterative calculation of the ion response from the 4D drift-kinetic equation outlined in Sec.3.1 is computationally and numerically challenging. While the three spatial dimensions $\{\xi, \theta, x\}$ were conveniently reduced to a 2D $\{\xi, p\}$ system in Sec.2.3.2, the code requires a high-resolution simulation mesh geometry to accurately resolve key physical details around the island. A further challenge is that the calculation must be iterated over for a self-consistent result. Together these set requirements for the simulation code, which are discussed here.

Boundary layers

Recall from Sec.1.5 that two narrow boundary layers are considered within Refs. [69, 70] and [50]: i) the *dissipation layer* in pitch-angle λ surrounding the trapped-passing boundary at $y = y_c \equiv 1$, and ii) the *separatrix layer* in $\{p, \xi\}$ phase-space surrounding specifically the *drift island* separatrix, of width $O(\rho_{\theta,i})$. The dissipation layer arises where there is a discontinuity in Eq.(2.3.47), due to the differing orbit-average processes for passing and trapped ions. For these distributions to be matched at the trapped-passing boundary, the y-mesh should be sufficiently-resolved there.

A more significant challenge, however, is posed by the separatrix layer of the drift island. High resolution in $\{\xi, p\}$ is required around this separatrix layer to accurately determine the polarisation current, a major contribution of which is localised to the vicinity of the magnetic island [45, 50]. However, this layer is hard to capture for three reasons. Firstly, the $\{\xi, p\}$-mesh itself is rectilinear, while the island is rounded in shape, which in practice means some regions will be over- or under-resolved. Secondly, we emphasise that this layer surrounds the *drift island* and not the magnetic island, which is the island-shaped contour the ion distribution exhibits in response to the magnetic island. Drift islands, as discussed in [70, 41], are of identical shape to the magnetic island (when $\hat{\Phi} = 0$) but shifted radially from it by a factor $\rho_{\theta,i}\hat{\omega}_D$, where $\hat{\omega}_D(y, \sigma, u)$ is the normalised drift frequency defined by 2.3.48. The drift island's location will vary with y and u, and so the radial $x-$ and p-meshes must accommodate all possible locations of a drift island, discussed further in Sec.3.1.2. The current itself is obtained from the velocity-space volume integral of the $v_\parallel$-weighted ion distribution over $\{y, \sigma, v\}$, and so all drift islands over this space

be resolved accurately. Thirdly, recall that in Sec.2.6, the $\frac{\partial^2 \hat{g}}{\partial p^2}$ coefficient was found to scale with $\hat{\rho}_{\theta,i}^2$ instead of $\hat{\rho}_{\theta,i}^0$ as in Eq.(A.1) of Ref. [70], therefore the gradients around the separatrix are expected to vary more steeply than previously observed in `DK-NTM` simulations in [70], meaning that we may be limited to a smaller parameter space than in earlier work.

Limitation on problem size

The primary limiting factor of the calculation is the availability and usage of memory. The shooting algorithm requires large arrays for $\underline{\boldsymbol{\alpha}}$ and $\boldsymbol{\beta}$ to be calculated and stored at every y-point (and for two values in σ in the passing region) when solving for $\hat{g}$ at a given value in u. By far the largest arrays used are the $\underline{\boldsymbol{\alpha}}$ arrays, which contain $n_\xi^2 n_p^2$ points at each y. An even larger number of linear algebra operations are performed on these arrays. The maximum mesh size is therefore subject to limits on available memory (and runtime on an HPC service), while the minimum mesh size is determined by the width and steepness of the separatrix gradients relative to the drift island for a given set of plasma parameters. For example, a lower collisionality $\nu_\star$ (i.e. a longer mean free path) will give steeper, narrower gradients at the separatrix, thereby requiring more p and x points to solve accurately. Likewise, a wider island in radial coordinate $x[r_s]$, which itself determines the dimensions of the meshes in x and p, will have a relatively narrower separatrix gradient if its collisional mean-free path is unchanged, thereby requiring more points to resolve. This results in a trade-off between the resolution of the simulation meshes and the available memory and runtime, and limits the range of certain plasma parameters. Flexibility can only be afforded when executing the code on an HPC platform. However, due to the nature by which the mesh is designed - a rectilinear $\{\xi, p\}$ grid for a round island shape - the accuracy of the solution is not expected to scale well with increasing n_ξ and n_p. The reduced-dimension `RDK-NTM` code of Refs. [41, 43] avoids this issue by converting p and ξ to a single streamline dimension valid only in the limit of very low $\nu_\star$. The contours of the streamline then follow the drift island structure, allowing fewer points to be used overall when resolving the necessary separatrix gradients. However, as this work concerns finite $\nu_\star$ plasmas and the effect on radial diffusion around the drift island, we avoid making this dimensional reduction and must continue to work in $\{p, \xi\}$ coordinates.

The mesh sizes used in this work are $n_\xi = 30$, $n_p = 145$, $n_{y(passing)} = 49$, $n_{y(trapped)} = 40$, and $n_u = 24$. The matrix rank $N = n_\xi n_p = 4350$, and there are $2(49) + 40 = 138$ arrays of $\underline{\boldsymbol{\alpha}}_l$ (size $N \times N$) and $\boldsymbol{\beta}$ (size N) to store when operating at each u-point. For double-precision

(8-byte) values, storing all $\underline{\boldsymbol{\alpha}}_l$ and $\boldsymbol{\beta}$ requires $\sim$ 16.6 GB of memory per u-point. Solving the recurrence relation equations (3.1.23) and (3.1.25) at one y-point for $\underline{\boldsymbol{\alpha}}$ and $\underline{\mathbf{M}}$ using the `DGESV` BLAS/LAPACK procedure [79] requires $0.67N^3 \approx O(5.5 \times 10^{10})$ operations. A run of this scale takes 0.4 hrs/u-point on the ARCHER2 supercomputer.

Based on the experience of using `DK-NTM`, a number of changes were made to reduce the memory usage within `kokuchou` to allow ξ- and p-mesh resolution to be increased. In `DK-NTM`, passing and anti-passing solution vectors were stored as one combined array with a σ-dimension as well as a ξ, p-dimension. In `kokuchou`, this was split into two, allowing each to be solved/stored separately and halving the memory overhead. The core solver (stages (4-6) of Fig.3.1) was redesigned to operate and store $\underline{\boldsymbol{\alpha}}$ and $\boldsymbol{\beta}$ for one u-point at a time, rather than storing multiple. In a given iteration, $\hat{\Phi}$ and $\hat{\bar{U}}_{\parallel,i}$ are updated in a single loop rather than in a nested loop (in `DK-NTM`, the updating of $\hat{\bar{U}}_{\parallel,i}$ is nested within iterative calculations of $\hat{\Phi}$), to simplify the calculation and the saving of outputs.

3.2 Project overview

Recalling the project objectives, for Objective (1) we have conducted tests to verify the algorithm that is now part of the simulation code `kokuchou`. New unit tests were developed to test procedures within the code. These are packaged within the code's repository and are tested when modifications to the code are made. Results from selected unit tests will be presented in Ch.4.

Next, the final result from a full-scale simulation over several iterations needs to be verified. This is the goal of Objective (2), and will be presented in Ch.5. To do so, we will conduct 4 "case study" runs of `kokuchou` for two values of island width w ($\ll \rho_{\theta,i}$ and $> \rho_{\theta,i}$), and also at two values of collisionality $\nu_\star$. We will qualitatively observe the physical phenomena in the ion response $\hat{g}$ and its associated quantities to look for expected features. This has been attempted in previous studies with the `DK-NTM` and `RDK-NTM` codes [69, 70, 41, 43]. However, we will also attempt to quantitatively verify the result we obtain by deriving predictions for the ion response far from the island, where an analytic result for 2.3.47 can be tractably obtained. Obtaining an accurate numerical result that agrees with this analytic benchmark requires a computationally-intensive calculation over the simulation domain. These challenges were discussed in 3.1.6.

Finally, after verifying by exploring a small number of runs in some detail, Objective (3) will involve obtaining an updated result for the threshold width scaling factor with the trapped ion banana orbit width $\rho_{b,i}$, to be obtained from a parameter scan of w and $\rho_{\theta,i}$. Extending objective (2), 5 values of plasma collisionality $\nu_\star$ are included in this scan. Previous `DK-NTM` simulations at $\nu_\star = 0.01$ in Ref. [70] predicted a scaling of $w_c \sim 2.76\rho_{\theta,i}$ which, for the operating value of $\epsilon = 0.1$, gives $w_c \sim 8.72\rho_{b,i}$. By comparison, the cross-machine experimental observations of Ref. [34] correlate to a value of $0.955\rho_{b,i}$ (in Ref. [34], the full island width is used, and this result is given as $1.91\rho_{b,i}$). Following amendments to the derivation and the development of `kokuchou`, we aim to provide an updated figure that is more closely aligned with the experimental result. Furthermore, a novel parameter scan is conducted in $\nu_\star$, in which we will examine its influence over the threshold island physics. We will also identify the operating window of the `kokuchou` code in w, $\rho_{\theta,i}$ and $\nu_\star$ - whose numerical stability depends on how accurately the drift island separatrix of the ion response is solved. Results from this parameter scan will be presented in Ch.6

3.2.1 Resources

`kokuchou` was written in Fortran 2018 with MPI task parallelism, such that the computation of

$\hat{g}$ described in Sec.3.1 can be computed in parallel over speed u. A number of computational and quality-of-life improvements were made, benefiting the speed and accessibility of gathering data, and addressing some of the computational challenges experienced with `DK-NTM`.

Software

As with `DK-NTM`, `kokuchou` used the Fortran-native BLAS and LAPACK libraries [79] for high-performance matrix algebra. New additions to `kokuchou` included a *CMake*-generated build system for compatibility across software architectures and with third-party libraries. One such library introduced was *neasy-f* [80], a wrapper for the reading and writing of data to compressed *netCDF4* (.nc) files, an industry-standard multidimensional data format. This replaced the previous raw ASCII data format used by `DK-NTM`, significantly reducing the size and number of data files to one per run. The .nc format has support from various libraries, notably *xarray* for Python, eliminating the need for dedicated codes to unpack and visualise the data. The reduction of file size allowed for all iterations of certain parameters to be saved.

MPI-parallelised testing used *pFUnit* [81, 82], a *JUnit*-style unit test framework. Unit tests in test-driven software development are designed to be short and readily executable over short timescales (i.e., seconds), rather than over the long timescales of a full simulation. These were used to perform value checks of short procedures throughout the program. A small number of larger tests (of $10-20$s runtime) were added to check more compute-intensive procedures, such as the velocity volume integral calculation of Eq.(2.2.16), which require a small-size 5D mesh to perform the base-level calculation.

Hardware

Development and testing of `kokuchou` was performed on the York Plasma Institute in-house Linux cluster and University of York Viking supercomputer. Full-scale simulations were conducted on the ARCHER2 UK National Supercomputer service [83]. Accounting for the memory structure of ARCHER2, the most efficient scheme for `kokuchou` used one run per node, parallelised over the 8 NUMA regions of that node, which each contain 16 physical cores. For the required resolution, runs were conducted solving either for 4 or 8 u-points in parallel at a time, depending on the memory required per u-point.

Summary

A new numerical code, `kokuchou`, a novel successor to the `DK-NTM` code of Ref. [69, 70, 41], was written to address computational issues in the original code, and obtain an updated result from the drift-kinetic NTM equation corrected in this work. The code was used to solve for the steady-state plasma response to a near-threshold size $m/n = 2/1$ magnetic island during the onset of a neoclassical tearing mode instability in a high aspect ratio tokamak. The code employs a shooting algorithm to construct a finite difference discretisation of Eq.(2.3.47) at each y-point, solve the equation at the trapped-passing boundary from a set of matching conditions, then use this result to solve at all other y from a linear recurrence relation. Limitations of the numerical method were discussed, particularly the scalability of meshes when resolving the steep gradients of the separatrix boundary, and the computational overhead in storing the large $\underline{\boldsymbol{\alpha}}$ and $\boldsymbol{\beta}$ arrays. The hardware requirements for this calculation (often requiring $O(100$ GB) RAM in total) impose limits on the parameter ranges that can be used, and hence considerations were made when designing the simulation domain and the algorithm. In response to computational issues encountered in `DK-NTM`, various modifications were made in `kokuchou` intended to improve the stability and accuracy of the result, including changes to the mesh structure, shooting algorithm and iteration procedure. New additions include a criterion for determining the converged state of the simulation, and unit tests to verify the intermediate steps of the calculation.

The results of this verification process will be presented in the following chapters, based on the project objectives. Unit tests will be discussed in Ch.4. Ch.5 will present results from four full-size iterated simulations. In Ch.6, the parameter scan experiment conducted by `DK-NTM` in Refs. [69, 70, 41] will be reattempted, with a new scan across collision frequency to identify both physical changes to the island growth physics, and any limitations of the procedure itself.

Chapter 4

Validation of the model

As part of Objective (1), this chapter covers the tests used to validate the methods used in the newly developed `kokuchou` code. Sec.4.1 discusses specific tests for the perturbed flux surface function $h(\Omega)$, the velocity volume integration for ion density and flow, and the collision frequency $\hat{\nu}_{ii}$. Sec.4.1.4 describes the testing of the shooting algorithm on a simple 1D boundary value problem. Sec.4.2 discusses the implementation of the trapped-passing boundary calculation that resolves a critical numerical issue encountered during development.

4.1 Example unit tests

4.1.1 Flux surface function $h(\Omega)$

The function $h(\Omega)$ from Ref. [50], where Ω is the perturbed magnetic flux function defined in Eq.(2.3.41), represents the analytic electron density that contributes to the electrostatic potential $\hat{\Phi}$ (Eq.(2.4.14)), and its x-derivative is used in the analytic electron flow u_e (Eq.(2.5.8)). Recalling Eq.(2.4.8), $h(\Omega)$ requires numerically evaluating the integral for $Q(\Omega)$ for each value in Ω. Unit tests for $h(\Omega)$ were implemented with the mesh parameters $n_x = 201$, $n_\xi = 30$, $n_\Omega = 1000$, similar to full-size runs but with a larger-than-usual x-mesh extent of $\pm 30\hat{w}$. Compared to the full-size runs presented later in Ch.5, the ξ and Ω mesh are comparable while the x-mesh is coarser, and so this test provides an estimate of the numerical error. Fig.4.1a shows the result for $h(\Omega)$. Re-arranging Ω in Eq.(2.3.41) for x, the corresponding value in $x(\Omega)$ for $\xi = 0$ is also shown in both plots.

Fig.4.1a shows the behaviour of $h(\Omega)$ near the island based on its definition in Ref. [50], where the function is checked to be zero inside the island and at its separatrix ($\Omega \leq 1$) shown by the

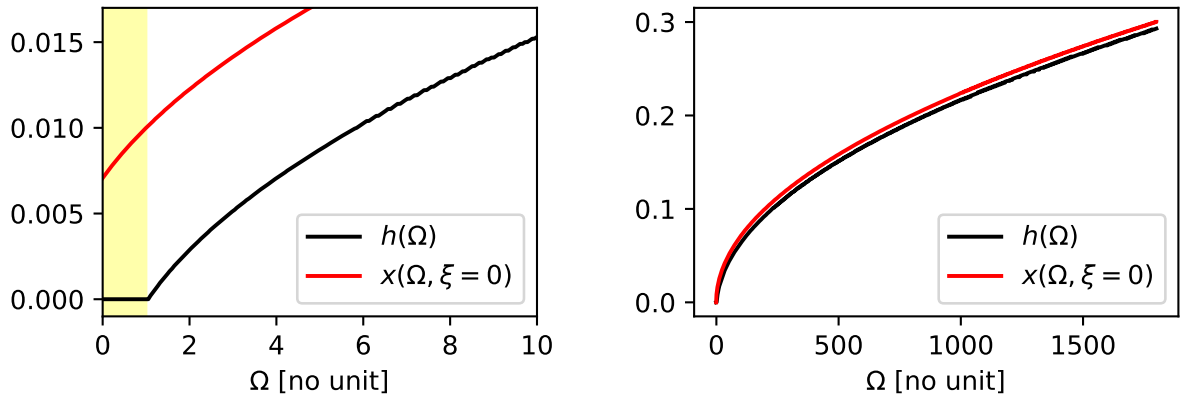

(a) Limited range close to island, shown in yellow.

(b) As in Fig.4.1a, over full range in Ω.

Figure 4.1: $h(\Omega)$ profile with x as function of $\Omega(\xi = 0)$, from unit test `"test_calculate_hOmega"` of `test_analytic.pf`. Island half-width $\hat{w} = 0.01 r_s$.

yellow region. Expanding to the full range in Ω and x, Fig.4.1b shows that far from the island $h(\Omega)$ assumes a shape similar to its asymptote at large x, given by $x(\Omega)$[50].

The code performs a linear interpolation to remap $h(\Omega)$ to $\{x, \xi\}$-space for its use in $\hat{\Phi}$. Its profile across the island O-point, $h(x, \xi = 0)$, is plotted in Fig.4.2. Here, a similar check is performed within $x = \pm\hat{w}$ to test if $h(x, \xi = 0)$ is zero inside the island. The x-dependence of $h(x, \xi = 0)$ is seen to be linear, albeit shifted vertically in opposite directions either side of the island due to the contribution of the ξ-integral in $h(\Omega)$. As before, $h(x, \xi = 0)$ lies parallel to x far from the island without approaching the function.

Lastly, we test the following constraint in Ref. [50] Eq.(52):

$$\left\langle \frac{\partial^2 h}{\partial x^2} \right\rangle_\Omega = 0 \tag{4.1.1}$$

which uses the code's Ω-averaging numerical procedure. The test finds this expression to be satisfied to within 10^{-7} absolute error, though this error is expected due to the multiple linear interpolations and trapezium integrations performed that each contribute error comparable to the square of each mesh's spacing (for a uniform mesh).

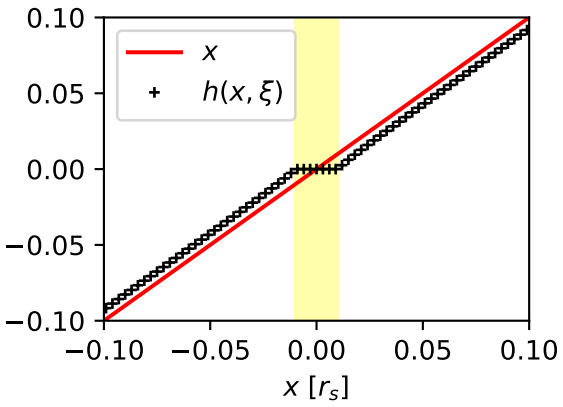

Figure 4.2: Profile of $h(x, \xi = 0)$ in x from subroutine `test_calculate_hOmega` of `test_analytic.pf` in [77]. Island of half-width $\hat{w} = 0.01 r_s$ highlighted in yellow.

4.1.2 Collision frequency $\hat{\nu}_{ii}$ and associated terms

Recall the ion-ion 90° collision frequency $\hat{\nu}_{ii}$ normalised to the Coulomb collision frequency ν_{ii}^C and ion thermal velocity $v_{\mathrm{th},i}$, given by Eq.(2.3.40):

$$\frac{\hat{\nu}_{ii}}{\nu_{ii}^C} = \frac{Rq}{v_{\mathrm{th},i}}\tilde{\nu}_{ii}(u) = \epsilon^{3/2}\nu_\star\tilde{\nu}_{ii} \tag{4.1.2}$$

where, from Eq.(3.45) of Ref. [17]:

$$\begin{aligned}
\tilde{\nu}_{ii}(u) &= \frac{\mathrm{erf}(u) - G(u)}{u^3}\ ; \qquad \tilde{\nu}_{ii}(u) \to \begin{cases} \frac{4}{3v^2\sqrt{\pi}} & v \to 0 \\ \frac{1}{v^3} & v \to \infty \end{cases} \\
G(u) &= \frac{\mathrm{erf}(u) - v\,\mathrm{erf}'(u)}{2u^2}\ ; \qquad G(u) \to \begin{cases} \frac{2u}{3\sqrt{\pi}} & v \to 0 \\ \frac{1}{2u^2} & v \to \infty \end{cases} \\
\mathrm{erf}(u) &= \frac{2}{\sqrt{\pi}}\int_0^u e^{-t^2}dt\ , \qquad \mathrm{erf}'(u) = \frac{d}{du}(\mathrm{erf}(u)) = \frac{2}{\sqrt{\pi}}e^{-u^2}
\end{aligned} \tag{4.1.3}$$

Fig.4.3 shows the variation of the u-dependent term $\tilde{\nu}_{ii}(u)$ only, comparing with its asymptotes in the limits of small and large u given in the literature: Unit tests were written for the calculation

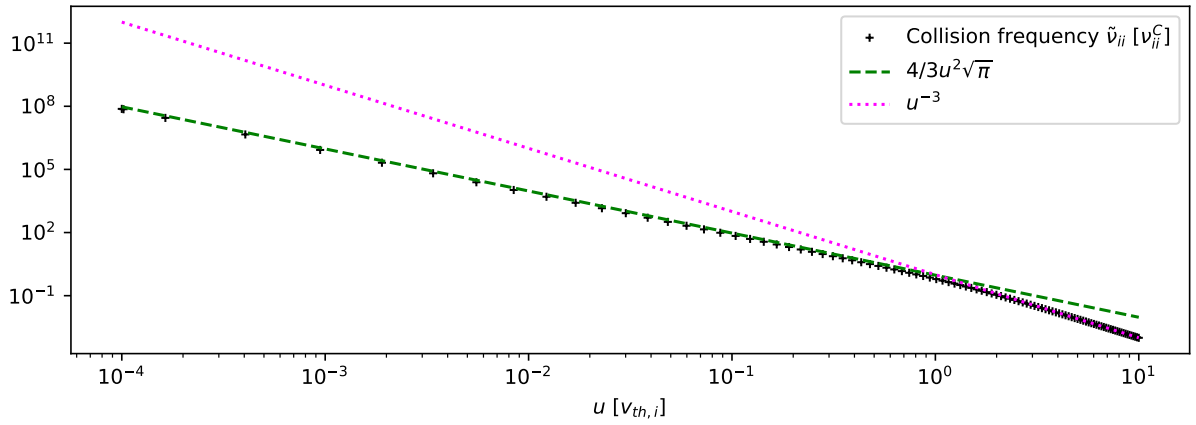

Figure 4.3: Test result for ion-ion collision frequency $\tilde{\nu}_{ii}(u)$ from `kokuchou` [77] subroutine`"test_collisional_funcs"` in `test_funcs.pf`. Asymptotes at $u \to 0$ (green, dashed) and at $u \to \infty$ (purple, dotted) shown.

of $\hat{\nu}_{ii}$ and its related terms, but as Fig.4.3 shows, care must be taken in performing numerical integration with this term due to the logarithmic growth of $\tilde{\nu}_{ii}(u)$ as $u \to 0$.

The first numerical test calculates the velocity average of $\langle\hat{\nu}_{ii}\rangle_u$, used in the momentum conservation term $\hat{\tilde{U}}_{\parallel,i}$ (Eq.(2.3.49)). While $\hat{\nu}_{ii}(u)$ is divergent at $u \to 0$, the velocity average

itself $\int du\ u^4 e^{-u^2} \hat{\nu}_{ii}(u)$ is well-behaved and can be evaluated numerically. However, we seek a more accurate analytic expression for $\langle \hat{\nu}_{ii} \rangle_u$to use in the main calculation, as only $n_u \sim 20$ u-points are used, which does not provide optimal accuracy. To verify that analytic expression, we numerically calculate over $n_u = 100$ points over a logarithmically-spaced mesh ranging from $\{10^{-4}, 10^2\}$, more points and a wider range than the u-mesh used in full-scale runs for this work. Plasma parameters $\nu_\star = 0.01$ and $\epsilon = 0.1$ are used. For the analytic expression, we start by writing out $\tilde{\nu}_{jj}(u)$ explicitly, substituting for $G(u)$:

$$\tilde{\nu}_{jj}(u) = \frac{\mathrm{erf}(u) - \frac{\mathrm{erf}(u) - u\,\mathrm{erf}'(u)}{2u^2}}{u^3} = \frac{\mathrm{erf}(u)}{u^3} + \frac{e^{-u^2}}{\sqrt{\pi} u^4} - \frac{\mathrm{erf}(u)}{2u^5}. \tag{4.1.4}$$

Recall the normalised velocity-average operator, Eq.(2.2.20):

$$\langle ... \rangle_u = \frac{8}{3\sqrt{\pi}} \int_0^\infty u^4 e^{-u^2} du \tag{4.1.5}$$

then the velocity-average of $\hat{\nu}_{ii}(u) = \epsilon^{3/2} \nu_\star \tilde{\nu}_{jj}$ is:

$$\langle \hat{\nu}_{ii}(u) \rangle_u = \frac{8\epsilon^{3/2}\nu_\star}{3\sqrt{\pi}} \int_0^\infty u e^{-u^2}\,\mathrm{erf}(u) + \frac{e^{-2u^2}}{\sqrt{\pi}} - \frac{e^{-u^2}\,\mathrm{erf}(u)}{2u} du$$

Using the standard integrals given in Sec.8.1:

$$\int_0^\infty u e^{-u^2}\,\mathrm{erf}(u) = \frac{1}{2\sqrt{2}}\ , \qquad \int_0^\infty e^{-2u^2} = \frac{1}{2}\sqrt{\frac{\pi}{2}}\ , \qquad \int_0^\infty u^{-1} e^{-u^2}\,\mathrm{erf}(u) = \ln(1+\sqrt{2}),$$

the analytic expression for the velocity-averaged collision frequency is:

$$\begin{aligned} \langle \hat{\nu}_{ii}(u) \rangle_u &= \frac{8\epsilon^{3/2}\nu_\star}{3\sqrt{\pi}} \left(\frac{1}{2\sqrt{2}} + \frac{1}{2\sqrt{\pi}} \sqrt{\frac{\pi}{2}} - \frac{1}{2} \ln(1+\sqrt{2}) \right) \\ &= \frac{4\epsilon^{3/2}\nu_\star}{3\sqrt{\pi}} \left(\sqrt{2} - \ln(1+\sqrt{2}) \right) \end{aligned} \tag{4.1.6}$$

During testing, using typical values for $\nu_\star = 0.01, \epsilon = 0.1$ and evaluating the integral numerically over the u-mesh, comparing the numerical result with Eq.(4.1.6):

```
Analytic result for nu_ii_ave =     1.267537E-004
Numerical result for nu_ii_ave =    1.267610E-004
```

Listing 4.1: `kokuchou` code output stream, displaying values of the speed-averaged collisionality that are compared during unit testing.

While the numerical result is in agreement with the analytic result to 0.5%, this is obtained using $n_u = 100$ points, and since n_u is typically lower in a full-size simulation, it is more appropriate to use the analytic expression Eq.(4.1.6) for $\langle \hat{\nu}_{ii} \rangle_u$ within the code. Nonetheless, using both the analytic and numerical evaluations of the expression within this test helped to validate its representation in the code.

The second test case using $\tilde{\nu}_{ii}(u)$ is to numerically determine the neoclassical ($\epsilon \ll 1$ banana regime) poloidal flow coefficient k_{neo}, which recalling Eq.(2.5.6) contains two separate velocity-averaged functions containing $\tilde{\nu}_{ii}$:

$$k_{neo} = \frac{\left\langle (u^2 - \frac{5}{2})\tilde{\nu}_{ii} \right\rangle_u}{\langle \tilde{\nu}_{ii} \rangle_u} \simeq -1.173... \ , \tag{4.1.7}$$

where the above value is given in Ref.[17], Eq.(11.26). Within the unit test `test_funcs.pf`, the numerical result to 5 decimal places is `k_neo = -1.1730`, in agreement with the result from the literature.

4.1.3 Velocity volume integral

Recall Eq.(2.2.16), presented here in normalised units ($n_s \pi^{-3/2} v_{\mathrm{th},i}^{-3}$):

$$\{...\}_u = \int d^3\boldsymbol{v} = \frac{b}{\sqrt{\pi}} \sum_\sigma \int_0^\infty du\, u^2 \int_0^{b^{-1}} \frac{dy}{\sqrt{1 - yb}}.$$

In stage (7) of the algorithm (see Fig.3.1), this operator provides the density n_i, flow $u_{\parallel,i}$ and momentum-conserving collision operator term $\bar{u}_{\parallel,i}$ (whose θ-average at fixed p is $\hat{\bar{U}}_\parallel$) from the ion distribution function. This numerical integral is evaluated at each point in $\{x, \xi, \theta\}$-space, which also requires remapping of $\hat{g} + p\hat{F}'_{\mathrm{M}s}$ from $\{p, \xi\}$-space. A further challenge is dealing with the divergent factor $(1 - yb)^{-1/2}$ near $y \to b^{-1}$. Numerical error in the result must be minimised to avoid computational instability between iterations. To validate this calculation and determine its relative error, unit tests for $\{...\}_u$ within `test_plasma_qty.pf` of `kokuchou` [77] involved using the 0^{th}-order perturbed ion distribution $p\hat{F}_{\mathrm{M}s}$ to calculate the ion density, flow and momentum-conserving flow respectively:

$$n_i(p\hat{F}'_{\mathrm{M}s}) = \left\{ p\hat{F}'_{\mathrm{M}s} \right\}_u , \qquad u_{\parallel,i}(p\hat{F}'_{\mathrm{M}s}) = v_\parallel(u) \left\{ p\hat{F}'_{\mathrm{M}s} \right\}_u , \qquad \bar{u}_{\parallel i}(p\hat{F}'_{\mathrm{M}s}) = \frac{v_\parallel(u)\hat{\nu}_{ii}(u)}{\pi^{3/2} \langle \hat{\nu}_{ii} \rangle_u} \left\{ p\hat{F}'_{\mathrm{M}s} \right\}_u ,$$

where $p = x - \hat{\rho}_{\theta,i} v_\parallel$ (see Eq.(2.3.44)), and $\hat{F}'_{\mathrm{M}s}(u) = L_n^{-1}(1 + \eta(u^2 - \frac{3}{2}))e^{-u^2}$. These unit tests used $n_y = 89$ and $n_u = 20$ mesh points. Uniform x and p meshes are used, with $n_x = 55$, $n_p = 55$ over an extent of size $\pm 11\hat{w}$.

In $\{x, \xi, \theta\}$-space, the $\sum_\sigma \sigma$ operator will eliminate any even σ^n terms, retain any odd σ^n terms, and introduce an additional factor 2. For n_i, the x survives while for $u_{\parallel,i}$ and $\bar{u}_{\parallel i}$ the factor $v_\parallel$ survives. Starting with density $n_i(p\hat{F}'_{\mathrm{M}s})$, the only odd-$\sigma$ term in p is x:

$$\begin{aligned} n_i(p\hat{F}'_{\mathrm{M}s}) &= \frac{b}{\sqrt{\pi}} \sum_\sigma \int_0^\infty du\ u^2 \int_0^{b^{-1}} \frac{p\hat{F}'_{\mathrm{M}s} dy}{\sqrt{1-yb}} \\ &= \frac{b}{\sqrt{\pi}} L_n^{-1}(2) \int_0^\infty du\ u^2 (1 + \eta(u^2 - \frac{3}{2}))e^{-u^2} \left[\frac{2x}{b}\sqrt{1-yb}\right]_0^{b^{-1}} \\ &= \frac{4}{\sqrt{\pi}} L_n^{-1} x \int_0^\infty du\ \left(1 - \frac{3}{2}\eta\right) u^2 e^{-u^2} + \eta u^4 e^{-u^2} \\ &= \frac{4}{\sqrt{\pi}} L_n^{-1} x \left[\left(1 - \frac{3}{2}\eta\right)\frac{\sqrt{\pi}}{4} + \eta\frac{3\sqrt{\pi}}{8}\right] \\ &= L_n^{-1} x \end{aligned} \tag{4.1.8}$$

Taking $\hat{L}_n = -1$, the numerical result for $n_i(p\hat{F}'_{\mathrm{M}s})$ was tested to be with this analytic result within `test_plasma_qty.pf` to within 1% error. These are plotted in Fig.4.4a. The absolute difference between the numerical and analytic results is shown in Fig.4.4b, which indicates less than 1% relative error at all x-points, satisfying the test.

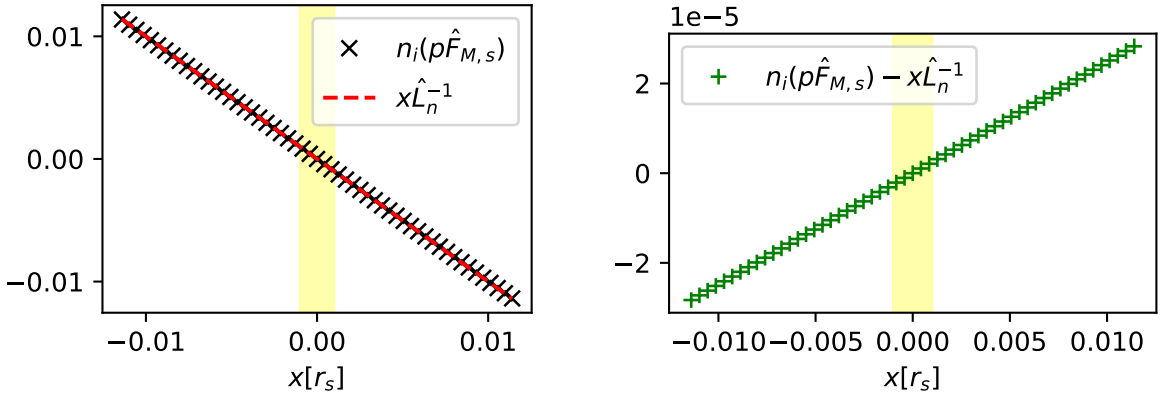

(a) Numerical and analytic $n_i(p\hat{F}'_{\mathrm{M}s})$.

(b) Difference in numerical and analytic $n_i(p\hat{F}'_{\mathrm{M}s})$.

Figure 4.4: Numerical result for ion density $n_i(p\hat{F}'_{\mathrm{M}s})$ and its analytic form $x\hat{L}_n^{-1}$ plotted vs x, from unit test `"test_update_density_flow_ubarpll"` of `test_plasma_qty.pf`. Island half-width $\hat{w} = \hat{\rho}_{\theta,i} = 0.001 r_s$, $\epsilon = 0.1$.

Next, for the perturbed flow $u_{\parallel,i}(p\hat{F}'_{\mathrm{M}s})$, due to the introduction of factor $v_\parallel$ (that also cancels

the denominator $\sqrt{1-yb}$), the term in p that survives is $-\hat{\rho}_{\theta,i}v_{\parallel}$. Starting with the y-integral, using the y-integral for $v_{\parallel}$ given in 8.1.12:

$$\begin{aligned} u_{\parallel,i}(p\hat{F}'_{\mathrm{M}s}) &= \frac{b}{\sqrt{\pi}}\sum_{\sigma}\sigma\int_0^{\infty}du\ u^3\int_0^{b^{-1}}dy\ p(y,\sigma,v)\hat{F}'_{\mathrm{M}s}(u) \\ &= \frac{b}{\sqrt{\pi}}\sum_{\sigma}\sigma\int_0^{\infty}du\ u^3\hat{F}'_{\mathrm{M}s}\left(\frac{-2\hat{\rho}_{\theta,i}\sigma v}{3b}\right) \\ &= \frac{-2\hat{\rho}_{\theta,i}}{3\sqrt{\pi}}\sum_{\sigma}\sigma^2\int_0^{\infty}du\ u^4\hat{F}'_{\mathrm{M}s} \\ &= \frac{-4\pi\hat{\rho}_{\theta,i}}{3}\int_0^{\infty}du\ u^4\hat{F}'_{\mathrm{M}s} \end{aligned}$$

Next, focusing only on the u-integral, using the identities given in the Appendix Eq.(8.1.1):

$$\begin{aligned} \int_0^{\infty}du\ u^4\hat{F}'_{\mathrm{M}s}(u) &= L_n^{-1}\int_0^{\infty}du\ \omega_T(u)u^4e^{-u^2} = L_n^{-1}\int_0^{\infty}du\ (1+\eta u^2-\frac{3}{2}\eta)u^4e^{-u^2} \\ &= L_n^{-1}\left[(1-\frac{3}{2}\eta)\frac{3\sqrt{\pi}}{8}+\eta\frac{15\sqrt{\pi}}{16}\right] \\ &= L_n^{-1}\frac{3\sqrt{\pi}}{8}(1+\eta), \end{aligned}$$

and inserting the above into the full expression gives:

$$u_{\parallel,i}(p\hat{F}'_{\mathrm{M}s}) = \frac{-1}{2}\hat{\rho}_{\theta,i}L_n^{-1}(1+\eta) \tag{4.1.9}$$

For $\hat{\rho}_{\theta,i} = 10^{-3}r_s$, $\hat{L}_n = -1$ and $\eta = +1$, this result gives $u_{\parallel,i}(p\hat{F}'_{\mathrm{M}s}) = 10^{-3}$. Within the unit test, the numerical result is 9.857×10^{-4}, which is $\sim 2\%$ of the analytic result.

Finally, the analytic expression for $\bar{u}_{\parallel i}(p\hat{F}'_{\mathrm{M}s})$ is calculated. Similar to Eq.(4.1.9), but with a different prefactor and a $\hat{\nu}_{ii}(u)$ term in the u-integral. Start by using the same result for the y-integral as in $u_{\parallel,i}(p\hat{F}'_{\mathrm{M}s})$, noting also that $\sum_{\sigma}\sigma^2 = +2$:

$$\begin{aligned} \bar{u}_{\parallel,i}(p\hat{F}'_{\mathrm{M}s}) &= \frac{b(\theta)}{\sqrt{\pi}\left\langle\hat{\nu}_{ii}\right\rangle_u}\sum_{\sigma}\sigma\int_0^{\infty}du\ u^3\hat{\nu}_{ii}(u)\int_0^{b^{-1}}dy\ p(y,\sigma,v)\hat{F}'_{\mathrm{M}s}(u) \\ &= \frac{-4\hat{\rho}_{\theta,i}}{3\sqrt{\pi}\left\langle\hat{\nu}_{ii}\right\rangle_u}\int_0^{\infty}du\ u^3\hat{\nu}_{ii}(u)\hat{F}'_{\mathrm{M}s}(u) \end{aligned}$$

Where $\hat{\nu}_{ii}(u) = \epsilon^{3/2}\nu_{\star}\frac{\mathrm{erf}(u)-G(u)}{u^3}$, as in Eq.(2.2.17). For the u-integral, the u-dependent terms are

u^3, u (from p), $\hat{\nu}_{ii}(u)$ and $\hat{F}'_{\mathrm{M}s}(u)$:

$$\int_0^\infty du\ u^4 \hat{\nu}_{ii}(u) \hat{F}'_{\mathrm{M}s}(u)$$
$$= \epsilon^{3/2} \nu_\star L_n^{-1} \int_0^\infty du\ v \left(\mathrm{erf}(u) + \frac{\mathrm{erf}'(u)}{2v} - \frac{\mathrm{erf}(u)}{2u^2} \right) (1 + \eta u^2 - \frac{3}{2}\eta) e^{-u^2}$$

Expanding the terms, using the standard definite integrals given in the Appendix, 8.1:

$$= \epsilon^{3/2} \nu_\star L_n^{-1} \int_0^\infty du\ \left(1 - \frac{3}{2}\eta\right) \overbrace{v e^{-u^2} \mathrm{erf}(u)}^{=\frac{1}{2\sqrt{2}}} + \left(1 - \frac{3}{2}\eta\right) \frac{1}{\sqrt{\pi}} \overbrace{e^{-2u^2}}^{=\frac{\sqrt{\pi}}{2\sqrt{2}}} - \left(1 - \frac{3}{2}\eta\right) \frac{1}{2} \overbrace{u^{-1} e^{-u^2} \mathrm{erf}(u)}^{=\ln(1+\sqrt{2})}$$
$$+ \eta \underbrace{u^3 e^{-u^2} \mathrm{erf}(u)}_{=\frac{5}{8\sqrt{2}}} + \frac{\eta}{\sqrt{\pi}} \underbrace{u^2 e^{-2u^2}}_{\frac{\sqrt{\pi}}{8\sqrt{2}}} - \frac{\eta}{2} \underbrace{v e^{-u^2} \mathrm{erf}(u)}_{=\frac{1}{2\sqrt{2}}}$$

$$\Rightarrow \int_0^\infty du\ u^4 \hat{\nu}_{ii}(u) \hat{F}'_{\mathrm{M}s}(u) = \frac{\epsilon^{3/2} \nu_\star L_n^{-1}}{2} \left[(1-\eta)\sqrt{2} + \left(\frac{3}{2}\eta - 1\right) \ln(1+\sqrt{2}) \right]$$

Then:

$$\bar{u}_{\parallel,i}(p\hat{F}'_{\mathrm{M}s}) = \frac{-2\hat{\rho}_{\theta,i} \epsilon^{3/2} \nu_\star L_n^{-1}}{3\sqrt{\pi} \left\langle \hat{\nu}_{ii} \right\rangle_u} \left[(1-\eta)\sqrt{2} + \left(\frac{3}{2}\eta - 1\right) \ln(1-\sqrt{2}) \right] \tag{4.1.10}$$

For $\epsilon = 0.1$, $\hat{\rho}_{\theta,i} = 10^{-3} r_s$, $\nu_\star = 10^{-3}$ and using the analytic result for $\left\langle \hat{\nu}_{ii} \right\rangle_u$ given in Eq.(4.1.6), the analytic expression for $\bar{u}_{\parallel,i}(p\hat{F}'_{\mathrm{M}s}) = 4.1353 \times 10^{-4}$, while the numerically-calculated result is 4.1304×10^{-4}, which is within 1% relative error. These tests demonstrate the validity and accuracy of the velocity volume integral calculation within `kokuchou`. The $O(1\%)$ errors in the numerical calculation of the $\left\{ p\hat{F}'_{\mathrm{M}s} \right\}_u$ contribution to density and flow can be avoided by using these analytic expressions in place of numerical calculation; this has since been implemented in the main code. However, $\hat{g}$ continues to be calculated numerically, and will likely produce errors of similar scale in its own density and flow contributions, assuming these errors are primarily numerical in origin.

4.1.4 Testing the shooting algorithm

The shooting algorithm of `kokuchou` and `DK-NTM` operate by applying boundary conditions in $\dfrac{\partial^2 \hat{g}}{\partial y^2}$ at the y-mesh limits, then solving the matrix equation 3.1.14 at each y-point towards $y = y_c$ to obtain $\underline{\boldsymbol{\alpha}}$ and $\boldsymbol{\beta}$ there. An issue encountered previously in `DK-NTM` and early versions of `kokuchou`

was that the boundary conditions were not implemented correctly. To address this, a special case was developed as a unit test within `kokuchou` in `test_solution.pf`, using the same procedures for calculating $\underline{\boldsymbol{\alpha}}$ and $\boldsymbol{\beta}$ as in the main program. Here, a different equation without most of the NTM physics is used, but the numerical procedures are the same as those in the full calculation.

In this test, a 1D simulation domain with $y = \{0, 2\}$ where $n_y = 33$ (indexed $l = \{1, 33\}$), with an internal boundary $y_c = 1$ (index 17) and 16 uniformly-spaced points either side. A simple exponential decay boundary value problem is solved, given by:

$$\frac{\partial \hat{g}}{\partial y} - f(y)\hat{g}(y) = 0 \ , \qquad \left.\frac{\partial^2 \hat{g}}{\partial y^2}\right|_{y=0,2} = 0 \ ; \quad \hat{g}(y = y_c) = 1.5 \tag{4.1.11}$$

where $f(y) = 1/g(y)$ from the previous iteration. By numerically solving for the equation via an iterative procedure, similar to how $\hat{\Phi}$ and $\hat{\tilde{U}}_{\|}$ are treated in the full algorithm, the equation should converge on a solution. The solution can be derived analytically to be:

$$\hat{g}(y) = \exp\left(1 - y + \ln(\hat{g}(y = y_c))\right) \tag{4.1.12}$$

The problem involves iteratively calculating Eq.(4.1.11) for $f(y)$ using the passing region matrix equations left of the $y = y_c$ boundary and trapped equations to the right. Here, $f(y) = -\hat{g}(y)$ of the previous iteration. There is no $\{\xi, p\}$ dependence and the matrices/vectors are of rank 1, making $\underline{\boldsymbol{\alpha}}$ and $\boldsymbol{\beta}$ scalars at each y-point. The purpose of this test is to check whether $\underline{\boldsymbol{\alpha}}$ and $\boldsymbol{\beta}$ are calculated correctly from the matrix equations described in 3.1.3, and if boundary conditions are being correctly imposed at the y-limits. The initial guess for $f(y) = -\hat{g}(y_c) = -1.5$.

Similar to the full algorithm, the passing forms of $\underline{\boldsymbol{\alpha}}$ and $\boldsymbol{\beta}$ (Eq.(3.1.23)) are calculated over the range $y = \{0 \rightarrow y_c\}$ (not including y_c) and the trapped forms (Eq.(3.1.25)) are calculated over $y = \{y_c \leftarrow 2\}$. Next, at $y = y_c$, $\hat{g}(y = y_c)$ is explicitly set to 1.5, and $\hat{g}$ is solved separately across $y = \{0 \leftarrow y_c\}$ via Eq.(3.1.22) and $y = \{y_c \rightarrow 2\}$ via Eq.(3.1.24). Once $\hat{g}(y)$ is found across all y, then we set $f(y) = -g(y)$ and repeat the procedure until the solution has 'converged', i.e., the residual $\mathcal{R}(\hat{g}(y)) < 10^{-3}$ at all y, where $\mathcal{R}$ is given by Eq.(3.1.5). Finally, the converged result for $g(y)$ is compared with Eq.(4.1.12), and the unit test checks if there is agreement with the expected analytic result at all points to within 1% error. Fig.4.5 shows the result of this test, where Fig.4.5a shows the profiles of $\hat{g}$ on the first and last (converged) iterations with the expected result also plotted, and Fig.4.5b showing the two values of $\hat{g}$ at the y-limits versus iteration number.

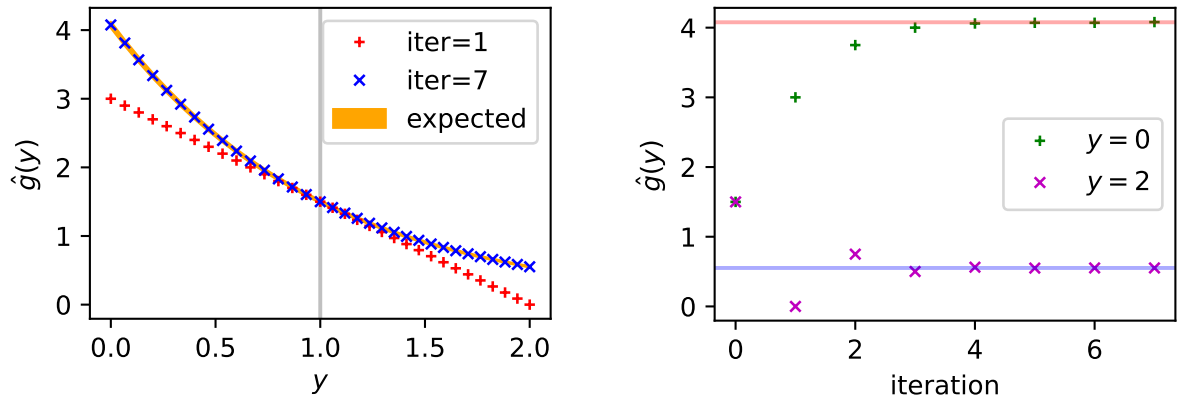

(a) Profile of $\hat{g}(y)$ at first and last iteration (7) from this unit test. Value at $y = y_c = 1.0$ shown by vertical line, which is constant at all iterations.

(b) Values of $\hat{g}(y = 0)$ and $\hat{g}(y = 2)$ vs. iteration number from this unit test. Expected values shown by solid lines.

Figure 4.5: Results from the boundary value problem unit test within the `kokuchou` simulation code to test the forms of matrix $\underline{\boldsymbol{\alpha}}$ and vector $\boldsymbol{\beta}$ used in the shooting algorithm, by solving Eq.(4.1.11) for $\hat{g}(y)$.

Here $g(y)$ did satisfy the convergence criterion at all y after 7 iterations, with all points lying well within 1% of the expected function shown by the orange region in Fig.4.5a. Both endpoints of $\hat{g}(y)$ converged towards their expected values in Fig.4.5b, the $y = 2$ point showing a slightly different trend between iterations than the $y = 0$ point having overshot the expected value on iteration 1, but importantly these results indicate that the boundary conditions in y are upheld.

4.2 New solution method for the trapped-passing boundary

During development of `kokuchou` it was found that, given a fixed set of parameters, the result for $\hat{g}$ varied significantly by a large degree between machines. Furthermore, the distribution of $\hat{g}(u)$ also displayed large non-physical noise shown in Fig.4.6, rather than a smooth continuous curve as expected. This critical issue rendered any iterated result invalid, as both $\hat{\Phi}$ and $\hat{\bar{U}}_{\parallel,i}$ depend on the integral of $\hat{g}$ in u-space.

The issue originated within the calculation of $\hat{g}$ at the trapped-passing boundary. Here, Eq.(3.1.4) was solved using the LAPACK procedure `DGESV`, a lower-upper (LU) decomposition with partial pivoting, as used previously in `DK-NTM`[72]. The properties of the individual matrix and vector terms were investigated, which found that the matrix[1] $\mathbf{A}$ was highly ill-conditioned.

[1]This is a large rank $n_\xi n_p \sim O(1000)$ dense square matrix whose diagonal values are often 10 or more of orders of magnitude larger than its smallest terms elsewhere.

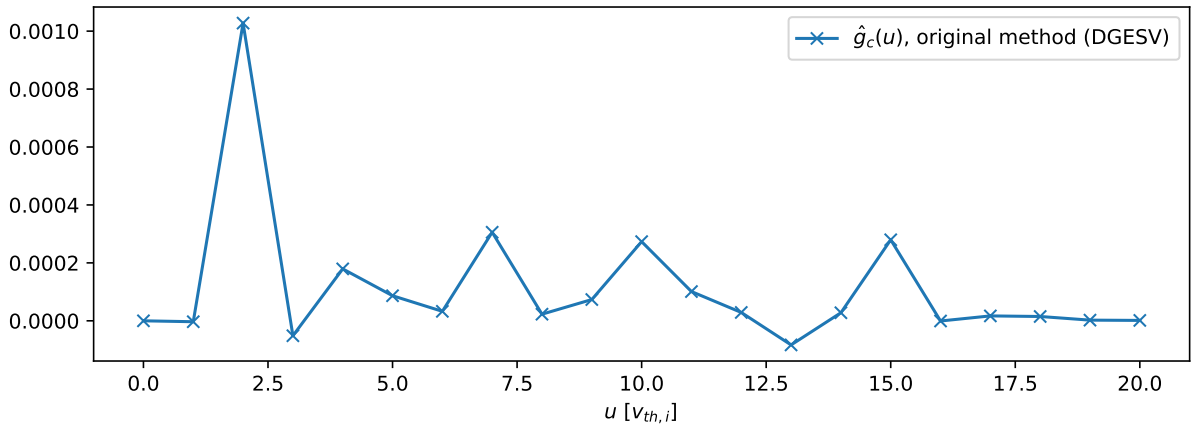

Figure 4.6: Perturbed ion distribution $\hat{g}$ versus speed u at $\xi = 0, p = 0.050 r_s, y = y_c, \sigma = -1$, using a simple LU-decomposition method in solving the linear matrix equation Eq.(3.1.4).

Fig.4.6 was obtained from a small-scale run of `kokuchou` v10.4.1 on the York Plasma Institute computer. Here, the original `DGESV` algorithm is substituted for `DGESVX`[2], which yields the *reciprocal condition number* `rcond` for matrix $\underline{\mathbf{A}}$. A lower `rcond` indicates greater ill-conditioning and numerical error in the LU-factorisation. Very small values of "rcond" close to the floating point precision (in this case, 10^{-16} for a double precision float) corresponds to a near-total loss of precision in the matrix equation solution, creating the 'noise' observed in $\hat{g}(u)$. Separately, the determinant, det($\underline{\mathbf{A}}$), was also calculated by using the LAPACK procedure `DGETRF` on a copy of $\underline{\mathbf{A}}$ to compute the LU-factorisation, then calculating the product of all diagonal points in the factorisation, accounting for row exchanges with sign changes. This procedure for calculating the determinant has been unit-tested[3]. Values of `rcond` and det($\underline{\mathbf{A}}$) were then extracted, as shown in Listing 4.2 which are representative of all u-space (index `"iv"`) in a `kokuchou` simulation.

```
... iv =  2] >> g_tpbdry rcond =    3.02187E-16, detA =  -0.00000E+00
... iv =  3] >> g_tpbdry rcond =    5.11790E-19, detA =      Infinity
... iv =  4] >> g_tpbdry rcond =    2.74914E-17, detA =      Infinity
...
... iv = 20] >> g_tpbdry rcond =    4.01716E-18, detA =      Infinity
... iv = 21] >> g_tpbdry rcond =    6.95110E-18, detA =     -Infinity
```

Listing 4.2: `kokuchou` code output stream showing matrix properties of $\underline{\mathbf{A}}$ from Eq.(3.1.4).

[2] `DGESVX` additionally refines the solution $\hat{g}_c$, though here we are concerned only with the factorisation of $\underline{\mathbf{A}}$ which is not affected by refinement.

[3] The numerically-derived determinant is calculated in subroutine `test_solve` of `test_solution.pf`, where it correctly obtains the expected determinant of an example rank 3×3 matrix problem to within 10^{-14} accuracy.

From the invalid determinants alone, it is clear this LU-factorisation of $\underline{\mathbf{A}}$ will not produce a valid inverse if numerically evaluated. The only non-infinite value of $\det(\underline{\mathbf{A}}) = 0$ indicates singularity. The values of `rcond` are notably below machine-precision ($\approx 10^{-16}$) at all u-points. The sensitivity of the ill-conditioned equation to machine precision-scale changes, such as the hardware and implementation, would explain the variation of the erroneous result between machines. We note that this issue was not previously observed in `DK-NTM`, however fixing separate numerical issues did reproduce the issue in that code [72].

4.2.1 Truncated singular value decomposition (TSVD)

If the numerical representation of matrix $\underline{\mathbf{A}}$ of Eq.(3.1.4) is singular and ill-conditioned, the equation cannot be solved accurately. The LU-decomposition method was then replaced with a singular value decomposition (SVD) method using the `DGESDD` algorithm of LAPACK. This performed the factorisation $\underline{\mathbf{A}} = \underline{\mathbf{U}}\underline{\mathbf{\Sigma}}\underline{\mathbf{V}}^T$, where $\underline{\mathbf{\Sigma}}$ is a diagonal matrix containing the *singular values* of $\underline{\mathbf{A}}$, transformed by two separate matrices $\underline{\mathbf{U}}$ and $\underline{\mathbf{V}}$. Specifically, the non-zero elements of $\underline{\mathbf{\Sigma}}$ are the square roots of eigenvalues of $\underline{\mathbf{A}}^*\underline{\mathbf{A}}$ and $\underline{\mathbf{A}}\underline{\mathbf{A}}^*$. However, introducing the SVD method alone did not fully eliminate the numerical artifacts. Instead, a *truncated SVD* (TSVD) method was required, in which only the largest singular values in $\underline{\mathbf{\Sigma}}$ are retained and the rest are truncated (zeroed). In our TSVD implementation, we retained most of these elements of $\underline{\mathbf{\Sigma}}$ (to keep the factorisation as close to $\underline{\mathbf{A}}$ as possible), but discarded those below a very small tolerance value we denote `trunc`. As a starting point, this value was set to `trunc` $= 10^{-7}$.Despite being a relatively low tolerance level, this was sufficient to filter the singular values from $\underline{\mathbf{\Sigma}}$ that caused the noise artifacts. The result of both SVD and truncated SVD methods in $g(u)$ is shown in Fig.4.7:

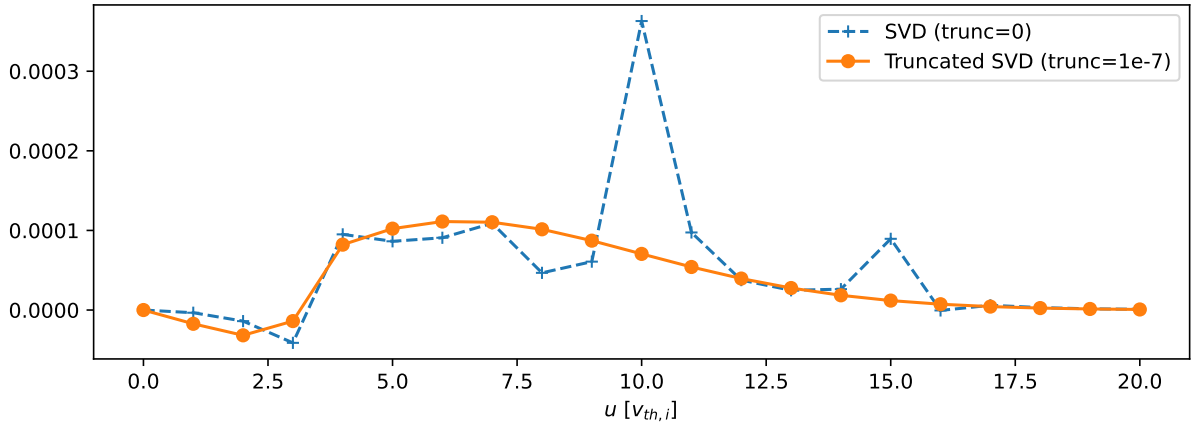

Figure 4.7: As in Fig.4.6, using new SVD and truncated SVD implementations.

In practice, it was also found that only one value of $\underline{\mathbf{\Sigma}}$ was truncated, as all others were of $O(0.1) - O(100)$, meaning the solution $\mathbf{g}_c$ could be re-inserted into Eq.(3.1.4) to reconstruct $\mathbf{B}$ to a very high degree of accuracy. This reinsertion of $\mathbf{g_c}$ from TSVD was unit-tested within subroutine `test_solve` of `test_solution.pf` on a small matrix problem to within $O(10^{-12})$ absolute error. While the use of TSVD rectified this issue, it is more computationally expensive than LU-decomposition[4] and hence is only used at the trapped-passing boundary. We emphasise that this issue is specific to this trapped-passing boundary calculation, likely due to the asymptotic behaviour of $v_{\|}^{-1}$-dependent equation terms, and that the matrix equations elsewhere do not display extreme ill-conditioning.

Summary

This chapter presented some of the tests used to validate stages of the newly-developed numerical code `kokuchou`, designed to solve the 4D drift-kinetic equation around a small near-threshold size magnetic island. To validate stages of the algorithm presented in Ch.3, unit tests were developed throughout development, several examples have been presented here. Tests for the numerical result for $h(\Omega)$ checked its agreement with its literature definition. Collision-dependent quantities including $\hat{\nu}_{ii}$ were tested with analytic values both from literature and new derivations from this work. The velocity volume integral operator $\{...\}_u$ was used to numerically calculate the ion density and flow using the 0^{th} order perturbed ion distribution $p\hat{F}'_{\mathrm{M}s}$, correct to no larger than $O(5\%)$ of the analytic results, using similar mesh and plasma parameters to full-size simulations presented in subsequent sections. The large size of this error led to the decision to replace numerical calculation of the $p\hat{F}'_{\mathrm{M}s}$ contribution to density and flow within the main code to instead use the analytic results. The matrix equations used in the shooting algorithm were tested with a model case with an expected result to check the application of boundary conditions in y. Together, these tests helped to develop confidence in the full-scale result of the new code `kokuchou`. They also helped to identify and address critical issues that were not previously observed in `DK-NTM`. Issues in the existing trapped-passing boundary procedure, for example, were resolved by diagnosing the ill-conditioning of the matrix equation there and replacing the procedure with a new truncated SVD method.

[4]The BLAS/LAPACK SVD solver `DGESVD` has $6.67 \times N^3$ operations (in full) compared to $0.67 \times N^3$ for `DGESV` according to Table 3.13 of the LAPACK user guide [79].

Chapter 5

Single run case studies

As part of Objective (2), presented in this chapter are numerical results from four full-scale runs of `kokuchou` v10.4.1 [77], at two values in collisionality $\nu_\star = \{0.005, 0.02\}$ and two values in island width $\hat{w} = \{0.3, 0.75\}\hat{\rho}_{\theta,i}$, for ion poloidal gyroradius $\hat{\rho}_{\theta,i} = 0.001 r_s$. These two collisionalities are extremes of the full parameter scan later in Ch.6, while the two $\hat{w}/\hat{\rho}_{\theta,i}$ values represent islands near and above the ion banana width $\hat{\rho}_{b,i} = \epsilon^{3/2}\hat{\rho}_{\theta,i} \approx 0.316\hat{\rho}_{\theta,i}$ respectively.

The plasma parameters used in this work are (except where otherwise stated): inverse aspect ratio $\epsilon = 0.1$, local safety q-factor $q_s = m/n = 2/1$, density gradient length scale $\hat{L}_n^{-1} = -1$, magnetic shear length scale $\hat{L}_q^{-1} = 1$, magnetic field strength scale $\hat{L}_B^{-1}(\theta) = -\epsilon\cos\theta$. These represent a high aspect ratio conventional tokamak plasma profile that is denser and hotter at the core than at the edge, and using similar parameters to Ref. [70]. The mesh sizes used in these runs are $n_\theta = 121$, $n_\xi = 30$, $n_p = 145$, $n_x = 337$, $n_y = 89$, $n_u = 24$ and $n_\Omega = 1000$. Each run included 4 iterations in which $\hat{g}$, $\hat{\Phi}$ and $\hat{\tilde{U}}_\parallel$ are updated self-consistently. Here, the convergence criterion described in 3.1.5 was not enforced, as these runs are exploratory and their convergence behaviour was not yet known.

From these four runs, Sec.5.1 presents the perturbed ion distribution $\hat{g}$ across ξ, p and y-space at the first and last iterations, without and with finite potential $\hat{\Phi}$ respectively. Sec.5.2 presents the density and flow moments of $\hat{g}$, and plasma quantities including the perturbed electrostatic potential $\hat{\Phi}$ from quasineutrality and momentum-conserving collision operator term $\hat{\tilde{U}}_\parallel$, both calculated self-consistently with $\hat{g}$. Finally, the parallel ion currents from the parallel flow $u_{\parallel,i}$ are shown, which will be used to determine the island growth rate. Both $\hat{\tilde{U}}_\parallel$ and $u_{\parallel,i}$ are validated by comparing the flows far from the island with the neoclassical equilibrium. Lastly, Sec.5.3 looks at two separate simulations under extreme values in $\nu_\star$ and $\hat{w}$ that failed to produce a convergent

physical result. We look for potential differences in behaviours to those seen previously in the `DK-NTM` code of Refs. [69, 70, 41] to assess how the recent changes to the 4D NTM equation in Sec.2.6 have affected the physics, where the collision frequency-dependent terms in $\frac{\partial \hat{g}}{\partial p}$ and $\frac{\partial^2 \hat{g}}{\partial p^2}$ were modified. This work is also more concerned with smaller near-threshold size islands where $\hat{w} \leq \hat{\rho}_{\theta,i}$, whereas the islands studied in Refs. [69, 70, 41] are generally larger. Comparing the two collisionalities, we also assess the effect of collisionality on the plasma response to the island, and relate this to previous comparisons of `DK-NTM` with the `RDK-NTM` code of Refs. [41, 43] that is valid in the limit of very low collisionality.

5.1 Ion distribution function

5.1.1 Profiles of $\hat{g}(p, \xi)$

Figs.(5.1) and (5.2) show the contours of the perturbed passing ion distribution $\hat{g}(p, \xi)$ for $y = 0.33$, $\sigma = +1$ and $u = v_{\mathrm{th},i}$, at iterations 1 and 4 respectively. For each figure, the p-derivative of $\hat{g}$ is also shown respectively in Figs.(5.3) and (5.4). Comparing $\hat{w} = 0.3\hat{\rho}_{\theta,i}$ and $\hat{w} = 0.75\hat{\rho}_{\theta,i}$ for a fixed $\hat{\rho}_{\theta,i}$, in all figures the ion distribution forms a 'drift island' structure resembling the island but shifted in p by a factor $O(\hat{\rho}_{\theta,i})$ due to magnetic drifts, as expected [70, 41]. For cases (a,c), where $\hat{w} = 0.3\hat{\rho}_{\theta,i}$, the shift is a factor 2.5 larger relative to the island than in (b,d) where $\hat{w} = 0.75\hat{\rho}_{\theta,i}$. The physical consequences of this shift on the island physics are discussed later in Sec.5.1.3. Comparing in $\nu_\star$, the effect of radial transport is seen. In the lower collisionality $\nu_\star = 0.005$ cases (a,b), the gradients in p surrounding the *drift island* separatrix are narrower than in the higher-collisionality $\nu_\star = 0.02$ cases (c,d) as expected. Simultaneously, the difference in $\hat{g}$ and $\dfrac{\partial \hat{g}}{\partial p}$ with $\nu_\star$ is greater between the small-island cases (a) and (c), as the collisional mean-free path is now larger with respect to the island, and any variation in $\nu_\star$ has a more significant effect on smaller islands.

Comparing by iteration, at iteration 1 where Fig.5.1 and Fig.5.3 are in the absence of electrostatic potential $\hat{\Phi}$, we see only the $\hat{w}^2 \cos\xi$ and $\hat{\nu}_{ii}\hat{\rho}_{\theta,i}$ terms of $\dfrac{\partial \hat{g}}{\partial p}$ in Eq.(2.3.47) are present. which results in a somewhat $\sin\xi$-like distribution in $\hat{g}$ across the drift island that varies in $\nu_\star$ between (a,c) with (b,d), changing the relative sizes of those two terms in $\dfrac{\partial \hat{g}}{\partial p}$. On iteration 4, as shown in Fig.5.2 and Fig.5.4, the potential $\hat{\Phi}$ is now present and introduces a contribution that competes with the other $\dfrac{\partial \hat{g}}{\partial p}$ terms. A notable difference is the presence of a 'jump' across the magnetic island in p, seen mostly in the large island cases (b,d) of Fig.5.2. The finite $\hat{\Phi}$ introduces a background contribution in p that increases $\hat{g}$ on the outboard ($p > 0$) side of the rational surface and reduces $\hat{g}$ on the inboard ($p < 0$) side, more visibly in the large-island cases (b,d). In the p-derivative, Fig.5.4 shows this contribution from $\hat{\Phi}$ is localised primarily inside the magnetic island, as contributions to $\hat{\Phi}$ come from the velocity volume integral of $\hat{g}$ in all y and u, including from drift islands whose shift is smaller and are closer to the magnetic island.

The results demonstrate that at the physical length scales observed, that the $\hat{\Phi}$-dependent $\mathbf{E} \times \mathbf{B}$ drift and magnetic drifts (that leads to 'drift island' behaviour) are the primary influences over the distribution of $\hat{g}$, while collisionality influences the ξ-asymmetry in the absence of $\hat{\Phi}$, its influence is only slight when $\hat{\Phi}$ is finite.

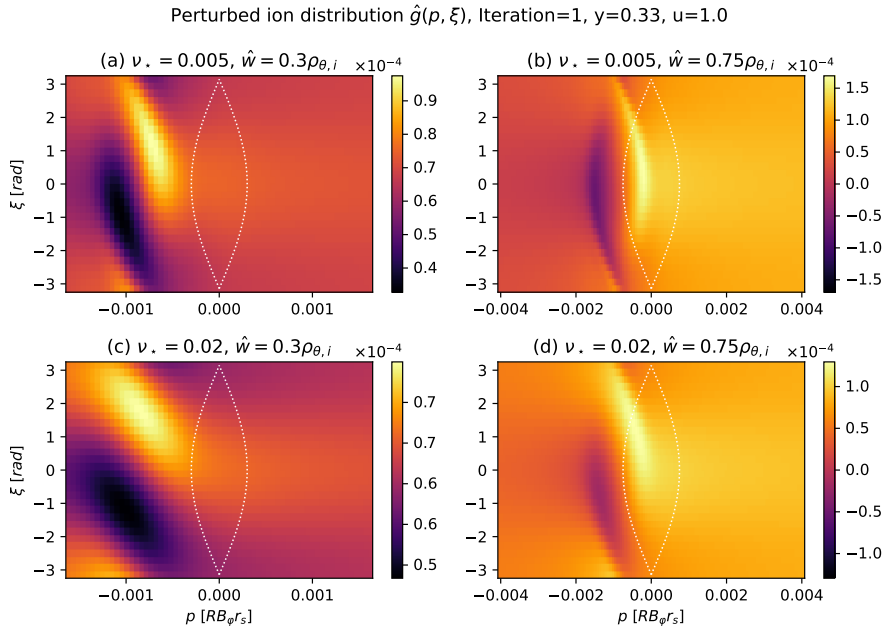

Figure 5.1: Contour plot of perturbed ion distribution $\hat{g}(p,\xi)$ at $u = 1v_{\mathrm{th}i}, \sigma = +1, y = 0.33$ on iteration 1 in absence of electrostatic potential $\hat{\Phi}$. Magnetic island shown by white dotted curve.

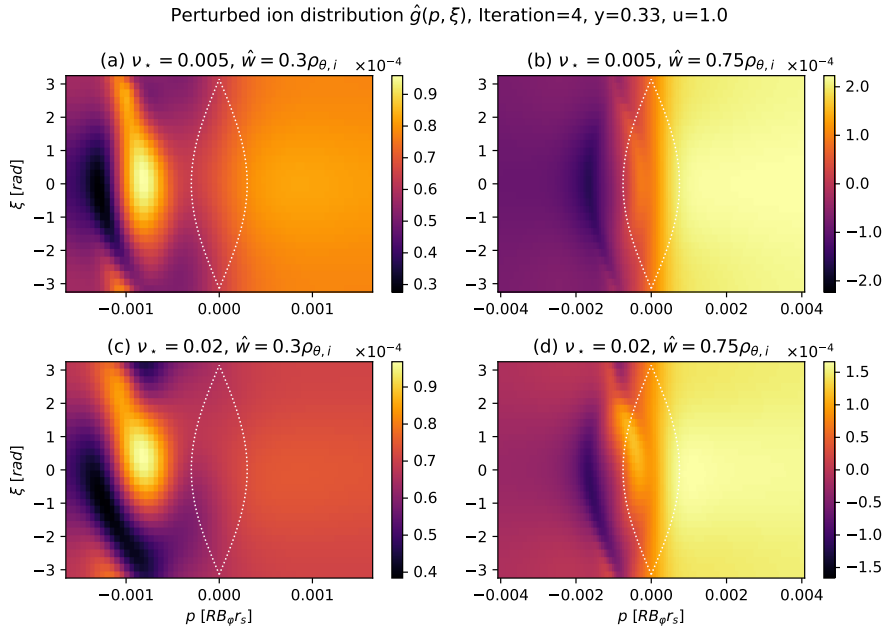

Figure 5.2: As in Fig.5.1, at iteration 4, in presence of $\hat{\Phi}$.

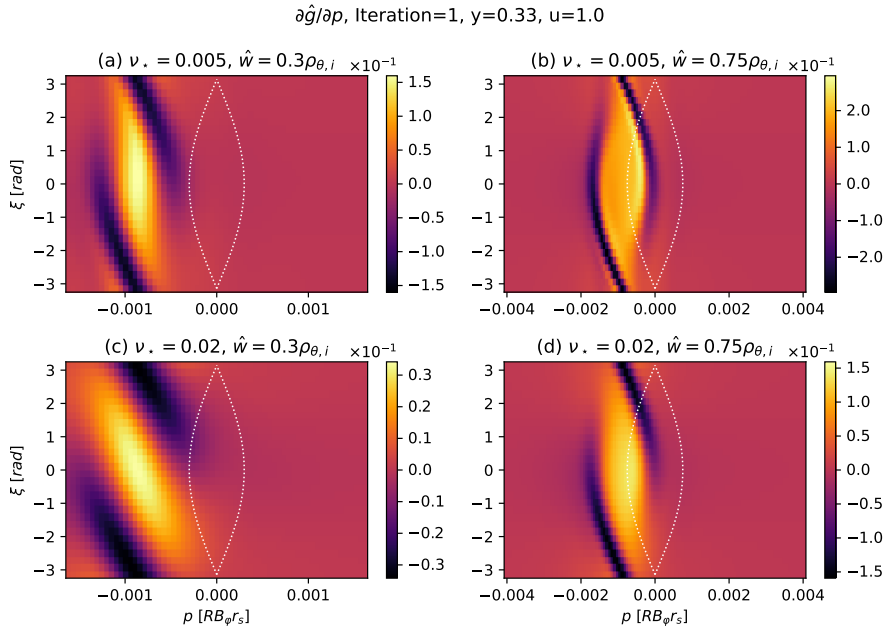

Figure 5.3: As in Fig.5.1, showing p-derivative of $\hat{g}$ in absence of $\hat{\Phi}$.

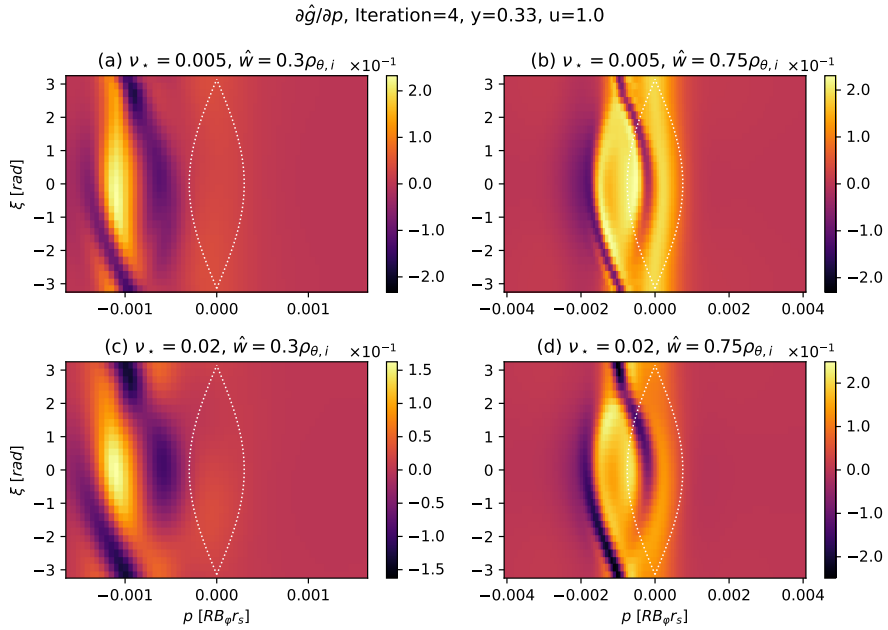

Figure 5.4: As in Fig.5.2, showing p-derivative of $\hat{g}$ in presence of $\hat{\Phi}$.

5.1.2 Profiles of $\hat{\mathbf{g}}(p, y)$ and $\hat{\mathbf{g}}(p, u)$

To study the y and u-dependence of the drift island shift in more detail, Fig.5.5 shows $\hat{g}(p, y)$ at fixed $\xi = 0$, $\sigma = +1$, $u = 1$, while Fig.5.6 shows $\hat{g}(p, u)$ at $y = 0.33$, both at iteration 4 in the presence of $\hat{\Phi}$.

In both figures, the edges of the shifted drift island are illustrated by the black dashed curve. The size of this shift is equal to the $\hat{\rho}_{\theta,i}\hat{\omega}_D\hat{L}_q^{-1}$ term of $\dfrac{\partial \hat{g}}{\partial \xi}$ within Eq.(2.3.47). Corresponding with the definition of $\hat{\omega}_D$ in Eq.(2.3.48), in Fig.5.6 the drift island shift has a linear dependence with u, while in Fig.5.5 the y-dependence is with the θ-averaged $\sqrt{1 - yb}$-dependent terms in $\hat{\omega}_D$. A similar $O(\hat{\rho}_{\theta,i})$-size drift island shift was seen in `DK-NTM` in Ref.[70] in which a similar coefficient $\hat{\rho}_{\theta,i}\hat{\omega}_D$ appears in the ξ-derivative of $\hat{g}$. Ref. [41] quotes the shift factor explicitly as $\hat{\rho}_{\theta,i}\hat{\omega}_D\hat{L}_q^{-1}$.

For $\hat{g}(p, y)$ in Fig.5.5, the drift island effect manifests differently for passing ($y < 1$) and trapped ($y > 1$) ion populations. For passing ions, the σ-dependence of $\hat{\omega}_D$ is retained, and $\hat{\omega}_D$ itself is largest in magnitude at the deeply passing end ($y = 0$). Recall Eq.(1.2.3) for the ∇B drift velocity, where field-parallel (and anti-parallel) particles whose pitch angle is zero will experience the fastest drift velocity. Because the passing particles carry the bootstrap current (see 1.3.4), the bootstrap current distribution with respect to the island (i.e. whether inside the island within the 'hole' it creates, or outside) will be significantly influenced by the drift island effect, particularly as $\hat{w}$ is reduced with respect to $\hat{\rho}_{\theta,i}$. This will be covered later in Sec.5.2.3 and Sec.6.2. In the trapped region, both σ streams are averaged, and $\hat{\omega}_D$ is smaller in magnitude as their mostly field-perpendicular guiding centre trajectories are less affected by ∇B-drift as the passing ions. The overall effect is that the trapped ion drift island, which is centred at $p = 0$ instead of at $\hat{\rho}_{\theta,i}\hat{\omega}_D\hat{L}_q^{-1}$, is broadened slightly.

It has been discussed previously in Sec.3.1.6 that a major computational challenge of the scheme used in `kokuchou` is that when $\hat{w} \gtrsim \hat{\rho}_{\theta,i}$, the 'inner region' of the p-mesh must extend to accommodate all positions of the drift island across y and u. Keeping the p-mesh number of points fixed, this would reduce the resolution of this region and the ability to resolve steep separatrix layer gradients.

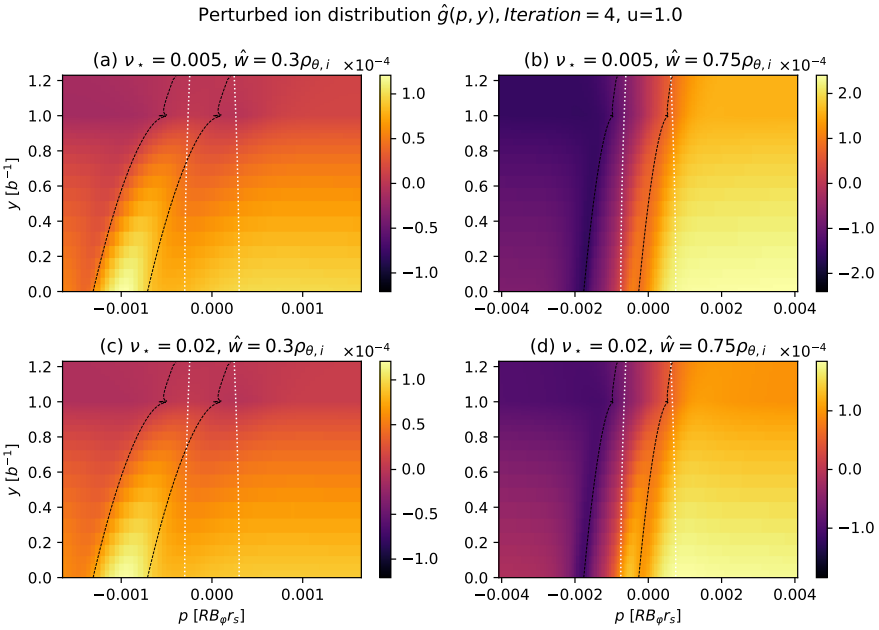

Figure 5.5: Contour plot of perturbed ion distribution $\hat{g}(p, y)$ at $u = 1v_{\mathrm{th}i}$, $\sigma = +1$, across island O-point ($\xi = 0$) on iteration 4. Magnetic island shown by white dotted curve. Drift island shift factor $\hat{\rho}_{\theta,i}\hat{\omega}_D(y, \sigma, u)\hat{L}_q^{-1} \pm \hat{w}$ shown by black dashed curve.

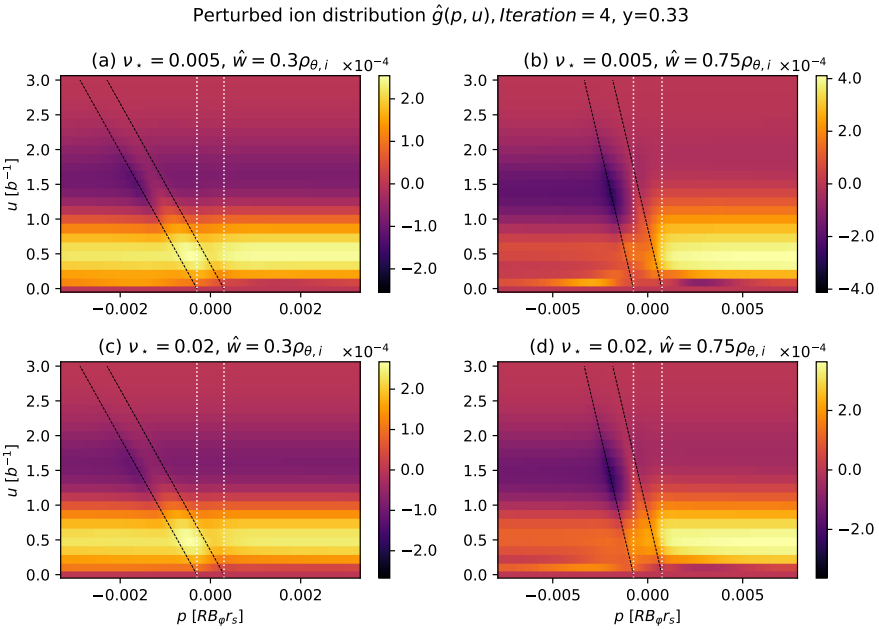

Figure 5.6: Perturbed ion distribution $\hat{g}(p, u)$ at $y = 0.33$, $\sigma = +1$, across island O-point ($\xi = 0$) on iteration 4. Magnetic island shown by white dotted curve. Drift island shift factor $\hat{\rho}_{\theta,i}\hat{\omega}_D(y, \sigma, u)\hat{L}_q^{-1} \pm \hat{w}$ shown by black dashed curve.

5.1.3 Density moments of $f_i(p)$

We now examine the effect the drift island behaviour has on the density gradient, and by extension $\hat{\Phi}$. 1D profiles of ion distributions across the island O-point $\xi = 0$ at $y = 0.33$ from these same runs are shown in Fig.5.7 and (5.8), again at iterations 1 and 4 respectively. Both figures resemble the schematic Fig.1.10 describing the physics of the drift island structures seen in $\hat{g}$ within Refs. [69, 70, 41]. Firstly, focusing on the $\sigma = \pm 1$ passing populations, in Fig.5.7 in the absence of $\hat{\Phi}$, we see a similar flattening of $\hat{g}$ across drift islands, and opposing radial shifts in each σ due to magnetic drifts represented by the $\hat{\omega}_D(y, \sigma, u)$ term of Eq.(2.3.47). The size of the shift, which is $\hat{w}$-independent, is again larger relative to the size of the island in the $\hat{w} = 0.3\hat{\rho}_{\theta,i}$ cases than the $\hat{w} = 0.75\hat{\rho}_{\theta,i}$ cases. Comparing in $\nu_\star$, the gradients of the drift island separatrix are notably smoother for the higher $\nu_\star = 0.02$ cases than the $\nu_\star = 0.005$ cases, with (c) having no flattening whatsoever compared to (a) at iteration 1.

Secondly, the σ-average of the drift island profiles combined give what we refer to as the *density moment* across the magnetic island O-point, shown by the black curve in both plots. This corresponds with the overall density gradient across the magnetic island, of which in the absence of the perturbation would resemble $p\hat{F}'_{\mathrm{M}s}$ shown by the dashed-dotted grey curve. In both figures, the density moment is flattened across the magnetic island (yellow region) for the $\hat{w}/\hat{\rho}_{\theta,i} = 2$ cases (b,d), but not for the $\hat{w} = 0.3\hat{\rho}_{\theta,i}$ cases (a,c), which roughly resemble the function $p\hat{F}'_{\mathrm{M}s}$ that the total ion distribution far from the island approaches toward. This behaviour has been documented previously in the `DK-NTM` and `RDK-NTM` codes in a comparison within Fig.C.2 of Ref. [41]. However we now also observe the effect of collisionality, which contributes to further restoration of gradient across the magnetic island by increasing cross-orbit transport in p in the $\nu_\star = 0.02$ cases.

Finally, we compare iterations 1 (Fig.5.7) and 4 (Fig.5.8), respectively without and with self-consistent $\hat{\Phi}$ that satisfies quasineutrality. In Fig.5.7, the passing ion profiles for $w = 0.3\hat{\rho}_{\theta,i}$ are flat at low collisionality, but thoroughly smoothed out at high collisionality. Here, in the absence of $\hat{\Phi}$ and $\mathbf{E} \times \mathbf{B}$ drift, cross-orbit transport is primarily influenced by the $\propto \hat{\nu}_{ii} \dfrac{\partial^2 \hat{g}}{\partial p^2}$ neoclassical diffusion term. In Eq.(5.8), the presence of $\hat{\Phi}$ has affected the vertical shift of the two passing profiles relative to $p\hat{F}'_{\mathrm{M}s}$, both being somewhat closer to $p\hat{F}'_{\mathrm{M}s}$ and having broader, more curved features after 4 iterations, likely due to the presence of $\mathbf{E} \times \mathbf{B}$ drift providing cross-field transport. These density moments directly affect the form of $\hat{\Phi}$ and vice versa, which we cover in the following section.

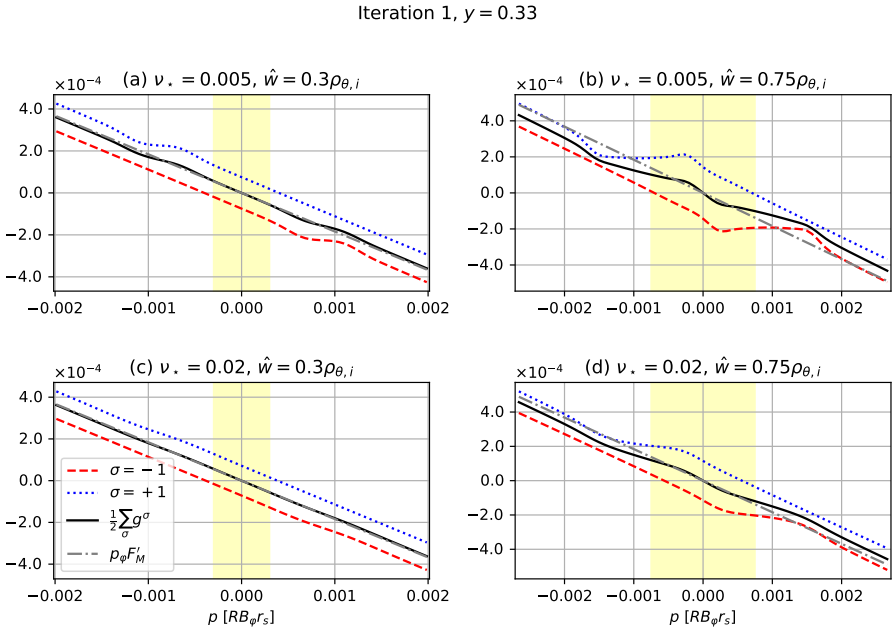

Figure 5.7: Total passing ion distribution profile $\hat{g}(p) + p\hat{F}'_{\mathrm{M}s}(u)$ across the magnetic island O-point at $\xi = 0, u = v_{th,i}, y = 0.33$. Shown are both passing streams in σ, the *density moment* given by their σ-average (black), and $p\hat{F}'_{\mathrm{M}s}$ itself (grey, dash-dot). Island indicated by the yellow region. Taken at end of iteration 1 in absence of $\hat{\Phi}$, and $\hat{\bar{U}}_\parallel = \hat{\bar{U}}_\parallel(p\hat{F}'_{\mathrm{M}})$.

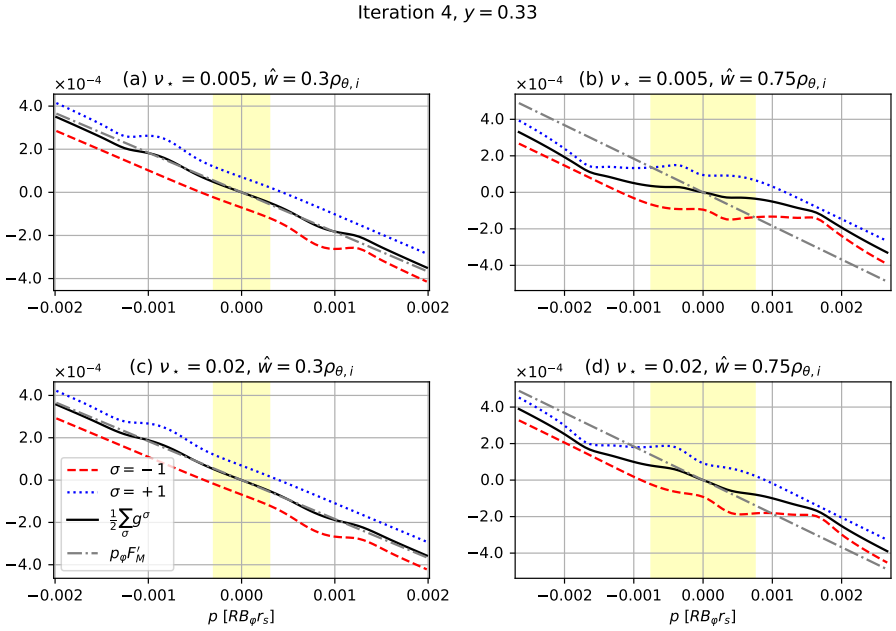

Figure 5.8: As in Fig.5.7, at iteration 4 in calculating $\hat{\Phi}$ and $\hat{\bar{U}}_\parallel$. Here, $\hat{\Phi}$ from quasineutrality is now finite.

5.2 Plasma quantities

5.2.1 Electrostatic potential $\hat{\Phi}$

Fig.5.9 shows the 2D contours of the normalised electrostatic potential $\hat{\Phi}(x, \xi, \theta = 0)$ that satisfies quasineutrality, taken at iteration 4 of each run. Fig.5.10 shows 1D profiles of $\hat{\Phi}(\xi = 0, \theta = 0)$ across the O-point in x for all 4 iterations. In cases (a-d), $\hat{\Phi}$ follows the shape of the magnetic island. The sharp boundary around the island separatrix is created by the analytic $h(\Omega)$-like contribution from electrons (see Fig.4.2), which is explicitly set to zero inside the island to represent the electron response to the much larger ion length scales of the island. The potential $\hat{\Phi}$ tends to different constants at either side far from the island due to the $\dfrac{\partial \hat{g}}{\partial p} = 0$ boundary condition, while $h(\Omega) \to x$ and $x\hat{L}_n^{-1}$ cancel each other out. Across the island, a gradient is sustained due to the drift island effect that occurs when $\hat{w} < \hat{\rho}_{\theta,i}$, which applies in all cases. The curved variations in $\hat{\Phi}(x)$ both within and just outside the magnetic island, were provided by the velocity volume integral of the *density moments* of $\hat{g}$ (see Fig.5.8), which is the part of $\hat{\Phi}$ that changed between iterations. These curved variations were more visible in (b,d), where the drift islands were closer to the magnetic island (for all y and u, see Fig.5.5 and (5.6)), increasing the spatial variation of the velocity-integral of $\hat{g}$ there. If $\hat{w} \gg \hat{\rho}_{\theta,i}$, all drift islands in y and u-space should align with the magnetic island in x-space, flattening the density profile inside the magnetic island [70, 41]. However, it is computationally challenging to explore higher $\hat{w}/\hat{\rho}_{\theta,i}$ in `kokuchou` to revisit those previous findings, as Sec.6.1 will discuss. Fig.5.10 shows how $\hat{\Phi}$ changes between iterations. Notably, the small-island cases (a,c) changed slowly between iterations, being largely unaffected by changes in $\hat{g}$. Again, this was likely due to the large drift island shift spreading out variations of the velocity-integral of $\hat{g}$ across radial space x. Conversely, the larger island cases (b,d) did change significantly between iterations, particularly far from the island, indicating higher sensitivity of $\hat{\Phi}$ to $\hat{g}$, and vice versa. With only a $\dfrac{\partial \hat{g}}{\partial p}$ boundary condition alone, the values in $\hat{g}$ and $\hat{\Phi}$ far from the island were able to vary significantly. Comparing in collisionality $\nu_\star$, cases (b) and (d) also showed greater variation with respect to each other in $\nu_\star$ than (a,c), as $\hat{\Phi}$ becomes dominant over the other $\nu_\star$-dependent terms in Eq.(2.3.47) (see Fig.5.7). Finally, we note that $\hat{g}$ is influenced by the derivatives of $\hat{\Phi}$ in x and ξ representing those components of the electric field, respectively shown in Figs.(5.11) and (5.12), which appear in Eq.(2.3.47) as coefficients of $\dfrac{\partial \hat{g}}{\partial \xi}$ and $\dfrac{\partial \hat{g}}{\partial p}$. Both derivatives have narrower and steeper gradients relative to the magnetic island at lower $\nu_\star$ and higher $\hat{w}/\hat{\rho}_{\theta,i}$, adding to the challenge of resolving the narrow drift island separatrix.

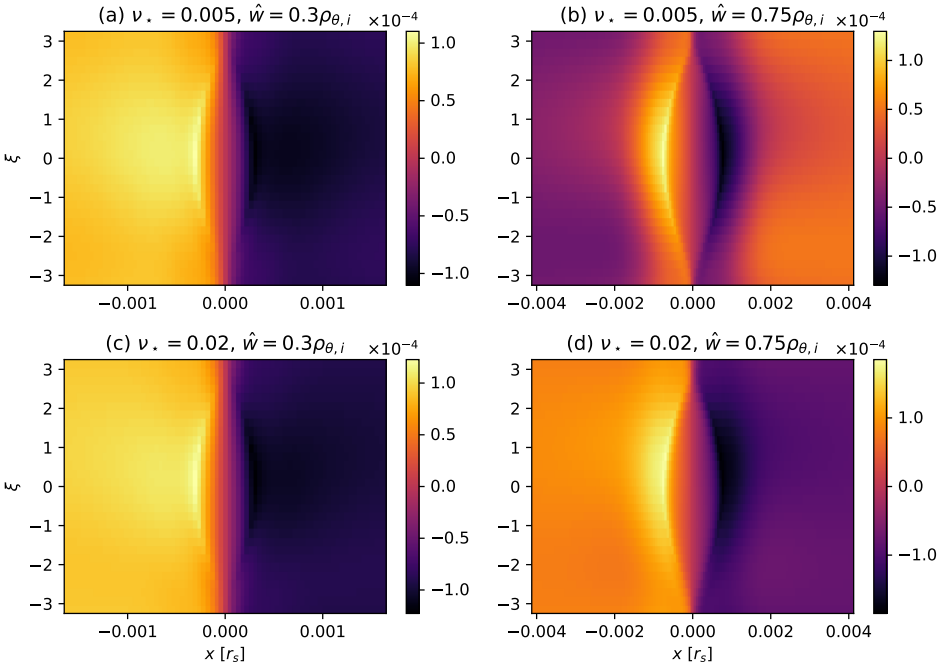

Figure 5.9: Contour plots of normalised electrostatic potential $\hat{\Phi}(x,\xi)[\frac{eZ_i}{T(\psi_s)}]$ at $\theta = 0$, iteration 4.

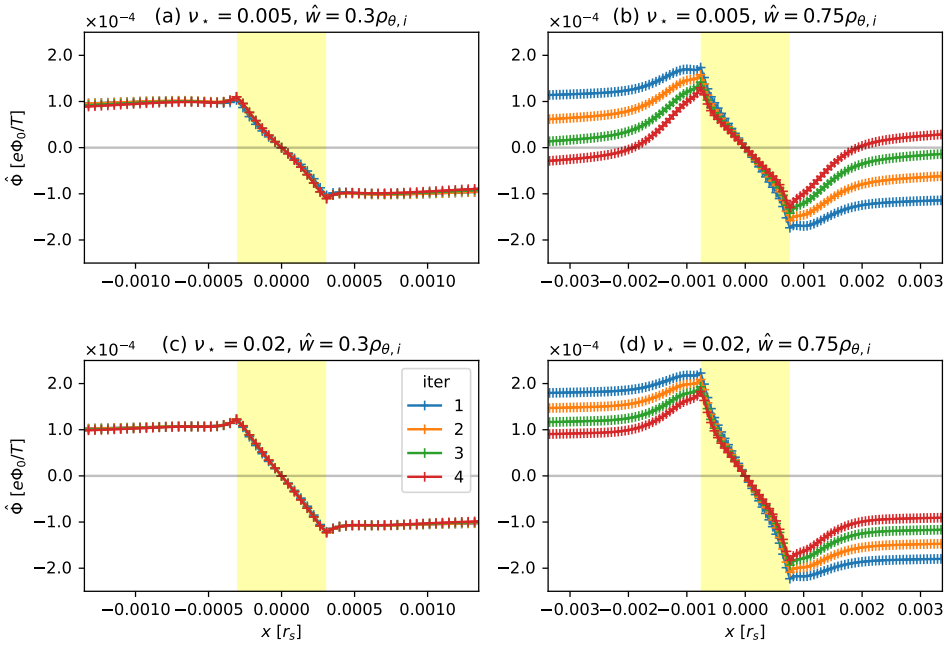

Figure 5.10: As in Fig.5.9, across island O-point at $\xi = 0$ at each iteration (hue). The values of the y-axis are shared between plots. The magnetic island extent is in yellow.

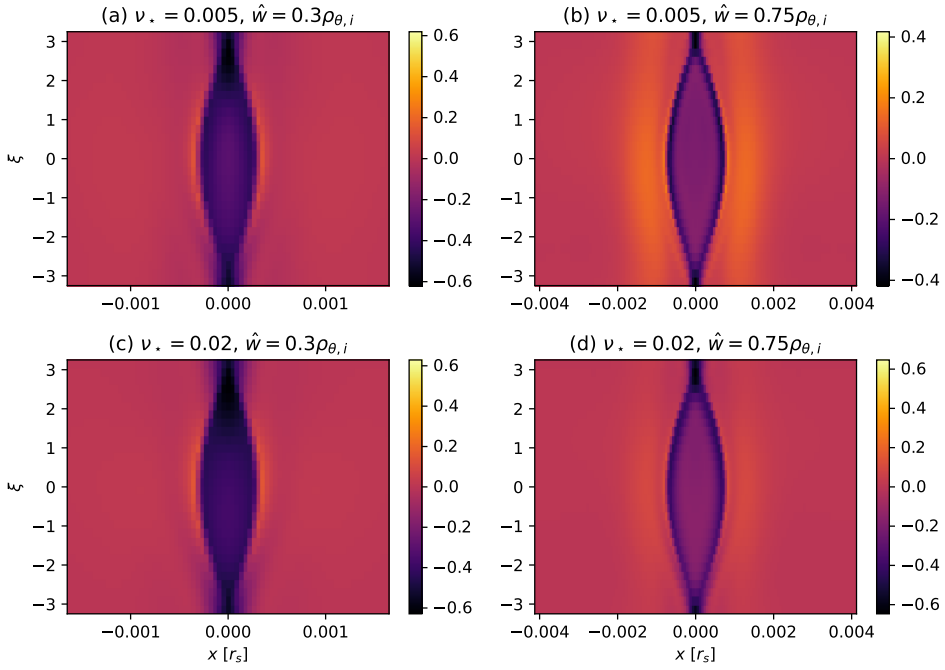

Figure 5.11: As in Fig.5.9, showing $\dfrac{\partial\hat{\Phi}}{\partial x}(x,\xi,\theta=0)$ at iteration 4.

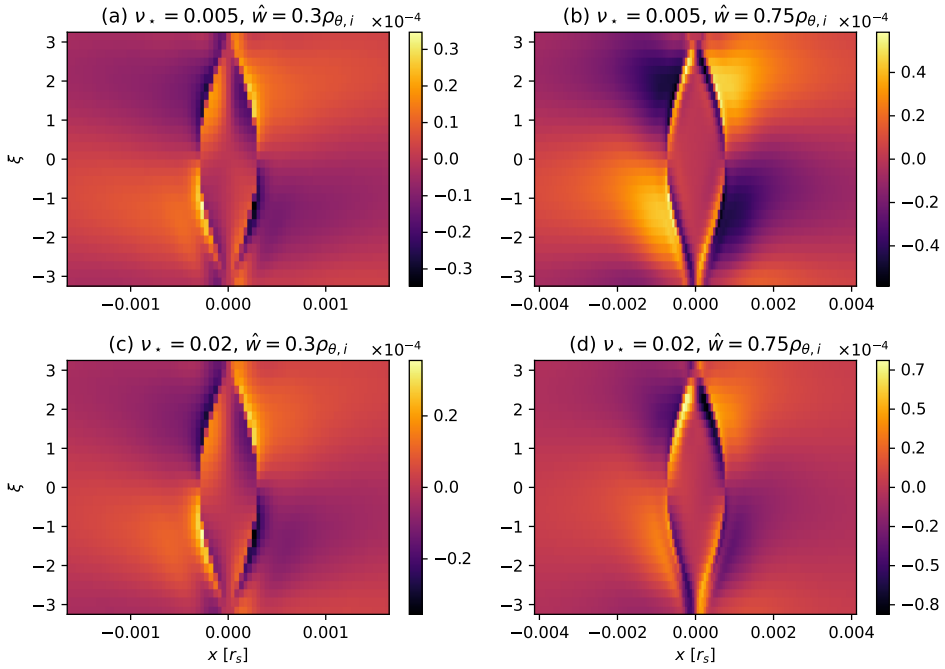

Figure 5.12: As in Fig.5.9, for $\dfrac{\partial\hat{\Phi}}{\partial\xi}(x,\xi,\theta=0)$.

5.2.2 Momentum-conserving ion flow $\hat{\bar{U}}_{\parallel,i}$

We now consider the flow-like momentum-conserving collision operator term $\hat{\bar{U}}_{\parallel,i}$ which, alongside $\hat{\Phi}$, is also updated iteratively with $\hat{g}$ in the `kokuchou` simulation code. This is obtained using the σ-average of $\sigma\hat{g}$, which we denote as the *flow moment* of the ion distribution [70, 41]. Fig.5.13 shows 2D contours of $\hat{\bar{U}}_{\parallel,i}(\theta = 0)$ for each of the four runs at iteration 4. Fig.5.14 shows 1D profiles of the momentum-conserving collision operator term $\hat{\bar{U}}_{\parallel,i}(\theta = 0, \xi = 0)$ at each iteration. In all cases, the profiles assume a distribution localised to the extent of the magnetic island, tending towards a constant at roughly 2-3 island widths away on either side.

Comparing in $\hat{w}/\hat{\rho}_{\theta,i}$ at fixed $\hat{\rho}_{\theta,i}$, the distribution of $\hat{\bar{U}}_{\parallel,i}(\theta = 0, \xi = 0)$ inside the magnetic island takes the form of a single peak in the small island cases (a,c), and a trough-like distribution in the large island cases (b,d) that evokes the separatrix gradients of the shifted passing particle populations in $\hat{g}$. These variations and are influenced by both drift island shifting and radial transport. Comparing in $\nu_\star$ between (a,b) versus (c,d), the profile in the island vicinity is generally flatter at $\nu_\star = 0.005$ than at $\nu_\star = 0.02$, a consequence of reduced radial diffusion across the island separatrix. In Fig.5.13 we also see a ξ-symmetric distribution in (a,b), and anti-symmetry in (c,d). This is likely due to the aforementioned dominance of the $w^2 \cos\xi$ term in $\dfrac{\partial \hat{g}}{\partial p}$ within Eq.(2.3.47) when $\nu_\star$ is lower, as is the case in (a,b). For Fig.5.14, in the low aspect ratio limit, an analytic expression for the momentum-conserving parallel flow can be derived for the neoclassical equilibrium [72] far from the magnetic island (see Eq.(68) of Ref. [50]) which can be compared with the numerical result. This analytic form is:

$$\frac{\hat{\bar{U}}_{\parallel,i}}{v_{\mathrm{th},i}} = -\frac{1}{2}\hat{\rho}_{\theta,i}\hat{L}_n^{-1}\left(1 + \eta(1 + k_{neo})\right) \ , \qquad k_{neo} = \frac{\left\langle (u^2 - \frac{5}{2})\hat{\nu}_{ii} \right\rangle_u}{\hat{\nu}_{ii}} \approx -1.173 \tag{5.2.1}$$

When $\hat{\rho}_{\theta,i} = 10^{-3} r_s$, $\hat{L}_n = -1$, $\eta = 1$ this equates to $\hat{\bar{U}}_{\parallel i,eqm}(x \to \pm\infty) \approx 4.135 \times 10^{-4}$. This analytic expression is shown in Fig.5.14 by the horizontal line, with a relative error of $O(\epsilon^{3/2})$ shown by the magenta region. The size of this error $\epsilon^{3/2} \approx 3.16\%$ is comparable to the $\sim 5\%$ error observed in the numerical test calculations of $\bar{u}_{\parallel,i}(p\hat{F}'_{\mathrm{M}s})$ in 4.1. In this scenario, $\hat{\bar{U}}_{\parallel}$, the θ-average of $b(\theta)\bar{u}_{\parallel,i}$ is calculated here by using the analytic expression for $\bar{u}_{\parallel,i}(p\hat{F}'_{\mathrm{M}s})$ and a the numerically-calculated contribution from $\hat{g}$, to minimise numerical error in the final result. All cases are within error of the analytic solution Eq.(5.2.1) far from the island in x at all iterations.

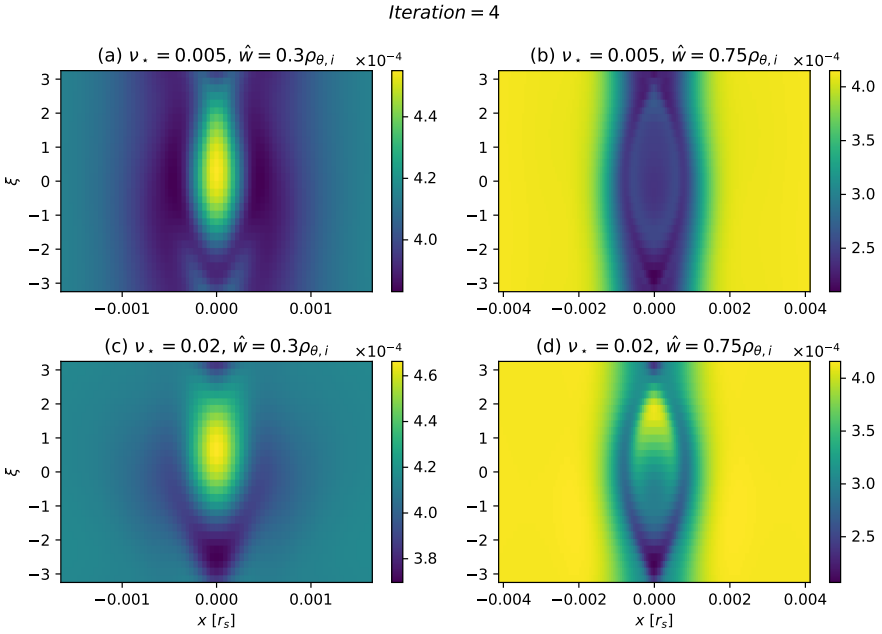

Figure 5.13: As in Fig.5.10, showing $\hat{\bar{U}}_{\parallel,i}(x,\xi)$ at $\theta = 0$ for iteration 4.

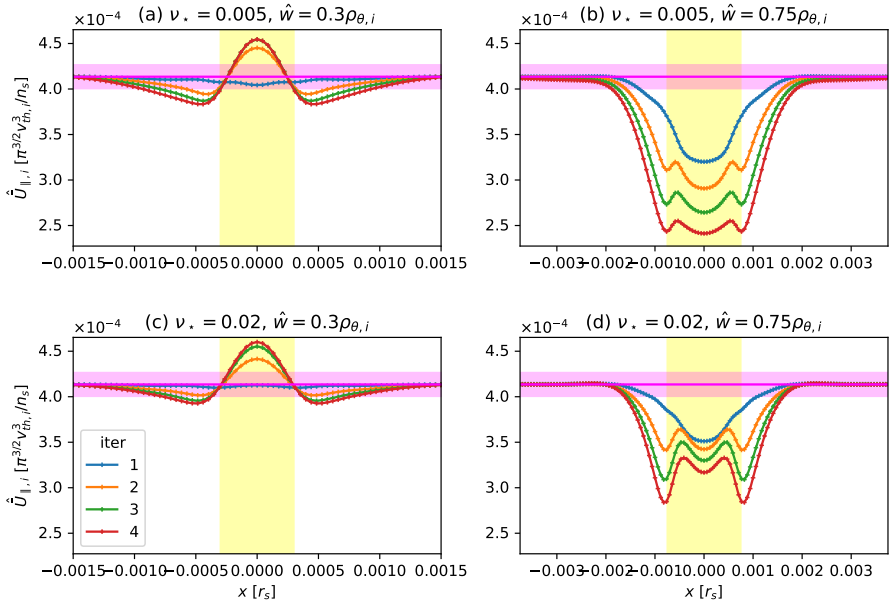

Figure 5.14: As in Fig.5.10, showing $\hat{\bar{U}}_{\parallel,i}(x, \theta = 0, \xi = 0)$ for each iteration. Shown in magenta is the analytic solution of $\bar{u}_\parallel$ far from the island, Eq.(5.2.1), with $O(\epsilon^{3/2})$ relative error bounds in the magenta region. Magnetic island extent shown by yellow region.

5.2.3 Ion parallel flow / Total current density $J_{\parallel,i}$

Distinct from $\hat{\tilde{U}}_\parallel$, the ion parallel flow $u_{\parallel,i}$ shares the same $\hat{g}$ spatial dependence as the former, and is related to the ion parallel current density by $J_{\parallel,i} = eZ_i u_{\parallel,i}$, and is obtained from:

$$u_{\parallel,i} = \frac{b}{\sqrt{\pi}} \sum_\sigma \sigma \int_0^\infty du\, u^3 \int_0^{b^{-1}} dy\, (\hat{g} + p\hat{F}'_{\mathrm{M}s}). \tag{5.2.2}$$

Similarly, the analytic expression for the neoclassical equilibrium [17, 72] ion flow far from the island (see Eq.(69) of Ref. [50]) is given by:

$$\frac{u_{\parallel,i}}{v_{\mathrm{th},i}} = -\frac{1}{2}\hat{\rho}_{\theta,i}\hat{L}_n^{-1}(1+\eta) \tag{5.2.3}$$

which for $\hat{\rho}_{\theta,i} = 10^{-3} r_s$, $\hat{L}_n = -1$, $\eta = 1$ has the value $u_{\parallel,i}(x \to \pm\infty) \approx 6.843 \times 10^{-4}$. Plotting the numerical result for $u_{\parallel,i}(\theta = 0, \xi = 0)$ at iteration 4 alongside Eq.(5.2.3) for each run, again all cases are within $\epsilon^{3/2} \approx 3.16\%$ relative error of the analytic result far from the island.

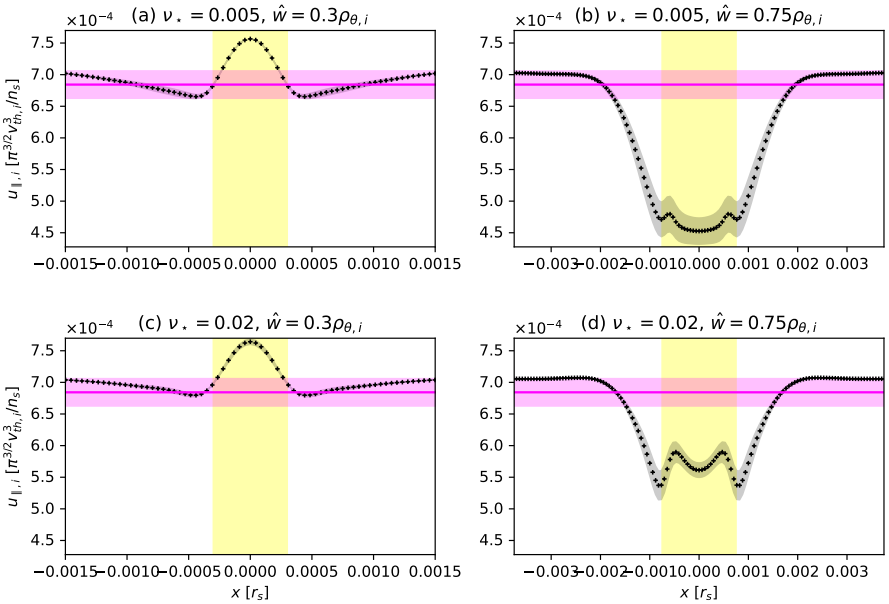

Figure 5.15: Profile of parallel ion flow $u_\parallel$ in radial coordinate x. Shown in magenta is the analytic $u_\parallel$ far from the island, Eq.(5.2.3), correct to $O(\epsilon^{3/2})$ error as shown by the magenta region. Error in $u_\parallel$ is the iterative residual of $\hat{\tilde{\mathcal{U}}}_\parallel$ at iteration 4. Magnetic island extent shown by yellow region. The y-axis is shared between plots.

5.3 Limit of algorithm's operating parameters

This section considered four runs at $\hat{w}/\hat{\rho}_{\theta,i} = \{0.3, 0.75\}$ and collisionality $\nu_\star = \{0.005, 0.020\}$ for $\hat{\rho}_{\theta,i} = 10^{-3} r_s$. Previous studies with the associated `DK-NTM` and `RDK-NTM` codes [70, 41] explored a broader range of parameters, particularly in the range $\hat{w} \gg \hat{\rho}_{\theta,i}$ and $\nu_\star < 0.005$. However, it is computationally challenging to explore those ranges within `kokuchou` in its present state. Fig.5.16 illustrates two separate cases where a similar result containing unstably-growing 'wing-like' profiles in $\hat{\Phi}$ and $\hat{\tilde{U}}_\parallel$ is encountered by (a) reducing $\nu_\star$ below 0.005 while using $\hat{w}/\hat{\rho}_{\theta,i} = 0.75$, and (b) using $\nu_\star = 0.005$ but increasing $\hat{w}/\hat{\rho}_{\theta,i}$ above 0.75. In both cases, $\hat{\rho}_{\theta,i} = 10^{-3} r_s$ is retained.

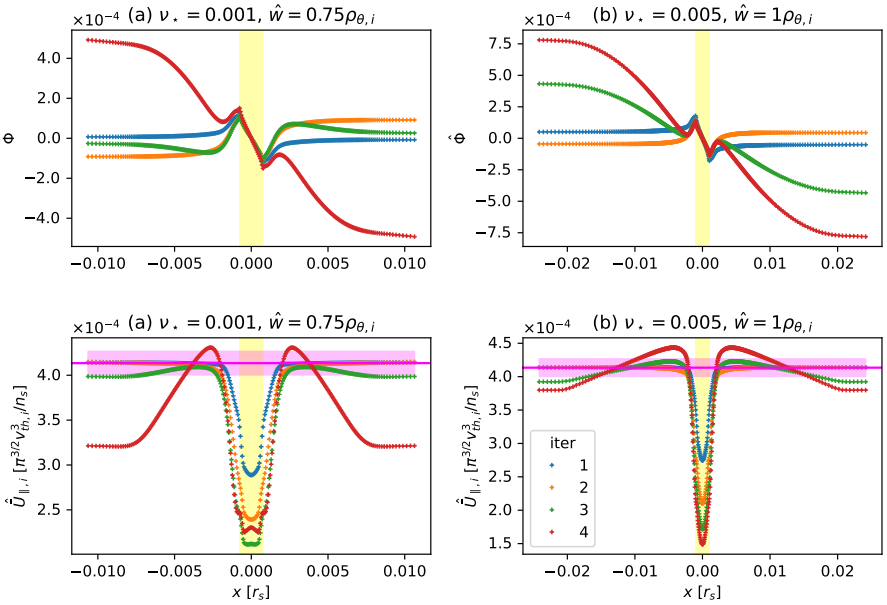

Figure 5.16: 1D profiles versus radial coordinate x, across the magnetic island O-point $\xi = 0$ at $\theta = 0$, for (top) electrostatic potential $\hat{\Phi}$ satisfying quasineutrality and (bottom) $\hat{\tilde{U}}_\parallel$. Two runs are shown, (a) a lower-than-usual collisionality case, and (b) a larger-than-usual magnetic island. Both runs show numerical instability between iterations. Magnetic island extent shown in yellow, equilibrium value of $\hat{\tilde{U}}_\parallel$ far from island with $O(\epsilon^{1/2}) =\sim 3\%$ error region shown in magenta.

Here, a typical distribution in $\hat{\Phi}$ and $\hat{\tilde{U}}_\parallel$ was seen at iterations 1 and 2, which changed to a new distribution on successive iterations with large variations as far as 8-10 island widths away. For $\hat{\tilde{U}}_\parallel$, this new result does not match with the neoclassical flow result far from the island (Eq.(5.2.1)). Similarly, $\hat{\Phi}$ changes from its usual sigmoid profile (see Fig.5.10) to then grow unstably outside the island on iterations 3 and 4. Because these results vary smoothly and tend to constants far from the island (reflecting boundary conditions for $\hat{g}$), the solution is considered numerically valid but not physical. As this same outcome occurs at low $\nu_\star$ and high $\hat{w}$, it is most likely due to

insufficient mesh resolution of the separatrix boundary, as discussed in Sec.3.1.6.

Summary

This chapter presented simulated plasma quantities from four full-size `kokuchou` simulations for two values in collisionality $\nu_\star = 0.005, 0.02$ and island width $\hat{w}/\hat{\rho}_{\theta,i} = 0.3, 0.75$ for a fixed ion poloidal gyroradius $\hat{\rho}_{\theta,i} = 10^{-3} r_s$, where r_s is the minor radius of the island-forming rational surface. Respectively, $\nu_\star$ and $\hat{w}/\hat{\rho}_{\theta,i}$ affect the ion response through collisional transport and drift island physics. For each simulation, the 1^{st}-order perturbed ion distribution $\hat{g}$, potential $\hat{\Phi}$ and momentum conservation term $\hat{\bar{U}}_\parallel$ were iteratively recalculated four times for sufficient self-consistency.

The perturbed ion distribution $\hat{g}$ was presented, including profiles of the passing ion distribution in $\{\xi, p\}$ physical space, and across $\{y, u\}$ velocity space. Profiles of $\hat{g}$ and its derivatives showed that while $\nu_\star$ affected the width of the separatrix layer relative to the island, the size of $\hat{w}/\hat{\rho}_{\theta,i}$ had a more influential effect on the island physics. As previously observed in Refs. [70, 41], magnetic drifts caused the passing ion response ($y < 1$) to resemble the island in shape but become radially-shifted from it by a factor $\hat{\rho}_{\theta,i}\hat{\omega}_D\hat{L}_q^{-1}$. Here, the magnetic drift frequency $\hat{\omega}_D(y, \sigma, u)$ has a velocity-dependence described by Eq.(2.3.48). These shifted structures were referred to as drift islands. If $\hat{w}/\hat{\rho}_{\theta,i}$ is larger, this shift is small and all drift islands at all velocities were aligned with the magnetic island, hence the velocity integral of $\hat{g}$ at a given point in physical space contains significant localised variations there. If $\hat{w}/\hat{\rho}_{\theta,i}$ is small, the drift islands were spread out across physical space, and these variations are reduced. As a result, the electrostatic potential $\hat{\Phi}$ and ion flow $\hat{\bar{U}}_\parallel$ exhibited slower changes between each iteration. Likewise, varying the collisionality $\nu_\star$ only had a significant effect when $\hat{w}/\hat{\rho}_{\theta,i}$ was larger, as it determined the variations of the drift island separatrices and such was relevant only when the drift islands overlapped. Collisionality had a lesser but significant role when $\hat{w} \sim \hat{\rho}_{\theta,i}$, as the separatrix width of drift islands was made narrower at lower $\nu_\star$, which led to differences in the velocity-integrated quantities including $\hat{\Phi}$ and flow that were not as prominent at $\hat{w} \ll \hat{\rho}_{\theta,i}$, where drift islands of different velocities were not closely aligned in physical space.

The results presented here are reminiscent of earlier drift-kinetic NTM studies [69, 70, 41]; a main difference being that this work focuses exclusively on the region $\hat{w} \lesssim \hat{\rho}_{\theta,i}$ and the effects of drift island physics and collisionality there. It builds on these results by: i) studying the variation of the ion response with collisionality and its relevance at larger $\hat{w}/\hat{\rho}_{\theta,i}$, and ii) validating the

model by demonstrating that the ion flow $u_{\parallel,i}$ and momentum conservation term $\hat{\tilde{U}}_{\parallel}$ tend towards the expected analytic neoclassical flows far from the magnetic island. Lastly, Sec.5.3 examined two additional 'extreme' cases at low $\nu_\star = 0.001$ and high $\hat{w} = 1.0\hat{\rho}_{\theta,i}$ that produced erroneous results, evidencing the challenges of using the `kokuchou` code to resolve the narrow island separatrix discussed in Sec.3.1.6. Here, $\hat{\Phi}$ and $\hat{\tilde{U}}_{\parallel}$ grew unstably far from the island as a result. This presents obstacles in directly comparing `kokuchou` with similar codes in Refs. [69, 70, 41] that have been operated at $\nu_\star = 0.001$.

Chapter 6

Parameter scan

Having studied the result for a small sample of runs, for Objective (3) a large parameter scan was conducted to identify the threshold width w_c and its relationship with respect to normalised ion poloidal gyroradius $\hat{\rho}_{\theta,i}[r_s]$ and plasma collisionality $\nu_\star$. The scan consisted of 5 values in each of $\nu_\star$, $\hat{\rho}_{\theta,i}$ and $\hat{w}$, listed in Tab. 6.1, or 125 runs total.

Parameter	Plasma collisionality	Ion poloidal gyroradius	Island half-width
Symbol	$\nu_\star$ [no unit]	$\hat{\rho}_{\theta,i}$ $[r_s]$	$\hat{w}$ $[r_s]$
Values	$\{1, 5, 10, 15, 20\} \times 10^{-3}$	$\{1, 2, 3, 4, 5\} \times 10^{-3}$	$\{0.3, 0.4, 0.5, 0.6, 0.75\} \times \hat{\rho}_{\theta,i}$

Table 6.1: `kokuchou` input plasma parameters varied for the Objective (3) parameter scan.

Here, $\hat{w}$ was chosen to be fractions of $\hat{\rho}_{\theta,i}$ ranging from $0.3 - 0.75$, or approximately between $1 - 2$ ion banana widths $\rho_{b,i} = \epsilon^{1/2}\hat{\rho}_{\theta,i} = 0.316\hat{\rho}_{\theta,i}$. This is the range over which the threshold width $w_c(\hat{\rho}_{\theta,i})$ is expected to lie, as Sec.6.3 will discuss. The range of $\hat{\rho}_{\theta,i}$ was also chosen to match Ref. [41] partly for the original intent of benchmarking, but also due to computational limitations as `kokuchou` cannot operate at the higher values of $\hat{\rho}_{\theta,i}$ that were used in `DK-NTM` [69, 70]. This was attributed to the change of diffusion term in $\dfrac{\partial^2 \hat{g}}{\partial p^2}$ from $\propto \hat{\rho}_{\theta,i}$ to $\hat{\rho}^2_{\theta,i}$ withinSec.2.6 since Ref. [70], however it is unclear why this change made higher $\hat{\rho}_{\theta,i}$ and $\hat{w}$ more numerically challenging to resolve. These values of $\hat{\rho}_{\theta,i}$ are an order of magnitude lower than the typical values of an ITER-like tokamak ($O(\text{cm})$). All other mesh and plasma parameters are same as those listed at the start of Ch.5.

A novel aspect of this scan that expands on previous attempts [70, 41, 43] is the variation of $\nu_\star$. A higher $\nu_\star$ increases the rate of radial transport across the drift island separatrix, which should partly restore lost bootstrap current and reduce its MRE drive term Δ_{bs} for a given $\hat{w}, \hat{\rho}_{\theta,i}$. The lowest value in $\nu_\star$ was chosen with the original intention of comparing directly with `RDK-NTM`

results from Ref. [41], however the difficultly of resolving the separatrix boundary layers has meant the result from `kokuchou` at the lowest $\nu_\star$ is unlikely to be valid, but we attempt here regardless to identify the known operating range.

Results in this section are organised as follows. Sec.6.1 assesses the convergence and numerical stability of $\hat{\Phi}$ and $\hat{\bar{U}}_{\parallel}$ of these runs. Sec.6.2 presents the total field-parallel current contribution to island growth Δ_{loc} in the vicinity of the resistive layer, and its components from ions/electrons and polarisation/bootstrap currents. In Sec.6.3, using the results where $\Delta_{loc}(\hat{w} = w_c) = 0$, the relationship of threshold island width w_c with respect to $\hat{\rho}_{\theta,i}$ and $\nu_\star$ is determined and compared with results in literature.

6.1 Numerical stability

6.1.1 Iterative residual

The maximum value of the iterative residual $\mathcal{R}$ (see Eq.(3.1.5)) of the electrostatic potential $\hat{\Phi}$ and momentum conservation term $\hat{\tilde{U}}_{\parallel}$ across all $\{x, \xi, \theta\}$-space at each iteration are plotted in Fig.6.1 and Fig.6.2 respectively. Here, each column denotes the iteration number, and lighter regions denote a larger maximum iterative residual for that quantity across all $\{x, \xi, \theta\}$, or a larger relative change between iterations for the whole quantity more broadly. Regions that darken on successive iterations indicate slower change and convergence toward a numerically stable result.

For both quantities, the maximum iterative residual is largest for runs where the absolute size of $\hat{w}$ $[r_s]$ is large at high ratio $\hat{w}/\hat{\rho}_{\theta,i}$ and high $\hat{\rho}_{\theta,i}$, i.e. the top-right of each panel. Notably, the maximum residual of $\hat{\Phi}$ is considerably larger than $\hat{\tilde{U}}_{\parallel}$ for most runs. There appears to be a rough threshold at roughly $\hat{w} \approx 10^{-3} r_s$ above which the maximum iterative residual of $\hat{\Phi}$ becomes larger than 100% per iteration. This does not necessarily result in the numerical drift-kinetic equation solution $\hat{g}$ being invalid, but rather more sensitive to changes in $\hat{\Phi}$; recall in Fig.5.10 cases (b,d) for $\hat{w}/\hat{\rho}_{\theta,i} = 0.75$ the profile in $\hat{\Phi}$ changed significantly between iterations. Likewise, higher values of $\nu_\star$ are also seen to have a lower maximum residual in $\hat{\Phi}$, as the collision-dependent terms of $\hat{g}$ are then able to compete with $\hat{\Phi}$ and reduce numerical sensitivity on that term. However, by being more sensitive to $\hat{\Phi}$, any error in calculating the derivatives of $\hat{\Phi}$ that appear in the equation for $\hat{g}$ would then introduce numerical stability on successive iterations.

For $\hat{\tilde{U}}_{\parallel}$ in Fig.6.2, the array maximum of $\mathcal{R}(\hat{\tilde{U}}_{\parallel})$ is consistently lower than 30% change per iteration and is decreasing in most runs, indicating that $\hat{\tilde{U}}_{\parallel}$ at all $\{x, \theta, \xi\}$ changes slowly between iterations, even from its initial value at the start of iteration 1, $\hat{\tilde{U}}_{\parallel}(p\hat{F}'_{\mathrm{M}s})$. This reflects the trends seen in Fig.5.14, where changes in $\hat{\tilde{U}}_{\parallel}$ were mostly localised to the vicinity of the island, while far from the island $\hat{\tilde{U}}_{\parallel}$ converged toward a constant representing neoclassical equilibrium. Here, the main parameter affecting the convergence state of $\hat{\tilde{U}}_{\parallel}$ is $\hat{w}/\hat{\rho}_{\theta,i}$, where the drift island shift is the main factor affecting the distribution of $\hat{\tilde{U}}_{\parallel}$, as seen prior in 5.2.2. With relation to Sec.3.1.5, the convergence criterion of array-*averaged* iterative residuals of both $\hat{\Phi}$ and $\hat{\tilde{U}}_{\parallel}$ did not come to within ($\epsilon = 10\%$) relative error after the maximum of 4 iterations for any of the runs. Future work would require more than 4 iterations for $\hat{\Phi}$ to converge, particularly when $\hat{\rho}_{\theta,i}$ and $\hat{w}$ are high. However, greater care is needed to ensure the simulation state does not then diverge or develop numerical errors at higher iteration numbers.

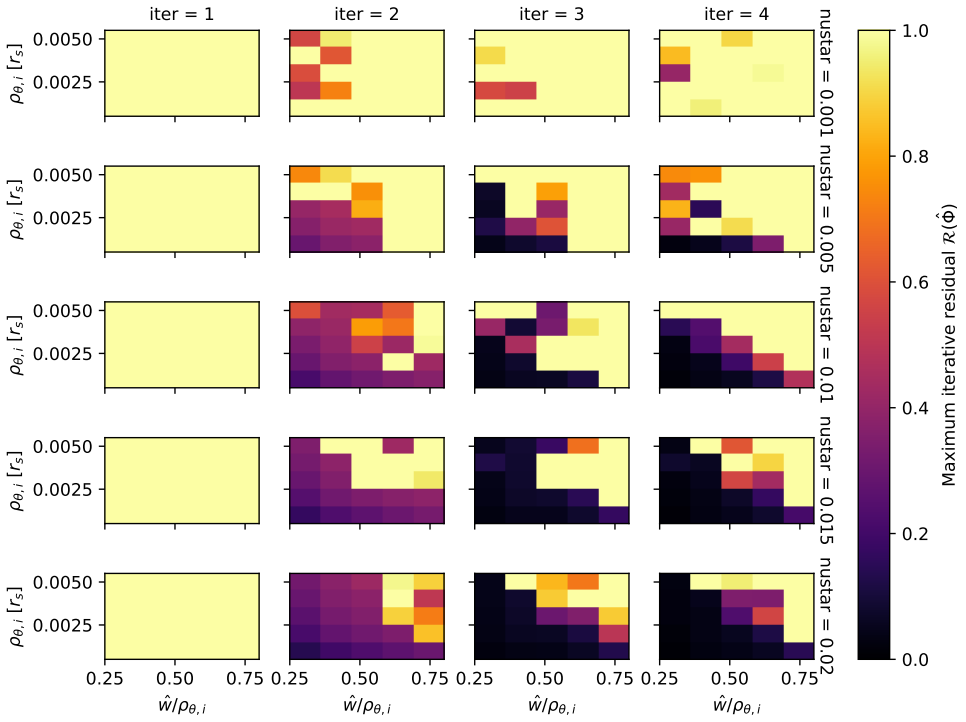

Figure 6.1: Array-maximum iterative residual of the electrostatic potential, $\max(\mathcal{R}(\hat{\Phi}))$ plotted vs. $\hat{w}/\hat{\rho}_{\theta,i}$ (x-axis) and $\hat{\rho}_{\theta,i}$ (y-axis), for each simulation iteration (column) and collisionality $\nu_\star$ (row) for all 125 runs.

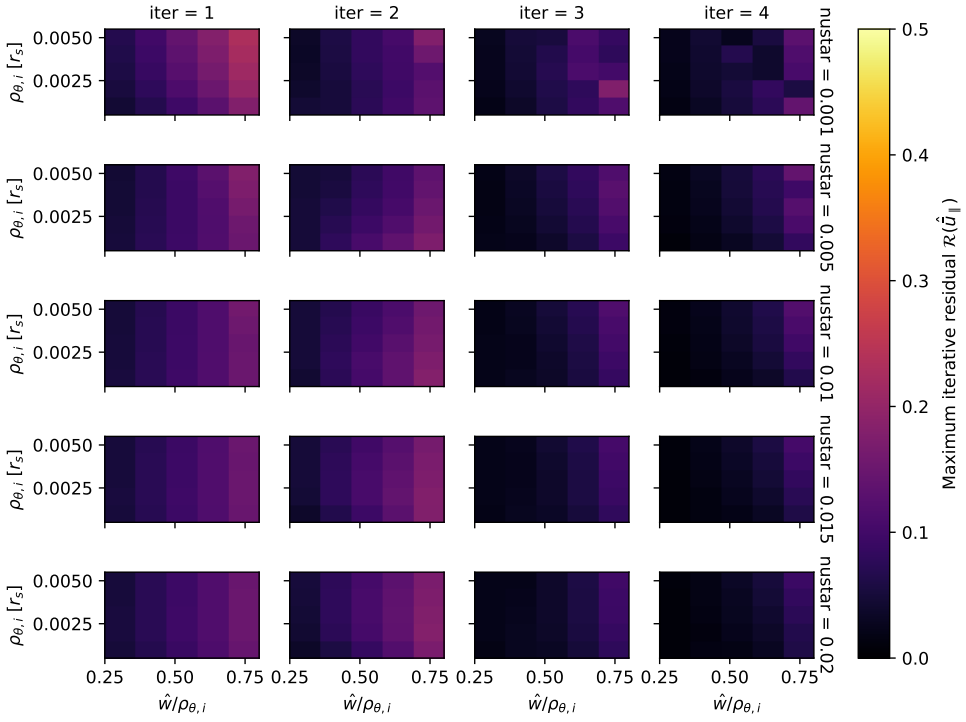

Figure 6.2: As in Fig.6.1, showing array-maximum iterative residual of momentum-conserving collision operator term $\max(\mathcal{R}(\hat{U}_\parallel))$.

6.1.2 Resolving the separatrix boundary layer

Sec.3.1.6 discussed the difficulty of iteratively solving the ion response equation (2.3.47) around the thin separatrix boundary layer from a computational perspective, particularly when collisionality $\nu_\star$ is lower. Fig.5.10 and Fig.6.1 also indicate a further challenge in attaining a result for electrostatic potential $\hat{\Phi}$ that converges after several iterative recalculations within the algorithm described. Larger changes per iteration were observed in $\hat{\Phi}$ at island widths $\hat{w}$ close to $\hat{\rho}_{\theta,i}$, which for the case of Fig.6.1, became unstably large with each iteration.

To assess how these two computational challenges may be related, we look at the physical terms affecting the separatrix layer in more detail. Firstly, we define the separatrix layer width in p-space Δ_p such that $\dfrac{\partial \hat{g}}{\partial p} \sim \frac{\hat{g}}{\Delta_p}$. Then, recalling the drift-kinetic equation Eq.(2.3.47), accounting for the scaling of each term near the magnetic island separatrix layer where $p \sim \pm\hat{w}$:

$$
\begin{aligned}
&- m\left[\overbrace{\frac{p}{\hat{L}_q}\Theta_y}^{O(\hat{w}\hat{L}_q^{-1})} + \overbrace{\frac{\hat{\rho}_{\theta,i}}{\hat{L}_q}\hat{\omega}_D}^{O(\hat{\rho}_{\theta,i}\hat{L}_q^{-1})} - \overbrace{\frac{\hat{\rho}_{\theta,i}}{2}\left\langle \frac{1}{u_\parallel}\frac{\partial \hat{\Phi}}{\partial x}\right\rangle_\theta^p}^{?}\right]\frac{\partial \hat{g}}{\partial \xi} \\
&+\left[\overbrace{\frac{m}{4}\frac{\hat{w}^2}{\hat{L}_q}\sin\xi\,\Theta_y}^{\hat{w}^2\hat{L}_q^{-1}} - \overbrace{m\frac{\hat{\rho}_{\theta,i}}{2}\left\langle \frac{1}{u_\parallel}\frac{\partial \hat{\Phi}}{\partial \xi}\right\rangle_\theta^p}^{?} - \underline{\underline{\hat{\nu}_{ii}\hat{\rho}_{\theta,i}\Theta_y}}\right]\left(\overbrace{\frac{\partial \hat{g}}{\partial p}}^{\Delta_p^{-1}} + \overbrace{\hat{F}'_{\mathrm{M}s}}^{O(r_s^{-1})}\right) \\
&- \overbrace{\underline{\underline{\frac{\hat{\nu}_{ii}}{2}\frac{\sigma u}{(1+\epsilon)}\hat{\rho}_{\theta,i}^2 y\left\langle \frac{1}{\sqrt{1-yb}}\right\rangle_\theta^x}}}^{O(\hat{\nu}_{ii}\hat{\rho}_{\theta,i}^2\Delta_p^{-2})}\frac{\partial^2 \hat{g}}{\partial p^2} - \overbrace{\underline{\underline{2\hat{\nu}_{ii}\hat{\rho}_{\theta,i}y\Theta_y}}}^{O(\hat{\nu}_{ii}\hat{\rho}_{\theta,i}\Delta_p^{-1})}\frac{\partial^2 \hat{g}}{\partial y \partial p} - \overbrace{\frac{\hat{\nu}_{ii}}{\sigma u}(1+\epsilon)\left\langle \frac{(2-3yb)}{\sqrt{1-yb}}\right\rangle_\theta^x}^{O(\hat{\nu}_{ii})}\frac{\partial \hat{g}}{\partial y}\bigg|_p} \\
&\qquad - \overbrace{\frac{2\hat{\nu}_{ii}}{\sigma u}(1+\epsilon)y\left\langle\sqrt{1-yb}\right\rangle_\theta^x}^{O(\hat{\nu}_{ii})}\frac{\partial^2 \hat{g}}{\partial y^2}\bigg|_p = \overbrace{2\hat{\nu}_{ii}(1+\epsilon)\hat{\bar{U}}_{\parallel i}(\hat{g}+p\hat{F}'_{\mathrm{M}s})\hat{F}_{\mathrm{M}s}}^{O(\hat{\nu}_{ii})}
\end{aligned}
$$

Above, the $\hat{\Phi}$-dependent $\mathbf{E}\times\mathbf{B}$ drift terms are of unknown size, as $\hat{\Phi}$ will change significantly with $\hat{g}$ between iterations as evidenced earlier by Fig.5.10. Focusing on the underlined terms that are coefficients of the p-derivatives of $\hat{g}$, these are small unless $\dfrac{\partial \hat{g}}{\partial p}$ becomes large, which is the case at $p \sim \pm\hat{w}$. Likewise, if also $\hat{w} \lesssim \hat{\rho}_{\theta,i}$, as is the case in this work, then the largest terms of the left-hand side of the above equation are of $O(\hat{w}\hat{L}_q^{-1})$, which are the coefficients of $\dfrac{\partial \hat{g}}{\partial \xi}$.

Starting with these $\frac{\partial \hat{g}}{\partial \xi}$ terms, for passing particles ($\Theta_y = 1$) if $\hat{w} \gtrsim \hat{\rho}_{\theta,i}$ then the left-hand side has the approximate scale:

$$\frac{p}{\hat{L}_q} \sim \frac{\hat{w}}{\hat{L}_q} \lesssim \frac{\hat{\rho}_{\theta,i}}{\hat{L}_q} \qquad \Rightarrow \text{LHS} \sim \frac{\hat{w}}{\hat{L}_q}\hat{g} \qquad \left(\frac{\partial \hat{g}}{\partial \xi} \sim \hat{g}\right)$$

Next, the diffusion term in $\frac{\partial^2 \hat{g}}{\partial p^2}$ is $O\left(\frac{\hat{\nu}_{ii}\hat{\rho}^2_{\theta,i}}{\Delta_p^2}\hat{g}\right)$ in the layer, and so the approximate width of the separatrix layer is provided by its balance with the $\partial\xi$ terms:

$$\frac{\hat{\nu}_{ii}\hat{\rho}^2_{\theta,i}}{\Delta_p^2}\cancel{\hat{g}} \sim \frac{\hat{w}}{\hat{L}_q}\cancel{\hat{g}} \qquad \Rightarrow \Delta_{p,pass} \sim \sqrt{\frac{\hat{\nu}_{ii}\hat{L}_q}{\hat{w}}}\hat{\rho}_{\theta,i}$$

Repeating the above for trapped particles, only $\hat{\rho}_{\theta,i}\hat{\omega}_D\hat{L}_q^{-1} \sim O(\hat{\rho}_{\theta,i}\hat{L}_q^{-1})$ contributes to $\frac{\partial \hat{g}}{\partial \xi}$ of the drift-kinetic equation.

$$\frac{p}{\hat{L}_q} \sim \frac{\hat{\nu}_{ii}\hat{\rho}^2_{\theta,i}}{\Delta_p^2} \Rightarrow \Delta_p^2 \sim \hat{\nu}_{ii}\hat{L}_q\hat{\rho}_{\theta,i} \sim \left(\frac{\hat{\nu}_{ii}\hat{L}_q}{\hat{w}}\right)\hat{w}\hat{\rho}_{\theta,i} \qquad \Rightarrow \ \Delta_{p,trap} \sim \sqrt{\frac{\hat{\nu}_{ii}\hat{L}_q}{\hat{w}}}\sqrt{\hat{w}\hat{\rho}_{\theta,i}}$$

Then, comparing the approximate separatrix width Δ_p for passing and trapped ions:

$$\frac{\Delta_{p,pass}}{\Delta_{p,trap}} \sim \sqrt{\frac{\hat{\rho}_{\theta,i}}{\hat{w}}}\ ,$$

hence the passing width is narrowest when $\hat{w} \gtrsim \hat{\rho}_{\theta,i}$, i.e. the island is 'large' by this work's scope where $\hat{w} = (0.3 - 2.0)\hat{\rho}_{\theta,i}$ is used. The p-mesh in the code must resolve a layer of width $\sim \sqrt{\hat{\nu}_{ii}\hat{L}_q\hat{w}^{-1}}\hat{\rho}_{\theta,i}$, which is harder for low collisionality $\nu_\star$ or high $\hat{w}$ *at fixed* $\hat{\rho}_{\theta,i}$.

Returning to the 'unknown' $\mathbf{E}\times\mathbf{B}$ drift terms, we have previously seen $\frac{\partial \hat{\Phi}}{\partial x}$ in 5.11 to be of $O(0.1)$, and so we may assume term is overall $O(\hat{\rho}_{\theta,i}) \sim O(\hat{w})$. Consider the scenario in which $\mathbf{E}\times\mathbf{B}$ drift is the dominant term on the LHS:

$$\frac{\partial \hat{\Phi}}{\partial x} \sim \frac{\hat{\Phi}}{\Delta_p} \sim \frac{\hat{w}}{\Delta_p} \qquad \Rightarrow \hat{\rho}_{\theta,i}\left\langle \frac{1}{v_\parallel}\frac{\partial \hat{\Phi}}{\partial x}\right\rangle^p_\theta \sim \frac{\hat{\rho}_{\theta,i}\hat{w}}{\Delta_p} \sim \frac{\hat{\nu}_{ii}\hat{\rho}_{\theta,i}}{\Delta_p^2}$$

$$\therefore \quad \boxed{\Delta_{p,\mathbf{E}\times\mathbf{B}} \sim \frac{\hat{\nu}_{ii}\hat{\rho}_{\theta,i}}{\hat{w}}} \tag{6.1.1}$$

Here, Δ_p is defined by the narrowest of $\Delta_{p,pass}$ and $\Delta_{p,\mathbf{E}\times\mathbf{B}}$. The latter is the case when:

$$\boxed{\frac{\hat{\nu}_{ii}}{\hat{w}\hat{L}_q} < 1} \tag{6.1.2}$$

Therefore, if the above condition is true, then the separatrix layer width is primarily influenced by $\hat{\Phi}$, and therefore the separatrix width will change between iterations as $\hat{\Phi}$ is recalculated. This complicates the numerical procedure, as at any time the separatrix may become too narrow to resolve under the existing mesh scheme.

Given $\hat{\nu}_{ii} = \epsilon^{1/2}\nu_\star\tilde{\nu}_{ii}(u)$ (Eq.(2.2.17)), the collision frequency varies significantly over the u-mesh used in this work, from $\tilde{\nu}_{ii}(0.1v_{\mathrm{th},i}) \approx O(100)$ to $\tilde{\nu}_{ii}(3v_{\mathrm{th}i}) \approx O(0.1)$ (see also Fig.4.3). From $\hat{\rho}_{\theta\{}1,5\}\times10^{-3}r_s$, the island width in r_s units ranges from $\hat{w} = \{0.3, 0.75\}\hat{\rho}_{\theta,i}$, which for this range in $\hat{\rho}_{\theta,i}$ gives island widths ranging from $\hat{w} = \{3\times10^{-4}, 3.75\times10^{-3}\}r_s$. The range of collisionality values used is $\nu_\star = \{0.001, 0.020\}$, therefore the condition (6.1.2) will be satisfied over at least part of the u-mesh in all of the runs presented. This means the p-mesh will need to resolve details at the scale of Eq.(6.1.1), but this will also vary between iterations as the numerical result for $\hat{\Phi}$ then changes between iterations. Therefore any future changes made to the `kokuchou` should focus on redesigning the meshing scheme to pack points around the drift island separatrix to accommodate possible variations in its width between iterations. The remainder of this section will present simulations over this parameter space in $\hat{w}$, $\hat{\rho}_{\theta,i}$ and $\nu_\star$, however $\nu_\star = 0.001$ is omitted as these results exhibited numerical instability between iterations similar to that of Fig.5.16.

6.2 Contributions to the modified Rutherford equation

Using Eq.(2.5.10), the $\cos\xi$ projection of parallel current density $J_\parallel$ from the ion and electron flows are used to determine their contribution to the modified Rutherford equation for island growth, Eq.(2.5.13). This section presents results for each current contribution with respect to collisionality $\nu_\star$, ion poloidal gyroradius $\hat{\rho}_{\theta,i}$ and its ratio with island width, $\hat{w}/\hat{\rho}_{\theta,i}$. Here, the results at $\nu_\star = 0.001$ were omitted.

Fig.6.3 shows the result for the total parallel current drive to island growth Δ_{loc} as contour plots, each column an iteration of the `kokuchou` code. Here, Δ_{loc} is seen to converge stably towards the result on iteration 4, mirroring a similar trend seen in $\hat{\bar{U}}_\parallel$ within Fig.6.2 despite the large iterative residual in $\hat{\Phi}$ in Fig.6.1. The contour plot indicates the location of the threshold width w_c in $\hat{w}/\hat{\rho}_{\theta,i}$ where $\Delta_{loc} = 0$, which occurs between roughly $\hat{w} = 0.4 - 0.6\hat{\rho}_{\theta,i}$, at higher $\hat{w}$ with increasing $\nu_\star$. Later, 6.3 will use this data to quantify the threshold width and its variation with respect to $\nu_\star$ and $\hat{\rho}_{\theta,i}$.

Fig.6.4 illustrates Δ_{loc} and its contributions from ions and electrons at the final iteration 4 as a line plot. The ion contribution alone is shown more visibly in Fig.6.5. Here, the dominant contribution to Δ_{loc} is provided by the ions, however the electron contribution is of a similar magnitude and able to compete with the ion term. Both the total and ion Δ_{loc} terms increase with $\hat{w}/\hat{\rho}_{\theta,i}$ over the range $0.3 \leq \hat{w}/\hat{\rho}_{\theta,i} \leq 0.75$, and are both stabilising (negative) at low $\hat{w}/\hat{\rho}_{\theta,i}$ and destabilising (positive) at higher $\hat{w}/\hat{\rho}_{\theta,i}$. The inverse is seen for the electron contribution, which decreases with increasing $\hat{w}/\hat{\rho}_{\theta,i}$ and also changes sign over this range. As with the total Δ_{loc}, the threshold in $\hat{w}$ where each of the species' contributions change sign is also seen to increase with both $\nu_\star$ and $\hat{\rho}_{\theta,i}$.

The trend in Δ_{loc} for ions is similar to the results of `DK-NTM` within Ref. [70] Fig.10, while the range in $\hat{w}/\hat{\rho}_{\theta,i}$ where a sign change is observed is similar to that of `RDK-NTM` in Ref. [41] Fig.8. A major difference from `DK-NTM` is seen within the electron contribution to Δ_{loc}. Though this is stabilising at $\hat{w} \sim \hat{\rho}_{\theta,i}$ as expected, at $\hat{w} \ll \hat{\rho}_{\theta,i}$ it becomes destabilising rather than strongly stabilising as in Ref. [70]. Toward $\hat{w} = 0.3\hat{\rho}_{\theta,i}$, Δ_{loc} and its contributions do not continue decreasing as expected [70, 41], instead flattening out and in some cases slightly increasing again. This is seen in the full ranges of $\nu_\star$ and $\hat{\rho}_{\theta,i}$, however at the lower value of $\hat{\rho}_{\theta,i} = 0.001r_s$, Δ_{loc} is higher than at $\hat{w}/\hat{\rho}_{\theta,i} = 0.3$ than at 0.4. These variations will be discussed later, when the components of the total current are presented later in Fig.6.6 and Fig.6.8.

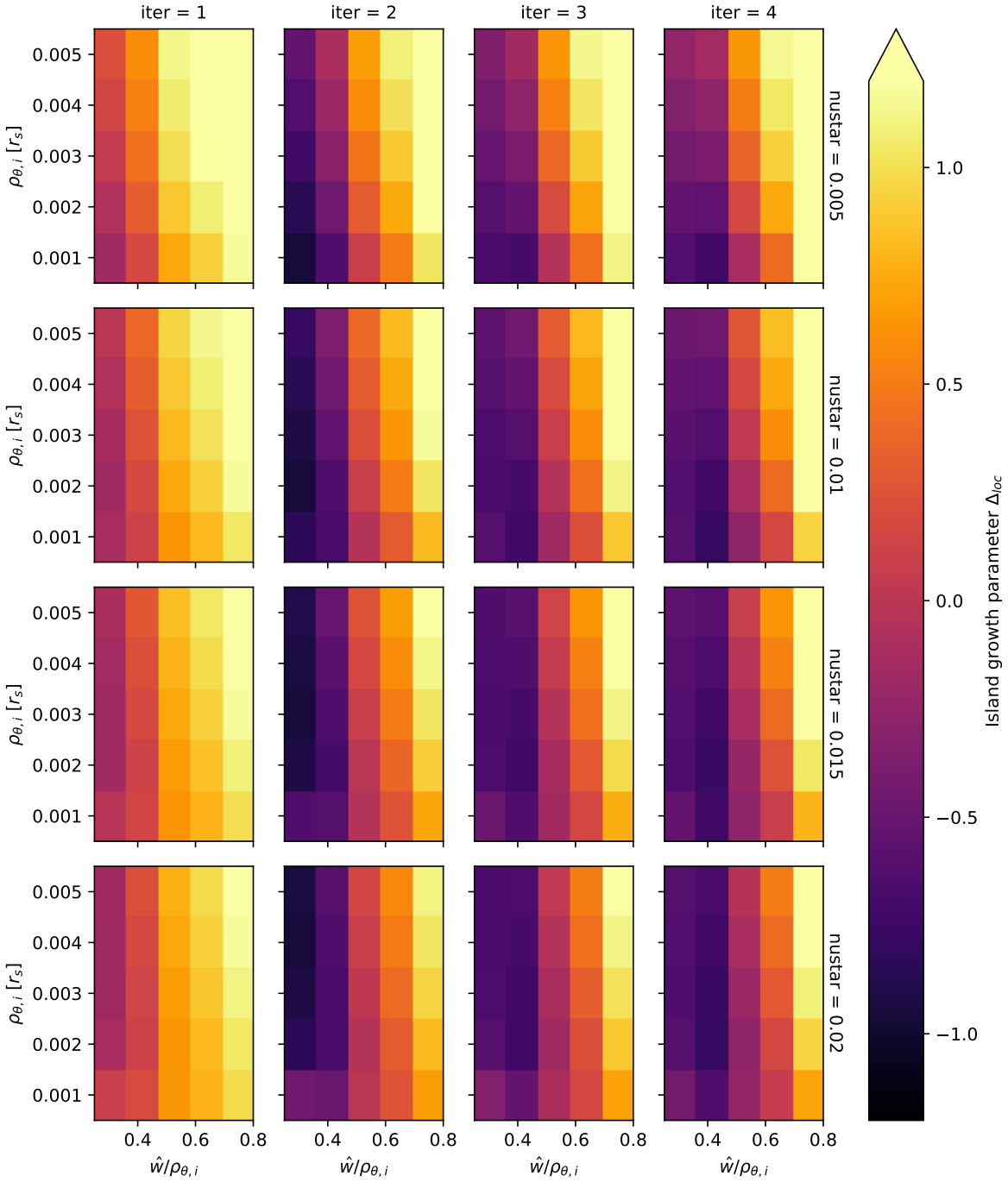

Figure 6.3: Contour plot of the total parallel current contribution Δ_{loc} to the modified Rutherford equation. In each panel Δ_{loc} (colour) is plotted vs. $\hat{w}/\hat{\rho}_{\theta,i}$ (x-axis) and $\hat{\rho}_{\theta,i}$ (y-axis), arranged by iteration number (column) and $\nu_\star$ (row).

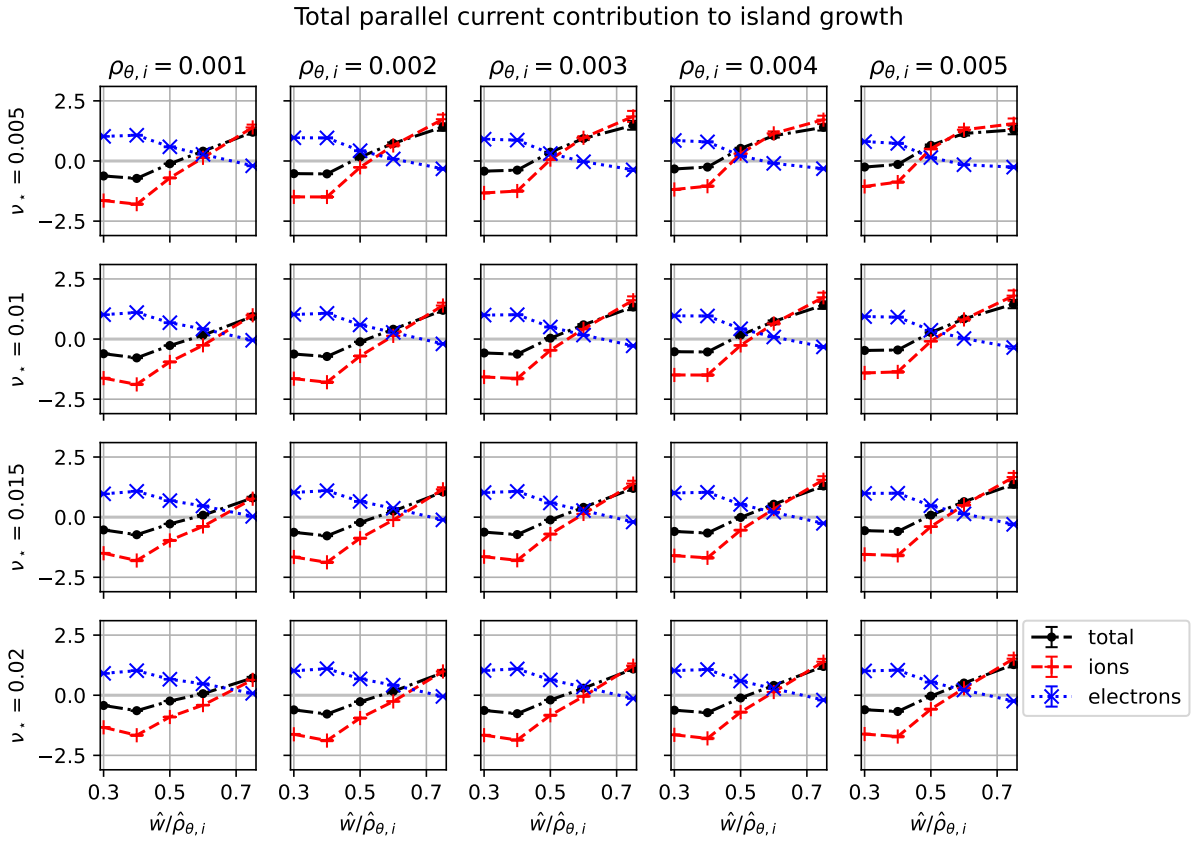

Figure 6.4: Line plot of the total neoclassical parallel current contribution Δ_{loc} to island growth and its contributions by species, including ions (red, dashed), electrons (blue, dotted) and the total (black, dash-dot), at iteration 4 of each simulation. In each panel Δ_{loc} is plotted vs. $\hat{w}/\hat{\rho}_{\theta,i}$, arranged by $\hat{\rho}_{\theta,i}$ (column) and $\nu_\star$ (row).

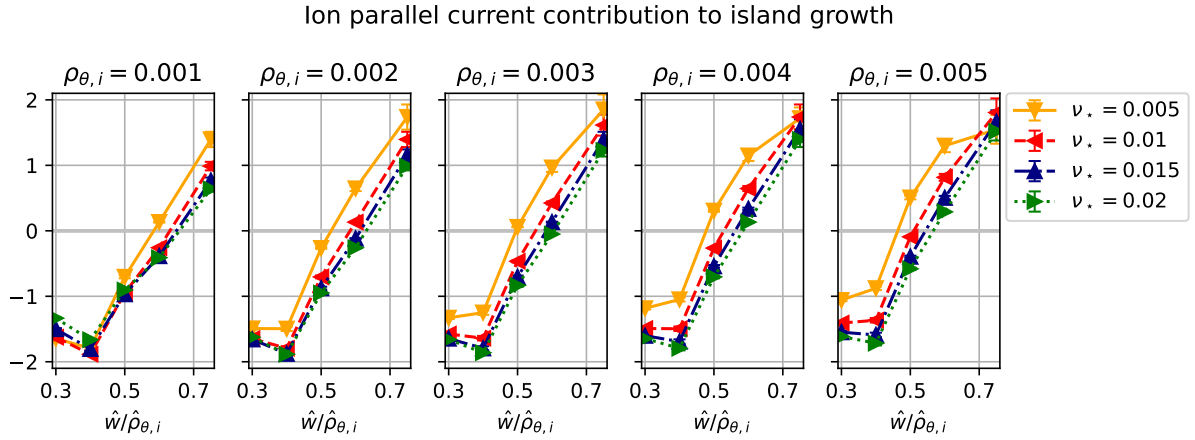

Figure 6.5: As in Fig.6.4, showing only the ion contribution to Δ_{loc}. Lines added for visual aid, line style indicates value of $\nu_\star$.

6.2.1 Bootstrap current drive

Fig.6.6 shows each species' contributions to Δ_{loc} from the flux surface-average of $J_{\|}$. These contributions to Δ_{loc} include the bootstrap current and curvature, however in our working limit $\epsilon \ll 1$, only the bootstrap current is non-negligible. Here, its contribution to Δ_{loc} is denoted Δ_{bs}.

Over the range $0.3 \leq \hat{w}/\hat{\rho}_{\theta,i} \leq 0.75$, the total bootstrap current Δ_{bs} is inversely proportional to $\hat{w}$ for the full range in $\hat{\rho}_{\theta,i}$ and $\nu_\star$. This is in agreement with previous work [50, 46] where a similar relationship $\Delta_{bs} \propto \hat{w}^{-3}$ was identified, as discussed previously in Sec.1.4. The dominant species contributing to the total Δ_{bs} is the electrons, whose contribution also scales inversely with increasing $\hat{w}$, and is significantly larger in magnitude than the ion contribution over this range in island width where $\hat{w} \lesssim \hat{\rho}_{\theta,i}$.

The ion contribution, shown by itself in Fig.6.7, increases smoothly with $\hat{w}/\hat{\rho}_{\theta,i}$, initially slowly at $\hat{w} = 0.3$, then changing from destabilising to stabilising above a value in $\hat{w}$ within the range $0.6 - 0.75\hat{\rho}_{\theta,i}$. At $\epsilon = 0.1$, this corresponds with roughly 2 ion banana widths $\rho_{b,i} = \epsilon^{1/2}\hat{\rho}_{\theta,i}$, where the magnetic island threshold width has been previously observed [66]. At the high end in $\hat{w} = 0.75\hat{\rho}_{\theta,i}$, for $\hat{\rho}_{\theta,i} \geq 4 \times 10^{-3} r_s$ and $\nu_\star \leq 0.01$, the ion term Δ_{bs} is seen to increase more slowly, making the Δ_{bs} curve for ions resembles the peak-shaped profile seen in previous work [70, 41], albeit at the low end in island width $\hat{w}$. As the same trend is seen in the *total ion current* contribution Δ_{loc} within Fig.6.4, the ion bootstrap current drive term Δ_{bs} is therefore the main contribution to the ion Δ_{loc} term. As collisionality $\nu_\star$ increases from $0.005 - 0.020$, the threshold width where the sign change in the ion Δ_{bs} term slightly increases. Both of these effects are consistent with the physical picture that the drift island behaviour of the ion distribution when $\hat{w} \lesssim \hat{\rho}_{\theta,i}$ is the primary influence over the ion bootstrap current contribution to island growth [70, 41]. At sufficiently low $\hat{w}$, the bootstrap current 'hole' created by the magnetic island is restored, of which a higher $\nu_\star$ partly contributes to by enhancing cross-orbit transport across the island separatrix, smoothing the gradients in the current profile across the magnetic island that are otherwise flattened by the island perturbation, recalling Fig.5.15. By the same principle, the opposite outcome is seen for the electrons, whose poloidal gyroradius $\hat{\rho}_{\theta e} \ll \hat{\rho}_{\theta i}$ and drift island shift is far smaller than that of ions. The electrons will therefore continue to respond to the perturbed electrostatic potential in the vicinity of the magnetic island, and hence the bootstrap current perturbation carried by (passing) electrons drives the island's growth.

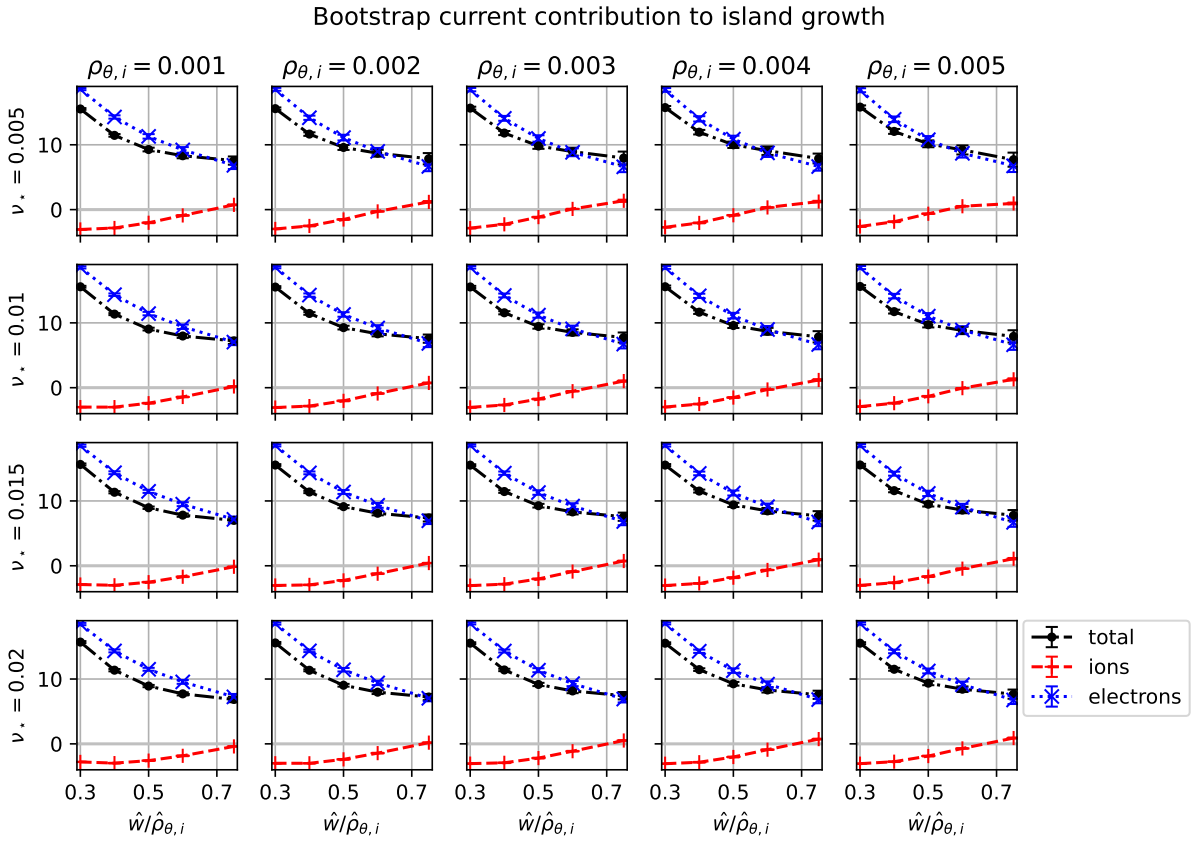

Figure 6.6: Bootstrap current contribution Δ_{bs} to the modified Rutherford equation by species, including ions (red, dashed), electrons (blue, dotted) and the total (black, dash-dot). In each panel Δ_{bs} is plotted vs. $\hat{w}/\hat{\rho}_{\theta,i}$, arranged by $\hat{\rho}_{\theta,i}$ (column) and $\nu_\star$ (row). Taken at the final iteration 4 of the simulation.

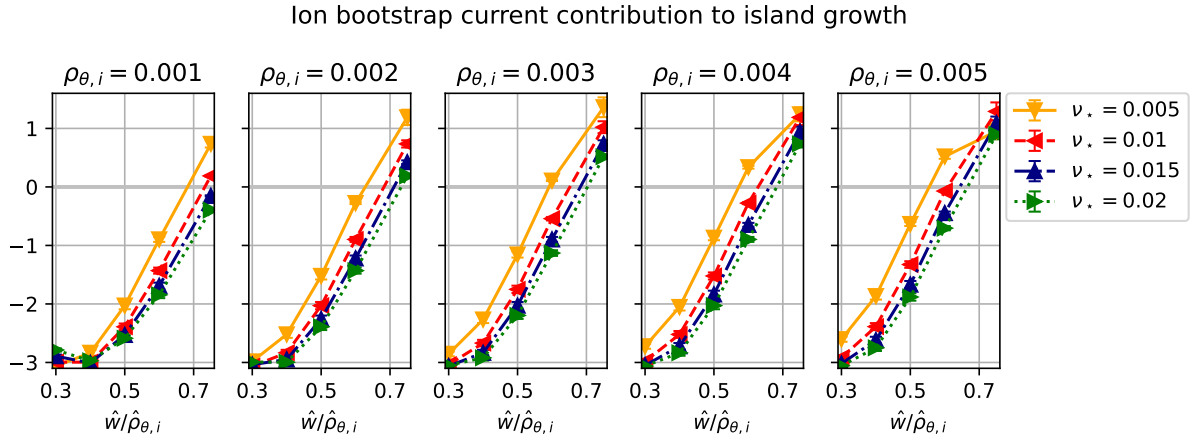

Figure 6.7: As in Fig.6.6, showing only the ion contribution to the bootstrap current drive Δ_{bs}. Lines added for visual aid, line style indicates value of $\nu_\star$.

6.2.2 Polarisation current drive

Fig.6.8 shows the contribution to Δ_{loc} from currents that disappear after flux surface-averaging, i.e. $\Delta_{loc} - \Delta_{bs}$. This is treated here to be the parallel return current that results from the polarisation current, whose contribution to the modified Rutherford equation Δ_{pol} was described within Sec.1.4. This result was previously unseen in Refs. [70, 41]. The ion polarisation current contribution, which is again smaller in magnitude than the total and electron contribution, is shown by itself in Fig.6.9. Here, over the full range in $0.3 \leq \hat{w}/\hat{\rho}_{\theta,i} \leq 0.75$, the ion contribution is destabilising and decreasing at higher $\hat{w}/\hat{\rho}_{\theta,i}$, but its value at $\hat{w}/\hat{\rho}_{\theta,i} = 0.4$ is noticeably smaller than at 0.3 and 0.5, thereby producing the 'flattened' profile seen earlier in Fig.6.6. There are insufficient datapoints in $\hat{w}/\hat{\rho}_{\theta,i}$ to determine the appropriate shape of the profile, but this same profile is seen across the full range in $\hat{\rho}_{\theta,i}$ and $\nu_\star$, indicating a possible physical origin.

The electron polarisation current Δ_{pol} is the largest contribution to Δ_{pol} as well as Δ_{bs}, and is also inversely proportional to $\hat{w}/\hat{\rho}_{\theta,i}$. It exceeds the electron contribution to Δ_{bs} in magnitude at higher $\hat{w}/\hat{\rho}_{\theta,i}$, causing Δ_{loc} for electrons to change sign in Fig.6.4. However, this large electron polarisation current is not explained by the present theory [50, 46], where the ion contribution is expected to dominate as the ions' transport is $\mathbf{E}\times\mathbf{B}$-dominated at the scale $\hat{\rho}_{\theta e} \ll \hat{\rho}_{\theta,i} \sim \hat{w}$. Both species' contributions change relatively little over the range of collisionality $\nu_\star = \{0.005, 0.020\}$ and ion poloidal gyroradii $\hat{\rho}_{\theta,i} = \{1, 5\} \times 10^{-3} r_s$. For ions, the profiles shown in Fig.6.9 appear to be more sensitive to $\nu_\star$ at high $\hat{w}/\hat{\rho}_{\theta,i}$ and at low $\hat{\rho}_{\theta,i}$, as indicated by the spread in values for each profile in $\nu_\star$.

Regarding the total Δ_{pol}, because this exceeds the (destabilising) Δ_{bs} term in magnitude over the range $\hat{w} \lesssim 0.6$, this produces the threshold width in $\Delta_{loc}(\hat{w}) = \Delta_{bs}(\hat{w}) + \Delta_{pol}(\hat{w}) = 0$ seen earlier in Fig.6.6. This is the expected behaviour at low $\hat{w}$, as described in Ref. [50] for the case where the polarisation current term for island growth is stabilising and able to surpass the bootstrap current's influence.

Finally, we note that presently we consider islands whose island rotation rate $\omega_E = 0$ relative to the rotational rest frame where the electric field $E_\parallel$ far from the magnetic island is zero as Refs. [50, 70] did, as island rotation is beyond the scope of this work. To more accurately represent the polarisation current, a scan across ω_E would be required, and the valid Δ_{pol} should be extracted at the value in ω_E that provides torque balance between the island and plasma bulk. This has been recently attempted in the low-collisionality limit `RDK-NTM` code [43], and should be considered for future work with `kokuchou`.

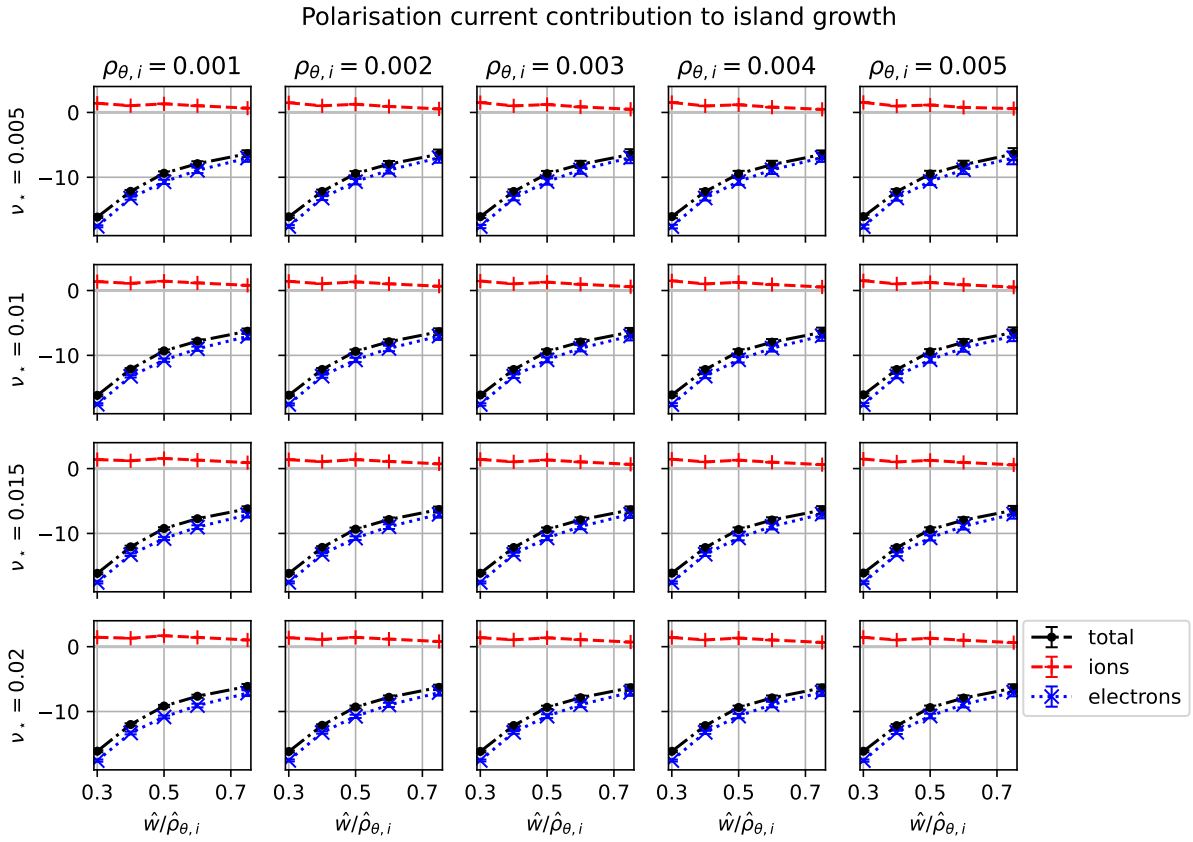

Figure 6.8: Polarisation current contribution Δ_{pol} to the modified Rutherford equation by species, including ions (red, dashed), electrons (blue, dotted) and the total (black, dash-dot). In each panel Δ_{pol} is plotted vs. $\hat{w}/\hat{\rho}_{\theta,i}$, arranged by $\hat{\rho}_{\theta,i}$ (column) and $\nu_\star$ (row).

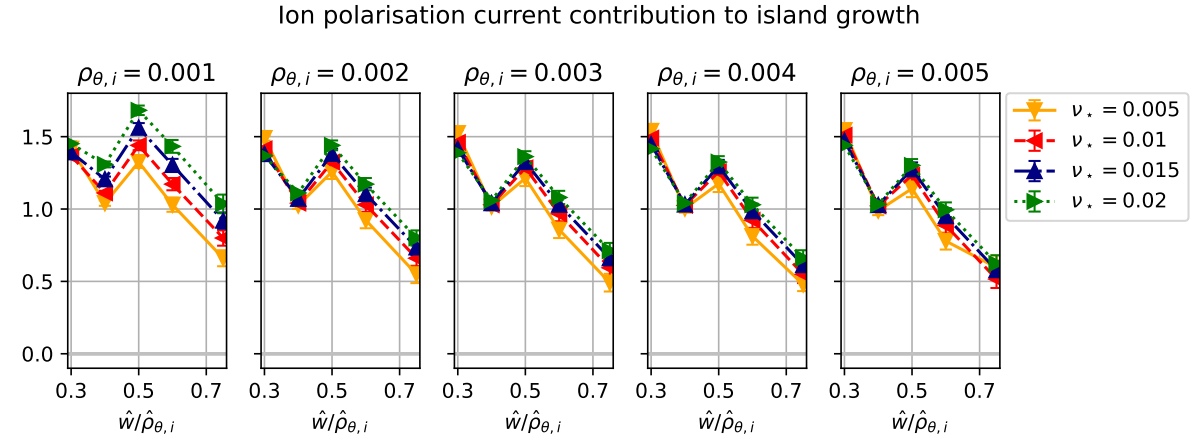

Figure 6.9: As in Fig.6.8, showing only the ion contribution to the polarisation current drive Δ_{pol}. Lines added for visual aid, line style indicates value of $\nu_\star$.

6.3 Threshold width scaling

6.3.1 1D linear regression of $w_c(\hat{\rho}_{\theta,i})$ at different $\nu_\star$

The NTM threshold island width w_c corresponds with the value of $\hat{w}$ where the total drive term $\Delta_{loc}(\hat{w}) = 0$; this is obtained via linear interpolation at fixed $\hat{\rho}_{\theta,i}$ and $\nu_\star$. Fig.6.10 shows these values of w_c plotted with respect to $\hat{\rho}_{\theta,i}$. For each value in $\nu_\star$, a least-squares linear fit is performed. The standard deviation of each fit is indicated by the shaded regions of each profile.

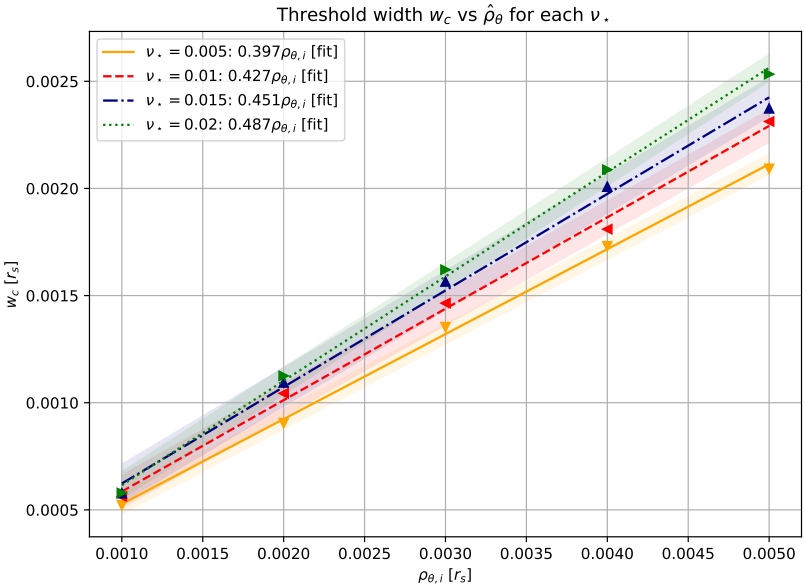

Figure 6.10: Linear fit functions of threshold width / ion poloidal gyroradius ratio $w_c/\hat{\rho}_{\theta,i}$ for each collisionality $\nu_\star$, fitting to points in $\hat{w}$ where $\Delta_{loc}(w_c) = 0$, versus $\hat{\rho}_{\theta,i}$. Lines added for visual aid. Error bars given by standard deviation of the least-squares fit.

For all 4 values in $\nu_\star$, Fig.6.10 illustrates a linear relationship of w_c with $\hat{\rho}_{\theta,i}$, which is in agreement with both experimental measurements of the threshold width in $m/n = 2/1$ NTMs [66] in finite ϵ tokamak geometries[1], and with the previous simulation results of the `DK-NTM` (Ref.[70] Fig.9) and `RDK-NTM` models (Ref.[41] Fig.10) for 2/1 NTMs in the $\epsilon \ll 1$ limit. A novel result seen here is that the gradient of w_c versus $\hat{\rho}_{\theta,i}$ also scales proportionally with collisionality $\nu_\star$, as shown by the gradient in each linear least squares fit in Fig.6.10. Though the magnitude of Δ_{loc} and its contributions in Fig.6.4 were seen to change little with collisionality over the range $\nu_\star = \{0.005, 0.020\}$, the value of $\hat{w}$ where $\Delta_{loc} = 0$ was seen to increase over the range in $\hat{w}/\hat{\rho}_{\theta,i}$,

[1] [66] Fig.6 is an empirical fit of the *full* marginal island width $w_{marg} = 2w_c$ vs $\epsilon^{1/2}$ containing data from the conventional tokamak DIII-D and the spherical (high ϵ) tokamak NSTX.

translating into a significant, albeit gradual $\nu_\star$-dependence of the threshold width w_c.

Fig.6.11 shows the values of the gradients of each fit across $w_c/\hat{\rho}_{\theta,i}$ from Fig.6.10 plotted with respect to $\nu_\star$. Shown here are previous $w_c/\hat{\rho}_{\theta,i}$ scaling results at $\nu_\star = 10^{-3}$ obtained from the 4D `DK-NTM` code in Ref. [70] (blue triangle), the reduced 3D code `RDK-NTM` of Ref. [41] (green star). Also shown by the magenta lines are values for the experimentally-derived result of the scaling of w_c with $\hat{\rho}_{\theta,i}$ (neglecting collisionality dependence) from Fig.6 of La Haye et al, Ref. [66] (solid line) and its standard deviation (dashed lines). The experimental dataset contained two real-world tokamaks (NSTX, DIII-D) for both $m/n = 2/1$ and $m/n = 3/2$ modes. The same data is also shown in Fig.6.12, illustrating the `kokuchou` data and its collision frequency dependence more visibly. Performing a further least-squares linear fit to the `kokuchou` datapoints, the threshold width is seen to scale linearly and proportionally with collisionality $\nu_\star$. The fitting function for the threshold width w_c with respect to ion poloidal gyroradius $\hat{\rho}_{\theta,i}$ and $\nu_\star$ in the high aspect ratio limit $\epsilon \ll 1$, within the range $\nu_\star = \{5, 20\} \times 10^{-3}$ and $10^{-3} r_s \leq \hat{\rho}_{\theta,i} \leq 5 \times 10^{-3} r_s$ is:

$$\frac{w_c}{\hat{\rho}_{\theta,i}} = 6.247\nu_\star + 0.367 \tag{6.3.1}$$

This novel result, where w_c scales linearly and proportionally to $\nu_\star$, is qualitatively in line with the existing picture that a higher collision frequency contributes to the healing of small islands through enhanced radial transport across the island [45, 46, 47]. Quantitatively, the linear relationship suggests that further increases in collisionality $\nu_\star$ (e.g. $O(10^0)$ or higher) will greatly increase the scaling of w_c versus $\hat{\rho}_{\theta,i}$ by factors $O(\hat{\rho}_{\theta,i})$, which has significant implications. However, we stress this scaling is valid only in this range in $\nu_\star$ and a broader range of $\nu_\star$ would be needed to determine the wider extent of the relationship of w_c with $\nu_\star$. Nonetheless, all points of the `kokuchou` dataset lie within one standard deviation of the linear least squares fit.

Comparing this new result from `kokuchou` with the `DK-NTM` result of Ref. [70], the former is now aligned with the reduced dimension `RDK-NTM` code of Ref. [41] that operates in the limit of low $\nu_\star$. It is also closer to the experimental fit result of La Haye et al in Ref. [66], but still lies beyond one standard deviation of that result. This outcome is attributed to the amendments made to the ion drift kinetic equation outlined in Sec.2.6, and careful testing and verification of intermediate terms within `kokuchou`. Unlike both the `DK-NTM` and `RDK-NTM` results presented here, no threshold width result for `kokuchou` was obtained at $\nu_\star = 0.001$, and so a direct comparison over the same operating parameter space would be desirable for future work.

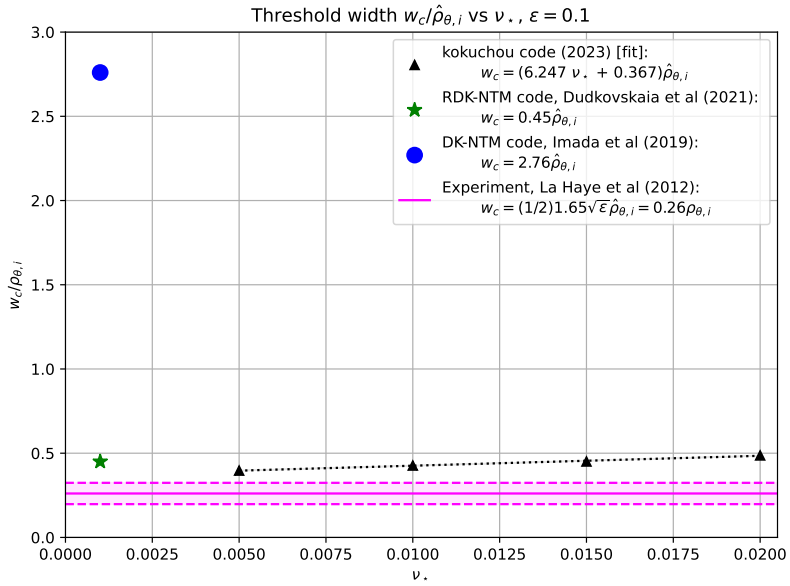

Figure 6.11: $w_c/\hat{\rho}_{\theta,i}$ dependence versus $\nu_\star$ for `kokuchou` results (linear least-squares fit of gradients of Fig.6.10), plotted with the original `DK-NTM` code result of Ref. [70], the reduced-dimension code `RDK-NTM` result of Ref. [41], and the empirical fit of experimental measurements of 2/1 NTMs extracted from Ref. [66] Fig.6, with standard deviations (magenta dashed lines).

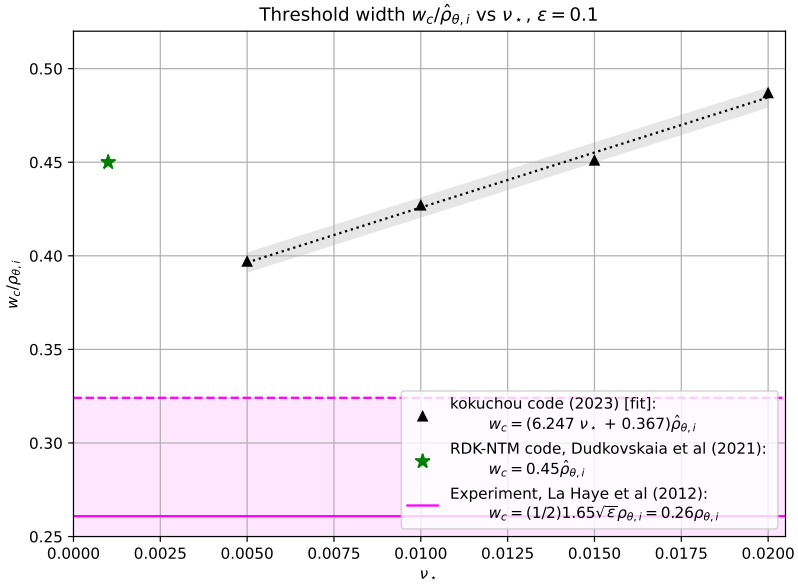

Figure 6.12: As in Fig.6.11, zoomed in on the `kokuchou` results to show the $\nu_\star$-dependence. A least-squares linear fit across `kokuchou` datapoints is shown by the dashed black line. The grey error bar indicates one standard deviation of the linear fit.

6.3.2 2D linear regression of $w_c(\hat{\rho}_{\theta,i}, \nu_\star)$

Previously in Fig.6.11-6.11, the scaling of w_c with $\hat{\rho}_{\theta,i}$ at different values in $\nu_\star$ was compared with corresponding $w_c(\hat{\rho}_{\theta,i})$ results in literature. Here, the $\nu_\star$ dependence of only the *gradient* of $w_c/\hat{\rho}_{\theta,i}$ was estimated to infer how the result may compare with the 3D code in the low-$\nu_\star$ limit.

Instead, we consider a 2D multiparameter fit of the threshold width w_c with both the variables $\hat{\rho}_{\theta,i}$ and $\nu_\star$. An ordinary least squares linear regression model[2] was fitted to the dataset of 20 w_c values. Given w_c is expected to scale linearly with both variables over this operating space, a planar function for the prediction of $w_c(\hat{\rho}_{\theta,i}, \nu_\star)$ is obtained:

$$w_c[r_s] \approx 0.440\hat{\rho}_{\theta,i}[r_s] + 0.0178\nu_\star - 7.54 \times 10^{-5} \tag{6.3.2}$$

Eq.(6.3.2) is plotted with the `kokuchou` w_c data set in Fig.6.14. In Fig.6.14, each of the 20 data points in $w_c(\hat{\rho}_{\theta,i}, \nu_\star)$ are plotted with respect to their predicted values from the regression. The prediction is accurate, as evidenced by the low mean squared error of the regression ($3.36\times10^{-9} r_s$) and its coefficient of determination $R^2 = 0.9916$ being close to the ideal value of 1. However, we anticipate the w_c dependence on $\nu_\star$ would no longer be linear as $\nu_\star$ approaches either extreme of 0 (the collisionless limit) or 1, outside the collisional banana regime required for neoclassical transport. These scenarios should be explored in future work to clarify this relationship.

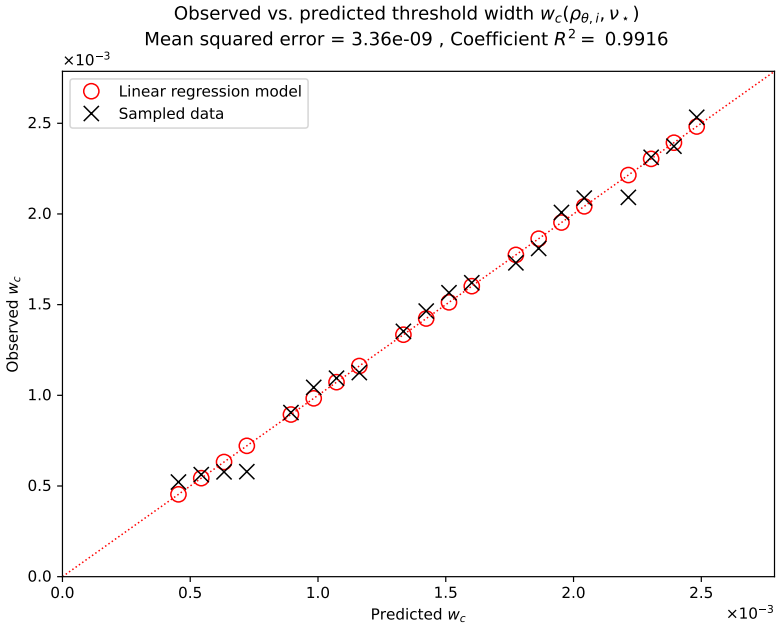

Figure 6.13: Prediction of $w_c(\hat{\rho}_{\theta,i}, \nu_\star)$ from the multivariate linear regression model.

[2] Using *scikit-learn* LinearRegression model, v.1.2.2.

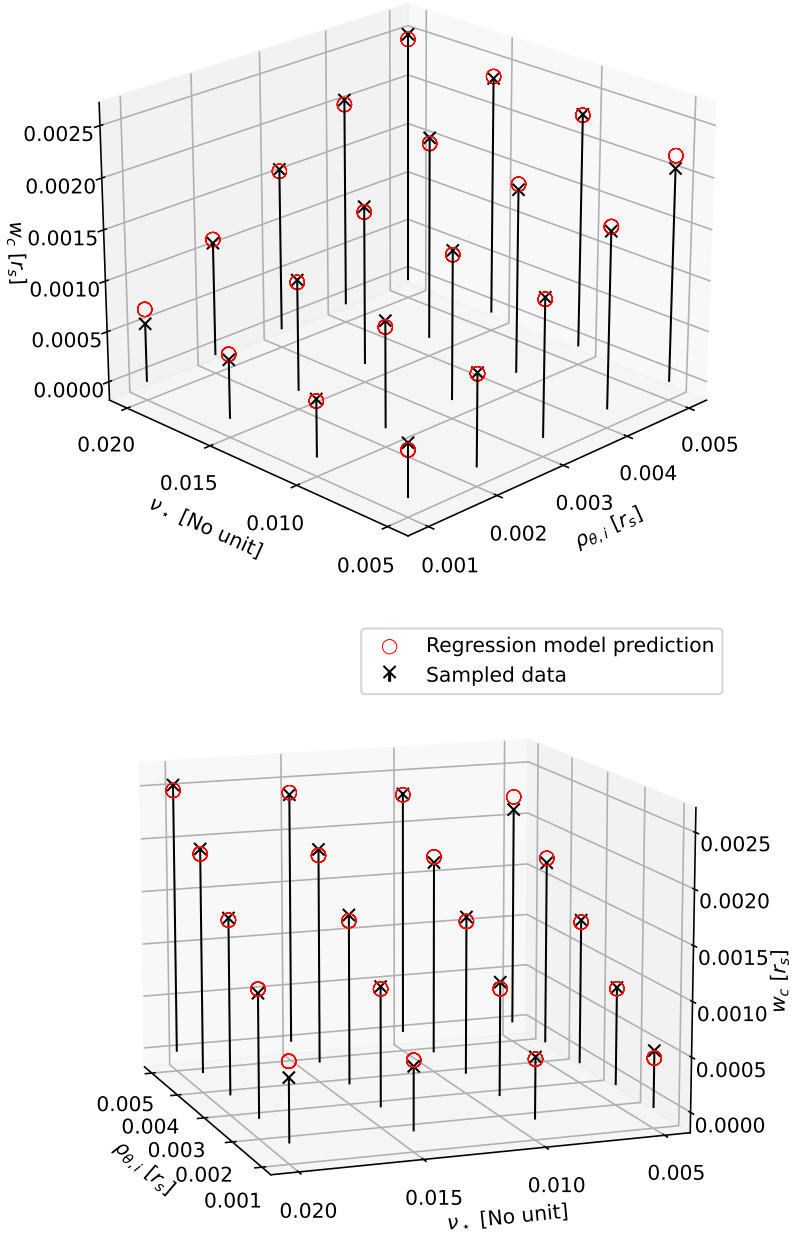

Figure 6.14: 3D plots of the simulated NTM threshold island width $w_c(\hat{\rho}_{\theta,i}, \nu_\star)$ obtained from `kokuchou` (black crosses), and their corresponding predicted values (red circles) from Eq.(6.3.2), a multiple linear regression fitted to the simulated values, plotted with respect to ion poloidal gyroradius $\hat{\rho}_{\theta,i}$ and collisionality $\nu_\star$.

Summary

This chapter presented a parameter scan over a range of values in collisionality, ion poloidal gyroradius and island width. The erroneous result presented in Sec.5.3 was investigated from the perspective of the electrostatic potential $\hat{\Phi}$, which was identified to be a dominant influence on the narrow separatrix layer surrounding the drift island in the perturbed ion distribution $\hat{g}$. At lower $\nu_\star$ and higher $\hat{w}$, $\hat{g}$ became highly sensitive to changes in $\hat{\Phi}$ (and vice versa), effectively imposing operating limits for these parameters within the simulation code. Valid results were obtained for all simulations conducted except those at $\nu_\star < 5 \times 10^{-3}$ due to numerical instability (see Sec.5.3).

From the final iteration of each run, the contributions of the neoclassical parallel 'layer current' density to the modified Rutherford equation for island growth were calculated, the total of these contributions was denoted Δ_{loc}. Its components included the so-called bootstrap (Δ_{bs}) and polarisation (Δ_{pol}) currents, each with ion and electron parts. The total Δ_{loc} was influenced mostly by the ion currents, both terms changing sign over the range $0.5 \leq \hat{w}/\hat{\rho}_{\theta,i} \leq 0.75$. At lower $\hat{w}$, the ion Δ_{loc} term was stabilising as expected, while the electron term was destabilising. Both species' terms changed sign at higher $\hat{w}/\hat{\rho}_{\theta,i}$, while at the very low value of 0.3 they were seen to flatten. The bootstrap term Δ_{bs} and polarisation term Δ_{pol} were both dominated by the electron currents, and were destabilising and stabilising over this range in $\hat{w}/\hat{\rho}_{\theta,i}$ respectively. The ion bootstrap term $\Delta_{bs,i}$ changed sign as Δ_{loc} did, while the polarisation term was destabilising and decreasing with increasing $\hat{w}/\hat{\rho}_{\theta,i}$ over this range. Notably, the ion Δ_{pol} term contained a jump at $\hat{w}/\hat{\rho}_{\theta,i} = 0.3 - 0.4$ whose cause is not fully understood, but appears consistently at all values in $\hat{\rho}_{\theta,i}$ and $\nu_\star$. The electron polarisation term Δ_{pol} was also stabilising over this range and significantly larger in magnitude than the ion term, which cannot be explained by the existing theory and is likely a result of the implementation used in this work where island rotation is not considered.

From the results for Δ_{loc}, novel results for the relationship of w_c and collisionality were found. Firstly, the 1D relationship of w_c with $\hat{\rho}_{\theta,i}$ at different values in $\nu_\star$ was obtained by interpolating in $\hat{w}/\hat{\rho}_{\theta,i}$ where $\Delta_{loc} = 0$ and performing a 1D least-squares linear fit across those values. These results were in alignment with the `RDK-NTM` code of Ref. [41] and a significant improvement over that of the previous 4D NTM code `DK-NTM` of Ref. [70]. Secondly, the 2D scaling law for the threshold width with both $\hat{\rho}_{\theta,i}$ and $\nu_\star$ was estimated via multiple linear regression to a very good degree of accuracy (see Eq.(6.3.2)). The positive correlation of $w_c[r_s]$ with $\nu_\star$ demonstrates the

healing effect of higher collision frequency on small islands, and its synergy with the drift island effect which scales as $\propto \hat{\rho}_{\theta,i}$.

The result of $w_c/\hat{\rho}_{\theta,i}$ from `kokuchou` is also closer to the experimental result of Ref. [66] but direct alignment remains to be achieved. Here we note that the data extracted from Ref. [66] in Fig.6.11 contained real-world physical details that are not regarded in `kokuchou`, including finite island rotation (which affects the polarisation current, see Sec.6.2.2), island widths of $O(0.01r_s)$ that are an order of magnitude greater than used in `kokuchou`, a larger aspect ratio $\epsilon \sim \{0.4 - 0.56\}$, and a shaped plasma cross-section.

Chapter 7

Conclusions

This work concerned plasma instabilities and the obstacles they present to the development of tokamaks, toroidal magnetic confinement fusion devices which generate energy by sustaining a high-temperature, high-pressure plasma in hydrodynamic equilibrium over long durations. Its focus was the performance-limiting resistive MHD instability known as the neoclassical tearing mode (NTM), characterised by the growth of magnetic island structures, driven by the filamentation of magnetic field-parallel neoclassical currents including the bootstrap current. NTMs are particularly problematic for modern 'high-gain' tokamaks such as ITER, due to their tendency to occur at high normalised plasma pressures or poloidal beta, and in low collisionality 'banana regime' scenarios where trapped particles and the bootstrap current can exist. To mitigate the possible disruptions NTMs can cause, magnetic islands must be quickly removed from the plasma before they grow to large size. Experiments indicated that both island width and poloidal beta must exceed threshold values for growth to occur, otherwise the island shrinks.

The main result of this work was to develop a predictive theory for the threshold island half-width w_c, given known plasma parameters. The growth rate of the magnetic island half width w was tracked by the modified Rutherford equation [60], where the evolution of small islands was determined primarily by the bootstrap and polarisation currents, and also influenced by radial diffusion across the island. Given that experimentally [32, 34, 66] the threshold width w_c was observed to be comparable to $\rho_{b,i}$, the trapped ion banana orbit width, a theoretical model of the threshold width island physics must account for the guiding centre motion of ions, finite trapped ion orbit effects and quasineutrality due to differing ion and electron responses to the island.

To this effort, a new 4D numerical simulation code `kokuchou` was developed based on the drift-kinetic formalism of Ref. [50] as a novel successor to the `DK-NTM` code of Ref. [70]. This employed a numerically-calculated kinetic treatment for ions, while an analytic representation for electrons [50] was used due to their smaller banana orbit width $\rho_{b,e} \ll \rho_{b,i} \sim w$. For simplicity, we worked in the limit of low inverse aspect ratio $\epsilon = r_s/R_0 \ll 1$ and expanded the drift-kinetic equation in terms of small $\Delta = w/r_s \ll 1$. Here, r_s is the minor radius of the rational surface where the simulated magnetic island was situated, and R_0 is the major radius. Within these limits, a dimensionality reduction was performed by noting the canonical angular momentum p_φ was a constant of motion along ion orbits. Higher order terms were then eliminated by taking their average in poloidal angle θ at fixed p_φ. This produced a 4D drift-kinetic equation for the perturbed ion distribution $\hat{g}$ in the vicinity of the island that is accurate to $O(\epsilon^{3/2})$, with different forms for passing and trapped ions that were matched at the trapped-passing boundary in velocity pitch angle y-space. An iterative approach was used where two equation terms that depended on $\hat{g}$, which included the electrostatic potential satisfying quasineutrality $\hat{\Phi}$ and the ion flow-like momentum-conserving collision operator term $\hat{\bar{U}}_\parallel$, were both updated each time perturbed ion solution $\hat{g}$ was recalculated. This provided a degree of self-consistency between the terms of the equation. Unit tests were developed to validate the intermediate stages of the algorithm in the new code `kokuchou`. These also helped to identify and address a critical numerical issue in the trapped-passing boundary calculation that was also identified in the `DK-NTM` code.

The main results consisted of `kokuchou` simulations over a range of island widths $\hat{w}$, ion poloidal gyroradius $\hat{\rho}_{\theta,i}$ (both normalised to r_s) and collisionality $\nu_\star$. This work led to the following conclusions, applicable to a small near-threshold size magnetic island (of the ordering $\rho_{b,e} \ll \rho_{b,i} \sim w_c \lesssim \rho_{\theta,i} \ll r_s$) at rest with respect to the bulk plasma on a $m/n = 2/1$ rational surface in a high aspect ratio ($\epsilon \ll 1$) circular cross section tokamak in the absence of Shafranov shift:

- As previously studied in Refs. [70, 41], when the normalised island half-width $\hat{w}$ and ion poloidal gyroradius $\hat{\rho}_{\theta,i}$ (each normalised to r_s) are comparable, the passing ion ($y < y_c$) distribution is flattened across structures described as 'drift islands', as opposed to the magnetic island proper.

- These drift island structures were radially shifted due to magnetic drifts. The size of the shift was provided by the ∇B drift coefficient of $\dfrac{\partial \hat{g}}{\partial \xi}$, that scaled as $\propto \hat{\rho}_{\theta,i}\hat{\omega}_D\hat{L}_q^{-1}$, where $\hat{\omega}_D(y,\sigma,u)$ is the drift frequency and $\hat{L}_q$ is the magnetic shear length scale normalised to r_s.

The drift island shift was largest when $\hat{w} < \hat{\rho}_{\theta,i}$, and also at high speed u, zero pitch-angle y (noting the form of $\hat{\omega}_D$ in Eq.(2.3.48)). This velocity-space dependence resulted in the differences in profile for $\hat{\Phi}$ and $\hat{\bar{U}}_{\parallel}$, both dependent on the velocity-integral of $\hat{g}$.

- Increasing the collisionality $\nu_\star$, which enhances radial transport across the drift island separatrix, was seen to slightly broaden the ion distribution at the separatrix, but only led to visible change at higher values of $\hat{w}/\hat{\rho}_{\theta,i}$ where the drift island shift is small and the separatrices of all drift islands are aligned.

- The presence of the electrostatic potential $\hat{\Phi}$ on further iterations provided a significant contribution to the drift-kinetic equation, particularly when $\hat{w} \gtrsim \hat{\rho}_{\theta,i}$. Larger island widths and lower $\nu_\star$ produced greater changes in $\hat{\Phi}$ between iterations, as the $\hat{\Phi}$-dependent $\mathbf{E} \times \mathbf{B}$ drift term then competes with the other terms in $\dfrac{\partial \hat{g}}{\partial p}$ that are of $O(\hat{w}^2)$ and $O(\nu_\star)$ respectively.

A large scale parameter scan was then conducted, which produced the following novel results:

- A novel relationship between threshold width w_c, ion poloidal gyroradius $\hat{\rho}_{\theta,i}$ and collisionality $\nu_\star$ over the working parameter space was identified, given by $w_c[r_s] \approx 0.440\hat{\rho}_{\theta,i}[r_s] + 0.0178\nu_\star - 7.54 \times 10^{-5}$. The threshold width $w_c/\hat{\rho}_{\theta,i}$ scaled proportionally and linearly with $\nu_\star$ was over the range $\nu_\star = 5 - 20 \times 10^{-3}$. This is in line with the present physical explanation that a higher collision frequency leads to enhanced radial transport across the magnetic island via collisions, contributing to the healing of small islands thereby raising the threshold width.

- Compared with the `DK-NTM` code [70], the result for w_c from `kokuchou` was closer to that of both the reduced-dimension low-collisionality limit `RDK-NTM` code of Ref. [41] and the experimentally-derived empirical result of Ref. [66] for $m/n = 2/1$ modes in NSTX and DIII-D, a spherical and conventional tokamak respectively.

- The improved result was attributed to the amendments made to the derivation of the 4D drift-kinetic equation for ions, originally presented in Ref. [70]. Testing capabilities within `kokuchou` were also critical in verifying the terms and procedures within the program.

- The amended equation introduced $\hat{\rho}_{\theta,i}^2$ dependence to the neoclassical diffusion term in $\dfrac{\partial^2 \hat{g}}{\partial p^2}$, making the narrow separatrix layer more numerically challenging to resolve, particularly at

low $\nu_\star$ and high $\hat{w}$ where the $\mathbf{E} \times \mathbf{B}$ drift (via $\hat{\Phi}$) had a significant influence over the separatrix layer physics.

- There are limitations to the operating parameter space of `kokuchou`, which developed unstably growing broad-scale numerical instabilities when $\nu_\star$ was too low or $\hat{w}$ was too high. Both led to the 'wing-shaped' profiles shown in Fig.5.16, likely due to the insufficient resolution of the $\{\xi, p\}$ spatial mesh at the narrow drift island separatrix, exacerbated by the large changes in $\hat{\Phi}$ between iteration at larger $\hat{w}$, as discussed in 6.1.

7.1 Future work

The 4D drift-kinetic NTM equation and its implementation in `kokuchou` demonstrated a proof-of-concept for a predictive model for the threshold island width. Further work is required to address prevailing computational limitations (see Sec.3.1.6) to facilitate more rigorous explorations of parameter space and the incorporation of additional physical detail.

The first priority for future work with `kokuchou` should be to implement a more efficient meshing scheme (via a finite element discretisation) that provides finer resolution around the steep gradients of the *drift island* separatrix. The present Cartesian spatial mesh and finite difference discretisation used in `kokuchou` does not provide the scalability necessary to explore large islands in lower-collisionality scenarios where the separatrix width is expected to be very narrow relative to the island. The main challenge of redesigning the spatial meshes to follow the drift island separatrix is handling the velocity-space dependence of the radial shift of the drift island. This may involve converting the radial p_φ coordinate (Eq.(2.3.13)) to a new coordinate [84], denoted here as $\tilde{p}$, that accounts for the shift of the drift island via the second term:

$$\tilde{p} = \psi - I(\psi) \left(\frac{v_\parallel(\theta)}{\omega_{c,i}(\theta)} - \frac{v_\parallel(\theta = 0)}{\omega_{c,i}(\theta = 0)} \right) \tag{7.1.1}$$

The form of Eq.(2.3.47) would be modified further, introducing many new terms to the y-derivatives that would then be evaluated at fixed $\tilde{p}$. By accounting for the drift island shift, the p mesh (Fig.3.2) would no longer need to span a large extent to capture islands of different radial shift, overcoming the limitations set by the maximum velocity and $\hat{\rho}_{\theta,i}$. Mesh points can then be packed around the steep gradients of the drift island separatrix at the same location in $\tilde{p}$ for all drift islands, and the drift island shift will be preserved in the other radial mesh coordinate x (normalised ψ). A similar approach has been accomplished within the reduced dimension

3D `RDK-NTM` code that is applicable only in the low-$\nu_\star$ limit, where the 2D (ξ, p) phase-space is reduced to a single 'streamline' dimension to provide finer mesh resolution localised to the drift island [41]. The more efficient meshing scheme also allowed for the numerical calculation of electrons within this work, whose orbit length scales are far smaller than those of ions. This approach however sacrifices the ability to explore finite collisionality and its effects studied within this work, which must then be introduced analytically or via partial numerical implementations.

Another computational issue to address is related to the 'winged' distribution in p-space observed in Fig.5.16 where a numerically-valid non-physical result was seen on later iterations. A more ambitious but equally valuable technical improvement would be to implement an analytic result for Eq.(2.3.47) in the limit of large p, to use in addition to (or in place of) the $\dfrac{\partial \hat{g}}{\partial p}$ boundary condition. This may also help the algorithm avoid the non-physical "winged" distributions seen in $\hat{\Phi}$ and $\hat{\bar{U}}_{\|}$ for low $\nu_\star$ and high $\hat{w}/\hat{\rho}_{\theta,i}$, if there are multiple numerically-valid solutions for $\hat{g}$ satisfying $\dfrac{\partial \hat{g}}{\partial p} = 0$. Computationally, this would also reduce the need for a finely resolved p-mesh far outside the island. Improving the efficiency of the coordinate system will assist in resolving the electrostatic potential $\hat{\Phi}$ and helping it to converge after several iterations. In the meantime, a possible short-term means of addressing the issue of $\hat{\Phi}$ growing unstably is to reuse $\hat{\Phi}$ from a 'numerically stable' run as the initial state of another run where a stable result is not obtainable when starting with $\hat{\Phi} = 0$.

Once improvements have been made to the `kokuchou` numerical code, there are many further parameter studies that can be conducted for threshold-size islands. Performing experiments in finite island rotation rate ω_E would allow a stationary solution to be found where there is torque balance between the island and the electrostatic field far from the island, thereby providing a more accurate representation of the polarisation current's behaviour [52]. This is represented by the dispersion relation Eq.(18) of Ref. [50], and would involve studying the $\sin\xi$ component of current density as opposed to the $\cos\xi$ component for Δ_{loc}. A mode of $m/n = 2/1$ is assumed but introducing n to the derivation would allow for the modelling of other common NTMs like the 3/2 mode [34]. A parameter scan in inverse aspect ratio ϵ would verify whether the $w_c : \hat{\rho}_{\theta,i}$ scaling result corresponds with the banana width $\rho_{bi} = \epsilon^{1/2}\hat{\rho}_{\theta,i}$, and to identify the operating limit where the low-ϵ assumption is no longer valid. If stable numerical simulations at lower collisionalities are possible, a direct comparison or benchmarking with the low-collisionality limit `RDK-NTM` code in the limit $\epsilon \ll 1$ [41] would allow the difference between the two approaches to be quantified.

To achieve a result closer to the empirically-derived result of Ref. [66] and to experiments more generally, future work should incorporate plasma shaping, Shafranov shift, and relaxing the

$\epsilon \ll 1$ working limit within `kokuchou`. As discussed briefly in Sec.1.4, finite curvature introduces a stabilising drive term to the MRE which, assuming it is stabilising, would reduce the $w_c : \hat{\rho}_{\theta,i}$ gradient for the `kokuchou` dataset and bring it closer to the experimental measurement. Likewise, a finite island rotation rate ω_E that is of $\sim O(\omega_{*,i})$ will also account for the effects of island propagation on the growth rate. Both of these pieces of important physics were introduced to the reduced-dimension `RDK-NTM` code in Refs. [41, 43], within which a result in better agreement with Ref. [66] was obtained compared to the previous $\epsilon \ll 1$ result for that code shown in Fig.6.12.

A challenge for the wider field of NTMs is identifying the other physical mechanisms - besides island rotation - that influence the polarisation current, particularly at island widths that approach the full ion gyroradius $\rho_\theta \ll \rho_{\theta,i}$. This would require a much more rigorous gyrokinetic treatment rather than a drift-kinetic treatment, and therefore remains an active area of work.

Chapter 8

Appendix

8.1 Useful Identities

Exponential integrals, based on Gradshteyn and Ryzhik's *Table of Integrals, Series and Products*:

$$\int_0^\infty dx\ e^{-ax^2} = \frac{1}{2}\sqrt{\frac{\pi}{a}}\ , \qquad \mathbb{R}(a) > 0 \tag{8.1.1}$$

$$\int_0^\infty dx\ x^2 e^{-ax^2} = \frac{\sqrt{\pi}}{4a^{3/2}}\ , \qquad \mathbb{R}(a) > 0 \tag{8.1.2}$$

$$\int_0^\infty dx\ x^4 e^{-x^2} = \frac{3\sqrt{\pi}}{8} \tag{8.1.3}$$

$$\int_0^\infty dx\ x^6 e^{-x^2} = \frac{15\sqrt{\pi}}{16} \tag{8.1.4}$$

Error function integrals, based on Ng and Murray (1969) Sec.4.3. in Ref.(J. Research. NTB B Maths 1969):

$$\int_0^\infty dx\ \frac{e^{-x^2}}{x}\,\mathrm{erf}(x) = \sinh^{-1}(1) = \ln(1+\sqrt{2}) \tag{8.1.5}$$

$$\int_0^\infty dx\ e^{-x^2}\,\mathrm{erf}(x) = \frac{\sqrt{\pi}}{4} \tag{8.1.6}$$

$$\int_0^\infty dx\ xe^{-x^2}\,\mathrm{erf}(x) = \frac{1}{2\sqrt{2}} \tag{8.1.7}$$

$$\int_0^\infty dx\ x^2 e^{-x^2}\,\mathrm{erf}(x) = \frac{2+\pi}{8\sqrt{2}} \tag{8.1.8}$$

$$\int_0^\infty dx\ x^3 e^{-x^2}\,\mathrm{erf}(x) = \frac{5}{8\sqrt{2}} \tag{8.1.9}$$

Integrals of some quantities within the program

The y-integral of $v_\parallel$:

$$\begin{aligned}\int_0^{b^{-1}} dy\ v_\parallel &= \sigma u \int_0^{b^{-1}} dy\ \sqrt{1-yb} \\ &= \sigma u \left[\frac{-2}{3b}(1-yb)^{3/2}\right]_0^{b^{-1}} \\ &= \frac{2\sigma u}{3b}\end{aligned} \tag{8.1.10}$$

The y-integral of $1/v_\parallel$:

$$\begin{aligned}\int_0^{b^{-1}} dy\ \frac{1}{v_\parallel} &= \frac{1}{\sigma u}\int_0^{b^{-1}} \frac{dy}{\sqrt{1-yb}} \\ &= \frac{1}{\sigma u}\left[\frac{2}{b}(1-yb)^{1/2}\right]_0^{b^{-1}} \\ &= \frac{2}{\sigma u}\end{aligned} \tag{8.1.11}$$

The y-integral of normalised canonical angular momentum p across all y-space, in explicit form, using Eq. 8.1.10:

$$\int_0^{b^{-1}} dy\ p = \int_0^{b^{-1}} dy\ x - \sigma v \rho_{\theta i} v_\parallel = \frac{x}{b} - \frac{2\sigma v \rho_{\theta i}}{3b} \tag{8.1.12}$$

The y-integral of shifted canonical angular momentum $\tilde{p}$ across all y-space, in explicit form:

$$\begin{aligned}&\int_0^{b^{-1}} dy\ p = \sigma v \int_0^{b^{-1}} dy\ x - \rho_{\theta i}(v_\parallel - v_{\parallel,0}) \\ &= \frac{x}{b} - \sigma v \rho_{\theta i}\int_0^{b^{-1}} dy\ \sqrt{1-yb} - \Theta(y-y_c)\sqrt{1-y} \\ &= \frac{x}{b} - \sigma v \rho_{\theta i}\left(\int_0^1 dy\ \sqrt{1-yb} - \sqrt{1-y} + \int_1^{b^{-1}} dy\ \sqrt{1-yb}\right) \\ &= \frac{x}{b} - \sigma v \rho_{\theta i}\left(\left[\frac{-2}{3}\left(\frac{(1-yb)^{3/2}}{b} - (1-y)^{3/2}\right)\right]_0^1 + \left[\frac{-2}{3}\frac{(1-yb)^{3/2}}{b}\right]_1^{b^{-1}}\right) \\ &= \frac{x}{b} + \frac{2\sigma v \rho_{\theta i}(b-1)}{3b}\end{aligned} \tag{8.1.13}$$

Scalar and vector products

Cross products between the basis vectors:

$$\nabla\psi \times \nabla\theta = \frac{|\nabla\psi||\nabla\theta|}{|\nabla\phi|}\nabla\phi = \frac{R^2 B_\theta}{r}\nabla\phi \tag{8.1.14}$$

$$\nabla\theta \times \nabla\phi = \frac{|\nabla\theta||\nabla\phi|}{|\nabla\psi|}\nabla\psi = \frac{1}{rR^2 B_\theta}\nabla\psi \tag{8.1.15}$$

$$\nabla\phi \times \nabla\psi = \frac{|\nabla\phi||\nabla\psi|}{|\nabla\theta|}\nabla\theta = rB_\theta\nabla\theta. \tag{8.1.16}$$

Scalar products between total magnetic field $\mathbf{B}$ and basis vectors:

$$\begin{aligned}\mathbf{B}\cdot\nabla\psi &= m\tilde{\psi}\sin\xi\,(\nabla\theta\times\nabla\phi)\cdot\nabla\psi \\ &= m\tilde{\psi}\sin\xi\,\frac{B_\theta}{r}.\end{aligned} \tag{8.1.17}$$

$$\begin{aligned}\mathbf{B}\cdot\nabla\theta &= (\nabla\phi\times\nabla\psi)\cdot\nabla\theta + \frac{\partial R}{\partial\psi}\frac{\tilde{\psi}}{R}\cos\xi\,(\nabla\phi\times\nabla\psi)\cdot\nabla\theta \\ &= \frac{B_\theta}{r}\left(1+\frac{\partial R}{\partial\psi}\frac{\tilde{\psi}}{R}\cos\xi\right), \qquad \frac{B_\theta}{r}\equiv\frac{B_\phi}{Rq}\end{aligned} \tag{8.1.18}$$

$$\mathbf{B}\cdot\nabla\phi = \frac{I}{R^2}. \tag{8.1.19}$$

$$\mathbf{B}\cdot\nabla\xi = \frac{mB_\phi}{Rq}\left(1+\frac{\partial R}{\partial\psi}\frac{\tilde{\psi}}{R}\cos\xi\right) - \frac{m}{q_s}\frac{I}{R^2}. \tag{8.1.20}$$

Cross products between $\mathbf{B}$ and basis vectors:

$$\begin{aligned}\mathbf{B}\times\nabla\psi &= I\nabla\phi\times\nabla\psi + \left(1+\frac{\partial R}{\partial\psi}\frac{\tilde{\psi}}{R}\cos\xi\right)\underbrace{(\nabla\phi\times\nabla\psi)\times\nabla\psi} \\ &\qquad = (\nabla\phi\cdot\nabla\psi)\nabla\psi - |\nabla\psi|^2\nabla\phi \\ \rightarrow\ \mathbf{B}\times\nabla\psi &= I\nabla\phi\times\nabla\psi - R^2B_\theta^2\left(1+\frac{\partial R}{\partial\psi}\frac{\tilde{\psi}}{R}\cos\xi\right)\nabla\phi.\end{aligned} \tag{8.1.21}$$

$$\begin{aligned}\mathbf{B}\times\nabla\theta &= I\nabla\phi\times\nabla\theta + m\tilde{\psi}\sin\xi\,\underbrace{(\nabla\phi\times\nabla\psi)\times\nabla\psi} \\ &\qquad = |\nabla\theta|^2 - (\nabla\theta\cdot\nabla\phi)\nabla\theta \\ \rightarrow\ \mathbf{B}\times\nabla\theta &= I\nabla\phi\times\nabla\theta + \frac{m\tilde{\psi}}{r^2}\sin\xi\,\nabla\phi.\end{aligned} \tag{8.1.22}$$

$$\mathbf{B}\times\nabla\phi=\left(1+\frac{\partial R}{\partial\psi}\frac{\tilde{\psi}}{R}\cos\xi\right)\underbrace{(\nabla\phi\times\nabla\psi)\times\nabla\phi}_{=|\nabla\phi|^2\nabla\psi}+m\tilde{\psi}\sin\xi\,\underbrace{(\nabla\theta\times\nabla\phi)\times\nabla\phi}_{=-|\nabla\phi|^2\nabla\theta}$$

$$\rightarrow\ \mathbf{B}\times\nabla\phi=\frac{1}{R^2}\left[\left(1+\frac{\partial R}{\partial\psi}\frac{\tilde{\psi}}{R}\cos\xi\right)\nabla\psi-m\tilde{\psi}\sin\xi\,\nabla\theta\right]. \tag{8.1.23}$$

$$\mathbf{B}\times\nabla\xi=m\mathbf{B}\times\left(\nabla\theta-\frac{1}{q_s}\nabla\phi\right),$$

$$\rightarrow\ \mathbf{B}\times\nabla\xi=mI\nabla\phi\times\nabla\theta+\frac{m^2}{r^2}\tilde{\psi}\sin\xi\,\nabla\phi - \frac{m}{q_sR^2}\left[\left(1+\frac{\partial R}{\partial\psi}\frac{\tilde{\psi}}{R}\cos\xi\right)\nabla\psi-m\tilde{\psi}\sin\xi\,\nabla\theta\right]. \tag{8.1.24}$$

8.2 Perturbed magnetic field

We derive the total perturbed magnetic field in a steady-state plasma containing a single helicity magnetic island of half-width w, expanding in the limits of small $\Delta = w/r_s \ll 1$ and $\epsilon = r_s/R \ll 1$. The perturbed magnetic field satisfying Maxwell's equation $\nabla \cdot \mathbf{B} = 0$:

$$\mathbf{B}_1 = \nabla \times \left(A_\parallel \boldsymbol{b}_0\right) \tag{8.2.1}$$

where $\nabla \cdot \mathbf{B}_1 = \nabla \cdot [\nabla \times (A_\parallel \boldsymbol{b}_0)] = 0$, since $\nabla \cdot (\nabla \times \boldsymbol{A}) = 0$ for any vector field $\boldsymbol{A}$. Here,

$$A_\parallel = -\frac{\tilde{\psi}}{R}\cos n\xi, \quad \tilde{\psi} = \frac{w_\psi^2}{4}\frac{q_s'}{q_s}, \quad w_\psi = RB_\theta w, \quad \xi = m\left(\theta - \frac{\phi}{q_s}\right),$$

where $q_s = m/n$ is the safety factor at the rational surface, m and n are poloidal and toroidal mode numbers respectively. The derivative of q_s with respect to ψ (indicated with superscript $'$) is:

$$q_s' = \left.\frac{dq}{d\psi}\right|_{\psi=\psi_s}.$$

Then, working in the island rest frame,

$$\mathbf{B}_1 = (\nabla A_\parallel) \times \boldsymbol{b}_0 + A_\parallel \nabla \times \boldsymbol{b}_0,$$

$$\nabla A_\parallel = \frac{\tilde{\psi}}{R}\sin\xi\,\nabla\xi, \qquad \nabla\xi = m\nabla\theta - \frac{m}{q_s}\nabla\phi \tag{8.2.2}$$

$$\begin{aligned}
\rightarrow \nabla A_\parallel \times \boldsymbol{b}_0 &= \frac{\tilde{\psi}}{RB_0}\sin\xi\,\nabla\xi \times \mathbf{B}_0 \\
&= \frac{m\tilde{\psi}}{RB_0}\sin\xi\Big[I\nabla\theta\times\nabla\phi - \frac{1}{q_s}\underbrace{\nabla\phi\times(\nabla\phi\times\nabla\psi)}\Big] \\
&\qquad\qquad = \nabla\phi(\nabla\phi\cdot\nabla\psi) - |\nabla\phi|^2\nabla\psi = -\frac{1}{R^2}\nabla\psi \\
&= \frac{m\tilde{\psi}}{RB_0}\sin\xi\left(\frac{I}{rR^2B_\theta}\nabla\psi + \frac{1}{q_sR^2}\nabla\psi\right) \\
&= \frac{m\tilde{\psi}B_\phi}{RB_0RB_\theta}\sin\xi\left(1 + \frac{rB_\theta}{q_sRB_\phi}\right)\nabla\psi \\
\therefore \nabla A_\parallel \times \boldsymbol{b}_0 &\simeq \frac{m\tilde{\psi}}{rR^2B_\theta}\sin\xi\,\nabla\psi \quad + O(\epsilon^2).
\end{aligned}$$

$$
\begin{aligned}
\to\ A_\parallel \nabla\times \boldsymbol{b}_0 &= -\frac{\tilde{\psi}}{R}\cos\xi\ \nabla\times\left[\frac{I\nabla\phi\ +\nabla\phi\times\nabla\psi}{B_0(\psi,\theta)}\right], \quad \text{N.B. } \nabla\times(\nabla f)=0;\\
&\qquad\qquad \nabla\times(\nabla\phi\times\nabla\psi) = \nabla\phi\cancelto{0}{(\nabla^2\psi)} - \nabla\psi\cancelto{0}{(\nabla^2\phi)}\\
&\qquad\qquad\qquad\qquad\qquad + \cancelto{0}{(\nabla\psi\cdot\nabla^2)\phi} - \cancelto{0}{(\nabla\phi\cdot\nabla^2)\psi} = 0;\\
&= -\frac{\tilde{\psi}}{R}\cos\xi\Bigg[\frac{\partial}{\partial\psi}\left(\frac{I}{B_0}\right)\nabla\psi\times\nabla\phi + \frac{\partial}{\partial\psi}\left(\frac{1}{B_0}\right)\nabla\psi\times(\nabla\phi\times\nabla\psi)\\
&\qquad\qquad + I\frac{\partial}{\partial\theta}\left(\frac{1}{B_0}\right)\nabla\theta\times\nabla\phi + \frac{\partial}{\partial\theta}\left(\frac{1}{B_0}\right)\nabla\theta\times(\nabla\phi\times\nabla\psi)\Bigg]\\
&= -\frac{\tilde{\psi}}{R}\cos\xi\Bigg[-rB_\theta\frac{\partial}{\partial\psi}\left(\frac{I}{B_0}\right)\nabla\theta + R^2B_\theta^2\frac{\partial}{\partial\psi}\left(\frac{1}{B_0}\right)\nabla\phi\\
&\qquad\qquad\qquad\qquad + \frac{I}{rR^2B_\theta}\frac{\partial}{\partial\theta}\left(\frac{1}{B_0}\right)\nabla\psi\Bigg]\\
&= +\frac{\tilde{\psi}}{R}\cos\xi\left[rB_\theta\frac{\partial}{\partial\psi}\left(\frac{I}{B_0}\right)\nabla\theta + R^2\frac{B_\theta^2}{B_0^2}\frac{\partial B_0}{\partial\psi}\nabla\phi + \frac{I}{rR^2B_0^2B_\theta}\frac{\partial B_0}{\partial\theta}\nabla\psi\right]
\end{aligned}
$$

$$
\begin{aligned}
\therefore\ A_\parallel\nabla\times\boldsymbol{b}_0 = +\frac{\tilde{\psi}}{R}\cos\xi\Bigg[&rB_\theta\frac{\partial}{\partial\psi}\left(\frac{I}{B_0}\right)\nabla\theta + \left(\frac{RB_\theta}{B_0}\right)^2\frac{\partial B_0}{\partial\psi}\nabla\phi\\
&+ \frac{1}{rRB_0B_\theta}\frac{\partial B_0}{\partial\psi}\nabla\psi\Bigg].
\end{aligned}
$$

$$
\begin{aligned}
\to\ \mathbf{B}_1 &= \frac{m\tilde{\psi}}{rR^2B_\theta}\sin\xi\left(\overset{①}{1} + \overset{②}{\frac{rB_\theta}{q_sRB_\phi}}\right)\nabla\psi\\
&\quad + \frac{\tilde{\psi}}{R}\cos\xi\left[\underset{③}{rB_\theta\frac{\partial}{\partial\psi}\left(\frac{I}{B_0}\right)\nabla\theta} + \underset{④}{\left(\frac{RB_\theta}{B_0}\right)^2\frac{\partial B_0}{\partial\psi}\nabla\phi} + \underset{⑤}{\frac{1}{rRB_0B_\theta}\frac{\partial B_0}{\partial\theta}\nabla\psi}\right].
\end{aligned}
\tag{8.2.3}
$$

Check the ordering of terms, with $\Delta = w/r$ as the ordering parameter:

$$\begin{aligned}
&\qquad\qquad\qquad\qquad\qquad\qquad\qquad\qquad\qquad\qquad \textcircled{1} \quad \textcircled{2} \\
\frac{\mathbf{B}_1}{B_0} &= \frac{m\tilde{\psi}}{RB_0}\sin\xi\frac{1}{rRB_\theta}\left(1+\frac{rB_\theta}{q_sRB_\phi}\right)\nabla\psi \\
&\quad + \frac{\tilde{\psi}}{RB_0}\cos\xi\left[rB_\theta\frac{\partial}{\partial\psi}\left(\frac{I}{B_0}\right)\nabla\theta + \left(\frac{RB_\theta}{B_0}\right)^2\frac{\partial B_0}{\partial\psi}\nabla\phi + \frac{1}{rRB_0B_\theta}\frac{\partial B_0}{\partial\theta}\nabla\psi\right] \\
&\qquad\qquad\qquad\qquad\qquad\qquad\qquad\qquad\qquad\qquad \textcircled{3} \qquad\qquad \textcircled{4} \qquad\qquad\quad \textcircled{5}
\end{aligned}$$

$$[\textcircled{1}]: \quad \tilde{\psi}\frac{1}{RB_0}\frac{|\nabla\psi|}{r}RB_\theta \sim \frac{w_\psi^2}{RB_0}\frac{q_s'}{q_s}\frac{\cancel{RB_\theta}}{r\cancel{RB_\theta}} \sim \frac{w^2R^2B_\theta^2}{RB_0}\frac{O(1)}{rRB_\theta}\frac{1}{r}$$

$$\therefore \underline{[\textcircled{1}] \sim \epsilon\Delta^2}.$$

Then

$$\begin{aligned}
&\frac{\textcircled{2}}{\textcircled{1}}: \quad \frac{rB_\theta}{q_sRB_\phi} \sim \epsilon^2, \\
\Rightarrow\ &\underline{[\textcircled{2}] \sim \epsilon^3\Delta^2}. \\
&\frac{\textcircled{3}}{\textcircled{1}}: \quad \frac{rRB_\theta}{|\nabla\psi|}rB_\theta\frac{\partial}{\partial\psi}\left(\frac{I}{B_0}\right)|\nabla\theta| \sim \frac{Rr^2B_\theta^2}{RB_\theta}\frac{\partial}{\partial\psi}\left(\frac{\cancel{RB_\phi}}{\cancel{B_0}}\right)\frac{1}{r} \sim \frac{rB_\theta}{RB_\theta}\frac{R}{r} \sim 1 \\
\Rightarrow\ &\underline{[\textcircled{3}] \sim \epsilon\Delta^2}. \\
&\frac{\textcircled{4}}{\textcircled{1}}: \quad r\frac{R^2B_\theta^2}{B_0^2}\frac{\partial B_0}{\partial\psi}|\nabla\phi| \sim \frac{rR^2B_\theta^2B_0}{B_0^2RB_\theta r} \sim \frac{B_\theta}{B_0} \sim \epsilon \\
\Rightarrow\ &\underline{[\textcircled{4}] \sim \epsilon^2\Delta^2}. \\
&\frac{\textcircled{5}}{\textcircled{1}}: \quad \frac{r}{rRB_0B_\theta}B_0\epsilon RB_\theta \sim \epsilon \\
\Rightarrow\ &\underline{[\textcircled{5}] \sim \epsilon^2\Delta^2}.
\end{aligned}$$

Therefore, to $O(\epsilon^{3/2}\Delta^2)$, the magnetic field perturbation is:

$$\mathbf{B}_1 \simeq \frac{m\tilde{\psi}}{rR^2B_\theta}\sin\xi\,\nabla\psi + \frac{\tilde{\psi}}{R}\cos\xi.rB_\theta\underbrace{\frac{\partial}{\partial\psi}\left(\frac{I}{B_0}\right)}_{\sim\frac{\partial R}{\partial\psi}}\nabla\theta,$$

$$\nabla\psi = rR^2B_\theta\nabla\theta\times\nabla\phi, \quad \nabla\theta = \frac{1}{rB_\theta}\nabla\phi\times\nabla\psi.$$

which, recalling Eq.(8.1.15) and (8.1.16) gives:

$$\boxed{\mathbf{B}_1 = m\tilde{\psi}\sin\xi\,\nabla\theta\times\nabla\phi + \frac{\partial R}{\partial\psi}\frac{\tilde{\psi}}{R}\cos\xi\,\nabla\phi\times\nabla\psi} + O(\epsilon^2\Delta^2). \tag{8.2.4}$$

The total magnetic field with the perturbation is then:

$$\boxed{\mathbf{B}_{\text{tot}} = I(\psi)\nabla\phi + \nabla\phi\times\nabla\psi + m\tilde{\psi}\sin\xi\,\nabla\theta\times\nabla\phi + \frac{\partial R}{\partial\psi}\frac{\tilde{\psi}}{R}\cos\xi\,\nabla\phi\times\nabla\psi}. \tag{8.2.5}$$

where the ordering of terms are $1 \;:\; \epsilon \;:\; \epsilon\Delta^2 \;:\; \epsilon\Delta^2$.

8.3 Extended theory derivation

This section contains additional derivation of steps covered previously in the Method chapter, Ch.3.

8.3.1 Differential Operators

The parallel derivative operator is defined as:

$$\nabla_{\parallel} = \frac{\mathbf{B}\cdot\nabla}{B}, \tag{8.3.1}$$

where $\mathbf{B}$ is the total magnetic field given by Eq.(2.1.7). Then, using results for the scalar products (8.1.17) $\sim$ (8.1.20),

$$\begin{aligned} v_{\parallel}\nabla_{\parallel} = v_{\parallel}\frac{\mathbf{B}\cdot\nabla}{B} &= \frac{v_{\parallel}}{B}\left(\mathbf{B}\cdot\nabla\psi\ \left.\frac{\partial}{\partial\psi}\right|_{\theta,\xi} + \mathbf{B}\cdot\nabla\theta\ \left.\frac{\partial}{\partial\theta}\right|_{\psi,\xi} + \mathbf{B}\cdot\nabla\xi\ \left.\frac{\partial}{\partial\xi}\right|_{\psi,\theta}\right) \\ &= \frac{v_{\parallel}}{B}\left[\frac{B_\phi}{Rq}m\tilde{\psi}\sin\xi\,\frac{\partial}{\partial\psi} + \frac{B_\phi}{Rq}\left(1+\frac{\partial R}{\partial\psi}\frac{\tilde{\psi}}{R}\cos\xi\right)\frac{\partial}{\partial\theta}\right. \\ &\qquad \left. + \frac{mB_\phi}{Rq}\left(1+\frac{\partial R}{\partial\psi}\frac{\tilde{\psi}}{R}\cos\xi\right)\frac{\partial}{\partial\xi} - \frac{m}{q_s}\frac{I}{R^2}\frac{\partial}{\partial\xi}\right] \end{aligned}$$

But $\dfrac{m}{q_s}\dfrac{I}{R^2} = \dfrac{mq}{q_s}\dfrac{B_\phi}{Rq}$ and $B \sim B_\phi + O(\epsilon^2)$, so:

$$v_{\parallel}\nabla_{\parallel} = \frac{v_{\parallel}}{B}\left[m\tilde{\psi}\sin\xi\,\frac{\partial}{\partial\psi} + \left(1+\frac{\partial R}{\partial\psi}\frac{\tilde{\psi}}{R}\cos\xi\right)\frac{\partial}{\partial\theta} + \left(1-\frac{q}{q_s}\right)\frac{\partial}{\partial\xi} + m\frac{\partial R}{\partial\psi}\frac{\tilde{\psi}}{R}\cos\xi\,\frac{\partial}{\partial\xi}\right].$$

Here,

$$\begin{aligned} \frac{\partial}{\partial\psi} = \frac{1}{RB_\theta}\frac{\partial}{\partial r} &\sim \frac{1}{RB_\theta r} \quad \text{on equilibrium quantities;} \\ &\sim \frac{1}{RB_\theta w} \quad \text{on perturbed quantities.} \end{aligned}$$

Then, for each term, checking orderings in $\Delta = w/r$:

$$\begin{aligned}
\tilde{\psi} &= \frac{w_\psi^2}{4}\frac{q_s'}{q_s} \sim RB_\theta \frac{w^2}{r}, \quad \text{so:} \\
\left[\frac{\partial R}{\partial \psi}\frac{\tilde{\psi}}{R}\right] &\sim \frac{R}{rB_\theta R}\frac{RB_\theta w^2}{rR} \sim \frac{w^2}{r^2} = \Delta^2. \\
\left[m\tilde{\psi}\sin\xi\,\frac{\partial}{\partial\psi}\right] &\sim \frac{RB_\theta w^2}{r}\frac{1}{RB_\theta}\frac{1}{w(r)_{\text{eqm}}} \sim \Delta\,(\Delta^2)_{\text{eqm}}
\end{aligned}$$

$$\begin{aligned}
1-\frac{q}{q_s} &= 1-\frac{1}{q_s}\left(q_s + w_\psi q_s' + ...\right) \quad \text{by Taylor expansion;} \\
&\simeq w_\psi q_s' + ... \\
&\sim \frac{w}{r} \sim \Delta.
\end{aligned}$$

Therefore:

$$\boxed{v_\parallel\nabla_\parallel = \frac{v_\parallel}{Rq}\left[\underset{1}{\left.\frac{\partial}{\partial\theta}\right|_\psi} + \underset{\Delta}{m\left(1-\frac{q}{q_s}\right)\frac{\partial}{\partial\xi}} + \underset{\Delta(\Delta^2)_{\text{eqm}}}{m\tilde{\psi}\sin\xi\,\frac{\partial}{\partial\psi}} + \underset{\Delta^2}{\frac{\partial R}{\partial\psi}\frac{\tilde{\psi}}{R}\cos\xi\left(\frac{\partial}{\partial\theta}+m\frac{\partial}{\partial\xi}\right)}\right]} \tag{8.3.2}$$

Next, consider the magnetic drift response:

$$\boldsymbol{v}_b\cdot\nabla[...] = -\frac{v_\parallel}{B}\mathbf{B}\times\nabla\left(\frac{v_\parallel}{\omega_{c(j)}}\right)\cdot\nabla[...] = \frac{v_\parallel}{B}\mathbf{B}(\mathbf{B}\times\nabla[...])\cdot\nabla\left(\frac{v_\parallel}{\omega_c}\right) \tag{8.3.3}$$

Using the scalar products (8.1.17) $\sim$ (8.1.20) and cross products (8.1.21) $\sim$ (8.1.24),

$$\begin{aligned}
\boldsymbol{v}_b\cdot\nabla\psi &= \frac{v_\parallel}{B}(\mathbf{B}\times\nabla\psi)\cdot\nabla\left(\frac{v_\parallel}{\omega_c}\right) \\
&= \frac{v_\parallel}{B}\left[I\underbrace{(\nabla\phi\times\nabla\psi)\cdot\nabla\theta}_{=J^{-1}=B_\phi/Rq}\frac{\partial}{\partial\theta}\left(\frac{v_\parallel}{\omega_c}\right) - R^2B_\theta^2\left(1+\frac{\partial R}{\partial\psi}\frac{\tilde{\psi}}{R}\cos\xi\right)|\nabla\phi|^2\cancelto{0}{\frac{\partial}{\partial\phi}\left(\frac{v_\parallel}{\omega_c}\right)}\right]
\end{aligned}$$

by axisymmetry

$$= \frac{v_\parallel}{Rq}I\frac{\partial}{\partial\theta}\left(\frac{v_\parallel}{\omega_c}\right).$$

$$\begin{aligned}\boldsymbol{v}_b \cdot \nabla\theta &= \frac{v_\parallel}{B}(\mathbf{B}\times\nabla\theta)\cdot\nabla\left(\frac{v_\parallel}{\omega_c}\right)\\ &= \frac{v_\parallel}{B}\left[I\underbrace{(\nabla\phi\times\nabla\theta)\cdot\nabla\theta}_{=-J^{-1}}\frac{\partial}{\partial\psi}\left(\frac{v_\parallel}{\omega_c}\right)+\frac{m\tilde{\psi}}{r^2}\sin\xi\,|\nabla\phi|^2\cancelto{0}{\frac{\partial}{\partial\phi}\left(\frac{v_\parallel}{\omega_c}\right)}\right]\\ &= -\frac{v_\parallel}{Rq}I\frac{\partial}{\partial\psi}\left(\frac{v_\parallel}{\omega_c}\right).\end{aligned}$$

$$\begin{aligned}\boldsymbol{v}_b \cdot \nabla\xi &= \frac{v_\parallel}{B}(\mathbf{B}\times\nabla\xi)\cdot\nabla\left(\frac{v_\parallel}{\omega_c}\right)\\ &= \frac{mv_\parallel}{B}\Bigg[I\underbrace{(\nabla\phi\times\nabla\theta)\cdot\nabla\theta}_{=-J^{-1}}\frac{\partial}{\partial\xi}\left(\frac{v_\parallel}{\omega_c}\right)+\frac{m\tilde{\psi}}{r^2}\sin\xi\,|\nabla\phi|^2\cancelto{0}{\frac{\partial}{\partial\phi}\left(\frac{v_\parallel}{\omega_c}\right)}\\ &\qquad+\frac{m\tilde{\psi}}{q_s r^2}\sin\xi\,\underbrace{|\nabla\theta|^2}_{=r^{-2}}\frac{\partial}{\partial\theta}\left(\frac{v_\parallel}{\omega_c}\right)-\frac{1}{q_s R^2}\left(1+\frac{\partial R}{\partial\psi}\frac{\tilde{\psi}}{R}\cos\xi\right)\underbrace{|\nabla\psi|^2}_{=R^2B_\theta^2}\frac{\partial}{\partial\psi}\left(\frac{v_\parallel}{\omega_c}\right)\Bigg]\end{aligned}$$

But:

$$\frac{Rq}{IB_\phi}\frac{B_\theta^2}{q_s}=\frac{q}{q_s}\frac{B_\theta^2}{B_\phi^2},\qquad \frac{Rq}{IB_\phi}\frac{m}{q_s}\frac{\tilde{\psi}}{r^2R^2}=m\frac{q}{q_s}\frac{\tilde{\psi}}{B_\phi^2 r^2R^2}:$$

$$\therefore\ \boldsymbol{v}_b\cdot\nabla\xi=-\frac{mv_\parallel}{Rq}I\frac{\partial}{\partial\psi}\left(\frac{v_\parallel}{\omega_c}\right)\left[1+\frac{B_\theta^2}{B_\phi^2}\frac{q}{q_s}\left(1+\frac{\partial R}{\partial\psi}\frac{\tilde{\psi}}{R}\cos\xi\right)\right]+\frac{mv_\parallel}{Rq}I\frac{\partial}{\partial\theta}\left(\frac{v_\parallel}{\omega_c}\right)\frac{q}{q_s}\frac{m\tilde{\psi}}{B_\phi^2r^2R^2}\sin\xi.$$

Combining these results,

$$\begin{aligned}\boldsymbol{v}_b\cdot\nabla &= \frac{Iv_\parallel}{Rq}\left[\frac{\partial}{\partial\theta}\left(\frac{v_\parallel}{\omega_c}\right)\frac{\partial}{\partial\psi}-\frac{\partial}{\partial\psi}\left(\frac{v_\parallel}{\omega_c}\right)\frac{\partial}{\partial\theta}\right]-\frac{mIv_\parallel}{Rq}\frac{\partial}{\partial\psi}\left(\frac{v_\parallel}{\omega_c}\right)\frac{\partial}{\partial\xi}\\ &\quad-\frac{mIv_\parallel}{Rq}\frac{\partial}{\partial\psi}\left(\frac{v_\parallel}{\omega_c}\right)\frac{B_\theta^2}{B_\phi^2}\frac{q}{q_s}\left(1+\frac{\partial R}{\partial\psi}\frac{\tilde{\psi}}{R}\cos\xi\right)\frac{\partial}{\partial\xi}+\frac{mIv_\parallel}{Rq}\frac{\partial}{\partial\theta}\left(\frac{v_\parallel}{\omega_c}\right)\frac{q}{q_s}\frac{m\tilde{\psi}\sin\xi}{(B_\phi rR)^2}\frac{\partial}{\partial\xi}.\end{aligned}\tag{8.3.4}$$

Here,

$$\frac{B_\theta^2}{B_\phi} \sim \epsilon^2, \qquad \frac{\partial R}{\partial \psi}\frac{\tilde{\psi}}{R} \sim \Delta^2.$$

$$I\frac{\partial}{\partial\theta}\left(\frac{v_\parallel}{\omega_c}\right)\frac{\partial}{\partial\psi} \sim RB_\phi\sigma v \underbrace{\frac{\partial}{\partial\theta}\left(\frac{\sqrt{1-\lambda B}}{\omega_c}\right)}_{\sim(\rho_L B)\partial B/\partial\theta\sim\epsilon\rho_L}\frac{1}{RB_\theta}\frac{1}{w(r)_{\rm eqm}}$$

$$\sim \epsilon\frac{\rho_\theta}{w(r)_{\rm eqm}} \sim \epsilon(\Delta_{\rm eqm}).$$

$$I\frac{\partial}{\partial\psi}\left(\frac{v_\parallel}{\omega_c}\right)\frac{\partial}{\partial\theta} \sim mI\frac{\partial}{\partial\psi}\left(\frac{v_\parallel}{\omega_c}\right)\frac{\partial}{\partial\xi} \sim \frac{1}{r}\frac{v_\parallel}{\omega_c} \sim \frac{\rho_\theta}{r} \sim \Delta.$$

$$\frac{m\tilde{\psi}}{(B_\phi r R)^2} \sim RB_\theta\frac{w^2}{r}\frac{1}{r^2R^2B_\phi^2} \sim \frac{w^2}{r^2}\frac{B_\theta}{rRB_\phi^2}$$

$$\rightarrow\ I\frac{\partial}{\partial\theta}\left(\frac{v_\parallel}{\omega_c}\right)\frac{m\tilde{\psi}}{(B_\phi r R)^2} \sim RB_\phi\epsilon\rho_L\frac{w^2}{r^2}\frac{B_\theta}{rRB_\phi^2} \sim \epsilon\frac{\rho_\theta}{r}\frac{w^2}{r^2}\frac{B_\theta^2}{B_\phi^2} \sim \epsilon^3\Delta^3.$$

Therefore, to $O(\epsilon^{3/2}\Delta^2)$:

$$\boxed{\boldsymbol{v}_b\cdot\nabla = \underbrace{\frac{Iv_\parallel}{Rq}\left[\frac{\partial}{\partial\theta}\left(\frac{v_\parallel}{\omega_c}\right)\frac{\partial}{\partial\psi} - \frac{\partial}{\partial\psi}\left(\frac{v_\parallel}{\omega_c}\right)\frac{\partial}{\partial\theta}\right]}_{\epsilon(\Delta)_{\rm eqm}} - \underbrace{\frac{mIv_\parallel}{Rq}\frac{\partial}{\partial\psi}\left(\frac{v_\parallel}{\omega_c}\right)\frac{\partial}{\partial\xi}}_{\Delta}}_{\Delta} \tag{8.3.5}$$

Now consider the $\mathbf{E}\times\mathbf{B}$ response:

$$\boldsymbol{v}_E\cdot\nabla[...] = \frac{\mathbf{B}\times\nabla\Phi}{B^2}\cdot\nabla[...] = -\frac{1}{B^2}(\mathbf{B}\times\nabla[...])\cdot\nabla\Phi \tag{8.3.6}$$

Noting the similarity with Eq.(8.3.3), with $v_\parallel/B \rightarrow -1/B^2$ and $v_\parallel/\omega_c \rightarrow \Phi$, but also taking into account that $\Phi = \Phi(\psi,\theta,\xi)$ in general:

$$\begin{aligned}\boldsymbol{v}_E\cdot\nabla\psi &= -\frac{1}{B^2}\left[I(\nabla\phi\times\nabla\psi)\cdot\nabla\theta\left(\frac{\partial\Phi}{\partial\theta}+m\frac{\partial\Phi}{\partial\xi}\right)\right.\\ &\qquad\left.-(RB_\theta)^2\left(1+\frac{\partial R}{\partial\psi}\frac{\tilde{\psi}}{R}\cos\xi\right)|\nabla\phi|^2\left(-\frac{m}{q_s}\right)\frac{\partial\Phi}{\partial\xi}\right]\\ &= -\frac{IB_\phi}{B^2Rq}\left(\frac{\partial\Phi}{\partial\theta}+m\frac{\partial\Phi}{\partial\xi}\right) - \frac{B_\theta^2}{B^2}\frac{m}{q_s}\left(1+\frac{\partial R}{\partial\psi}\frac{\tilde{\psi}}{R}\cos\xi\right)\frac{\partial\Phi}{\partial\xi}\\ &= -\frac{1}{q}\frac{\partial\Phi}{\partial\theta} - \frac{m}{q}\frac{\partial\Phi}{\partial\xi} - \frac{B_\theta^2}{B^2}\frac{m}{q_s}\left(1+\frac{\partial R}{\partial\psi}\frac{\tilde{\psi}}{R}\cos\xi\right)\frac{\partial\Phi}{\partial\xi}.\end{aligned}$$

$$\begin{aligned}\boldsymbol{v}_E\cdot\nabla\theta &= -\frac{1}{B^2}\left[I(\nabla\phi\times\nabla\theta)\cdot\nabla\psi\frac{\partial\Phi}{\partial\psi}+\frac{m\tilde{\psi}}{r^2}\sin\xi|\nabla\phi|^2\left(-\frac{m}{q_s}\right)\frac{\partial\Phi}{\partial\xi}\right]\\ &= +\frac{1}{q}\frac{\partial\Phi}{\partial\psi}+\frac{m^2\tilde{\psi}}{q_s(rRB)^2}\sin\xi\,\frac{\partial\Phi}{\partial\xi}.\end{aligned}$$

$$\begin{aligned}\boldsymbol{v}_E\cdot\nabla\xi &= -\frac{1}{B^2}\left[mI(\nabla\phi\times\nabla\theta)\cdot\nabla\psi\frac{\partial\Phi}{\partial\psi}+\frac{m^2\tilde{\psi}}{r^2}\sin\xi|\nabla\phi|^2\left(-\frac{m}{q_s}\right)\frac{\partial\Phi}{\partial\xi}\right.\\ &\quad\left.-\frac{m}{q_sR^2}\left(1+\frac{\partial R}{\partial\psi}\frac{\tilde{\psi}}{R}\cos\xi\right)|\nabla\psi|^2\frac{\partial\Phi}{\partial\psi}+\frac{m^2\tilde{\psi}}{q_sR^2}\sin\xi|\nabla\theta|^2\left(\frac{\partial\Phi}{\partial\theta}+m\frac{\partial\Phi}{\partial\xi}\right)\right]\\ &= +\frac{I}{B^2}\frac{B_\phi}{Rq}m\frac{\partial\Phi}{\partial\psi}+\frac{B_\theta^2}{B^2}\frac{m}{q_s}\left(1+\frac{\partial R}{\partial\psi}\frac{\tilde{\psi}}{R}\cos\xi\right)\frac{\partial\Phi}{\partial\psi}-\frac{m^2\tilde{\psi}}{q_s(rRB)^2}\sin\xi\,\frac{\partial\Phi}{\partial\theta}\\ &= \frac{m}{q}\frac{\partial\Phi}{\partial\psi}+\frac{B_\theta^2}{B^2}\frac{m}{q_s}\left(1+\frac{\partial R}{\partial\psi}\frac{\tilde{\psi}}{R}\cos\xi\right)\frac{\partial\Phi}{\partial\psi}-\frac{m^2\tilde{\psi}}{q_s(rRB)^2}\sin\xi\,\frac{\partial\Phi}{\partial\theta}.\end{aligned}$$

Combining the results,

$$\begin{aligned}\boldsymbol{v}_E\cdot\nabla &= \frac{1}{q}\left(\frac{\partial\Phi}{\partial\psi}\frac{\partial}{\partial\theta}-\frac{\partial\Phi}{\partial\theta}\frac{\partial}{\partial\psi}\right)+\frac{m}{q}\left(\frac{\partial\Phi}{\partial\psi}\frac{\partial}{\partial\xi}-\frac{\partial\Phi}{\partial\xi}\frac{\partial}{\partial\psi}\right)\\ &\quad+\frac{m^2\tilde{\psi}\sin\xi}{q_s(rRB)^2}\left(\frac{\partial\Phi}{\partial\xi}\frac{\partial}{\partial\theta}-\frac{\partial\Phi}{\partial\theta}\frac{\partial}{\partial\xi}\right)+\frac{B_\theta^2}{B^2}\frac{m}{q_s}\left(1+\frac{\partial R}{\partial\psi}\frac{\tilde{\psi}}{R}\cos\xi\right)\left(\frac{\partial\Phi}{\partial\psi}\frac{\partial}{\partial\xi}-\frac{\partial\Phi}{\partial\xi}\frac{\partial}{\partial\psi}\right)\end{aligned}\tag{8.3.7}$$

Here,

$$\begin{aligned}\frac{1}{q}\frac{\partial\Phi}{\partial\psi}\Big/\frac{v_\parallel}{Rq} &\sim \frac{Rq}{qv_\parallel}\frac{\Phi}{RB_\theta w}\sim\frac{e\Phi}{T}\frac{mv_{\rm th}^2}{eB_\theta}\frac{1}{v_{\rm th}w}\\ &\sim\frac{e\Phi}{T}\frac{\rho_\theta}{w}\sim\frac{\rho_\theta}{w}\Delta.\\ \frac{m^2\tilde{\psi}\sin\xi}{q_s(rRB)^2}\frac{\partial\Phi}{\partial\xi}\Big/\frac{\partial\Phi}{\partial\psi} &\sim\frac{RB_\theta^2w^2}{r^3R^2B^2}RB_\theta w\sim\frac{w^3}{r^3}\frac{B_\theta^2}{B^2}\sim\epsilon^2\Delta^3.\end{aligned}$$

Since the last set of terms in Eq.(8.3.7) are ϵ^2 smaller than the leading term, to $O(\epsilon^{3/2}\Delta^2)$:

$$\boxed{\begin{aligned}\boldsymbol{v}_E\cdot\nabla &= \frac{1}{q}\left(\frac{\partial\Phi}{\partial\psi}\frac{\partial}{\partial\theta}-\frac{\partial\Phi}{\partial\theta}\frac{\partial}{\partial\psi}\right)+\frac{m}{q}\left(\frac{\partial\Phi}{\partial\psi}\frac{\partial}{\partial\xi}-\frac{\partial\Phi}{\partial\xi}\frac{\partial}{\partial\psi}\right)\\ &\qquad\Delta\qquad\Delta(\Delta^2)_{\rm eqm}\qquad\qquad\Delta\qquad\Delta(\Delta^2)_{\rm eqm}\end{aligned}}\tag{8.3.8}$$

Then, the leading order terms (to $O(\Delta^2)$) in $v_\parallel \nabla_\parallel \Phi$ and $\boldsymbol{v}_b \cdot \nabla\Phi$ are:

$$v_\parallel \nabla_\parallel \Phi = \frac{v_\parallel}{Rq}\left[\left.\frac{\partial\Phi}{\partial\theta}\right|_\psi + m\left(1-\frac{q}{q_s}\right)\frac{\partial\Phi}{\partial\xi} + m\psi\tilde{\sin}\xi\,\frac{\partial\Phi}{\partial\psi}\right] \tag{8.3.9}$$

$$\Delta \qquad \Delta^2 \qquad \Delta^2$$

$$\boldsymbol{v}_b \cdot \nabla\Phi = \frac{Iv_\parallel}{Rq}\left[\frac{\partial}{\partial\theta}\left(\frac{v_\parallel}{\omega_c}\right)\frac{\partial\Phi}{\partial\psi} - \frac{\partial}{\partial\psi}\left(\frac{v_\parallel}{\omega_c}\right)\frac{\partial\Phi}{\partial\theta} - m\frac{\partial}{\partial\psi}\left(\frac{v_\parallel}{\omega_c}\right)\frac{\partial\Phi}{\partial\xi}\right] \tag{8.3.10}$$

$$\epsilon\Delta \qquad \Delta^2 \qquad \Delta^2 \tag{8.3.11}$$

In summary, the differential operators and their orderings in Δ are given by:

$$\begin{aligned}
v_\parallel \nabla_\parallel &= \frac{v_\parallel}{Rq}\left[\left.\frac{\partial}{\partial\theta}\right|_\psi + m\left(1-\frac{q}{q_s}\right)\frac{\partial}{\partial\xi} + m\tilde{\psi}\sin\xi\,\frac{\partial}{\partial\psi} + \frac{\partial R}{\partial\psi}\frac{\tilde{\psi}}{R}\cos\xi\left(\frac{\partial}{\partial\theta} + m\frac{\partial}{\partial\xi}\right)\right] \\
&\qquad 1 \qquad\qquad \Delta \qquad\qquad \Delta(\Delta^2)_{\text{eqm}} \qquad\qquad \Delta^2 \\
\boldsymbol{v}_b \cdot \nabla &= \frac{Iv_\parallel}{Rq}\left[\frac{\partial}{\partial\theta}\left(\frac{v_\parallel}{\omega_c}\right)\frac{\partial}{\partial\psi} - \frac{\partial}{\partial\psi}\left(\frac{v_\parallel}{\omega_c}\right)\frac{\partial}{\partial\theta}\right] - \frac{mIv_\parallel}{Rq}\frac{\partial}{\partial\psi}\left(\frac{v_\parallel}{\omega_c}\right)\frac{\partial}{\partial\xi} \\
&\qquad \epsilon(\Delta)_{\text{eqm}} \qquad\qquad \Delta \qquad\qquad \Delta \\
\boldsymbol{v}_E \cdot \nabla &= \frac{1}{q}\left(\frac{\partial\Phi}{\partial\psi}\frac{\partial}{\partial\theta} - \frac{\partial\Phi}{\partial\theta}\frac{\partial}{\partial\psi}\right) + \frac{m}{q}\left(\frac{\partial\Phi}{\partial\psi}\frac{\partial}{\partial\xi} - \frac{\partial\Phi}{\partial\xi}\frac{\partial}{\partial\psi}\right) \\
&\qquad \Delta \qquad \Delta(\Delta^2)_{\text{eqm}} \qquad\qquad \Delta \qquad \Delta(\Delta^2)_{\text{eqm}}
\end{aligned} \tag{8.3.12}$$

8.3.2 Coefficient normalisation

Using the normalisations given in Sec.2.3.5, returning to Eq.(2.3.38), starting with terms in $\frac{\partial \bar{g}}{\partial \xi}$ originating from the magnetic drift:

$$
\begin{aligned}
\frac{q_s'}{q_s} p_\varphi &= \frac{p}{\hat{L}_q}, \\
\frac{q_s'}{q_s} I \left\langle \frac{v_\parallel}{\omega_{ci}} \right\rangle_\theta^\psi &= \frac{q_s'}{q_s} R B_\phi \frac{\sigma v B_0}{\omega_{ci0}} \left\langle \frac{\sqrt{1-\lambda B}}{B} \right\rangle_\theta^\psi \\
&= \frac{\cancel{R B_\phi}}{\cancel{R B_\theta} r_s \hat{L}_q} \sigma u \frac{v_{\mathrm{th}}}{\cancel{\omega_{ci0}}^{\omega_{c\theta}}} \frac{\cancel{B_0}^{1/1+\epsilon}}{\cancel{B}_{\max}} \left\langle \frac{\sqrt{1-yb}}{b} \right\rangle_\theta^x \\
&= \frac{\sigma u}{1+\epsilon} \frac{\hat{\rho}_\theta}{\hat{L}_q} \left\langle \frac{\sqrt{1-yb}}{b} \right\rangle_\theta^x . \\
I \left\langle \frac{\partial}{\partial \psi} \left(\frac{v_\parallel}{\omega_{c,i}} \right) \right\rangle_\theta^\psi &= -\frac{\sigma v B_0}{\omega_{ci0}} \left[\left\langle \frac{B' \lambda B}{2 B^2 \sqrt{1-\lambda B}} \right\rangle_\theta^\psi + \left\langle \frac{B' \sqrt{1-\lambda B}}{B^2} \right\rangle_\theta^\psi \right] \\
&= -\frac{\sigma v}{2} \frac{B_0}{\omega_{ci0}} \left\langle \frac{(2-\lambda B)}{\sqrt{1-\lambda B}} \frac{B'}{B^2} \right\rangle_\theta^\psi \\
&= -\frac{\sigma u}{2} \frac{v_{\mathrm{th}}}{\cancel{\omega_{ci0}}^{\omega_{c\theta}}} \frac{\cancel{B_0}}{\cancel{R B_\theta} r_s} \frac{\cancel{R B_\phi}^{1/1+\epsilon}}{\cancel{B}_{\max}} \left\langle \frac{(2-yb)}{b^2 \sqrt{1-yb}} \frac{\partial b}{\partial x} \right\rangle_\theta^x \\
&= -\frac{\sigma u}{2} \frac{\hat{\rho}_\theta}{(1+\epsilon)} \left\langle \frac{b'}{b^2} \frac{(2-yb)}{\sqrt{1-yb}} \right\rangle_\theta^x .
\end{aligned}
$$

Define the normalised ion drift frequency $\hat{\omega}_D$ (a length-less drift velocity), to be the combination of the terms above, such that:

$$
\begin{aligned}
\frac{p}{\hat{L}_q} + \frac{\hat{\rho}_\theta}{\hat{L}_q} \hat{\omega}_D &= \frac{q_s'}{q_s} p_\varphi + \frac{q_s'}{q_s} I \left\langle \frac{v_\parallel}{\omega_{ci}} \right\rangle_\theta^\psi + I \left\langle \frac{\partial}{\partial \psi} \left(\frac{v_\parallel}{\omega_{c,i}} \right) \right\rangle_\theta^\psi , \\
\hat{\omega}_D &= \frac{\sigma u}{(1+\epsilon)} \left[\left\langle \frac{\sqrt{1-yb}}{b} \right\rangle_\theta^x - \frac{\hat{L}_q}{2} \left\langle \frac{b'}{b^2} \frac{(2-yb)}{\sqrt{1-yb}} \right\rangle_\theta^x \right] .
\end{aligned}
\tag{8.3.13}
$$

Next, the electrostatic potential-dependent $\mathbf{E}\times\mathbf{B}$ terms in Eq.(2.3.38), $\frac{\partial\bar{g}}{\partial\xi}$ and $\frac{\partial\bar{g}}{\partial p}$:

$$\begin{aligned}\left\langle \frac{R}{v_\parallel}\frac{\partial\Phi}{\partial\psi}\right\rangle_\theta^{p_\varphi} &= \frac{T_i}{e_i v_{\mathrm{th}i}}\left\langle \frac{R}{u_\parallel}\frac{1}{RB_\theta r_s}\frac{\partial\hat{\Phi}}{\partial x}\right\rangle_\theta^{p} = \frac{m_i v_{\mathrm{th}i}}{2e_i B_\theta}\frac{1}{r_s}\left\langle \frac{1}{u_\parallel}\frac{\partial\hat{\Phi}}{\partial x}\right\rangle_\theta^{p}\\ &= \frac{\hat{\rho}_\theta}{2}\left\langle \frac{1}{u_\parallel}\frac{\partial\hat{\Phi}}{\partial x}\right\rangle_\theta^{p}.\\ \left\langle \frac{R}{v_\parallel}\frac{\partial\Phi}{\partial\xi}\right\rangle_\theta^{p_\varphi}\frac{\partial}{\partial p_\varphi} &= \frac{T_i}{e_i v_{\mathrm{th}i}}\frac{1}{RB_\theta r_s}\left\langle \frac{R}{u_\parallel}\frac{\partial\hat{\Phi}}{\partial\xi}\right\rangle_\theta^{p}\frac{\partial}{\partial p}\\ &= \frac{\hat{\rho}_\theta}{2}\left\langle \frac{1}{u_\parallel}\frac{\partial\hat{\Phi}}{\partial\xi}\right\rangle_\theta^{p}\frac{\partial}{\partial p}.\end{aligned}$$

Then, the island perturbation term in $\frac{\partial\bar{g}}{\partial p}$:

$$\begin{aligned}m\tilde{\psi}\sin\xi\frac{\partial}{\partial p_\varphi} &= \frac{m}{4}\sin\xi\frac{\hat{w}^2}{\hat{L}_q}\frac{RB_\theta r_s}{RB_\theta r_s}\frac{\partial}{\partial p_\varphi}\\ &= \frac{m\hat{w}^2}{4\hat{L}_q}\sin\xi\frac{\partial}{\partial p}.\end{aligned}$$

Lastly, the terms within $\frac{\partial \bar{g}}{\partial p}$, $\frac{\partial^2 \bar{g}}{\partial p^2}$, $\frac{\partial^2 \bar{g}}{\partial dp dy}$, introduced by the collision operator:

$$\begin{aligned}
\nu_{ii}\frac{R_0 q_0 I}{\omega_{ci0}}\frac{\partial}{\partial p_\varphi} &= \hat{\nu}_{ii}\frac{v_{\text{th}}}{Rq}\frac{RqRB_\phi}{\omega_{ci0}}\frac{1}{RB_\theta r_s}\frac{\partial}{\partial p} \\
&= \hat{\nu}_{ii}\hat{\rho}_\theta\frac{\partial}{\partial p}. \\
\frac{\nu_{ii}}{2}\sigma v R_0 q_0 \lambda B_0\left(\frac{I}{\omega_{ci0}}\right)^2\left\langle\frac{1}{\sqrt{1-\lambda B}}\right\rangle_\theta^\psi\frac{\partial^2}{\partial p_\varphi^2} & \\
&= \frac{\hat{\nu}_{ii}}{2}\frac{v_{\text{th}}}{Rq}\sigma u v_{\text{th}} R_0 q_0\frac{y}{(1+\epsilon)}\left(\frac{RB_\phi}{\omega_{ci0}RB_\theta r_s}\right)^2\left\langle\frac{1}{\sqrt{1-yb}}\right\rangle_\theta^x\frac{\partial^2}{\partial p^2} \\
&= \frac{\hat{\nu}_{ii}}{2}\frac{\sigma u}{(1+\epsilon)}\hat{\rho}_\theta^2 y\left\langle\frac{1}{\sqrt{1-yb}}\right\rangle_\theta^x\frac{\partial^2}{\partial p^2}. \\
2\nu_{ii}R_0 q_0\frac{I}{\omega_{ci0}}\lambda\frac{\partial^2}{\partial\lambda\partial p_\varphi} &= \frac{2\hat{\nu}_{ii}}{v_{\text{th}}}\frac{v_{\text{th}}}{Rq}R_0 q_0 y\frac{RB_\phi}{\omega_{ci0}}\frac{1}{RB_\theta r_s}\frac{\partial^2}{\partial y\partial p} \\
&= 2\hat{\nu}_{ii}\hat{\rho}_\theta y\frac{\partial^2}{\partial y\partial p}. \\
\frac{\nu_{ii}}{\sigma v}\frac{R_0 q_0}{B_0}\left\langle\frac{(2-3\lambda B)}{\sqrt{1-\lambda B}}\right\rangle_\theta^\psi\frac{\partial}{\partial\lambda} &= \frac{\hat{\nu}_{ii}}{\sigma u v_{\text{th}}}\frac{v_{\text{th}}}{Rq}\frac{R_0 q_0}{B_0}B_{\max}\left\langle\frac{(2-3yb)}{\sqrt{1-yb}}\right\rangle_\theta^x\frac{\partial}{\partial y} \\
&= \frac{\hat{\nu}_{ii}}{\sigma u}(1+\epsilon)\left\langle\frac{(2-3yb)}{\sqrt{1-yb}}\right\rangle_\theta^x\frac{\partial}{\partial y}. \\
\frac{2\nu_{ii}}{\sigma v}\frac{R_0 q_0}{B_0}\lambda\left\langle\sqrt{1-\lambda B}\right\rangle_\theta^x\frac{\partial^2}{\partial\lambda^2} &= \frac{2\hat{\nu}_{ii}}{\sigma u v_{\text{th}}}\frac{v_{\text{th}}}{Rq}\frac{R_0 q_0}{B_0}B_{\max}y\left\langle\sqrt{1-yb}\right\rangle_\theta^x\frac{\partial^2}{\partial y^2} \\
&= \frac{2\hat{\nu}_{ii}}{\sigma u}(1+\epsilon)y\left\langle\sqrt{1-yb}\right\rangle_\theta^x\frac{\partial^2}{\partial y^2}.
\end{aligned}$$

The velocity volume integral (2.2.16) applied to some distribution function $f(\lambda,\sigma,v)$ in normalised units becomes:

$$\begin{aligned}
\int f\ d^3\boldsymbol{v} &\equiv \pi B\sum_\sigma\int_0^\infty dv\ v^2\int_0^{B^{-1}}\frac{f\ d\lambda}{\sqrt{1-\lambda B}} \\
&= \pi b v_{\text{th}}^3\sum_\sigma\int_0^\infty du\ u^2\int_0^{b^{-1}}\frac{dy}{\sqrt{1-yb}}.
\end{aligned} \tag{8.3.14}$$

Normalising $\hat{f} = \frac{\pi^{3/2} v_{\mathrm{th},i}^3}{n} f$, then the collision operator term (2.2.14) becomes:

$$\begin{aligned}
\bar{u}_{\parallel j}(f) &= \frac{1}{n_s \langle \nu_{jj} \rangle_v} \int d^3\boldsymbol{v}\, \nu_{jj}(v) v_\parallel\, f(\boldsymbol{v}) \\
&= \frac{\pi b v_{\mathrm{th}}^4}{n_s \langle \hat{\nu}_{ii} \rangle_v} \sum_\sigma \sigma \int_0^\infty du\, \hat{\nu}_{ii} u^3 \int_0^{b^{-1}} \frac{\sqrt{1-yb}}{\sqrt{1-yb}} dy\, \frac{n_s}{\pi^{3/2} v_{\mathrm{th}}^3} \hat{f} \\
&= \frac{v_{\mathrm{th}} b}{\sqrt{\pi} \langle \hat{\nu}_{ii} \rangle_v} \sum_\sigma \sigma \int_0^\infty du\, \hat{\nu}_{ii} u^3 \int_0^{b^{-1}} dy\, \hat{f}.
\end{aligned} \tag{8.3.15}$$

Therefore, the corresponding term in Eq.(2.3.38) becomes:

$$\begin{aligned}
2\nu_{ii} \frac{R_0 q_0}{B_0} \frac{\langle B \bar{u}_{\parallel,i}(g_1) \rangle_\theta^{p_\varphi}}{v_{\mathrm{th}i}^2} &= 2\hat{\nu}_{ii} \frac{v_{\mathrm{th}}}{Rq} \frac{R_0 q_0 B_{\max}}{B_0 v_{\mathrm{th}}^2} \langle b \bar{u}_{\parallel,i}(g_i) \rangle_\theta^p \\
&= 2\hat{\nu}_{ii} \frac{(1+\epsilon)}{v_{\mathrm{th},i}} \frac{v_{\mathrm{th},i}}{\sqrt{\pi}} \frac{1}{\langle \hat{\nu}_{ii} \rangle_v} \left\langle b^2 \sum_\sigma \sigma \int_0^\infty du\, u^3 \hat{\nu}_{ii} \int_0^{b^{-1}} dy\, g_i \right\rangle_\theta^p
\end{aligned} \tag{8.3.16}$$

Define:

$$\hat{\bar{U}}_{\parallel i}(\hat{f}) = \frac{1}{\sqrt{\pi} \langle \hat{\nu}_{ii} \rangle_v} \left\langle \sum_\sigma \sigma \int_0^\infty du\, u^3 \hat{\nu}_{ii} \int_0^{b^{-1}} dy\, \hat{f} \right\rangle_\theta^p. \tag{8.3.17}$$

Note that $b^2 = O(\epsilon^2)$, so $\langle b^2 \rangle_\theta \to 1$, which means that $\hat{\bar{U}}_{\parallel i}(\hat{f})$ can be used to approximate Eq.(8.3.16):

$$\Rightarrow\ 2\nu_{ii} \frac{R_0 q_0}{B_0} \frac{\langle B \bar{u}_{\parallel i}(\hat{g}_1) \rangle_\theta^{p_\varphi}}{v_{\mathrm{th}i}^2} = 2\hat{\nu}_{ii}(1+\epsilon) \hat{\bar{U}}_{\parallel i}(\hat{g} + p\hat{F}'_{\mathrm{M}}).$$

Putting everything together, the normalised drift-kinetic NTM equation for $\hat{g}$ (2.3.47) is:

$$\begin{aligned}
&- m \left[\frac{p}{\hat{L}_q} \Theta_y + \frac{\hat{\rho}_\theta}{\hat{L}_q} \hat{\omega}_D - \frac{\hat{\rho}_\theta}{2} \left\langle \frac{1}{u_\parallel} \frac{\partial \hat{\Phi}}{\partial x} \right\rangle_\theta^p \right] \frac{\partial \hat{g}}{\partial \xi} \\
&+ \left[\frac{m}{4} \frac{\hat{w}^2}{\hat{L}_q} \sin\xi\, \Theta_y - m \frac{\hat{\rho}_\theta}{2} \left\langle \frac{1}{u_\parallel} \frac{\partial \hat{\Phi}}{\partial \xi} \right\rangle_\theta^p - \hat{\nu}_{ii} \hat{\rho}_\theta \Theta_y \right] \left(\frac{\partial \hat{g}}{\partial p} + \hat{F}'_{\mathrm{M}s} \right) \\
&- \frac{\hat{\nu}_{ii}}{2} \frac{\sigma u}{(1+\epsilon)} \hat{\rho}_\theta^2 y \left\langle \frac{1}{\sqrt{1-yb}} \right\rangle_\theta^x \frac{\partial^2 \hat{g}}{\partial p^2} - 2\hat{\nu}_{ii} \hat{\rho}_\theta y \Theta_y \frac{\partial^2 \hat{g}}{\partial y \partial p} - \frac{\hat{\nu}_{ii}}{\sigma u}(1+\epsilon) \left\langle \frac{(2-3yb)}{\sqrt{1-yb}} \right\rangle_\theta^x \left. \frac{\partial \hat{g}}{\partial y} \right|_p \\
&\qquad - \frac{2\hat{\nu}_{ii}}{\sigma u}(1+\epsilon) y \left\langle \sqrt{1-yb} \right\rangle_\theta^x \left. \frac{\partial^2 \hat{g}}{\partial y^2} \right|_p = 2\hat{\nu}_{ii}(1+\epsilon) \hat{\bar{U}}_{\parallel i}(\hat{g} + p\hat{F}'_{\mathrm{M}s}) \hat{F}_{\mathrm{M}s}
\end{aligned} \tag{8.3.18}$$

where $\Theta_y = 1$ for passing particles, and $\Theta_y = 0$ for trapped particles.

8.4 Velocity volume integral

Recall in Sec. 1.2.4 that by taking fluid moments of the distribution function, we obtain the density and flow. For this, we use the velocity volume integral operator, given by:

$$\{f\}_v = \pi B \sum_\sigma \int_0^\infty dv\ v^2 \int_0^{B^{-1}} \frac{f d\lambda}{\sqrt{1-\lambda B}} \tag{8.4.1}$$

In normalised units, taking account the normalisation of the particle distribution $\hat{f}_j = \frac{\pi^{3/2} v_{\mathrm{th},i}^3}{n_s} f_j$:

$$\left\{\hat{f}\right\}_v = \frac{n_s}{v_{\mathrm{th},i}^3} \frac{b}{\sqrt{\pi}} \sum_\sigma \int_0^\infty dv\ v^2 \int_0^{b^{-1}} \frac{\hat{f} dy}{\sqrt{1-yb}} \tag{8.4.2}$$

8.4.1 Calculating the divergent y-integral

We note $(1-yb)^{-1/2}$ is asymptotic at $y \to b^{-1}$, hence the integral is split into two parts for $(0, y_0)$ and (y_0, b^{-1}), evaluated numerically and analytically (through fitting) respectively:

$$\int_0^{b^{-1}} \frac{f dy}{\sqrt{1-yb}} = \int_0^{y_0} \frac{f dy}{\sqrt{1-yb}} + \int_{y_0}^{b^{-1}} \frac{f dy}{\sqrt{1-yb}} \tag{8.4.3}$$

Here, $y_0 = b^{-1} - \delta y_0$, where δy_0 is the spacing of the nearest mesh point to y_0. For the analytic part $y = (y_0, b^{-1})$, we assume $f(y)$ varies slowly from y_0 to b^{-1}, and approximate this as a linear function $f(y) = Ay + C$. Then:

$$\int_{y_0}^{b^{-1}} \frac{Ay + C dy}{\sqrt{1-yb}} = \frac{2\sqrt{1-y_0 b}}{3b^2}(A(y_0 b + 2) + 3bC) \tag{8.4.4}$$

Within the code, this analytic expression is provided by function `IinvB`.

8.5 Numerical Algorithm

8.5.1 Finite difference discretisation

The 4D drift-kinetic equation (2.3.47) and other derivatives (e.g., of $\hat{\Phi}$ and $h(\Omega)$) are discretised using the 2$^{\text{nd}}$-order accurate central difference method. For a general monotonically-increasing mesh X (not to be confused with radial coordinate x), at an index i, defining the mesh spacing $h_i = X_i - X_{i-1}$ at that point, the individual terms of the k-th derivative finite difference approximation are represented by $\Delta^{\pm}_{kx}$ (not to be confused with the expansion parameter $\Delta = w/r_s$ or island growth parameter Δ_{loc}). The 1$^{\text{st}}$ derivative is approximated by:

$$\frac{\partial f}{\partial X_i} = \Delta^{-}_{1X(i)} f(X_{i-1}) + \Delta^{0}_{1X(i)} f(X_i) + \Delta^{+}_{1X(i)} f(X_{i+1}) \tag{8.5.1}$$

$$= \frac{-h_{i+1}}{h_i(h_{i+1}+h_i)} f(X_{i-1}) + \frac{h_{i+1}-h_i}{h_{i+1}h_i} f(X_i) + \frac{h_i}{h_{i+1}(h_{i+1}+h_i)} f(X_{i+1}) \tag{8.5.2}$$

The 2$^{\text{nd}}$ derivative is approximated by:

$$\frac{\partial^2 f}{\partial X_i^2} = \Delta^{-}_{2X(i)} f(X_{i-1}) + \Delta^{0}_{2X(i)} f(X_i) + \Delta^{+}_{2X(i)} f(X_{i+1}) \tag{8.5.3}$$

$$= \frac{2}{h_i(h_{i+1}+h_i)} f(X_{i-1}) - \frac{2}{h_{i+1}h_i} f(X_i) + \frac{2}{h_{i+1}(h_{i+1}+h_i)} f(X_{i+1}) \tag{8.5.4}$$

For uniform meshes (ξ, θ), where h_i is equal at all i, these reduce to: The 1$^{\text{st}}$ derivative is approximated by:

$$\frac{\partial f}{\partial X_i} = \Delta^{-}_{1X(i)} f(X_{i-1}) + \Delta^{0}_{1X(i)} f(X_i) + \Delta^{+}_{1X(i)} f(X_{i+1}) \tag{8.5.5}$$

$$= \frac{-1}{2h} f(X_{i-1}) + 0 + \frac{1}{2h} f(X_{i+1}) \tag{8.5.6}$$

The 2$^{\text{nd}}$ derivative is approximated by:

$$\frac{\partial^2 f}{\partial X_i^2} = \Delta^{-}_{2X(i)} f(X_{i-1}) + \Delta^{0}_{2X(i)} f(X_i) + \Delta^{+}_{2X(i)} f(X_{i+1}) \tag{8.5.7}$$

$$= \frac{1}{2h^2} f(X_{i-1}) - \frac{2}{h^2} f(X_i) + \frac{1}{2h^2} f(X_{i+1}) \tag{8.5.8}$$

Discretised boundary conditions

At the p-mesh limits ($p = p_{\min} \equiv p_{j=1}$), the Dirichlet boundary condition $\dfrac{\partial \hat{g}}{\partial p} = 0$ is applied:

$$\Delta^{+}_{1p1} g_2 + \Delta^{0}_{1p1} g_1 + \Delta^{-}_{1p1} g_0 = 0,$$

where g_0 corresponds to the value of the solution just beyond the mesh boundary, if it were to exist. Then:

$$\begin{aligned} g_0 &= -\left(\frac{\Delta^{0}_{1p1}}{\Delta^{-}_{1p1}} g_1 + \frac{\Delta^{+}_{1p1}}{\Delta^{-}_{1p1}} g_2 \right) \\ &= -\left[-\frac{(h_2 - h_1)}{h_2 h_1} \frac{h_1(h_2 + h_1)}{h_2} g_1 - \frac{h_1 h_1 (h_2 + h_1)}{h_2 (h_1 + h_2) h_2} g_2 \right] \\ \therefore \; g_0 &= \frac{(h_2^2 - h_1^2)}{h_2^2} g_1 + \frac{h_1^2}{h_2^2} g_2. \end{aligned}$$

Then,

$$\begin{aligned} \left. \frac{\partial^2 g}{\partial p^2} \right|_{j=1} &= \frac{2g_2}{h_2(h_2 + h_1)} - \frac{2g_1}{h_2 h_1} + \frac{2g_0}{h_1(h_2 + h_1)} \\ &= \frac{2g_2}{h_2(h_2 + h_1)} - \frac{2g_1}{h_2 h_1} + \frac{2h_1^2 g_2}{h_1(h_2 + h_1)h_2^2} + \frac{2(h_2^2 - h_1^2) g_1}{h_1(h_2 + h_1)h_2^2} \\ &= 2\left[\frac{g_2}{h_2^2} - \frac{h_1(h_1 + h_2)}{h_1 h_2^2 (h_1 + h_2)} g_1 \right] \\ \therefore \; \left. \frac{\partial^2 g}{\partial p^2} \right|_{j=1} &= \frac{2}{h_2^2}(g_2 - g_1), \qquad \Delta^{0}_{2p1} = -\frac{2}{h_2^2}, \quad \Delta^{+}_{2p1} = +\frac{2}{h_2^2}. \end{aligned} \tag{8.5.9}$$

Likewise, at $p = p_{\max} \equiv p_{j=n_p}$,

$$\Delta^{+}_{1pn_p} g_{\prime n_p + 1\prime} + \Delta^{0}_{1pn_p} g_{n_p} + \Delta^{-}_{1pn_p} g_{n_p - 1} = 0,$$

$$\begin{aligned} \Rightarrow \; g_{n_p+1} &= -\left(\frac{\Delta^{0}_{1pn_p}}{\Delta^{+}_{1pn_p}} g_{n_p} + \frac{\Delta^{-}_{1pn_p}}{\Delta^{+}_{1pn_p}} g_{n_p - 1} \right) \\ &= -\frac{(h_{n_p+1} - h_{n_p})}{h_{n_p}^2} g_{n_p} + \frac{h_{n_p+1}^2}{h_{n_p}^2} g_{n_p - 1}. \end{aligned}$$

$$\Rightarrow \left.\frac{\partial^2 g}{\partial p^2}\right|_{j=n_p} = -2\frac{(h_{n_p+1}-h_{n_p})(h_{n_p+1}+h_{n_p})}{h_{n_p+1}(h_{n_p+1}+h_{n_p})}g_{n_p} + 2\frac{h_{n_p}^2}{h_{n_p+1}(h_{n_p+1}+h_{n_p})h_{n_p}^2}g_{n_p} - \frac{2g_{n_p}}{h_{n_p+1}h_{n_p}^2} + \frac{2g_{n_p-1}}{h_{n_p}(h_{n_p+1}+h_{n_p})}$$

$$= -2g_{n_p}\frac{(h_{n_p+1}-h_{n_p})}{h_{n_p+1}h_{n_p}^2} + 2g_{n_p-1}\frac{(h_{n_p+1}+h_{n_p})}{(h_{n_p+1}+h_{n_p})h_{n_p}^2}$$

$$\therefore \left.\frac{\partial^2 g}{\partial p^2}\right|_{j=n_p} = -\frac{2}{h_{n_p}^2}(g_{n_p}-g_{n_p-1}), \qquad \Delta^0_{2pn_p} = -\frac{2}{h_{n_p^2}}, \quad \Delta^-_{2pn_p} = +\frac{2}{h_{n_p^2}}. \tag{8.5.10}$$

For ξ-space, the mesh is constructed to be uniform, so:

$$\left.\frac{\partial g}{\partial \xi}\right|_k = \frac{g_{k+1}-g_{k-1}}{2h_\xi}, \tag{8.5.11}$$

where k is the ξ-mesh index. At the ξ-mesh edges, the periodic condition (2.3.50) implies:

$$\left.\frac{\partial g}{\partial \xi}\right|_{k=n_\xi} = \left.\frac{\partial g}{\partial \xi}\right|_{k=1} = \frac{g_{k=2}-g_{n_\xi-1}}{2h_\xi}. \tag{8.5.12}$$

Cross-derivatives, such as the $\left.\frac{\partial^2 \hat{g}}{\partial p \partial y}\right|_y$ term, are represented by a product:

$$\frac{\partial^2 \hat{g}}{\partial p \partial y} = \Delta^+_{1yl}\left.\frac{\partial g_{l+1}}{\partial p}\right|_j + \Delta^0_{1yl}\left.\frac{\partial g_l}{\partial p}\right|_j + \Delta^-_{1yl}\left.\frac{\partial g_{l-1}}{\partial p}\right|_j$$

$$\rightarrow \frac{\partial^2 \hat{g}}{\partial p \partial y} = \Delta^+_{1yl}\left(\Delta^+_{1pj}g_{j+1,l+1} + \Delta^0_{1pj}g_{j,l+1} + \Delta^-_{1pj}g_{j-1,l+1}\right) + \Delta^0_{1yl}\left(\Delta^+_{1pj}g_{j+1,l} + \Delta^0_{1pj}g_{j,l} + \Delta^-_{1pj}g_{j-1,l}\right) + \Delta^-_{1yl}\left(\Delta^+_{1pj}g_{j+1,l-1} + \Delta^0_{1pj}g_{j,l-1} + \Delta^-_{1pj}g_{j-1,l-1}\right). \tag{8.5.13}$$

At p-mesh limits, the boundary condition (2.3.51) applies, so $\frac{\partial^2 \hat{g}}{\partial p \partial y} = 0$. At y-mesh limits, the boundary condition $\frac{\partial^2 \hat{g}}{\partial y^2} = 0$ applies, and the special form for $\frac{\partial \hat{g}}{\partial y}$ is used.

8.5.2 Matrix equation

Recall the general matrix equation coupling three general y-points:

$$\underline{\mathbf{P}}_l \cdot \mathbf{g}_{l+1} + \underline{\mathbf{Q}}_l \cdot \mathbf{g}_l + \underline{\mathbf{R}}_l \cdot \mathbf{g}_{l-1} + \underline{\mathbf{L}}_l \cdot \mathbf{g}_l = \mathbf{D}_l, \tag{8.5.14}$$

Recurrence relation

For Eq.(8.5.14), At a general y-point, the equation be approximated by using a linear recurrence relation between the neighbouring y-points. For the passing region we can write:

$$\mathbf{g}_l^p = \underline{\boldsymbol{\alpha}}_l^p \cdot \mathbf{g}_{l+1}^p + \boldsymbol{\beta}_l^p, \tag{8.5.15}$$

$$\Rightarrow \quad \mathbf{g}_{l-1}^p = \underline{\boldsymbol{\alpha}}_{l-1}^p \cdot \mathbf{g}_l^p + \boldsymbol{\beta}_{l-1}^p. \tag{8.5.16}$$

(Superscript p denotes passing particles.) Inserting Eq.(8.5.16) into Eq.(8.5.14) gives:

$$\underline{\mathbf{P}}_l^p \cdot \mathbf{g}_{l+1}^p + (\underline{\mathbf{Q}}_l^p + \underline{\mathbf{L}}_l^p) \cdot \mathbf{g}_l^p + \underline{\mathbf{R}}_l^p \cdot \underline{\boldsymbol{\alpha}}_{l-1}^p \cdot \mathbf{g}_l^p + \underline{\mathbf{R}}_l^p \cdot \boldsymbol{\beta}_{l-1}^p = \mathbf{D}_l^p. \tag{8.5.17}$$

By letting:

$$\underline{\mathbf{M}}_l^p = \underline{\mathbf{Q}}_l^p + \underline{\mathbf{L}}_l^p + \underline{\mathbf{R}}_l^p \cdot \underline{\boldsymbol{\alpha}}_{l-1}^p, \tag{8.5.18}$$

rearranging Eq.(8.5.17):

$$\mathbf{g}_l^p = -\left[(\underline{\mathbf{M}}_l^p)^{-1} \cdot \underline{\mathbf{P}}_l^p\right] \cdot \mathbf{g}_{l+1}^p + (\underline{\mathbf{M}}_l^p)^{-1} \cdot \left(\mathbf{D}_l^p - \underline{\mathbf{R}}_l^p \cdot \boldsymbol{\beta}_{l-1}^p\right),$$

and comparing with Eq.(8.5.15), we arrive at the recursion relation for $\underline{\boldsymbol{\alpha}}_l^p$ and $\boldsymbol{\beta}_l^p$:

$$\boxed{\underline{\boldsymbol{\alpha}}_l^p = -(\underline{\mathbf{M}}_l^p)^{-1} \cdot \underline{\mathbf{P}}_l^p, \quad \boldsymbol{\beta}_l^p = (\underline{\mathbf{M}}_l^p)^{-1} \cdot \left(\mathbf{D}_l^p - \underline{\mathbf{R}}_l^p \cdot \boldsymbol{\beta}_{l-1}^p\right), \quad \underline{\mathbf{M}}_l^p = \underline{\mathbf{Q}}_l^p + \underline{\mathbf{L}}_l^p + \underline{\mathbf{R}}_l^p \cdot \underline{\boldsymbol{\alpha}}_{l-1}^p} \tag{8.5.19}$$

$\underline{\boldsymbol{\alpha}}_{l=1}^p$ and $\boldsymbol{\beta}_{l=1}^p$ are to be determined using the deeply passing end y-boundary condition, as described in next subsection.

Similarly, for trapped particles, the linear recurrence relation is in the opposite direction:

$$\mathbf{g}_l^t = \underline{\boldsymbol{\alpha}}_l^t \cdot \mathbf{g}_{l-1}^t + \boldsymbol{\beta}_l^t, \tag{8.5.20}$$

$$\Rightarrow \quad \mathbf{g}_{l+1}^t = \underline{\boldsymbol{\alpha}}_{l+1}^t \cdot \mathbf{g}_l^t + \boldsymbol{\beta}_{l+1}^t. \tag{8.5.21}$$

Inserting Eq.(8.5.16) into Eq.(8.5.14) gives:

$$(\underline{\mathbf{P}}_l^t \cdot \underline{\boldsymbol{\alpha}}_{l+1}^t + \underline{\mathbf{Q}}_l^t + \underline{\mathbf{L}}_l^t) \cdot \mathbf{g}_l^t + \underline{\mathbf{R}}_l^t \cdot \mathbf{g}_{l-1}^t = \mathbf{D}_l^t - \underline{\mathbf{P}}_l^t \cdot \boldsymbol{\beta}_{l+1}^t \tag{8.5.22}$$

By letting

$$\underline{\mathbf{M}}_l^t = \underline{\mathbf{Q}}_l^t + \underline{\mathbf{L}}_l^t + \underline{\mathbf{P}}_l^t \cdot \underline{\boldsymbol{\alpha}}_{l+1}^t, \tag{8.5.23}$$

rearranging Eq.(8.5.22):

$$\mathbf{g}_l^t = -\left[(\underline{\mathbf{M}}_l^t)^{-1} \cdot \underline{\mathbf{R}}_l^t\right] \cdot \mathbf{g}_{l-1}^t + (\underline{\mathbf{M}}_l^t)^{-1} \cdot \left(\mathbf{D}_l^t - \underline{\mathbf{P}}_l^t \cdot \boldsymbol{\beta}_{l+1}^t\right),$$

and comparing with Eq.(8.5.15), we arrive at the recursion relation for $\underline{\boldsymbol{\alpha}}_l^p$ and $\boldsymbol{\beta}_l^p$:

$$\boxed{\underline{\boldsymbol{\alpha}}_l^t = -(\underline{\mathbf{M}}_l^t)^{-1} \cdot \underline{\mathbf{R}}_l^p, \quad \boldsymbol{\beta}_l^t = (\underline{\mathbf{M}}_l^t)^{-1} \cdot \left(\mathbf{D}_l^t - \underline{\mathbf{P}}_l^t \cdot \boldsymbol{\beta}_{l+1}^t\right), \quad \underline{\mathbf{M}}_l^t = \underline{\mathbf{Q}}_l^t + \underline{\mathbf{L}}_l^t + \underline{\mathbf{P}}_l^t \cdot \underline{\boldsymbol{\alpha}}_{l+1}^t} \tag{8.5.24}$$

$\underline{\boldsymbol{\alpha}}_{l=1}^p$ and $\boldsymbol{\beta}_{l=1}^p$ are to be determined using the deeply trapped end y-boundary condition, as described in next subsection.

λ-boundary conditions

To discretise the boundary conditions at y-mesh limits, quadratic fitting is performed at the three points at each limit. By defining a quadratic function:

$$\mathbf{g}_l^{t/p} = \mathbf{a} y_l^2 + \mathbf{b} y_l + \mathbf{c}, \tag{8.5.25}$$

$$\left.\frac{\partial \mathbf{g}}{\partial y}\right|_{y_l} = 2\mathbf{a} y_l + \mathbf{b}, \tag{8.5.26}$$

and solving coefficients $\mathbf{a}$, $\mathbf{b}$ and $\mathbf{c}$, special forms of the finite difference for y can be obtained. These are to be determined separately for the deeply passing and trapped ends, respectively.

Deeply passing end

At the deeply passing end ($l = 1$), we fit across $l = 1$, 2 and 3 (some subscripts and superscripts are dropped for simplicity):

$$\mathbf{g}_1 = \mathbf{a} y_1^2 + \mathbf{b} y_1 + \mathbf{c} \tag{8.5.27}$$

$$\mathbf{g}_2 = \mathbf{a} y_2^2 + \mathbf{b} y_2 + \mathbf{c} \tag{8.5.28}$$

$$\mathbf{g}_3 = \mathbf{a} y_3^2 + \mathbf{b} y_3 + \mathbf{c} \tag{8.5.29}$$

Firstly, (8.5.27)−(8.5.28) and (8.5.28)−(8.5.29):

$$\begin{aligned}\mathbf{g}_1 - \mathbf{g}_2 &= \mathbf{a}(y_1^2 - y_2^2) + \mathbf{b}(y_1 - y_2)\\ &= \mathbf{a}(y_1 + y_2)(y_1 - y_2) + \mathbf{b}(y_1 - y_2)\\ \mathbf{g}_2 - \mathbf{g}_3 &= \mathbf{a}(y_2 + y_3)(y_2 - y_3) + \mathbf{b}(y_2 - y_3)\end{aligned}$$

Letting $h_1 = y_1 - y_2$, $h_2 = y_2 - y_3$ and $h_3 = y_1 - y_3$ $(= h_1 + h_2)$, (note: this deviates from the usual definition of mesh spacing $h_i = y_i - y_{i-1}$):

$$\begin{aligned}\frac{\mathbf{g}_1 - \mathbf{g}_2}{h_1} &= \mathbf{a}(y_1 + y_2) + \mathbf{b}\\ \frac{\mathbf{g}_2 - \mathbf{g}_3}{h_2} &= \mathbf{a}(y_2 + y_3) + \mathbf{b}\\ \rightarrow\ (y_1 - y_3)\mathbf{a} &= \frac{\mathbf{g}_1 - \mathbf{g}_2}{h_1} - \frac{\mathbf{g}_2 - \mathbf{g}_3}{h_2}\end{aligned}$$

$$\begin{aligned}\mathbf{a} &= \frac{\mathbf{g}_1}{h_1 h_3} - \frac{\mathbf{g}_2}{h_1 h_3} - \frac{\mathbf{g}_2}{h_2 h_3} + \frac{\mathbf{g}_3}{h_2 h_3}\\ &= \frac{\mathbf{g}_1}{h_1 h_3} - \frac{(h_1 + h_2)\mathbf{g}_2}{h_1 h_2 h_3} + \frac{\mathbf{g}_3}{h_2 h_3}\end{aligned}$$

$$\therefore\ \underline{\mathbf{a} = \frac{h_2\mathbf{g}_1 - h_3\mathbf{g}_2 + h_1\mathbf{g}_3}{h_1 h_2 h_3}}. \tag{8.5.30}$$

And, trivially,

$$\underline{\mathbf{b} = \frac{(\mathbf{g}_1 - \mathbf{g}_2)}{h_1} - (y_1 + y_2)\mathbf{a}}. \tag{8.5.31}$$

Then, returning to Eq.(8.5.26), at $y = y_1$:

$$\begin{aligned}\left.\frac{\partial \mathbf{g}}{\partial y}\right|_{y_1} &= 2\mathbf{a}y_1 + \mathbf{b}\\ &= (2y_1 - y_1 - y_2)\mathbf{a} + \frac{(\mathbf{g}_1 - \mathbf{g}_2)}{h_1}\\ &= h_1\mathbf{a} + \frac{h_2 h_3(\mathbf{g}_1 - \mathbf{g}_2)}{h_1 h_2 h_3}\\ &= \frac{h_1 h_2\mathbf{g}_1 + h_2 h_3\mathbf{g}_1 - h_1 h_3\mathbf{g}_2 - h_2 h_3\mathbf{g}_2 + h_1^2\mathbf{g}_3}{h_1 h_2 h_3}\\ \therefore\ \left.\frac{\partial \mathbf{g}}{\partial y}\right|_{y_1} &= \frac{h_1 + h_3}{h_1 h_3}\mathbf{g}_1 - \frac{h_3}{h_1 h_2}\mathbf{g}_2 + \frac{h_1}{h_2 h_3}\mathbf{g}_3.\end{aligned} \tag{8.5.32}$$

Now, returning to the matrix equation (8.5.14), at $l = 1$ $(y = y_1)$ we couple the first 3 mesh

points (note the offset in **g** indices):

$$\underline{\mathbf{P}}_1 \cdot \mathbf{g}_3 + \underline{\mathbf{Q}}_1 \cdot \mathbf{g}_2 + \underline{\mathbf{R}}_1 \cdot \mathbf{g}_1 + \mathbf{L}_1 \cdot \mathbf{g}_1 = \mathbf{D}_1, \tag{8.5.33}$$

where [in the absence of the cross-differential term] the diagonal elements of $\underline{\mathbf{P}}$, $\underline{\mathbf{Q}}$ and $\underline{\mathbf{R}}$ are:

$$\begin{aligned} &P_{1(qq)} = C^9_{1(qq)}\Delta^+_{1yl=1}, \quad Q_{1(qq)} = C^9_{1(qq)}\Delta^0_{1yl=1}, \quad R_{1(qq)} = C^9_{1(qq)}\Delta^-_{1yl=1}, \\ &\Delta^+_{1yl=1} = \frac{h_1}{h_2 h_3}, \quad \Delta^0_{1yl=1} = -\frac{h_3}{h_1 h_2}, \quad \Delta^-_{1yl=1} = \frac{(h_1+h_3)}{h_1 h_3}. \end{aligned} \tag{8.5.34}$$

N.B. $C^{10}_{l=1} = 0$ at the deeply passing end. At $y = y_2$ the matrix equation takes the standard form, as in Eq.(8.5.14):

$$\underline{\mathbf{P}}_2 \cdot \mathbf{g}_3 + \underline{\mathbf{Q}}_2 \cdot \mathbf{g}_2 + \underline{\mathbf{R}}_2 \cdot \mathbf{g}_1 + \mathbf{L}_2 \cdot \mathbf{g}_2 = \mathbf{D}_2, \tag{8.5.35}$$

where the matrices are as defined in the previous section. Then, from Eq.(8.5.33):

$$\underline{\mathbf{P}}_1 \cdot \mathbf{g}_3 = \mathbf{D}_1 - \underline{\mathbf{Q}}_1 \cdot \mathbf{g}_2 - (\underline{\mathbf{R}}_1 + \underline{\mathbf{L}}_1) \cdot \mathbf{g}_1.$$

Multiplying both sides by $\underline{\mathbf{P}}_2 \cdot \underline{\mathbf{P}}_1^{-1}$:

$$\underline{\mathbf{P}}_2 \cdot \mathbf{g}_3 = \underline{\mathbf{P}}_2 \cdot \underline{\mathbf{P}}_1^{-1} \cdot \left[\mathbf{D}_1 - \underline{\mathbf{Q}}_1 \cdot \mathbf{g}_2 - (\underline{\mathbf{R}}_1 + \underline{\mathbf{L}}_1) \cdot \mathbf{g}_1\right]$$

Inserting this into Eq.(8.5.35) gives:

$$\begin{aligned} &\underline{\mathbf{P}}_2 \cdot \underline{\mathbf{P}}_1^{-1} \cdot \left[\mathbf{D}_1 - \underline{\mathbf{Q}}_1 \cdot \mathbf{g}_2 - (\underline{\mathbf{R}}_1 + \underline{\mathbf{L}}_1) \cdot \mathbf{g}_1\right] + (\underline{\mathbf{Q}}_2 + \underline{\mathbf{L}}_2) \cdot \mathbf{g}_2 + \underline{\mathbf{R}}_2 \cdot \mathbf{g}_1 = \mathbf{D}_2 \\ &\left[\underline{\mathbf{R}}_2 - \underline{\mathbf{P}}_2 \cdot \underline{\mathbf{P}}_1^{-1} \cdot (\underline{\mathbf{R}}_1 + \underline{\mathbf{L}}_1)\right] \cdot \mathbf{g}_1 = \left(\underline{\mathbf{P}}_2 \cdot \underline{\mathbf{P}}_1^{-1} \cdot \underline{\mathbf{Q}}_1 - \underline{\mathbf{Q}}_2 - \underline{\mathbf{L}}_2\right) \cdot \mathbf{g}_2 \\ &\qquad\qquad + \mathbf{D}_2 - \underline{\mathbf{P}}_2 \cdot \underline{\mathbf{P}}_1^{-1} \cdot \mathbf{D}_1 \end{aligned}$$

Therefore, by inspection, we arrive at the results for $\underline{\boldsymbol{\alpha}}_1$ and $\boldsymbol{\beta}_1$ for the deeply-passing end:

$$\boxed{\begin{aligned} \underline{\boldsymbol{\alpha}}_1 &= \underline{\mathbf{M}}_1^{-1} \cdot \left(\underline{\mathbf{P}}_2 \cdot \underline{\mathbf{P}}_1^{-1} \cdot \underline{\mathbf{Q}}_1 - \underline{\mathbf{Q}}_2 - \underline{\mathbf{L}}_2\right), \\ \boldsymbol{\beta}_1 &= \underline{\mathbf{M}}_1^{-1} \cdot \left(\mathbf{D}_2 - \underline{\mathbf{P}}_2 \cdot \underline{\mathbf{P}}_1^{-1} \cdot \mathbf{D}_1\right), \\ \underline{\mathbf{M}}_1 &= \underline{\mathbf{R}}_2 - \underline{\mathbf{P}}_2 \cdot \underline{\mathbf{P}}_1^{-1} \cdot (\underline{\mathbf{R}}_1 + \underline{\mathbf{L}}_1) \end{aligned}} \tag{8.5.36}$$

Deeply trapped end

At the deeply trapped end, we make the fitting across $l = n-2$, $n-1$ and n (here, $n = n_y$) (again, some subscripts and superscripts are dropped for simplicity):

$$\mathbf{g}_{n-2} = \mathbf{a}y_{n-2}^2 + \mathbf{b}y_{n-2} + \mathbf{c} \tag{8.5.37}$$

$$\mathbf{g}_{n-1} = \mathbf{a}y_{n-1}^2 + \mathbf{b}y_{n-1} + \mathbf{c} \tag{8.5.38}$$

$$\mathbf{g}_{n} = \mathbf{a}y_{n}^2 + \mathbf{b}y_{n} + \mathbf{c}. \tag{8.5.39}$$

Then, Eq.(8.5.37)−Eq.(8.5.38) and Eq.(8.5.38)−Eq.(8.5.39) give:

$$\mathbf{g}_{n-2} - \mathbf{g}_{n-1} = \mathbf{a}(y_{n-2} + y_{n-1})(y_{n-2} - y_{n-1}) + \mathbf{b}(y_{n-2} - y_{n-1})$$
$$\mathbf{g}_{n-1} - \mathbf{g}_{n} = \mathbf{a}(y_{n-1} + y_{n})(y_{n-1} - y_{n}) + \mathbf{b}(y_{n-1} - y_{n}).$$

Letting $h_{n-2} = y_{n-2} - y_{n-1}$, $h_{n-1} = y_{n-1} - y_n$, and $h_n = y_{n-2} - y_n$ $(= h_{n-2} + h_{n-1})$,

$$\frac{\mathbf{g}_{n-2} - \mathbf{g}_{n-1}}{h_{n-2}} = \mathbf{a}(y_{n-2} + y_{n-1}) + \mathbf{b}$$
$$\frac{\mathbf{g}_{n-1} - \mathbf{g}_{n}}{h_{n-1}} = \mathbf{a}(y_{n-1} + y_{n}) + \mathbf{b}$$
$$\rightarrow\ (y_{n-2} - y_n)\mathbf{a} = \frac{\mathbf{g}_{n-2} - \mathbf{g}_{n-1}}{h_{n-2}} - \frac{\mathbf{g}_{n-1} - \mathbf{g}_{n}}{h_{n-1}}\mathbf{a} \quad = \frac{\mathbf{g}_{n-2}}{h_{n-2}h_n} - \frac{(h_{n-1} + h_{n-2})\mathbf{g}_{n-1}}{h_{n-2}h_{n-1}h_n} + \frac{\mathbf{g}_n}{h_{n-1}h_n}$$

$$\therefore\ \underline{\mathbf{a} = \frac{h_{n-1}\mathbf{g}_{n-2} - h_n\mathbf{g}_{n-1} + h_{n-2}\mathbf{g}_n}{h_{n-2}h_{n-1}h_n}}. \tag{8.5.40}$$

And, trivially,

$$\underline{\mathbf{b} = \frac{\mathbf{g}_{n-1} - \mathbf{g}_n}{h_{n-1}} - (y_{n-1} + y_n)\mathbf{a}}. \tag{8.5.41}$$

Then, returning to Eq.(8.5.26), at $y = y_n$:

$$\begin{aligned}
\left.\frac{\partial \mathbf{g}}{\partial y}\right|_{y_n} &= 2\mathbf{a}y_n + \mathbf{b} \\
&= (2y_n - y_{n-1} - y_n)\mathbf{a} + \frac{\mathbf{g}_{n-1} - \mathbf{g}_n}{h_{n-1}} \\
&= -h_{n-1}\mathbf{a} + \frac{h_{n-2}h_n\mathbf{g}_{n-1} - h_{n-2}h_n\mathbf{g}_n}{h_{n-2}h_{n-1}h_n} \\
&= \frac{-h_{n-1}^2\mathbf{g}_{n-2} + h_{n-1}h_n\mathbf{g}_{n-1} + h_{n-2}h_n\mathbf{g}_{n-1} - h_{n-2}h_{n-1}\mathbf{g}_n - h_{n-2}h_n\mathbf{g}_n}{h_{n-2}h_{n-1}h_n} \\
\therefore \left.\frac{\partial \mathbf{g}}{\partial y}\right|_{y_n} &= -\frac{h_{n-1}}{h_{n-2}h_n}\mathbf{g}_{n-2} + \frac{h_n}{h_{n-2}h_{n-1}}\mathbf{g}_{n-1} - \frac{(h_{n-1}+h_n)}{h_{n-1}h_n}\mathbf{g}_n. \qquad (8.5.42)
\end{aligned}$$

Now, returning to the matrix equation (8.5.14), at $l = n_{(y)}$ $(y = y_n)$ we couple the final 3 mesh points (note, again, the offset in $\mathbf{g}$ indices):

$$\underline{\mathbf{P}}_n \cdot \mathbf{g}_n + \underline{\mathbf{Q}}_n \cdot \mathbf{g}_{n-1} + \underline{\mathbf{R}}_n \cdot \mathbf{g}_{n-2} + \underline{\mathbf{L}}_n \cdot \mathbf{g}_n = \mathbf{D}_n, \qquad (8.5.43)$$

where [in the absence of the cross-differential term] the diagonal elements of $\underline{\mathbf{P}}$, $\underline{\mathbf{Q}}$ and $\underline{\mathbf{R}}$ are:

$$\begin{aligned}
&P_{n(qq)} = C^9_{n(qq)}\Delta^+_{1yl=n}, \quad Q_{n(qq)} = C^9_{n(qq)}\Delta^0_{1yl=n}, \quad R_{n(qq)} = C^9_{n(qq)}\Delta^-_{1yl=n}, \\
&\Delta^+_{1yl=n} = -\frac{(h_{n-1}+h_n)}{h_{n-1}h_n}, \quad \Delta^0_{1yl=n} = \frac{h_n}{h_{n-2}h_{n-1}}, \quad \Delta^-_{1yl=n} = -\frac{h_{n-1}}{h_{n-2}h_n}.
\end{aligned} \qquad (8.5.44)$$

N.B. $C^{10}_{l=n} = 0$ at the deeply trapped end as well. At $y = y_{n-1}$ the matrix equation takes the standard form, as in Eq.(8.5.14):

$$\underline{\mathbf{P}}_{n-1} \cdot \mathbf{g}_n + \underline{\mathbf{Q}}_{n-1} \cdot \mathbf{g}_{n-1} + \underline{\mathbf{R}}_{n-1} \cdot \mathbf{g}_{n-2} + \underline{\mathbf{L}}_{n-1} \cdot \mathbf{g}_{n-1} = \mathbf{D}_{n-1}, \qquad (8.5.45)$$

where the matrices are as defined in the previous section. Then, from Eq.(8.5.43),

$$\underline{\mathbf{R}}_n \cdot \mathbf{g}_{n-2} = \mathbf{D}_n - \underline{\mathbf{Q}}_n \cdot \mathbf{g}_{n-1} - (\underline{\mathbf{P}}_n + \underline{\mathbf{L}}_n) \cdot \mathbf{g}_n.$$

Multiplying both sides by $\underline{\mathbf{R}}_{n-1} \cdot \underline{\mathbf{R}}_n^{-1}$:

$$\underline{\mathbf{R}}_{n-1} \cdot \mathbf{g}_{n-2} = \underline{\mathbf{R}}_{n-1} \cdot \underline{\mathbf{R}}_n^{-1} \cdot \left[\mathbf{D}_n - \underline{\mathbf{Q}}_n \cdot \mathbf{g}_{n-1} - (\underline{\mathbf{P}}_n + \underline{\mathbf{L}}_n) \cdot \mathbf{g}_n\right].$$

Inserting this into Eq.(8.5.45) gives:

$$\underline{\mathbf{P}}_{n-1}\cdot\mathbf{g}_n+(\underline{\mathbf{Q}}_{n-1}+\underline{\mathbf{L}}_{n-1})\cdot\mathbf{g}_{n-1}+\underline{\mathbf{R}}_{n-1}\cdot\underline{\mathbf{R}}_n^{-1}\cdot\Big[\mathbf{D}_n-\underline{\mathbf{Q}}_n\cdot\mathbf{g}_{n-1}-(\underline{\mathbf{P}}_n+\underline{\mathbf{L}}_n)\cdot\mathbf{g}_n\Big]=\mathbf{D}_{n-1}$$

$$\big[\underline{\mathbf{P}}_{n-1}-\underline{\mathbf{R}}_{n-1}\cdot\underline{\mathbf{R}}_n^{-1}\cdot(\underline{\mathbf{P}}_n+\underline{\mathbf{L}}_n)\big]\cdot\mathbf{g}_n=\Big(\underline{\mathbf{R}}_{n-1}\cdot\underline{\mathbf{R}}_n^{-1}\cdot\underline{\mathbf{Q}}_n-\underline{\mathbf{Q}}_{n-1}-\underline{\mathbf{L}}_{n-1}\Big)\cdot\mathbf{g}_{n-1}$$
$$+\mathbf{D}_{n-1}-\underline{\mathbf{R}}_{n-1}\cdot\underline{\mathbf{R}}_n^{-1}\cdot\mathbf{D}_n$$

Therefore, by inspection, we arrive at the results for $\underline{\boldsymbol{\alpha}}_n$ and $\boldsymbol{\beta}_n$ for the deeply-trapped end:

$$\boxed{\begin{aligned}\underline{\boldsymbol{\alpha}}_n&=\underline{\mathbf{M}}_n^{-1}\cdot\Big(\underline{\mathbf{R}}_{n-1}\cdot\underline{\mathbf{R}}_n^{-1}\cdot\underline{\mathbf{Q}}_n-\underline{\mathbf{Q}}_{n-1}-\underline{\mathbf{L}}_{n-1}\Big),\\ \boldsymbol{\beta}_n&=\underline{\mathbf{M}}_n^{-1}\cdot\big(\mathbf{D}_{n-1}-\underline{\mathbf{R}}_{n-1}\cdot\underline{\mathbf{R}}_n^{-1}\cdot\mathbf{D}_n\big)\\ \underline{\mathbf{M}}_n&=\underline{\mathbf{P}}_{n-1}-\underline{\mathbf{R}}_{n-1}\cdot\underline{\mathbf{R}}_n^{-1}\cdot(\underline{\mathbf{P}}_n+\underline{\mathbf{L}}_n)\end{aligned}} \tag{8.5.46}$$

Ion solution at the trapped-passing boundary

Recall the matching conditions given by Eq.(2.3.52), (2.3.53), (2.3.54):

$$\sum_\sigma \sigma\hat{g}_p^\sigma=0 \tag{8.5.47}$$

$$\sum_\sigma \hat{g}_p^\sigma=2\hat{g}_t \tag{8.5.48}$$

$$\sum_\sigma \frac{\partial\hat{g}_p^\sigma}{\partial y}=2\frac{\partial\hat{g}_t}{\partial y}, \tag{8.5.49}$$

Within the code, Eqs.(8.5.47)$\sim$(8.5.49) couple the solutions at $y=y_c$ and its neighbours. Defining $\hat{g}_{cp}^{\pm}=\hat{g}_c-\epsilon$ and $\hat{g}_{ct}=\hat{g}_c+\epsilon$, the first two conditions imply that:

$$\lim_{\epsilon\to0}\quad \hat{g}_{cp}^{+}=\hat{g}_{cp}^{-},\quad \hat{g}_{cp}^{+}+\hat{g}_{cp}^{-}=2\hat{g}_{ct}\equiv2\hat{g}_c,$$

i.e. $\hat{g}_c$ is continuous and single-valued at exactly $y=y_c$. Using quadratic fitting, Eq.(8.5.49) links the 5 neighbouring points, centred about y_c (links three points at a time on the either side of, and including, y_c).

On the marginally passing side, write the quadratic fitting for the solution vectors:

$$\mathbf{g}_c^{\pm} = \mathbf{a}^{\pm} y_c^2 + \mathbf{b}^{\pm} y_c + \mathbf{c}$$
$$\mathbf{g}_p^{\pm} = \mathbf{a}^{\pm} y_p^2 + \mathbf{b}^{\pm} y_p + \mathbf{c}$$
$$\mathbf{g}_{pp}^{\pm} = \mathbf{a}^{\pm} y_{pp}^2 + \mathbf{b}^{\pm} y_{pp} + \mathbf{c}$$

Subtracting one from another:

$$\mathbf{g}_c^{\pm} - \mathbf{g}_p^{\pm} = \mathbf{a}^{\pm}(y_c^2 - y_p^2) + \mathbf{b}^{\pm}(y_c - y_p)$$
$$\mathbf{g}_p^{\pm} - \mathbf{g}_{pp}^{\pm} = \mathbf{a}^{\pm}(y_p^2 - y_{pp}^2) + \mathbf{b}^{\pm}(y_p - y_{pp}).$$

Defining $h_{pp} = y_p - y_{pp}$, $h_p = y_c - y_p$, and $h_{cp} = y_c - y_{pp} = h_p + h_{pp}$,

$$\frac{\mathbf{g}_c - \mathbf{g}_p^{\pm}}{h_p} = \mathbf{a}^{\pm}(y_p + y_c) + \mathbf{b}^{\pm}$$
$$\frac{\mathbf{g}_p^{\pm} - \mathbf{g}_{pp}^{\pm}}{h_{pp}} = \mathbf{a}^{\pm}(y_p + y_{pp}) + \mathbf{b}^{\pm}$$

Subtracting one from the other:

$$(y_c - y_{pp})\mathbf{a}^{\pm} = \frac{\mathbf{g}_c - \mathbf{g}_p^{\pm}}{h_p} - \frac{\mathbf{g}_p^{\pm} - \mathbf{g}_{pp}^{\pm}}{h_{pp}}$$
$$h_{cp}\mathbf{a}^{\pm} = \frac{h_{pp}\mathbf{g}_c - (h_{pp} + h_p)\mathbf{g}_p^{\pm} + h_p \mathbf{g}_{pp}^{\pm}}{h_{pp} h_p}$$

$$\therefore\ \mathbf{a}^{\pm} = \frac{h_{pp}\mathbf{g}_c - h_{cp}\mathbf{g}_p^{\pm} + h_p \mathbf{g}_{pp}^{\pm}}{h_{pp} h_p h_{cp}}, \tag{8.5.50}$$

$$\text{and}\ \ \mathbf{b}^{\pm} = \frac{\mathbf{g}_c - \mathbf{g}_p^{\pm}}{h_p} - (y_p + y_c)\mathbf{a}^{\pm}. \tag{8.5.51}$$

Then, the y-derivative on the marginally passing side:

$$\left.\frac{\partial \mathbf{g}^{\sigma}}{\partial y}\right|_{y_l} = 2\mathbf{a}^{\sigma} y_l + \mathbf{b}^{\sigma},$$
$$\rightarrow \sum_{\sigma} \left.\frac{\partial \mathbf{g}^{\sigma}}{\partial y}\right|_{y_c} = 2(\mathbf{a}^{+} + \mathbf{a}^{-}) y_c + \mathbf{b}^{+} + \mathbf{b}^{-}. \tag{8.5.52}$$

Next, derive the quadratic fitting on the marginally trapped side:

$$\mathbf{g}_{tt} = \mathbf{a}^t y_{tt}^2 + \mathbf{b}^t y_{tt} + \mathbf{c}$$
$$\mathbf{g}_{t} = \mathbf{a}^t y_{t}^2 + \mathbf{b}^t y_{t} + \mathbf{c}$$
$$\mathbf{g}_{c} = \mathbf{a}^t y_{c}^2 + \mathbf{b}^t y_{c} + \mathbf{c}$$

Subtracting one from another:

$$\frac{\mathbf{g}_{tt} - \mathbf{g}_t}{h_{tt}} = (y_t + y_{tt})\mathbf{a}^t + \mathbf{b}^t$$
$$\frac{\mathbf{g}_{t} - \mathbf{g}_c}{h_{t}} = (y_c + y_{t})\mathbf{a}^t + \mathbf{b}^t,$$

where $h_t = y_t - y_c$, $h_{tt} = y_{tt} - y_t$ and $h_{ct} = y_{tt} - y_c \equiv h_{tt} + h_t$. Subtracting one from another in the above pair of equations:

$$(y_{tt} - y_c)\mathbf{a}^t = \frac{\mathbf{g}_{tt} - \mathbf{g}_t}{h_{tt}} - \frac{\mathbf{g}_t - \mathbf{g}_c}{h_t}$$
$$h_{ct}\mathbf{a}^t = \frac{h_t \mathbf{g}_{tt} - (h_t + h_{tt})\mathbf{g}_t + h_{tt}\mathbf{g}_c}{h_{tt} h_t}$$

$$\therefore \ \mathbf{a}^t = \frac{h_{tt}\mathbf{g}_c - h_{ct}\mathbf{g}_t + h_t \mathbf{g}_{tt}}{h_{tt} h_t h_{ct}}, \tag{8.5.53}$$

$$\text{and} \ \ \mathbf{b}^t = \frac{\mathbf{g}_t - \mathbf{g}_c}{h_t} - (y_c + y_t)\mathbf{a}^t. \tag{8.5.54}$$

Then, the y-derivative on the marginally trapped side:

$$2\,\frac{\partial \mathbf{g}}{\partial y}\bigg|_{y_c} = 4\mathbf{a}^t y_c + 2\mathbf{b}^t. \tag{8.5.55}$$

Now the matching condition (8.5.49), together with Eqs.(8.5.52) and (8.5.55), can be used to derive the equation for $\mathbf{g}_c$, starting from:

$$2(\mathbf{a}^+ + \mathbf{a}^-)y_c + \mathbf{b}^+ + \mathbf{b}^- = 4\mathbf{a}^t y_c + 2\mathbf{b}^t. \tag{8.5.56}$$

Firstly, the right hand side:

$$\begin{aligned}\text{RHS} = 4\mathbf{a}^t y_c + 2\mathbf{b}^t &= 4\mathbf{a}^t y_c - 2(y_t + y_c)\mathbf{a}^t + 2\frac{(\mathbf{g}_t - \mathbf{g}_c)}{h_t} \\ &= -2h_t\mathbf{a}^t + 2\frac{(\mathbf{g}_t - \mathbf{g}_c)}{h_t} \\ &= -2\frac{h_t}{h_t h_{ct}}\mathbf{g}_c + 2\frac{h_t}{h_t h_{tt}}\mathbf{g}_t - 2\frac{h_t}{h_{tt}h_{ct}}\mathbf{g}_{tt} - 2\frac{h_{ct}}{h_t h_{ct}}\mathbf{g}_c + 2\frac{h_{tt}}{h_{tt}h_{ct}}\mathbf{g}_t\end{aligned}$$

Defining $\Delta_{ct} = -\dfrac{h_t + h_{ct}}{h_t h_{ct}}$, $\Delta_t = \dfrac{h_{ct}}{h_t h_{tt}}$, $\Delta_{tt} = -\dfrac{h_t}{h_{tt}h_{ct}}$,

$$\text{RHS} = 2\Delta_{ct}\mathbf{g}_c + 2\Delta_t\mathbf{g}_t + 2\Delta_{tt}\mathbf{g}_{tt}.$$

But, by the linear recursion relation (8.5.20) and (8.5.24),

$$\begin{aligned}&\mathbf{g}_{tt} = \underline{\boldsymbol{\alpha}}_{tt}\cdot\mathbf{g}_t + \boldsymbol{\beta}_{tt} \\ \rightarrow\ &\text{RHS} = 2\Delta_{ct}\mathbf{g}_c + 2(\Delta_t\underline{\mathbf{I}} + \Delta_{tt}\underline{\boldsymbol{\alpha}}_{tt})\cdot\mathbf{g}_t + 2\Delta_{tt}\boldsymbol{\beta}_{tt},\end{aligned}$$

where $\underline{\mathbf{I}}$ is an identity matrix. But also:

$$\begin{aligned}&\mathbf{g}_t = \underline{\boldsymbol{\alpha}}_t\cdot\mathbf{g}_c + \boldsymbol{\beta}_t \\ \rightarrow\ &\text{RHS} = 2\Delta_{ct}\mathbf{g}_c + 2(\Delta_t\underline{\mathbf{I}} + \Delta_{tt}\underline{\boldsymbol{\alpha}}_{tt})\cdot(\underline{\boldsymbol{\alpha}}_t\cdot\mathbf{g}_c + \boldsymbol{\beta}_t) + 2\Delta_{tt}\boldsymbol{\beta}_{tt},\end{aligned}$$

$$\therefore\ \underline{\text{RHS} = 2\left[\Delta_{ct}\underline{\mathbf{I}} + (\Delta_t\underline{\mathbf{I}} + \Delta_{tt}\underline{\boldsymbol{\alpha}}_{tt})\cdot\underline{\boldsymbol{\alpha}}_t\right]\cdot\mathbf{g}_c + 2\left[(\Delta_t\underline{\mathbf{I}} + \Delta_{tt}\underline{\boldsymbol{\alpha}}_{tt})\cdot\boldsymbol{\beta}_t + \Delta_{tt}\boldsymbol{\beta}_{tt}\right]} \tag{8.5.57}$$

Next, the left hand side of Eq.(8.5.56):

$$\begin{aligned}\text{LHS} = 2(\mathbf{a}^+ + \mathbf{a}^-)y_c + \mathbf{b}^+ + \mathbf{b}^- &= 2y_c(\mathbf{a}^+ + \mathbf{a}^-) + \frac{2\mathbf{g}_c - \mathbf{g}_p^+ - \mathbf{g}_p^-}{h_p} - (y_p + y_c)(\mathbf{a}^+ + \mathbf{a}^-) \\ &= h_p(\mathbf{a}^+ + \mathbf{a}^-) + \frac{2\mathbf{g}_c - (\mathbf{g}_p^+ + \mathbf{g}_p^-)}{h_p} \\ &= 2\frac{h_p}{h_p h_{cp}}\mathbf{g}_c - \frac{h_p}{h_p h_{pp}}(\mathbf{g}_p^+ + \mathbf{g}_p^-) + \frac{h_p}{h_{pp}h_{cp}}(\mathbf{g}_{pp}^+ + \mathbf{g}_{pp}^-) + 2\frac{h_{cp}}{h_p h_{cp}}\mathbf{g}_c - \frac{h_{pp}}{h_p h_{pp}}(\mathbf{g}_p^+ + \mathbf{g}_p^-)\end{aligned}$$

Defining $\Delta_{cp} = \dfrac{h_p + h_{cp}}{h_p h_{cp}}$, $\Delta_p = -\dfrac{h_{cp}}{h_p h_{pp}}$, $\Delta_{pp} = \dfrac{h_p}{h_{pp}h_{cp}}$,

$$\text{LHS} = 2\Delta_{cp}\mathbf{g}_c + \Delta_p(\mathbf{g}_p^+ + \mathbf{g}_p^-) + \Delta_{pp}(\mathbf{g}_{pp}^+ + \mathbf{g}_{pp}^-).$$

But, again by the linear recursion relation (8.5.15) and (8.5.19),

$$\begin{aligned} \mathbf{g}_{pp}^{\pm} &= \underline{\boldsymbol{\alpha}}_{pp}^{\pm} \cdot \mathbf{g}_{p}^{\pm} + \boldsymbol{\beta}_{pp}^{\pm} \\ \rightarrow \ \text{LHD} &= 2\Delta_{cp}\mathbf{g}_c + (\Delta_p \underline{\mathbf{I}} + \Delta_{pp}\underline{\boldsymbol{\alpha}}_{pp}^{+}) \cdot \mathbf{g}_{p}^{+} + (\Delta_p \underline{\mathbf{I}} + \Delta_{pp}\underline{\boldsymbol{\alpha}}_{pp}^{-}) \cdot \mathbf{g}_{p}^{-} + \Delta_{pp}(\boldsymbol{\beta}_{pp}^{+} + \boldsymbol{\beta}_{pp}^{-}). \end{aligned}$$

But also:

$$\begin{aligned} \mathbf{g}_{p}^{\pm} &= \underline{\boldsymbol{\alpha}}_{p}^{\pm} \cdot \mathbf{g}_{c}^{\pm} + \boldsymbol{\beta}_{p}^{\pm} \\ \rightarrow \ \text{LHS} &= 2\Delta_{cp}\mathbf{g}_c + (\Delta_p \underline{\mathbf{I}} + \Delta_{pp}\underline{\boldsymbol{\alpha}}_{pp}^{+}) \cdot (\underline{\boldsymbol{\alpha}}_{p}^{+} \cdot \mathbf{g}_c + \boldsymbol{\beta}_{p}^{+}) \\ &\quad + (\Delta_p \underline{\mathbf{I}} + \Delta_{pp}\underline{\boldsymbol{\alpha}}_{pp}^{-}) \cdot (\underline{\boldsymbol{\alpha}}_{p}^{-} \cdot \mathbf{g}_c + \boldsymbol{\beta}_{p}^{-}) + \Delta_{pp}(\boldsymbol{\beta}_{pp}^{+} + \boldsymbol{\beta}_{pp}^{-}) \end{aligned}$$

$$\begin{aligned} \therefore \ \text{LHS} = &\left[2\Delta_{cp}\underline{\mathbf{I}} + (\Delta_p \underline{\mathbf{I}} + \Delta_{pp}\underline{\boldsymbol{\alpha}}_{pp}^{+}) \cdot \underline{\boldsymbol{\alpha}}_{p}^{+} + (\Delta_p \underline{\mathbf{I}} + \Delta_{pp}\underline{\boldsymbol{\alpha}}_{pp}^{-}) \cdot \underline{\boldsymbol{\alpha}}_{p}^{-}\right] \cdot \mathbf{g}_c \\ &+ (\Delta_p \underline{\mathbf{I}} + \Delta_{pp}\underline{\boldsymbol{\alpha}}_{pp}^{+}) \cdot \boldsymbol{\beta}_{p}^{+} + (\Delta_p \underline{\mathbf{I}} + \Delta_{pp}\underline{\boldsymbol{\alpha}}_{pp}^{-}) \cdot \boldsymbol{\beta}_{p}^{-} + \Delta_{pp}(\boldsymbol{\beta}_{pp}^{+} + \boldsymbol{\beta}_{pp}^{-}). \end{aligned} \tag{8.5.58}$$

Finally, LHS (8.5.58) = RHS (8.5.57) results in the equation for $\mathbf{g}_c$:

$$\boxed{\begin{aligned} \underline{\mathbf{A}} \cdot \mathbf{g}_c \ &= \ \mathbf{B}, \\ \underline{\mathbf{A}} = &\ 2\Delta_{cp}\underline{\mathbf{I}} + (\Delta_p \underline{\mathbf{I}} + \Delta_{pp}\underline{\boldsymbol{\alpha}}_{pp}^{+}) \cdot \underline{\boldsymbol{\alpha}}_{p}^{+} + (\Delta_p \underline{\mathbf{I}} + \Delta_{pp}\underline{\boldsymbol{\alpha}}_{pp}^{-}) \cdot \underline{\boldsymbol{\alpha}}_{p}^{-} \\ &- 2\Delta_{ct}\underline{\mathbf{I}} - 2(\Delta_t \underline{\mathbf{I}} + \Delta_{tt}\underline{\boldsymbol{\alpha}}_{tt}) \cdot \underline{\boldsymbol{\alpha}}_{t} \\ \mathbf{B} = &-(\Delta_p \underline{\mathbf{I}} + \Delta_{pp}\underline{\boldsymbol{\alpha}}_{pp}^{+}) \cdot \boldsymbol{\beta}_{p}^{+} - (\Delta_p \underline{\mathbf{I}} + \Delta_{pp}\underline{\boldsymbol{\alpha}}_{pp}^{-}) \cdot \boldsymbol{\beta}_{p}^{-} - \Delta_{pp}(\boldsymbol{\beta}_{pp}^{+} + \boldsymbol{\beta}_{pp}^{-}) \\ &+ 2(\Delta_t \underline{\mathbf{I}} + \Delta_{tt}\underline{\boldsymbol{\alpha}}_{tt}) \cdot \boldsymbol{\beta}_t + 2\Delta_{tt}\boldsymbol{\beta}_{tt} \end{aligned}} \tag{8.5.59}$$

Bibliography

[1] H. A. Bethe. "Energy Production in Stars". In: *Physical Review* 55.1 (Jan. 1939), pp. 103–103. ISSN: 0031-899X. DOI: 10.1103/PhysRev.55.103. URL: https://link.aps.org/doi/10.1103/PhysRev.55.103.

[2] Katherine Calvin et al. *IPCC, 2023: Climate Change 2023: Synthesis Report. Contribution of Working Groups I, II and III to the Sixth Assessment Report of the Intergovernmental Panel on Climate Change [Core Writing Team, H. Lee and J. Romero (eds.)]. IPCC, Geneva, Switzerland.* Tech. rep. Intergovernmental Panel on Climate Change, July 2023. DOI: 10.59327/IPCC/AR6-9789291691647. URL: https://www.ipcc.ch/report/ar6/syr/.

[3] World Energy Council (WEC). *World Energy Issues Monitor 2022.* URL: https://www.worldenergy.org/publications/entry/world-energy-issues-monitor-2022.

[4] International Energy Agency (IEA). *World Energy Outlook 2022.* Tech. rep. URL: https://www.iea.org/reports/world-energy-outlook-2022.

[5] International Atomic Energy Agency (IAEA). *Fusion Physics.* Ed. by Kikuchi Mitsuru et al. Vienna, 2012.

[6] Samuel E. Wurzel and Scott C. Hsu. "Progress toward fusion energy breakeven and gain as measured against the Lawson criterion". In: *Physics of Plasmas* 29.6 (June 2022). ISSN: 1070-664X. DOI: 10.1063/5.0083990. URL: https://pubs.aip.org/pop/article/29/6/062103/2847827/Progress-toward-fusion-energy-breakeven-and-gain.

[7] International Atomic Energy Agency (IAEA). *World Survey of Fusion Devices 2022.* Tech. rep. Vienna, 2023. URL: https://www.iaea.org/publications/15253/world-survey-of-fusion-devices-2022.

[8] J Wesson. "Tokamaks". In: *Clarendon Press, Oxford* (2004).

[9] Roger M. White et al. "Evaluation of Charged-Particle Reactions for Fusion Applications". In: 1992, pp. 834–839. DOI: 10.1007/978-3-642-58113-7{_}230. URL: http://link.springer.com/10.1007/978-3-642-58113-7_230.

[10] J D Lawson. "Some Criteria for a Power Producing Thermonuclear Reactor". In: *Proceedings of the Physical Society. Section B* 70.1 (Jan. 1957), pp. 6–10. ISSN: 0370-1301. DOI: 10.1088/0370-1301/70/1/303. URL: https://iopscience.iop.org/article/10.1088/0370-1301/70/1/303.

[11] J. Mailloux et al. "Overview of JET results for optimising ITER operation". In: *Nuclear Fusion* 62.4 (Apr. 2022), p. 042026. ISSN: 0029-5515. DOI: 10.1088/1741-4326/ac47b4. URL: https://iopscience.iop.org/article/10.1088/1741-4326/ac47b4.

[12] B J Green et al. "ITER: burning plasma physics experiment". In: *Plasma Physics and Controlled Fusion* 45.5 (May 2003), pp. 687–706. ISSN: 0741-3335. DOI: 10.1088/0741-3335/45/5/312. URL: https://iopscience.iop.org/article/10.1088/0741-3335/45/5/312.

[13] E J Doyle et al. "Chapter 2: Plasma confinement and transport". In: *Nuclear Fusion* 47.6 (June 2007), S18. DOI: 10.1088/0029-5515/47/6/S02. URL: https://dx.doi.org/10.1088/0029-5515/47/6/S02.

[14] G. Federici et al. "DEMO design activity in Europe: Progress and updates". In: *Fusion Engineering and Design* 136 (Nov. 2018), pp. 729–741. ISSN: 09203796. DOI: 10.1016/j.fusengdes.2018.04.001. URL: https://linkinghub.elsevier.com/retrieve/pii/S0920379618302898.

[15] UKAEA. *Spherical tokamak for energy production (STEP)*. Aug. 2023. URL: https://step.ukaea.uk.

[16] Francis F. Chen. *Introduction to Plasma Physics and Controlled Fusion*. Cham: Springer International Publishing, 2016. ISBN: 978-3-319-22308-7. DOI: 10.1007/978-3-319-22309-4. URL: http://link.springer.com/10.1007/978-3-319-22309-4.

[17] Per Helander and Dieter J Sigmar. *Collisional transport in magnetized plasmas*. eng. Cambridge monographs on plasma physics. Cambridge: Cambridge University Press, 2005. ISBN: 9780521807982.

[18] R D Hazeltine and J D Meiss. *Plasma Confinement*. Dover books on physics. Dover Publications, 2003. ISBN: 9780486432427. URL: https://books.google.co.uk/books?id=s3LQU_04GccC.

[19] T.C Hender et al. "Chapter 3: MHD stability, operational limits and disruptions". In: *Nuclear Fusion* 47.6 (June 2007), S128–S202. ISSN: 0029-5515. DOI: 10.1088/0029-5515/47/6/S03. URL: https://iopscience.iop.org/article/10.1088/0029-5515/47/6/S03.

[20] Marshall N. Rosenbluth et al. "Fokker-Planck Equation for an Inverse-Square Force". In: *Physical Review* 107.1 (July 1957), pp. 1–6. ISSN: 0031-899X. DOI: 10.1103/PhysRev.107.1. URL: https://link.aps.org/doi/10.1103/PhysRev.107.1.

[21] B B Kadomtsev. "Magnetic field line reconnection". In: *Reports on Progress in Physics* 50.2 (Feb. 1987), pp. 115–143. ISSN: 0034-4885. DOI: 10.1088/0034-4885/50/2/001. URL: https://iopscience.iop.org/article/10.1088/0034-4885/50/2/001.

[22] Allen H. Boozer. "Physics of magnetically confined plasmas". In: *Reviews of Modern Physics* 76.4 (Jan. 2005), pp. 1071–1141. ISSN: 0034-6861. DOI: 10.1103/RevModPhys.76.1071. URL: https://link.aps.org/doi/10.1103/RevModPhys.76.1071.

[23] R. J. Bickerton et al. "Diffusion Driven Plasma Currents and Bootstrap Tokamak". In: *Nature Physical Science* 229.4 (Jan. 1971), pp. 110–112. ISSN: 0300-8746. DOI: 10.1038/physci229110a0. URL: https://www.nature.com/articles/physci229110a0.

[24] W X Qu and J D Callen. *Nonlinear growth of a single neoclassical MHD tearing mode in a tokamak*. Tech. rep. Madison, Wisconsin, USA: Dept. of Nuclear Engineering, Wisconsin Univ., 1985.

[25] R. Carrera et al. "Island bootstrap current modification of the nonlinear dynamics of the tearing mode". In: *The Physics of Fluids* 29.4 (Apr. 1986), pp. 899–902. ISSN: 0031-9171. DOI: 10.1063/1.865682. URL: https://pubs.aip.org/pfl/article/29/4/899/819084/Island-bootstrap-current-modification-of-the.

[26] Allen H. Boozer. "Helicity content and tokamak applications of helicity". In: *The Physics of Fluids* 29.12 (Dec. 1986), pp. 4123–4130. ISSN: 0031-9171. DOI: 10.1063/1.865756. URL: https://pubs.aip.org/pfl/article/29/12/4123/943936/Helicity-content-and-tokamak-applications-of.

[27] M Shimada et al. "Chapter 1: Overview and summary". In: *Nuclear Fusion* 47.6 (June 2007), S1–S17. ISSN: 0029-5515. DOI: 10.1088/0029-5515/47/6/S01. URL: https://iopscience.iop.org/article/10.1088/0029-5515/47/6/S01.

[28] Harold P. Furth et al. "Finite-Resistivity Instabilities of a Sheet Pinch". In: *Physics of Fluids* 6.4 (1963), p. 459. ISSN: 00319171. DOI: 10.1063/1.1706761. URL: https://aip.scitation.org/doi/10.1063/1.1694467%20https://aip.scitation.org/doi/10.1063/1.1706761.

[29] R. J. Buttery et al. "Neoclassical tearing modes". In: *Plasma Physics and Controlled Fusion* 42.12B (Dec. 2000), B61–B73. ISSN: 0741-3335. DOI: 10.1088/0741-3335/42/12B/306. URL: https://iopscience.iop.org/article/10.1088/0741-3335/42/12B/306.

[30] A. Gude et al. "Seed island of neoclassical tearing modes at ASDEX Upgrade". In: *Nuclear Fusion* 39.1 (Jan. 1999), pp. 127–131. ISSN: 0029-5515. DOI: 10.1088/0029-5515/39/1/308. URL: https://iopscience.iop.org/article/10.1088/0029-5515/39/1/308.

[31] E J Strait et al. *MHD Instabilities near the P Limit in the Doublet III-D Tokamak*. Tech. rep. 11. 1989.

[32] R. J. La Haye. "Neoclassical tearing modes and their control". In: *Physics of Plasmas* 13.5 (2006), pp. 1–18. ISSN: 1070664X. DOI: 10.1063/1.2180747.

[33] M.F.F. Nave and J.A. Wesson. "Mode locking in tokamaks". In: *Nuclear Fusion* 30.12 (Dec. 1990), pp. 2575–2583. ISSN: 0029-5515. DOI: 10.1088/0029-5515/30/12/011. URL: https://iopscience.iop.org/article/10.1088/0029-5515/30/12/011.

[34] R. J. La Haye et al. "Cross-machine benchmarking for ITER of neoclassical tearing mode stabilization by electron cyclotron current drive". In: *Nuclear Fusion* 46.4 (2006), pp. 451–461. ISSN: 00295515. DOI: 10.1088/0029-5515/46/4/006.

[35] O. Sauter et al. "Beta limits in long-pulse tokamak discharges". In: *Physics of Plasmas* 4.5 (May 1997), pp. 1654–1664. ISSN: 1070-664X. DOI: 10.1063/1.872270. URL: http://aip.scitation.org/doi/10.1063/1.872270.

[36] L. Garzotti et al. "Scenario development for D-T operation at JET". In: *Nuclear Fusion* 59.7 (2019). ISSN: 17414326. DOI: 10.1088/1741-4326/ab1cca.

[37] P. H. Rutherford. "Nonlinear growth of the tearing mode". In: *The Physics of Fluids* 16.11 (Nov. 1973), pp. 1903–1908. ISSN: 0031-9171. DOI: 10.1063/1.1694232. URL: https://pubs.aip.org/pfl/article/16/11/1903/942918/Nonlinear-growth-of-the-tearing-mode.

[38] Roscoe B. White et al. "Saturation of the tearing mode". In: *The Physics of Fluids* 20.5 (May 1977), pp. 800–805. ISSN: 0031-9171. DOI: 10.1063/1.861939. URL: https://pubs.aip.org/pfl/article/20/5/800/457926/Saturation-of-the-tearing-mode.

[39] A. H. Glasser et al. "Resistive instabilities in general toroidal plasma configurations". In: *The Physics of Fluids* 18.7 (July 1975), pp. 875–888. ISSN: 0031-9171. DOI: 10.1063/1.861224. URL: https://pubs.aip.org/pfl/article/18/7/875/446894/Resistive-instabilities-in-general-toroidal-plasma.

[40] R. J. Buttery et al. "Neoclassical Tearing Physics in the Spherical Tokamak MAST". In: *Physical Review Letters* 88.12 (Mar. 2002), p. 125005. ISSN: 0031-9007. DOI: 10.1103/PhysRevLett.88.125005. URL: https://link.aps.org/doi/10.1103/PhysRevLett.88.125005.

[41] A V Dudkovskaia et al. "Drift kinetic theory of neoclassical tearing modes in a low collisionality tokamak plasma: magnetic island threshold physics". In: *Plasma Physics and Controlled Fusion* 63.5 (May 2021), p. 054001. ISSN: 0741-3335. DOI: 10.1088/1361-6587/abea2e. URL: https://iopscience.iop.org/article/10.1088/1361-6587/abea2e.

[42] A.V. Dudkovskaia et al. "Drift kinetic theory of the NTM magnetic islands in a finite beta general geometry tokamak plasma". In: *Nuclear Fusion* 63.1 (Jan. 2023), p. 016020. ISSN: 0029-5515. DOI: 10.1088/1741-4326/aca48d. URL: https://iopscience.iop.org/article/10.1088/1741-4326/aca48d.

[43] A.V. Dudkovskaia et al. "Drift kinetic theory of neoclassical tearing modes in tokamak plasmas: polarisation current and its effect on magnetic island threshold physics". In: *Nuclear Fusion* 63.12 (Dec. 2023), p. 126040. ISSN: 0029-5515. DOI: 10.1088/1741-4326/acfe8c. URL: https://iopscience.iop.org/article/10.1088/1741-4326/acfe8c.

[44] Z. Chang et al. "Observation of Nonlinear Neoclassical Pressure-Gradient–Driven Tearing Modes in TFTR". In: *Physical Review Letters* 74.23 (June 1995), pp. 4663–4666. ISSN: 0031-9007. DOI: 10.1103/PhysRevLett.74.4663. URL: https://link.aps.org/doi/10.1103/PhysRevLett.74.4663.

[45] Richard Fitzpatrick. "Helical temperature perturbations associated with tearing modes in tokamak plasmas". In: *Physics of Plasmas* 2.3 (Mar. 1995), pp. 825–838. ISSN: 1070-664X. DOI: 10.1063/1.871434. URL: http://aip.scitation.org/doi/10.1063/1.871434.

[46] N. N. Gorelenkov et al. "A threshold for excitation of neoclassical tearing modes". In: *Physics of Plasmas* 3.9 (Sept. 1996), pp. 3379–3385. ISSN: 1070-664X. DOI: 10.1063/1.871614. URL: https://pubs.aip.org/pop/article/3/9/3379/443124/A-threshold-for-excitation-of-neoclassical-tearing.

[47] R. D. Hazeltine et al. "Plasma transport near the separatrix of a magnetic island". In: *Physics of Plasmas* 4.8 (Aug. 1997), pp. 2920–2927. ISSN: 1070664X. DOI: 10.1063/1.872423. URL: http://aip.scitation.org/doi/10.1063/1.872423.

[48] H.R. Wilson. "Neoclassical Tearing Modes". In: *Fusion Science and Technology* 53.2T (Feb. 2008), pp. 152–160. ISSN: 1536-1055. DOI: 10.13182/FST08-A1701. URL: https://www.tandfonline.com/doi/full/10.13182/FST08-A1701.

[49] A I Smolyakov. "Nonlinear evolution of tearing modes in inhomogeneous plasmas". In: *Plasma Physics and Controlled Fusion* 35.6 (June 1993), pp. 657–687. ISSN: 0741-3335. DOI: 10.1088/0741-3335/35/6/002. URL: https://iopscience.iop.org/article/10.1088/0741-3335/35/6/002.

[50] H. R. Wilson et al. "Threshold for neoclassical magnetic islands in a low collision frequency tokamak". In: *Physics of Plasmas* 3.1 (Jan. 1996), pp. 248–265. ISSN: 1070-664X. DOI: 10.1063/1.871830. URL: https://pubs.aip.org/pop/article/3/1/248/263428/Threshold-for-neoclassical-magnetic-islands-in-a.

[51] J. W. Connor et al. "The role of polarization current in magnetic island evolution". In: *Physics of Plasmas* 8.6 (June 2001), pp. 2835–2848. ISSN: 1070-664X. DOI: 10.1063/1.1370062. URL: https://pubs.aip.org/pop/article/8/6/2835/730533/The-role-of-polarization-current-in-magnetic.

[52] F. L. Waelbroeck et al. "Finite Larmor-Radius Theory of Magnetic Island Evolution". In: *Physical Review Letters* 87.21 (Nov. 2001), p. 215003. ISSN: 0031-9007. DOI: 10.1103/PhysRevLett.87.215003. URL: https://link.aps.org/doi/10.1103/PhysRevLett.87.215003.

[53] M James et al. "Modelling the effect of cross-field diffusion on tearing mode stability". In: *Plasma Physics and Controlled Fusion* 52.7 (July 2010), p. 075008. ISSN: 0741-3335. DOI:

10.1088/0741-3335/52/7/075008. URL: https://iopscience.iop.org/article/10.1088/0741-3335/52/7/075008.

[54] H R Wilson et al. "The collisionality dependence of tokamak -limits". In: *Plasma Physics and Controlled Fusion* 38.12A (Dec. 1996), A149–A163. ISSN: 0741-3335. DOI: 10.1088/0741-3335/38/12A/012. URL: https://iopscience.iop.org/article/10.1088/0741-3335/38/12A/012.

[55] A. Bergmann et al. "Collisionality dependence of the polarization current caused by a rotating magnetic island". In: *Physics of Plasmas* 12.7 (July 2005), p. 072501. ISSN: 1070-664X. DOI: 10.1063/1.1937338. URL: http://aip.scitation.org/doi/10.1063/1.1937338.

[56] F. L. Waelbroeck and R. Fitzpatrick. "Rotation and Locking of Magnetic Islands". In: *Physical Review Letters* 78.9 (Mar. 1997), pp. 1703–1706. ISSN: 0031-9007. DOI: 10.1103/PhysRevLett.78.1703. URL: https://link.aps.org/doi/10.1103/PhysRevLett.78.1703.

[57] E. Poli et al. "Kinetic calculation of the polarization current in the presence of a neoclassical tearing mode". In: *Nuclear Fusion* 45.5 (May 2005), pp. 384–390. ISSN: 0029-5515. DOI: 10.1088/0029-5515/45/5/009. URL: https://iopscience.iop.org/article/10.1088/0029-5515/45/5/009.

[58] R. J. La Haye et al. "Propagation of magnetic islands in the Er=0 frame of co-injected neutral beam driven discharges in the DIII-D tokamak". In: *Physics of Plasmas* 10.9 (Sept. 2003), pp. 3644–3648. ISSN: 1070-664X. DOI: 10.1063/1.1602452. URL: https://pubs.aip.org/pop/article/10/9/3644/463336/Propagation-of-magnetic-islands-in-the-Er-0-frame.

[59] H. Reimerdes et al. "From Current-Driven to Neoclassically Driven Tearing Modes". In: *Physical Review Letters* 88.10 (Feb. 2002), p. 105005. ISSN: 0031-9007. DOI: 10.1103/PhysRevLett.88.105005. URL: https://link.aps.org/doi/10.1103/PhysRevLett.88.105005.

[60] O Sauter et al. "Marginal β-limit for neoclassical tearing modes in JET H-mode discharges". In: *Plasma Physics and Controlled Fusion* 44.9 (Sept. 2002), pp. 1999–2019. ISSN: 0741-3335. DOI: 10.1088/0741-3335/44/9/315. URL: https://iopscience.iop.org/article/10.1088/0741-3335/44/9/315.

[61] G. Gantenbein et al. "Complete Suppression of Neoclassical Tearing Modes with Current Drive at the Electron-Cyclotron-Resonance Frequency in ASDEX Upgrade Tokamak". In: *Physical Review Letters* 85.6 (Aug. 2000), pp. 1242–1245. ISSN: 0031-9007. DOI: 10.1103/PhysRevLett.85.1242. URL: https://link.aps.org/doi/10.1103/PhysRevLett.85.1242.

[62] H Zohm et al. "The physics of neoclassical tearing modes and their stabilization by ECCD in ASDEX Upgrade". In: *Nuclear Fusion* 41.2 (Feb. 2001), pp. 197–202. ISSN: 0029-5515. DOI: 10.1088/0029-5515/41/2/306. URL: https://iopscience.iop.org/article/10.1088/0029-5515/41/2/306.

[63] R. J. La Haye et al. "Control of neoclassical tearing modes in DIII–D". In: *Physics of Plasmas* 9.5 (May 2002), pp. 2051–2060. ISSN: 1070-664X. DOI: 10.1063/1.1456066. URL: https://pubs.aip.org/pop/article/9/5/2051/1070453/Control-of-neoclassical-tearing-modes-in-DIII-D.

[64] O Sauter et al. "On the requirements to control neoclassical tearing modes in burning plasmas". In: *Plasma Physics and Controlled Fusion* 52.2 (Feb. 2010), p. 025002. ISSN: 0741-3335. DOI: 10.1088/0741-3335/52/2/025002. URL: https://iopscience.iop.org/article/10.1088/0741-3335/52/2/025002.

[65] E. Poli et al. "On recent results in the modelling of neoclassical-tearing-mode stabilization via electron cyclotron current drive and their impact on the design of the upper EC launcher for ITER". In: *Nuclear Fusion* 55.1 (Jan. 2015), p. 013023. ISSN: 0029-5515. DOI: 10.1088/0029-5515/55/1/013023. URL: https://iopscience.iop.org/article/10.1088/0029-5515/55/1/013023.

[66] R. J. La Haye et al. "Aspect ratio effects on neoclassical tearing modes from comparison between DIII-D and National Spherical Torus Experiment". In: *Physics of Plasmas* 19.6 (June 2012), pp. 857–860. ISSN: 1070-664X. DOI: 10.1063/1.4729658. URL: https://pubs.aip.org/pop/article/19/6/062506/381167/Aspect-ratio-effects-on-neoclassical-tearing-modes.

[67] E. Poli et al. "Monte Carlo δf simulation of the bootstrap current in the presence of a magnetic island". In: *Plasma Physics and Controlled Fusion* 45.2 (Feb. 2003), pp. 71–87. ISSN: 0741-3335. DOI: 10.1088/0741-3335/45/2/301. URL: https://iopscience.iop.org/article/10.1088/0741-3335/45/2/301.

[68] Huishan Cai et al. "Influence of ion orbit width on onset threshold of neoclassical tearing modes". In: *Physics of Plasmas* 22.10 (Oct. 2015). ISSN: 1070-664X. DOI: 10.1063/1.4934214. URL: https://pubs.aip.org/pop/article/22/10/102512/109866/Influence-of-ion-orbit-width-on-onset-threshold-of.

[69] K. Imada et al. "Nonlinear Kinetic Ion Response to Small Scale Magnetic Islands in Tokamak Plasmas: Neoclassical Tearing Mode Threshold Physics". In: *Physical Review Letters* 121.17 (Oct. 2018). ISSN: 10797114. DOI: 10.1103/PhysRevLett.121.175001.

[70] K. Imada et al. "Finite ion orbit width effect on the neoclassical tearing mode threshold in a tokamak plasma". In: *Nuclear Fusion* 59.4 (Apr. 2019), p. 046016. ISSN: 0029-5515. DOI: 10.1088/1741-4326/ab00ba. URL: https://iopscience.iop.org/article/10.1088/1741-4326/ab00ba.

[71] B.B. Kadomtsev. "Plasma transport in tokamaks". In: *Nuclear Fusion* 31.7 (July 1991), pp. 1301–1314. ISSN: 0029-5515. DOI: 10.1088/0029-5515/31/7/006. URL: https://iopscience.iop.org/article/10.1088/0029-5515/31/7/006.

[72] Koki Imada. *private communication*. 2020.

[73] O. Sauter and S.Yu. Medvedev. "Tokamak coordinate conventions: COCOS". In: *Computer Physics Communications* 184.2 (Feb. 2013), pp. 293–302. ISSN: 00104655. DOI: 10.1016/j.cpc.2012.09.010. URL: https://linkinghub.elsevier.com/retrieve/pii/S0010465512002962.

[74] K Imada and H R Wilson. "Influence of collision frequency on neoclassical polarization current". In: *Plasma Physics and Controlled Fusion* 51.10 (Oct. 2009), p. 105010. ISSN: 0741-3335. DOI: 10.1088/0741-3335/51/10/105010. URL: https://iopscience.iop.org/article/10.1088/0741-3335/51/10/105010.

[75] K. Imada and H. R. Wilson. "Collision frequency dependence of polarization current in neoclassical tearing modes". In: *Physics of Plasmas* 19.3 (Mar. 2012). ISSN: 1070664X. DOI: 10.1063/1.3698618.

[76] S.P. Hirshman and D.J. Sigmar. "Neoclassical transport of impurities in tokamak plasmas". In: *Nuclear Fusion* 21.9 (Sept. 1981), pp. 1079–1201. ISSN: 0029-5515. DOI: 10.1088/0029-5515/21/9/003.

[77] kokuchou authors. *kokuchou: 4D Drift-Kinetic NTM Solver v10.4.1 (release pending)*. 2023.

[78] Dudkovskaia A. V. *private communication*. 2023.

[79] E. Anderson et al. *LAPACK Users' Guide*. Society for Industrial and Applied Mathematics, Jan. 1999. ISBN: 978-0-89871-447-0. DOI: 10.1137/1.9780898719604.

[80] neasy-f Authors. *neasy-f*. URL: https://github.com/PlasmaFAIR/neasy-f.

[81] pFUnit Authors. *pFUnit*. 2023. URL: https://github.com/Goddard-Fortran-Ecosystem/pFUnit.

[82] Michael Rilee and Thomas Clune. "Towards Test Driven Development for Computational Science with pFUnit". In: *2014 Second International Workshop on Software Engineering for High Performance Computing in Computational Science and Engineering*. IEEE, Nov. 2014, pp. 20–27. ISBN: 978-1-4799-7035-3. DOI: 10.1109/SE-HPCCSE.2014.5. URL: http://ieeexplore.ieee.org/document/7017328/.

[83] ARCHER2 National Supercomputing Service. *ARCHER2*. Nov. 2023. URL: https://www.archer2.ac.uk/.

[84] Howard R Wilson. *private communication*. 2023.